

**CONDUIT AND ERUPTION DYNAMICS OF THE 1912 VULCANIAN
EXPLOSIONS AT NOVARUPTA, ALASKA**

A DISSERTATION SUBMITTED TO THE GRADUATE DIVISION OF
THE UNIVERSITY OF HAWAI'I AT MĀNOA IN PARTIAL
FULFILLMENT OF THE REQUIREMENTS FOR THE DEGREE OF

DOCTOR OF PHILOSOPHY

IN

GEOLOGY AND GEOPHYSICS

December 2017

By

Samantha Jo Isgett

Dissertation Committee:

Bruce F. Houghton, Chairperson
Helge M. Gonnermann
Christina Neal
Thomas Shea
John Allen

© 2017, Samantha Jo Isgett

Acknowledgements

I probably would not be “standing here today” if my advisor Bruce Houghton had not introduced me to the wonderful world of volcanology. I entered his 300 level volcanology class as a naïve sophomore who had no ambitions of going to graduate school and left knowing that I wanted to be volcanologist and the steps that I needed to take to get there. Bruce has a passion not only for solving the big science question, but also in passing on his knowledge and skill-sets to his students. I cannot thank Bruce enough for seeing in me the potential makings of a scientist and guiding me there. It was, and always will be, a privilege to work with you.

I would like to thank my committee — Helge Gonnermann, Thomas Shea, Christina Neal, and John Allen — for pushing me to take every problem and interpretation just a little (or a lot) further. I am especially grateful to Tom and John for stepping in at the last hour. Thank you all for your time and patience. Alain Burgisser, Laurent Arbaret, and Sarah Fagents also brought outside perspectives and skill-sets that were crucial for this project.

Field work was both an exciting and rugged experience, and such a large data-set would not have been collected if not for the guidance from Bruce, Alain, Laurent, Ed Llewellyn, and Tim Orr and for the assistance from Hannah Azouz and Jaclyn Guenther.

Laboratory work would not have been possible without the training and assistance from others, especially considering the wide range of data-sets. Caroline Tisdale, Hannah, Jaclyn, Samuel Clairmont, and Eva Kakone were invaluable in density measurements and endless image processing. Thanks go to: Chinh Nguyen for showing me the porosity and permeability methodologies and for analyzing samples; Tom for training me in Raman

spectroscopy; Laurent and Marielle at the Université d'Orléans for getting me situated with sample prep and for running samples on the Flash 2000; Val Finlayson for introducing me to isotope sample prep; Ilya Bindeman and Mike Hudak at the University of Oregon for running samples on the TCEA and for crucial insight to hydrogen isotope data; Gary Huss and Kazu Nagashima for helping with (and dealing with) my long runs on the SEM; and JoAnn Sinton for meticulous thin section making and polishing.

I would also like to recognize and express gratitude towards the sources that funded my research and travel to meetings: the National Science Foundation, UH Mānoa Graduate Student Organization and the Department of Geology and Geophysics, and the Don Richter Memorial Scholarship fund. I view the money that was awarded to me and my advisor through grants and scholarships not only as support for my research, but also as a jump-start to my career. I will always be grateful to the agencies that see value in young researchers. Also, thanks to our administrators — Alison, Lily, Connie, and Susan — who keep our department running and make it easier for us to do our research.

Thanks to my office-mates and other Geology grads have helped make the long days durable — from lots of chocolate to those much needed pep talks. It's a long list of friends, peers, and colleagues that are due their gratitude, but I would like to highlight Maria Janebo, Val Finlayson, Penny Larin, Sam Mitchell, Emily First, Kendra Lynn, Brett Walker, Erin Fitch, Carolyn Parcheta, Laura Carter, and Emily Lynch. Thanks for all of the love and support throughout the years.

Finally, I am forever grateful to my family; I do not know what I would have done without you. My Mom always encouraged and fostered my dreams. My sister and her

family were always excited to have an Auntie who works on volcanoes. The Isgetts welcomed me to the family and loved me no matter who I am. Most importantly, my wife Shelley: you were my strength throughout this tough journey. There is not enough space to express how grateful I am for everything you have done to get me to this point. I love you, always.

Abstract

The Vulcanian phase of the 1912 eruption of Novarupta comprised only a very small part of the most voluminous eruption of the twentieth century, yet it served as an important transition from very powerful and sustained explosions to effusive dome growth. The Novarupta eruption is divided into five episodes: Episodes I–III comprised, cumulatively, of 60 hours of strong Plinian explosions that produced voluminous rhyolitic and dacitic ignimbrites and widespread, predominantly dacite, Plinian fall beds. Episode IV produced a dacite block apron, interpreted as the product of complete destruction of a dacite plug/dome via Vulcanian explosions, before extrusion of a rhyolite dome in Episode V. Compensatory caldera collapse during the Plinian episodes occurred 10 km from vent, preserving the ultra-proximal deposits from Episodes I–IV to within 200 m from source. This dissertation explores the pre- and syn-fragmentation conduit and eruption processes occurring throughout Episode IV through careful examination of the uniquely well-preserved Vulcanian block deposit. Block distributions suggest that Episode IV consisted of multiple small explosions that disrupted only small regions of the dome and shallow conduit. Significant textural heterogeneity, including dense, pumiceous, texturally banded, and breadcrusted blocks, and estimates of their source depths reveal that the texturally diverse magmas were juxtaposed to one another within the upper 400 m of the shallow conduit and/or dome. Blocks representing magmas in varying stages of degassing and outgassing imply that very small packages of magma arrived to, and were stored at, their fragmentation depths at/for varying times and durations. Pyroclast textures suggest that the rapid vesiculation of the pumice-forming magma after emplacement at shallow depths likely provided the energy for explosions throughout Episode IV.

Table of Contents

Chapter 1: Introduction and Background

1.1	Introduction.....	1
1.2	Explosive volcanic eruptions.....	1
1.2.1	Controls on eruption style.....	3
1.2.1.1	Degassing and outgassing.....	3
1.2.1.2	Crystallization.....	5
1.2.1.3	Fragmentation.....	6
1.2.2	Vulcanian eruptions.....	7
1.3	Geologic setting.....	11
1.4	Eruption background.....	14
1.4.1	Contributions from early workers.....	14
1.4.2	Chronology of the eruption.....	17
1.4.3	Key previous volcanological findings.....	26
1.4.3.1	Magma storage.....	26
1.4.3.2	Implications of proximal deposits.....	32
1.4.3.3	Transitions in eruption style.....	36
1.5	Motivation for research.....	38

Chapter 2: Eruptive and shallow conduit dynamics during Vulcanian explosions:

Insights from the Episode IV block field of the 1912 eruption of Novarupta, Alaska

<i>Abstract</i>	41	
2.1	Introduction.....	42

2.2	Methodology.....	45
2.3	Block data.....	48
2.3.1	Episode IV block componentry.....	48
2.3.2	Block distribution by lithology and size.....	53
2.3.3	Block trajectory modeling results.....	59
2.3.3.1	General features.....	59
2.3.3.2	Median velocity.....	60
2.3.3.3	Spread in velocity.....	60
2.3.3.4	Dependence of ejection velocity on launch angle.....	62
2.3.3.5	Velocity versus distance.....	63
2.4	Interpretations.....	63
2.4.1	Block componentry interpretations.....	63
2.4.2	Block distribution interpretations.....	65
2.4.3	Constraints on modeled ejection velocity and angle.....	66
2.5	Discussion.....	70
2.5.1	Eruptive conditions at Novarupta and comparisons with historical Vulcanian eruptions.....	70
2.5.2	Implications and comparisons with respect to other Vulcanian eruptions.....	75
2.5.3	General implications for modeling ballistic block trajectories.....	78
2.6	Conclusions.....	79

**Chapter 3: Complex patterns of vesiculation, outgassing, and re-vesiculation during a
Vulcanian eruption: Implications for conduit processes**

<i>Abstract</i>	81
3.1 Introduction.....	82
3.1.1 Vulcanian eruptions.....	82
3.1.2 Degassing, outgassing, and vesiculation.....	85
3.1.3 Porosity and permeability.....	87
3.1.4 Breadcrusting.....	88
3.1.5 Novarupta.....	89
3.2 Methodology.....	92
3.2.1 Mapping and sampling.....	92
3.2.2 Bulk and 2D vesicularity.....	93
3.2.3 Porosity and permeability.....	93
3.3 Bulk and 2D vesicularity data for juvenile clasts.....	94
3.3.1 Homogeneous clasts.....	94
3.3.1.1 Vesicle size and number density data.....	98
3.3.2 Heterogeneous clasts.....	102
3.4 Porosity and permeability data.....	108
3.5 Vesicularity interpretations.....	110
3.5.1 Homogeneous clasts.....	112
3.5.2 Heterogeneous clasts.....	112
3.6 Permeability and connected porosity interpretations.....	114

3.7	Discussion	116
3.7.1	Controls on degassing and outgassing of Episode IV magma	116
3.7.1.1	Microvesicular pumice	116
3.7.1.2	Dense dacite	117
3.7.1.3	Breadcrusted blocks	117
3.7.1.4	Banded	118
3.7.2	Development of breadcrust textures	118
3.7.3	Juxtaposition of contrasting magma in flow-banded blocks	119
3.8	Conclusions	121

Chapter 4: Constraints from residual water contents on eruptive processes during the 1912 Vulcanian explosions at Novarupta, Alaska

	<i>Abstract</i>	122
4.1	Introduction	123
4.1.1	Vulcanian explosions	123
4.1.2	Theoretical models of the Vulcanian conduit	124
4.1.3	Glass H ₂ O measurement and pressure/depth estimates	125
4.1.4	Novarupta Episode IV	127
4.2	Methodology	130
4.2.1	Glass H ₂ O measurement	130
4.3	Results	134
4.4	Interpretations	139

4.4.1	Discriminating primary magmatic water from secondary hydration by meteoric water.....	139
4.4.2	Implications of measured water contents.....	143
4.4.3	Dense dacites.....	143
4.4.4	Microvesicular pumices.....	144
4.4.5	Breadcrusted clasts.....	145
4.5	Discussion.....	146
4.5.1	Variation in measured water contents.....	146
4.5.2	The rehydration problem.....	146
4.5.3	Architecture of the dome and shallow conduit.....	147
4.5.4	Magma ascent and storage histories.....	151
4.5.4.1	Microvesicular pumice.....	151
4.5.4.2	Complex combinations of degassing histories.....	153
4.5.4.3	Dense dacite.....	154
4.5.5	Formation of textural differences in banded clasts.....	155
4.6	Conclusions.....	159

Chapter 5: Conclusions

5.1	Future directions.....	165
5.1.1	Further micro-analytical approaches to Episode IV.....	165
5.1.2	Breadcrusted blocks.....	165
5.1.3	Numerical modeling.....	166
5.1.4	Integration with further micro-textural data from Episode III.....	166

5.1.5	Extension of these approaches to other Vulcanian eruptions.....	167
Appendix A: Chapter 2 Supplementary Material		
A.1	Modeling methodology.....	168
A.2	Spinning ballistics.....	170
A.3	Additional figures.....	171
Appendix B: Chapter 3 Supplementary Material		
B.1	Porosity and permeability methodology.....	177
B.1.1	Porosity measurement.....	177
B.1.2	Equations governing permeability.....	178
B.1.3	Permeability measurement.....	180
B.2	Images of porous pathways in thin section.....	182
B.3	Additional data.....	184
Appendix C: Chapter 4 Supplementary Material		
C.1	Additional figures.....	189
References		194

List of Tables

<u>Table</u>		<u>Page</u>
1.1	Key characteristics of each eruptive episode.....	17
1.2	Storage conditions of the 1912 magmas.....	27
2.1	Range of block travel distances.....	59
2.2	Summary of ejection velocities.....	62
2.3	Examples of componentry described in the Vulcanian literature.....	72
2.4	Comparison of velocities calculated for ballistic particles.....	76
3.1	Micro-textural data for the microvesicular pumices.....	100
4.1	Summary of water, pressure, and depth estimates.....	135
B.1	Timescales for diffusion of water.....	188

List of Figures

<u>Figure</u>		<u>Page</u>
1.1	Spectrum of dry eruption styles.....	2
1.2	Progression of magma texture with ascent.....	8
1.3	Regional location map.....	13
1.4	Aerial panorama of Novarupta basin and the Valley of Ten Thousand Smokes.....	15
1.5	Compositions erupted with time.....	18
1.6	Isopach maps of the Plinian fall layers.....	19
1.7	Compositionally equivalent fall units and flow packages of Episode I.....	20
1.8	The nested vent structure.....	24
1.9	Photo of Novarupta dome.....	25
1.10	The plumbing system beneath Katmai and Trident.....	29
1.11	Photo of banded pumice clasts.....	32
1.12	Regimes that produced the complex proximal deposits.....	35
1.13	Schematic of a “top-hat” velocity profile.....	36
1.14	Evolution of conduit processes during Episodes III and IV.....	37
1.15	Heterogeneity of Episode IV magma and dome.....	38
2.1	Distribution of the Episode IV blocks.....	46
2.2	Episode IV block lithologies.....	49
2.3	Proportions of the block components.....	51
2.4	Breadcrust blocks.....	52

2.5	Proportion of breadcrusted pumice and dense dacite.....	52
2.6	Isopleth maps for the component groups.....	56
2.7	Overlapping isopleths from different lithological groups.....	57
2.8	Plots of average diameter versus distance.....	58
2.9	Modeled block ejection velocity versus launch angle.....	61
2.10	Modeled launch velocity versus ejection distance.....	64
2.11	Reynolds numbers data.....	68
2.12	Models for the shallow conduit architecture.....	77
3.1	Examples of Vulcanian pyroclast textures.....	83
3.2	The 1912 eruptive deposits.....	90
3.3	Categories of clast types in the Episode IV block apron.....	91
3.4	Bulk vesicularities for the different clast types.....	95
3.5	Grayscale micro-texture images of the pumice.....	96
3.6	Grayscale micro-texture images of dense dacites.....	97
3.7	Micro-textural data for the microvesicular pumices.....	99
3.8	Volumetric ratio of vesicles to melt versus vesicle number density.....	101
3.9	Grayscale micro-texture images of the crusts.....	104
3.10	Grayscale micro-texture images of the interiors.....	106
3.11	Connectivity and Darcian permeability versus total porosity.....	109
3.12	Relative durations of degassing, outgassing, and renewed vesiculation.....	111

4.1	Examples of block textures within the Episode IV deposit.....	129
4.2	Falsely colored 1000x magnification image of a breadcrust rind.....	132
4.3	Comparison of water estimates from multiple methods.....	136
4.4	Dissolved H ₂ O versus vesicularity for dense, pumiceous, and intermediate blocks, and crusts of the breadcrusted blocks.....	137
4.5	Dissolved H ₂ O versus vesicularity for crust, transition, and interior samples.....	138
4.6	δD versus water content.....	141
4.7	Theoretical model of the shallow conduit throughout Episode IV.....	150
A.1	Block maps for each of the components.....	171
A.2	Images of density of the pumice lapilli bed.....	174
A.3	<i>Eject!</i> modeling results.....	176
B.1	Fluid flow through a sample during a permeability measurement.....	179
B.2	Estimation of permeability.....	181
B.3	Examples of porous pathways within grayscale images of the crusts.....	182
B.4	Connectivity and permeability for individual breadcrusted blocks.....	184
C.1	Calibration for the estimate of glass H ₂ O content via microRaman spectroscopy..	189
C.2	Phenocryst crystallinities.....	190
C.3	Reflected light image of thick section.....	191
C.4	Photographs of fluid dynamics experiments.....	192
C.5	Conceptual model for the in-situ formation of texturally contrasting bands.....	193

List of Abbreviations and Symbols

Abbreviation/symbol	Meaning
1D	one-dimensional
2D	two-dimensional
A	area
<i>A</i>	cross-sectional area
A	early (primary) degassing
α_{v-m}	isotopic fractionation factor
ADGGS	Alaska Division of Geological and Geophysical Surveys
ASF	aluminosilicate framework
AVO	Alaska Volcano Observatory
B	partial outgassing
br	breccia
BSE	back-scattered electron
<i>bu</i>	bubbles
C	renewed or 'secondary' vesiculation
C_d	drag coefficient
<i>cr</i>	crystals
CVVD	cumulative vesicle volume distribution
D	deuterium
δD	D/H relative to SMOW

δD_i	initial δD of the melt
δD_{met}	δD of local meteoric water
ΔP	pressure difference
D_{avg}	mean of three orthogonal block dimensions
DRE	dense rock equivalent
η	atmospheric viscosity
F	ratio of the H ₂ O remaining in the melt
FTIR	Fourier-transform infrared spectroscopy
g	gravitational acceleration
gl	glass
H	protium
H ₂ O _{mol}	molecular water
I_{mix}	dimensionless mixing parameter
k_1	viscous permeability
k_2	inertial permeability
k_a	apparent permeability
L	sample length
μ	fluid viscosity
MER	mass eruption rate
MΩ	Milli-Q — ultrapure
M _S	surface wave magnitude
N ^m v	number of vesicles per reference volume of melt

NSS	NORAN system SIX
OH ⁻	hydroxyl
<i>ox</i>	oxides
<i>P</i>	pressure
PDC	pyroclastic density current
ϕ	vesicularity of magma
φ_{con}	connected porosity
φ_{total}	total porosity
$\varphi_{con}/\varphi_{total}$	connectivity
PTS	polished thin section
<i>Q</i>	volumetric flow rate
ρ	density
R ²	coefficient of determination
Re	Reynolds number
SEM	Scanning Electron Microscope
SMOW	Standard Mean Ocean Water
θ	trajectory angle from horizontal
<i>t</i>	time
TCEA	Thermal Conversion Elemental Analyzer
<i>v</i>	velocity
<i>V</i>	volume
V_{con}	volume of connected pores

V_G/V_L	volume ratio of vesicles to melt
V_{iso}	volume of isolated pores
V_{sample}	volume of cylindrical sample
V_{ske}	skeletal volume
V_{solid}	volume of solid skeleton
VTTS	Valley of Ten Thousand Smokes
wt%	weight percent
x	proportion
X	meteoric water/total water
$X_{H_2O}^{bu}$	bulk water content
$X_{H_2O}^{gl}$	glass water content

CHAPTER 1

Introduction and Background

1.1 Introduction

On June 6, 1912, a vent opened on the floor of a valley between Trident and Griggs stratovolcanoes in a remote area of the Alaska Peninsula, initiating the largest eruption of the 20th century. Novarupta, Latin for “new vent”, has become one of the best studied eruptions in the world, as scientists from a wide range of specialties and disciplines have been attracted by its unique and defining characteristics. Exceptional diversity of compositions in the juvenile eruptive products, suspected magma storage located 10 km from the penultimate eruptive vent, unique preservation of complex ultra-proximal deposits, and several large earthquakes prior to and concurrent with the eruption are just a few of these distinctive features. This introduction reviews the results from previous works on understanding explosive volcanic eruptions and sets the stage for the work completed in this dissertation. The chapter gives an overview of the 1912 eruption of Novarupta, Alaska, and reviews the spectrum of explosive eruption styles and the controls on their intensities and behaviors.

1.2 Explosive volcanic eruptions

Volcanic explosions are broadly categorized into wet and dry eruptions. Wet eruptions involve the interaction of magma with external water which can increase the thermal efficiency of the eruption whereas dry eruptions are driven by magmatic volatiles. Dry eruptions involve a range

of intensities, durations (and magnitudes), and are classified into ‘eruption styles’ according to these characteristics (Figure 1.1). Plinian eruptions are the most powerful, producing high, sustained, convective eruption columns containing a wide range of particle sizes and forming widespread sheet-like fall and pyroclastic density current deposits (Cioni et al. 2015). Cone-forming Hawaiian and Strombolian eruptions occupy the weak end of the spectrum, with generally low eruption columns and a predominance of coarse ejecta that fall mostly within 500 m of the vent (Taddeucci et al. 2015). Of particular interest to this study, short-lived Vulcanian eruptions — which are somewhat intermediate in size and intensity between Plinian and Hawaiian/Strombolian eruptions — are covered in greater detail later in this introduction.

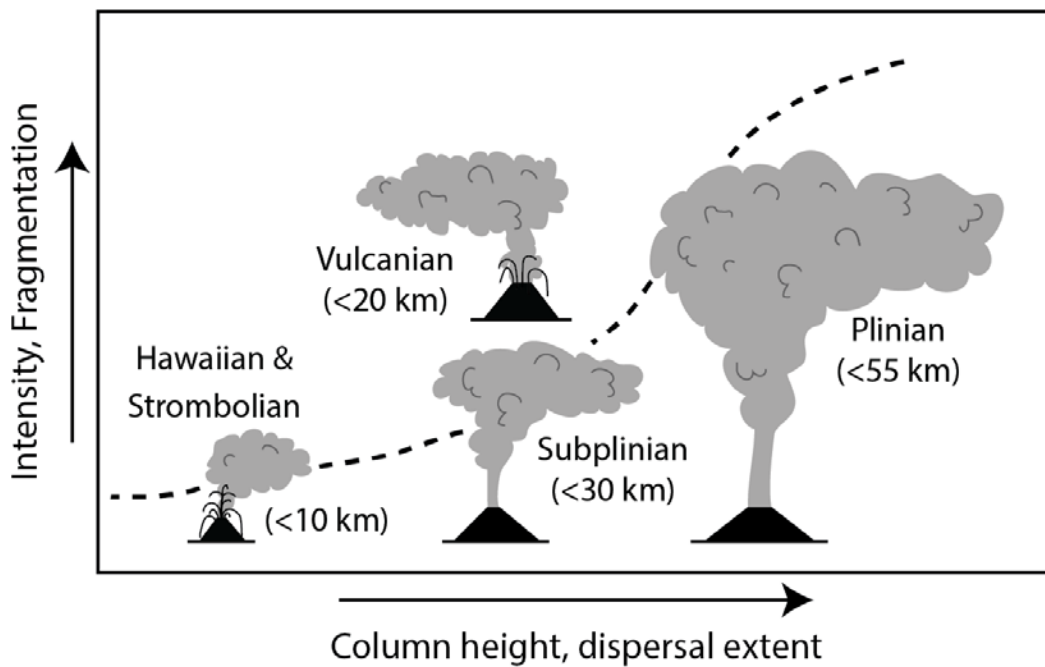


Figure 1.1 Spectrum of dry eruption styles. Adapted from Cas and Wright (1987), originally by Walker (1973).

1.2.1 Controls on eruption style

The dominant control on eruption style is the behavior of exsolved volatiles as magma travels towards the Earth's surface, specifically whether or not the bubbles are capable of growing and escaping from the system. This behavior is largely dependent on the viscosity of the melt and the magma ascent rate. Hawaiian and Strombolian eruptions occur at volcanoes consisting of fluid mafic magmas, whereas Vulcanian, sub-Plinian, and Plinian eruptions involve more viscous and typically, but not always, felsic magmas.

Magma ascent rates control the amount of time that bubbles have to grow. Slow ascent rates supply more time for equilibrium bubble growth (or steady bubble expansion without overpressure) thus inhibiting explosive eruption. During rapid ascent, equilibrium expansion of bubbles is suppressed and over-pressure builds within the system resulting in explosive eruptions. This section covers the processes occurring during magma ascent that influence the style and intensity of explosive volcanic eruptions.

1.2.1.1 Degassing and outgassing

At depths of >6–10-km, a melt contains volatiles held in solution by pressure. As the magma ascends, and pressure decreases, volatile solubility decreases promoting nucleation of the volatiles into a gas phase. Degassing is thus the exsolution of volatiles from the melt during ascent (Sparks 1978). Homogeneous nucleation involves the formation of bubbles uniformly throughout the melt whereas bubbles nucleate on a surface (such as a microlite or crystal) during heterogeneous nucleation. High volatile supersaturations and thus high ascent rates are required to overcome the activation energy (the energy required to form a stable surface separating the gas and melt phases) in homogeneous nucleation, delaying vesiculation to pressures well below

the equilibrium saturation pressure (i.e. volatiles remained dissolved in the melt above their solubility levels for the ambient pressure; Mangan and Sisson 2000). Heterogeneities such as Fe-Ti oxides are good nucleation sites because the surface tension between e.g., a crystal and the gas is less than the surface tension between the gas and melt alone. Therefore, heterogeneous nucleation requires much lower supersaturations and promotes conditions closer to (but not at) equilibrium degassing (Hurwitz and Navon 1994). The bubble nucleation mechanism influences the number of bubbles and their sizes because very high supersaturations (and homogeneous nucleation) facilitate high nucleation rates and smaller bubbles whereas lower supersaturations (and heterogeneous nucleation) tend to lead to less nucleation and larger bubbles (Mangan and Sisson 2000; Mourtada-Bonnefoi and Laporte 2004).

Bubbles grow through three processes: diffusion of volatiles into existing bubbles, expansion due to decompression, and coalescence. The first two processes can be grouped as a 'free growth' stage without interactions between adjacent bubbles. Controls on free bubble growth include the number of the volatile molecules in the melt (or the volatile concentration), diffusion rate, and viscosity of the melt (Prousevitch et al. 1993; Toramaru 1995; Gonnermann and Manga 2007). If volatile diffusion is slower than the decompression-driven solubility decrease, then a second stage of supersaturation may ensue favoring nucleation over growth. In this case, bubbles grow by volume through expansion due to the drop in pressure rather than by the addition of molecules. However, viscous resistance of the surrounding melt shell can limit expansion (Sparks et al. 1994; Toramaru 1995) causing the gas pressure inside bubbles to become significantly larger than the ambient pressure. This buildup of overpressure increases the likelihood of an eruption becoming explosive. Bubble coalescence involves the merging of

bubbles, requiring the rupture and drainage of melt from the film between two bubbles (Cashman and Mangan 1994; Klug and Cashman 1996; Gonnermann and Manga 2007).

Open system degassing involves outgassing or the escape of gas from the magma. In low-viscosity mafic magmas the bubbles can decouple from the melt due to buoyant rise. If magma ascent rate is slow relative to bubble ascent, then gas bubbles may rise to the surface, burst and release gas to the atmosphere (Taddeucci et al. 2015). In more silicic systems, viscosity inhibits buoyant ascent, but bubble growth, shearing, and coalescence may develop permeable pathways through which gas can escape (Mueller et al. 2005; Gonnermann and Manga 2007). Laboratory experiments have shown that significant coalescence and the development of permeability can occur on timescales on the order of minutes to hours depending on the bulk viscosity (melt + bubbles) of the magma (Martel and Iacono-Marziano 2015). Gas can also escape through fractures developed along conduit margins via brittle deformation of the ascending magma (Gonnermann and Manga 2003; Rust et al. 2004). Once open-system degassing is initiated, the potential for an eruption to become or remain explosive is reduced with respect to effusive eruption. However, the subsequent collapse of permeable pathways can close the system resulting in a build-up in pressure that can result in a shift to explosive eruptions (e.g. Matthews et al. 1997; Yokoo et al. 2013).

1.2.1.2 Crystallization

Crystals in ascending hydrous magmas nucleate and grow in response to undercooling which is the consequence of decreasing temperature or degassing (Hammer et al. 1999; Blundy and Cashman 2001, 2005). As water exsolves from the melt in response to decompression, a corresponding increase in the liquidus temperature causes anhydrous phases to crystallize

(Geschwind and Rutherford 1995; Hammer et al. 1999). Rates of nucleation of new crystals depends on the magma ascent rate. The degree of undercooling increases with faster decompression rates, resulting in more crystal nucleation. Conversely, lower degrees of undercooling due to slower magma ascent and decompression facilitate growth of existing crystals over nucleation (Hammer et al. 2002; Couch 2003).

1.2.1.3 Fragmentation

The type and efficiency of fragmentation has a direct impact on the style of dry eruptions by controlling pyroclast size and the proportion of gas within the erupted mixture. Five models have been proposed for the mechanism of fragmentation (Gonnermann and Manga 2013). First, a fragmentation threshold is thought to be met once the magma reaches a critical vesicularity, possibly due to some form of instability that develops in the thin bubble walls when the volume fraction of bubbles reaches ~ 0.75 (Sparks 1978). Second, high-viscosity magmas may fragment when a threshold tensile stress is exceeded (Alidibirov 1994; Zhang 1999). During bubble growth, the melt of the bubble walls must stretch to accommodate the volume increase of the gas. If this stress on the bubble walls exceeds the tensile strength of the magma, then the magma will tear. This occurs when there is a significant gradient between the ambient pressure and the bubble gas pressure (i.e. significant bubble overpressure, ΔP). Third, the structural relaxation rate of the melt may exceed the rate at which strain is applied, causing the magma to cross the glass transition from ductile to brittle behavior (Papale 1999; Gonnermann and Manga 2003). Magma relaxation time increases with increasing magma viscosity; therefore, magma is more likely to fragment at high viscosities and strain rates. Fourth, Namiki and Manga (2005) established a potential energy threshold above which fragmentation takes place. Potential energy

depends on the magma's vesicularity (ϕ) and the difference between the inside and outside pressure of the bubbles (ΔP). It determines the velocity and style of expansion of the bubbly fluid during rapid decompression. A larger potential energy due to a higher ϕ and larger ΔP causes faster expansion of magma which promotes fragmentation (Namiki and Manga 2005). Finally, inertial fragmentation applies to low viscosity mafic magmas, where the fragmentation mechanism is governed by fluid mechanics rather than brittle fracture or other processes that depend on the viscoelasticity of the melt. During rapid expansion, bubbly mafic fluids expand or stretch, tearing into several pieces when the critical Reynolds number reaches ~ 1 . For these magmas, the inertia of the expanding melt ultimately controls whether the melt fragments into discrete particles or is allowed to increase vesicularity until it reaches a threshold of $\sim 70\%$ and becomes permeable (Namiki and Manga 2007).

1.2.2 Vulcanian eruptions

Vulcanian eruptions consist of transient, impulsive explosions that are generally unsteady (i.e. fluctuating mass eruption rates), episodic, and, with present knowledge, unpredictable. Their intensities are considered moderate on the scale of explosive volcanic eruptions (Figure 1.1). The impacts associated with Vulcanian eruptions are typically less devastating than their steady and sustained counterparts, yet they are much more common and can pose protracted risks when they occur in sequences lasting weeks to decades (Clarke 2013).

Vulcanian eruptions have been modeled as a consequence of the sudden decompression of a conduit containing a vertically stratified, rheologically heterogeneous melt in varying states of degassing and outgassing (Self et al. 1979; Turcotte et al. 1990; Fagents and Wilson 1993; Alidibirov 1994; Woods 1995; Stix et al. 1997; Clarke et al. 2002a, b; Druitt et al. 2002; Clarke

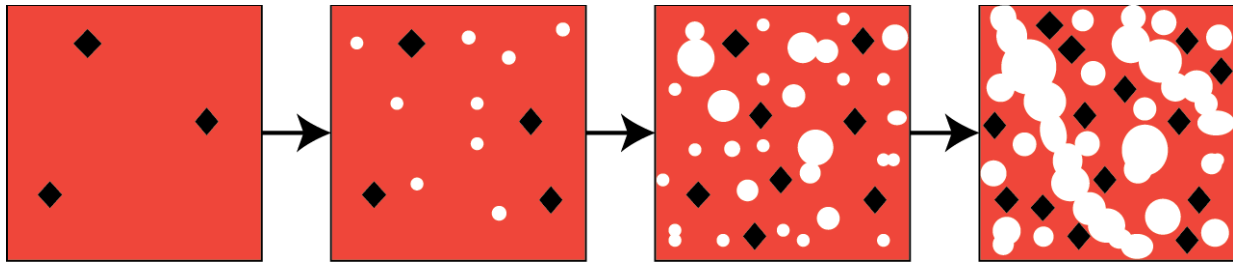


Figure 1.2 Schematic of the textural progression as magma rises within the conduit and shifts from closed- to open-system degassing prior to Vulcanian explosions.

2013). They can be triggered by the disruption of a sealing plug/cryptodome or dome by 1) failure of all or some portion of the dome, 2) pressurization of the underlying magma, and/or 3) sudden vaporization of externally-derived water. This plug and the underlying rheologically heterogeneous melt are developed by a series of processes occurring within the conduit. The pressure drop from the magma chamber to the surface drives the magma upwards at slow ascent rates. Decompression due to ascent decreases solubility and drives volatile exsolution which increases the liquidus temperature and initiates crystallization of anhydrous phases (Geschwind and Rutherford 1995; Hammer et al. 1999). Crystallization increases the concentration of residual volatiles in the melt, forcing further degassing, and provides sites for heterogeneous nucleation reducing the supersaturation pressure required to nucleate bubbles. An increase in bubble and crystal number densities forces vesicles to coalesce and expand into the interstices between crystals enhancing coalescence and the development of permeable pathways (Figure 1.2). The system thus shifts from closed- to open-system degassing as volatiles are lost through these permeable networks. This gas loss may reduce the stability of the magma driving bubble collapse and create the dense plug at the top of the magma body (Hammer et al. 1999; Cashman and McConnell 2005; Clarke et al. 2007). Parts of the system becomes pressurized due to

continued magma ascent, a total increase in volume due to bubble nucleation and growth throughout the conduit, and possible development of overpressures as viscosity increases near the surface and prevents growth of bubbles (Sparks 1978, 1997; Stix et al. 1997; Melnik and Sparks 1999).

In the models, three waves develop upon disruption of the conduit sealing plug or dome. A decompression wave travels downward at the local sound speed followed by a slower fragmentation wave. The fragmentation wave quenches and breaks the magma apart creating a gas-pyroclast mixture that travels upwards and is expelled from the conduit at velocities of 50–400 m/s (Self et al. 1979; Fagents and Wilson 1993; Clarke et al. 2002a, b). The depth at which the fragmentation wave stops varies throughout the conduit and has been known to reach the magma chamber (Druitt et al. 2002; Coombs et al. 2010); it depends on when the conditions for fragmentation (section 1.2.1.3) are no longer met (Sparks 1978; Alidibirov 1994; Papale 1999; Zhang 1999; Melnik and Sparks 2002a; Gonnermann and Manga 2003; Namiki and Manga 2005). A shock wave travels outward and ahead of the pyroclastic mixture at a velocity greater than the local sound speed and is indicative of the significant pressure difference between the atmosphere and the gas-rich magma in the conduit (Chojnicki et al. 2006; Clarke 2013). Once the explosion ends, the system is set to begin a new cycle of magma rise, plug formation and disruption, and sudden decompression (Voight et al. 1999). This cycle has been recorded on timescales of hours to days and up to years (Hoblitt 1986; Matthews et al. 1997; Druitt et al. 2002; Yokoo et al. 2013).

Hazards associated with Vulcanian eruptions include dense ballistic blocks, airborne tephra and tephra fall, pyroclastic density currents (PDCs), and lahars. Ballistic blocks range in

size from 10s of centimeters to 10s of meters in diameter and are ejected to distances typically <5 km from vent. Notably, the largest block ejected during the 1975 eruption of Ngauruhoe, New Zealand, was 27 m long, 15 m wide, and weighed ~3000 tons (Morrissey and Mastin 2000). The explosion(s) may last only seconds to minutes and yield small volumes of tephra, yet they produce initial eruption plumes that typically rise to <10 km. Particularly large events or a series of explosions may produce plumes that reach as high as 20 km (Self et al. 1979; Clarke 2013). Airborne ash can pose a hazard to aircraft as cruising altitude for commercial air traffic is 9–12-km. Lower altitude ash plumes pose a hazard when adjacent to airports or landing/take off corridors. Tephra falls can greatly impact local communities through multiple hazards, including: building collapse due to the accumulated weight of tephra; destruction of crops and livestock; health impacts due to respirable ash and skin and eye irritation; and disruption to key utilities such as electricity, water, and transportation systems. The transient and episodic nature of Vulcanian eruptions forms unsteady columns that often collapse into PDCs. These gravity-controlled, lateral flows of pyroclasts and gas can travel at velocities of 100–300 m/s and reach temperatures up to 1000° C (Hoblitt 1986; Cas and Wright 1987; Wilson and Houghton 2000). If externally derived water is involved in the eruption or if hot tephra falls on snow or ice, lahars, or water saturated debris flows, may form. They are often restricted to valleys, may travel 10s–100s of km from source, and travel at velocities of 10s of m/s (Manville et al. 2013). Both PDCs and lahars are completely destructive and permanently change the landscape.

The deposits produced by ballistic block ejection, PDCs, and lahars are the most enduring products of this type of eruption. This is simply because the thin, widely dispersed, and fine-grained fall deposits are easily re-worked shortly after the eruption. Flow deposits can be valley

filling at proximal-medial distances and <10–100s of cm thick and 10s of m across at the distal ends of individual lobes (Druitt et al. 2002; Vallance et al. 2010). Block fields can cover areas up to several km², with block size decreasing with distance from vent (Adams et al. 2006a). A wide range of textures and juvenile and lithic components characterize the eruption products, including a range of dense to highly vesicular juveniles and brecciated and massive wall rock lithics, with a range of breadcrusting on varying proportions of all these components (Adams et al. 2006a; Clarke et al. 2007; Wright et al. 2007; Burgisser et al. 2010; Giachetti et al. 2010). This variation is the result of the fragmentation wave disrupting magma with varying degrees of viscosity, vesicularity, and crystallinity (Clarke 2013). It may be assumed that the finer-grained eruptive products represent to some extent the pre-fragmentation state of the magma because 1) the fragmentation wave quenches the magma faster than volatiles can exsolve due to decompression, and 2) the magma may be considered stationary as the velocity of the fragmentation front is much greater than magma ascent velocity (which may have stalled by the sealing plug; Sparks 1978; Woods 1995; Clarke et al. 2002a, b; Melnik and Sparks 2002b; Clarke 2013). It should be noted, however, that syn-explosion bubble nucleation and growth may increase vesicularity by several percent from its original state in the conduit (Giachetti et al. 2010).

1.3 Geologic setting

The 2,500-km-long arc of the Aleutian-Alaskan subduction zone, formed by dipping of the oceanic Pacific plate below the North American plate, is the source of Alaska's volcanoes. The magma that was erupted in 1912 is thought to have been stored below Mount Katmai, which sits

mid-way along a 95-km-long linear segment of the arc (Hildreth and Fierstein 2000). Katmai joins Alagogshak, Martin, Mageik, Griggs, and Trident in a group of small andesite-dacite stratovolcanoes called the 'Katmai volcanic cluster' (Figure 1.3). All volcanoes of the group except Mount Griggs lie along a N65°E trend that defines the Quaternary volcanic front along a pre-existing range crest known as the Pacific-Bristol Bay drainage divide. Elevations reach 1,200–1,600 m along the pre-volcanic basement which is exposed within Katmai Pass and Kejulik Pass (Figure 1.3). Mount Griggs is unique within the Katmai cluster in being centered 12 km behind the volcanic front. Alagogshak is the only volcano of the group that has not erupted in the Holocene and is considered to be extinct (Hildreth and Fierstein 2000).

Strata beneath the Katmai volcanic cluster consist of ~5,500 m thick horizontally stratified Mesozoic sedimentary rocks. Marine sedimentary rocks belonging to the Late Jurassic Naknek Formation are underlain by about 3,500 m of Triassic and older Jurassic sedimentary strata. Marine siltstone, arkosic sandstone, and lesser lithic wacke and conglomerate comprise the 1,700–2000 m thick subhorizontal to gently warped layers of the Naknek Formation (Detterman et al. 1996; Hildreth and Fierstein 2012).

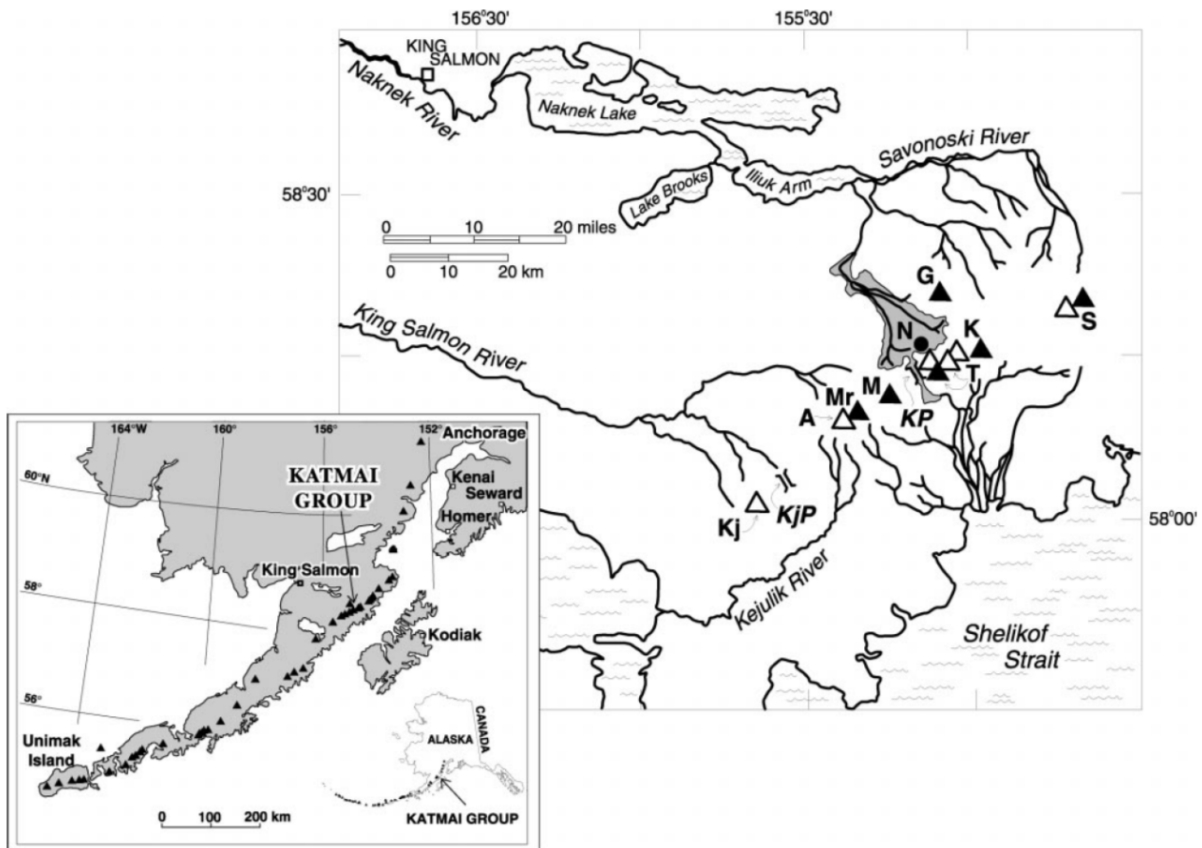


Figure 1.3 Regional location map showing the Katmai volcano cluster. *Solid triangles* indicate volcanoes active during the Holocene; *open triangles* represent inactive cones from the Pleistocene; (A) Alagoshak; (Mr) Martin; (M) Mageik; (G) Griggs; (T) Trident (three extinct cones and one recently active cone); (K) Katmai. Southwest of the cluster is (Kj) Kejulik volcano and northeast is the (S) Snowy Mountain volcano pair. *Solid circle* (N) indicates Novarupta and *shaded valley fill* is the ignimbrite within the Valley of Ten Thousand Smokes. Low points along the volcanic axis include (KP) Katmai Pass and (KjP) Kejulik Pass. Inset shows the location of the Katmai group along the arc. Figure from Hildreth and Fierstein, 2000.

1.4 Eruption background

The deposits of the 1912 eruption of Novarupta are some of the best studied products of any large-volume eruption in the world to-date. Several publications present data on the pre-, syn-, and post-eruption and depositional processes and this section provides a brief overview of those works. An estimated 13 km^3 of zoned magma was erupted over five recognized episodes during the 1912 eruption. Stratigraphy and eye witness accounts reveal that the first three episodes consisted of 60 hours of strong Plinian explosions separated by lulls of at most a few hours that formed 1) a far-traveled eruption cloud, 2) a wide-spread tephra fall deposit, and 3) the valley-filling ignimbrite known as the Valley of Ten Thousand Smokes. The transition to weaker and unsteady activity throughout the fourth episode involved extrusion and explosive destruction of a dacite dome resulting in a discontinuous block and lapilli apron (Hildreth and Fierstein 2000; Houghton et al. 2004). The eruption ended after stable lava effusion during the fifth episode, forming the rhyolite dome (Novarupta) that is present on the valley floor today and enclosed by an ejecta ring formed by the later stages of Episodes II and III (Figure 1.4).

1.4.1 Contributions from early workers

Immediate interest in the eruption of 1912 and its deposits prompted several field investigations into pre- and post-eruptive processes at Katmai and the Valley of Ten Thousand Smokes (VTTS) in the early 1900s. George Curtis Martin, a field geologist familiar with the Katmai coast prior to 1912, was the first to collect witness accounts of the eruption impacts and to compile a regional isopach map of total fallout, noting three principal layers of tephra fall (Martin 1913;

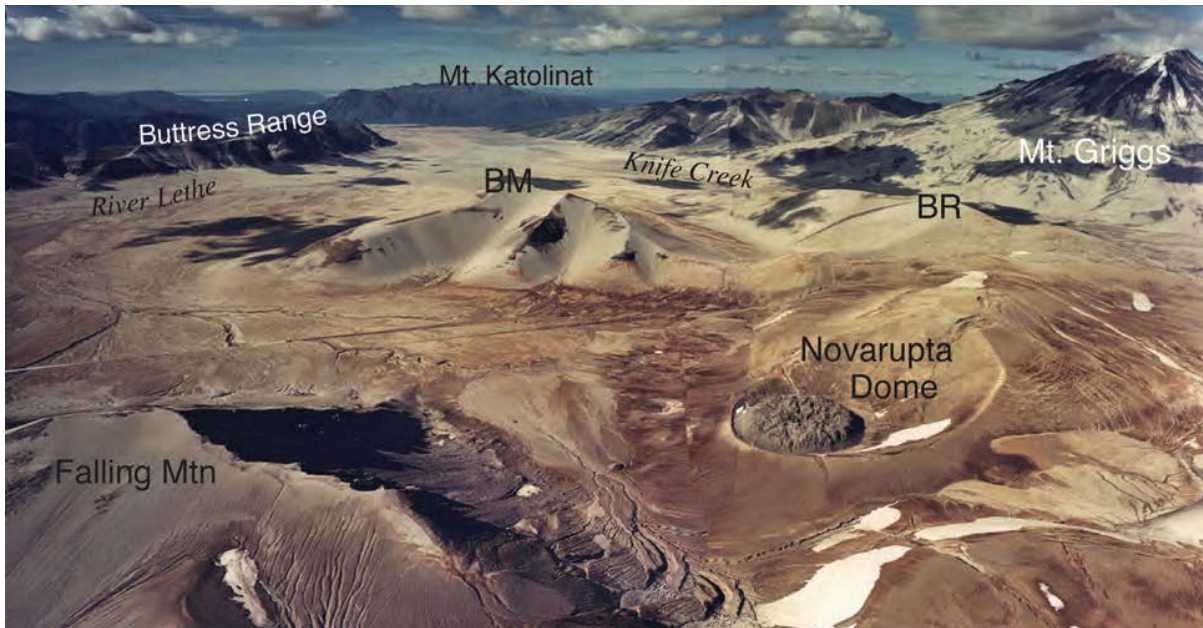


Figure 1.4 Aerial panorama of Novarupta basin and the Valley of Ten Thousand Smokes, extending 20 km northwest from Novarupta dome to the ignimbrite terminus at the base of Mount Katolinat. The three arms of the upper valley (*River Lethe*, *Knife Creek*, and an unnamed valley between them) are separated by Baked (*BM*) and Broken (*BR*) Mountains which are pumice mantled ridges of glaciated Jurassic siltstone. *Falling Mtn* is a pre-1912 dacite dome, *Mt. Griggs* is a 2,330-m-high andesitic stratovolcano, *Buttriss Range* and *Mt. Katolinat* are formed from subhorizontal sedimentary strata from the Naknek formation. Figure from Fierstein and Hildreth (2012).

Hildreth and Fierstein 2012). Naming of the VTTS is attributed to Robert Fiske Griggs, a field-based botanist who was the first scientist to visit and document Katmai caldera, Novarupta dome, and the VTTS. His work into the impact of ash burial upon vegetation, the source of the VTTS and Novarupta dome, the changing nature and behavior of the fumaroles, and mapping of Katmai and surrounding volcanoes culminated into a book titled *The Valley of Ten Thousand Smokes* (Griggs 1922).

Griggs hypothesized that the VTTS was formed by a hot mudflow, but colleagues Clarence Fenner and Emanuel George Zies later proposed that the source was a dry flow of hot ash and pumice analogous to nuées ardentes (Fenner 1920; Griggs 1922). Fenner, a petrologist, correctly noted that Katmai caldera could not have been the source of the VTTS ignimbrite; however, he erroneously attributed it to the injection of a great sill based on 1) the sill shattered the rocks above it and created openings or fissures through which magma could ascend, 2) “extrusion and inflation” of the magma formed the great “ash or sand flow”, 3) Novarupta, which formed by the extrusion of stiff lava similar to the spine of Pelée, formed within a parasitic cone that resulted from the enlargement of a channel along one of the fissures, and 4) the active fumaroles discharged volatiles from this large magma body (Fenner 1920). The sill theory was disproved by geochemists Eugene Thomas Allen and Emanuel George Zies, whose papers on the composition of the fumarolic gases and the morphology, mineralogy, and chemistry of the vents and deposits concluded that most of the fumarolic steam was from vaporization of surface waters that had infiltrated into the hot tuff (Allen and Zies 1923; Hildreth and Fierstein 2012).

Garniss Curtis, a field geologist, volcanologist, and geochronologist helped establish a modern volcanological framework through which the 1912 eruption could be interpreted. He showed that the fumaroles in the VTTS came from within the ignimbrite sheet itself and estimated that the valley-filling ignimbrite might be more than 200 m thick. Most notably, Curtis recognized that both the ignimbrite and the fallout sheet came from Novarupta basin through the generation of isopach maps for the deposits. He was also the first to propose

hydraulic interconnections between the main vent at Novarupta and the collapse caldera 10 km away at Mount Katmai (Curtis 1968; Hildreth and Fierstein 2012).

1.4.2 Chronology of the eruption

The five episodes (Table 1.1) are recognized by their distinctive eruptive deposits and eyewitness accounts of initiation, pause, and termination of local lapilli- and ash-fall. A wide range of compositions were erupted with changing proportions throughout the eruption (Figure 1.5), defining a chemical stratigraphy that enabled correlation of coeval products of variable transport mechanisms at widely spaced localities (Fierstein and Hildreth 1992). The eruption broke out through the Naknek formation, which supplied the majority of wall-rock lithics identified in the deposits, and formed a series of three nested vents that were active during specific episodes (Hildreth 1983, 1987; Hildreth and Fierstein 2000).

Table 1.1 Key characteristics of each eruptive episode (Ep.).

Ep.	Style	Duration (hours)	MER* (kg/s)	Column ht. (km)	Volume (km ³)	Deposits
I	Plinian	16	1.6x10 ⁸	27–28	8.8 fallout 11 flows	Fallout layers A–B; valley-filling ignimbrite
II	Plinian	7–9	1.7x10 ⁸	27–28	4.8	Fallout layers C–E; proximal PDCs
III	Plinian/ sub-Plinian	10	1.1x10 ⁸	24	3.4	Fallout layers F–H; proximal PDCs
IV	Effusive/ Vulcanian	u/k**	u/k	n/a***	<0.0005	Block apron
V	Effusive	u/k	u/k	n/a	0.005	Novarupta lava dome

*Mass eruption rate; **Unknown; ***Not applicable

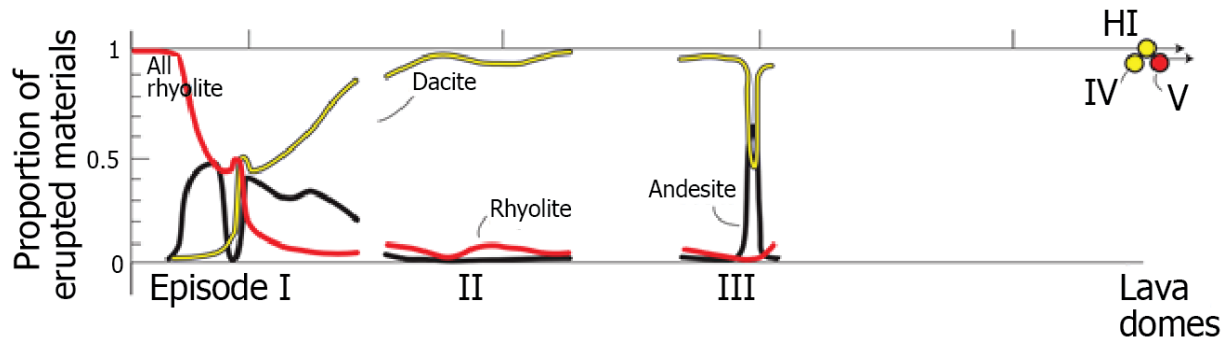


Figure 1.5 Changing proportions of rhyolite, dacite, and andesite pumice that erupted concurrently within each episode. Figure from Hildreth and Fierstein, 2012. *HI* Horseshoe Island.

Episode I was the largest and most powerful, erupting 70% of the eruption's total volume including nearly all of the ignimbrite and roughly half of the fall deposits (Table 1.1).

Concurrently emplaced deposits are comprised of two widespread fallout layers A and B and nine packages of the main VTTS ignimbrite. Fallout of layer A to the east-southeast (Figure 1.6) and accompanying radial emplacement of ignimbrite forming PDCs (package 1) both contained juvenile material exclusively of crystal-poor rhyolite (Figure 1.7; Fierstein and Hildreth 1992). Increasing contributions of dacite and andesite to the sustained eruption column is reflected in the compositionally zoned layer B and main valley-filling ignimbrite. Eight successive compositionally distinguishable packages of ignimbrite correlate with three sub-fall-units, the latter contain a lower andesite fraction indicating it was preferentially excluded from the high Plinian plume (Figure 1.7; Curtis 1968; Hildreth 1983; Fierstein and Hildreth 1992; Houghton et al. 2004; Fierstein and Wilson 2005). A shift in the relative significance of emplacement mechanisms also marks the transition from phase A to B as 90% of A was deposited as fallout and 80% of B was emplaced as ignimbrite (Hildreth and Fierstein 2012).

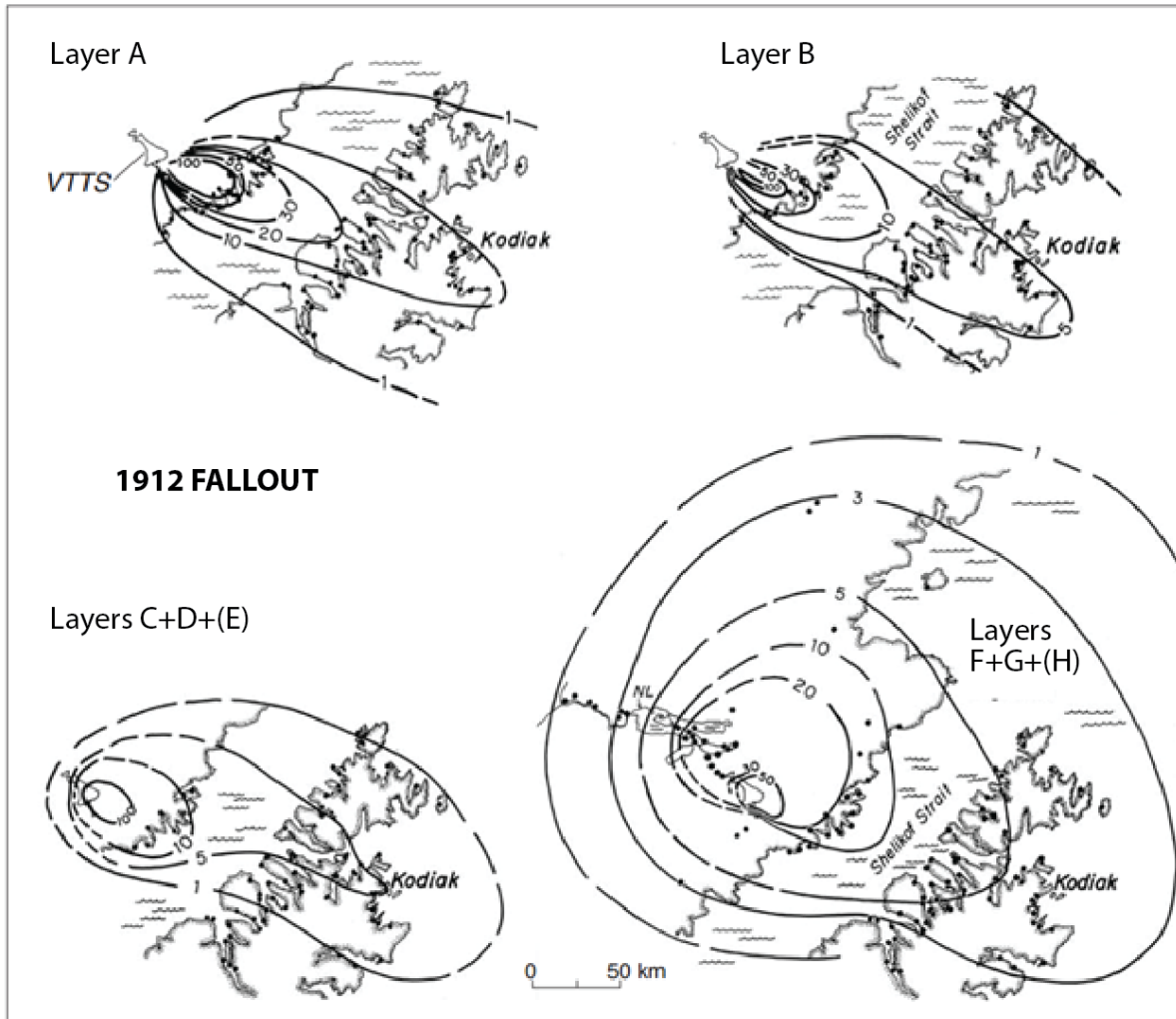


Figure 1.6 Isopach maps (contours in cm) of the 1912 fall layers: A and B (Episode I); C–E (Episode II); F–H (Episode III). Outline of VTTs is shown for reference. Dots are sites of measured sections. *NL*, Naknek Lake. Figure from Hildreth and Fierstein (2012).

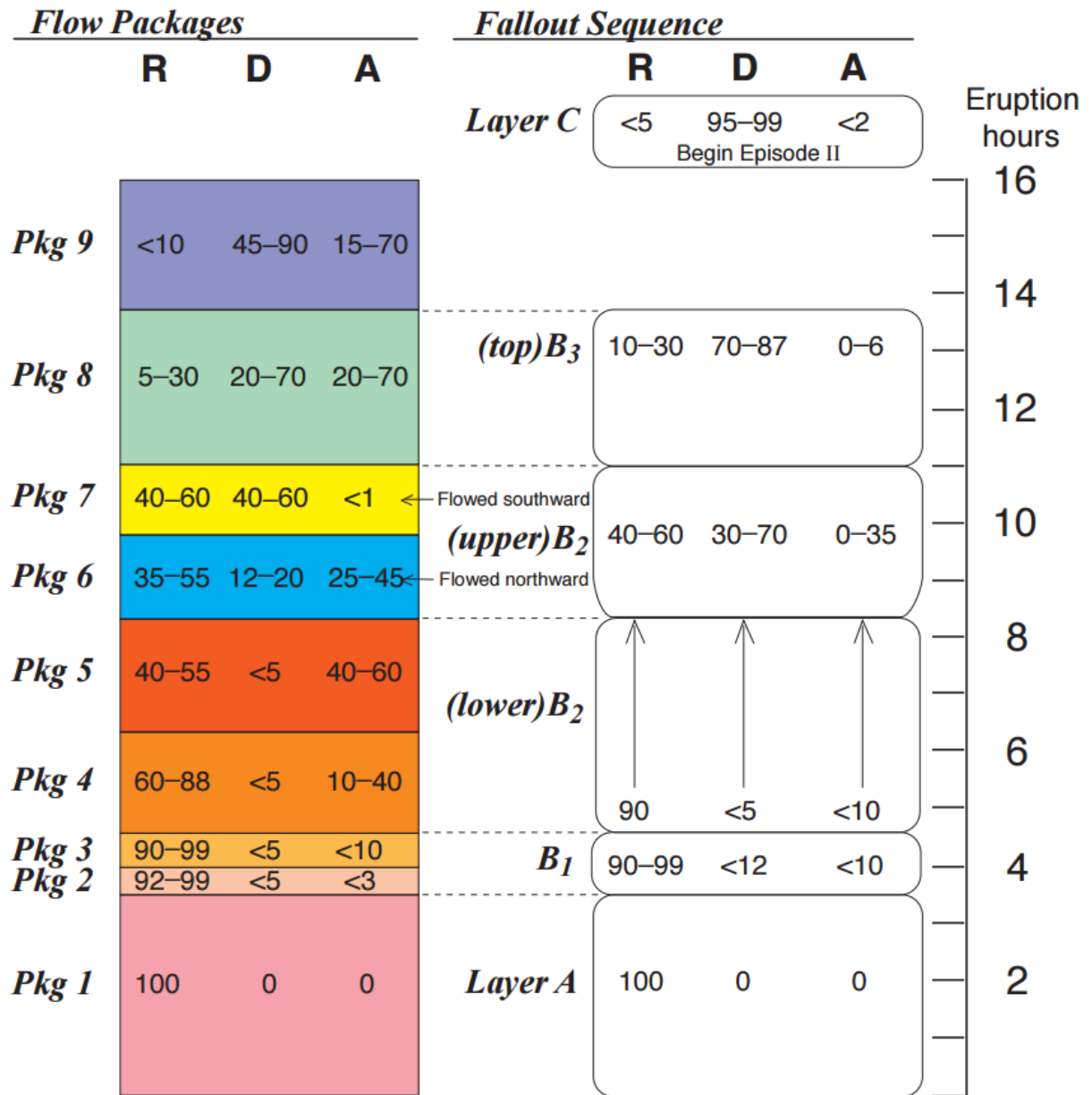


Figure 1.7 Schematic diagram illustrating the correlation between compositionally equivalent fall units and flow packages of Episode I. Vertical scale is time; no thickness data intended. *R*, Rhyolite; *D*, Dacite; *A*, Andesite. Figure from Hildreth and Fierstein (2012).

Layers A and B are Plinian fallout; however they have markedly different defining characteristics. In addition to the change in composition, Layer B is thinner than A (Figure 1.6) and unit A is fairly well sorted, with sorting improving downwind, whereas unit B shows variable sorting throughout its three subunits. Subunit B1 is poorly sorted due to co-ignimbrite ash containment, B2 is moderately to well sorted with slight inverse grading, and B3 is fairly well sorted and inversely to normally graded (Fierstein and Hildreth 1992).

Reports of a great explosion, earthquakes, and eruption cloud at 1300 Alaskan time on June 6, 1912 mark the beginning of Episode I. It broke through the Naknek formation at the foot of Trident volcano, eventually forming a 2-km-wide open flaring funnel-shaped vent. The truncated scarps of Falling Mountain (a Pleistocene dacite dome), distal Trident lava flows, and Broken Mountain (uplifted Jurassic sedimentary rocks) define the highest parts of the rim of the vent (Figures 1.4 and 1.8; Hildreth 1983; Hildreth and Fierstein 2000, 2012). Layers of mud studded with Katmai-derived lithics are intercalated with Novarupta pumice fall layers and the timing of the first major seismic event ($M_S > 6$) indicate that initial caldera collapse at Mount Katmai occurred ~11 hours into the eruptive sequence. This was after ~8.5 km³ of magma had erupted during Episode I (Hildreth 1991; Abe 1992; Hildreth and Fierstein 2000). Episode I ended after ~16 hours, back-filling the <1.5 km deep flared vent with ejecta.

After a few hours break, initiation of subsequent explosive activity bore through the backfill ejecta to form a smaller, 450-m-wide nested vent that was active throughout the second and third episodes (Hildreth and Fierstein 2012). Deposits of Episodes II and III consist of simple medial-distal Plinian fall layers and complex proximal, sector confined fall and PDC beds. Similar to Episode I, Episode II's fall deposits are distributed to the east-southeast of

Novarupta whereas Episode III's Plinian falls deposited over a broader area. This slightly asymmetrical accumulation toward the NE may be attributed to northeasterly drift of slow settling fine ash (Figure 1.6; Fierstein and Hildreth 1992). The flow deposits amount to no greater than 1% of each episode's eruptive volumes.

Curtis (1968) divided the Plinian falls into six units (Layers C–H) with virtually continuous pairs C–D and F–G deposited during Episodes II and III, respectively. Proximally to medially, the paired beds contain characteristics of deposition from the umbrella cloud of a sustained Plinian plume: moderate sorting, aerodynamic equivalence among pumice and lithic clasts, and weak internal mantle bedding (Fierstein and Hildreth 1992). Ash-rich layers E and H resulted from the slower settling of fines from Episode I–III Plinian plumes and small co-PDC plumes. It is estimated that layer E formed during a temporary (few hours) shutdown of the stable plume between Episodes II and III, which is attributed to failure of the conduit/vent walls (Adams et al. 2006b). This is evident in the proximal blast-like vent-clearing PDC deposits at the beginning of Episode III (Houghton et al. 2004) and constant vesicularity and bubble nucleation and growth textures in all pumices erupted throughout Episode II. Conversely, increasing pumice density and textures indicative of more bubble growth and collapse (over nucleation) in clasts from layer G (end of Episode III) suggest a progressive shift to open-system degassing is responsible for the end of Plinian activity (Adams et al. 2006b). This shift was likely due to a combination of 1) decreasing magma ascent rates and 2) shear fragmentation allowing limited permeable outgassing along the conduit walls and producing a low-porosity and high-viscosity magma annulus toward the end of episode III (Adams et al. 2006b; Nguyen et al. 2014).

Compositional contrasts between the regional fallout and the coeval proximal deposits prevent confident correlation of their deposition in time. Alternations of locally and regionally dispersed fall ejecta and thin flow and surge deposits that have no regional equivalents characterize the proximal deposits (Houghton et al. 2004). Overall, dacite pyroclasts dominated the eruptive products of Episodes II and III, but the local fall and most of the proximal PDC deposits are richer in lithics and in andesitic and banded pumice than regional layers C–D and F–G (Fierstein et al. 1997; Houghton et al. 2004). Additionally, the locally dispersed fall deposits form sector-confined lobes and wedges that half in thickness within 100–300 m of the vent (compared to several kilometers for the medial-distal fall deposits; Houghton et al. 2004).

The Episode II–III vent was backfilled by late-stage ejecta, and so the lava that was extruded in the fourth and fifth episodes reached the surface through a narrower conduit that was nested inside the larger backfilled vents (Figure 1.8; Hildreth and Fierstein 2012). Episode IV comprised of extrusion and complete destruction of a dacite dome through Vulcanian explosions. Its deposit consists of an apron of decimeter to meter sized blocks and lapilli with a range of textures including pumiceous, dense, and flow-foliated dacites, and variably welded breccia (Adams et al. 2006a). The juvenile components include small portions of andesite. Vesicle textures, porosity, and permeability data suggest a continuation of outgassing processes that began in late Episode III ultimately resulted in extrusion of a dense/outgassed dome that enabled the system to become pressurized and primed for Vulcanian explosion(s) (see section 1.4.3.3; Adams et al. 2006a; Nguyen et al. 2014).

The eruption terminated with extrusion of Novarupta lava dome, which is ~380 m in diameter, 65–70 m high, and circular in plan (Figure 1.4). This steep-sided dome has a coarse

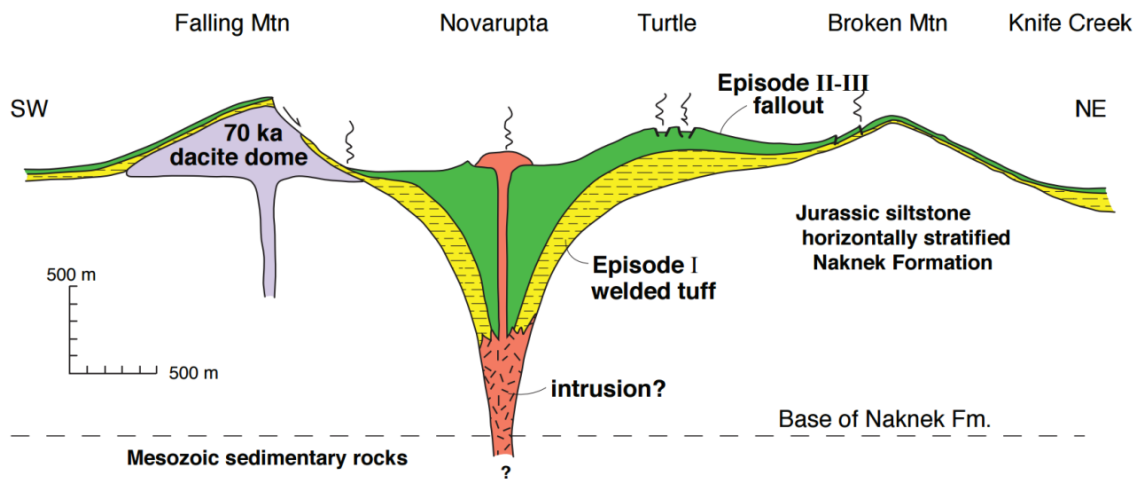


Figure 1.8 Conceptual cross section, to scale, showing the nested vent structure. No vertical exaggeration. Figure from Hildreth and Fierstein (2012).

blocky surface that is lacking any tephra (either uplifted by the dome or deposited subsequently) and a peripheral apron of coarse talus blocks. 95% of the Episode V dome is glassy, flow-foliated rhyolite that carries the same assemblage of sparse phenocrysts as that erupted during Episode I (Figure 1.9; Hildreth and Fierstein 2012). The remaining 5% consists of intermediate lava in the form of layers, lenses, and angular chunks of a darker brown color (compared to the pale to medium gray of the rhyolites). Complex shaped voids in thin sections are similar to those of the Episode IV dense dacites, indicating prolonged partial outgassing (Adams et al. 2006a).

The durations of Episodes IV and V are unknown as the dacite dome was never observed and the rhyolite dome was first observed on July 1916 when Griggs and Fenner first entered the VTTS and after lava extrusion had terminated. Earthquakes continued after the end of local Plinian ash fall, with felt earthquakes recorded on 50 of the next 70 days through to mid-August



Figure 1.9 Middle section of Novarupta dome viewed from the west. Note the blocky surface, the apron of talus blocks at the base, and the foliation in the large, pinkish blocks in the middle of the dome.

(Martin 1913). The most severe of these earthquakes were said to be on 11 and 21 June and 30 July whereas the only remotely instrumentally recorded earthquake was a M_S 6.2 event on 17 June (Abe 1992). Reports were also of continued dust at Puale Bay (called Cold Bay in 1912 ~60 km SSW of Novarupta) until 24 June, ‘smoke’ coming from the new crater, and smoke and acid fumes preventing getting close to the volcano (Hildreth and Fierstein 2012). This activity could indicate continued activity within Novarupta basin at least through the summer of 1912, but it also could have been the result of 1) seismicity accompanying continued slumping of the steep inner walls of Katmai caldera, 2) continued dust due to the slow settling and resuspension of fines by strong winds, and 3) fumes and acid species coming from fumaroles at Novarupta, within Katmai Caldera, and the VTTS. The only conclusive fact is that the Episode IV block

apron sits on top of shallow erosive gullies in layer H, indicating that the dacite dome was explosively destroyed after up to 50 cm of fines had accumulated locally and had been exposed to limited local erosion. Geochemical and petrological evidence suggests that the rhyolite dome extruded less than a week after the Plinian eruptions (Hildreth 1983; Hammer et al. 2002), providing a much shorter time-frame for post-Plinian dome extrusion than has been observed at other volcanoes (e.g. the 2008 and 2011 eruptions of Chaitén and Cordón Caulle, Chile).

1.4.3 Key previous volcanological findings

Certain aspects about the eruption and its deposits have provided the opportunity to investigate pre- and syn-eruption dynamics in ways that are not available at most other volcanoes. This has resulted in new insight into magma storage and transport, near vent column dynamics and sedimentation, and processes controlling transitions in eruption style. This section addresses three key findings out of several that have contributed to advances in volcanology.

1.4.3.1 Magma storage

Studies into Novarupta's production of a large volume of rhyolite within the wide compositional range of its products contributed to the highly debated subjects of storage within a zoned magma chamber and magma mingling processes. A compositional gap of ~8 wt% SiO₂ separates the juvenile rhyolite from a continuum between the dacite and andesite compositions of the remaining juvenile material. Hildreth (1983) demonstrated that there is continuity in both magma temperature and oxygen fugacity among all 3 components (Table 1.2) suggesting physical contiguity of the pre-eruptive magma. Coombs and Gardner (2001) and Hammer et al. (2002) conducted phase equilibrium experiments on the natural rhyolite and the dacite-andesite

ends of the continuum, respectively. Their results (Table 1.2) support the theory of shallow storage of a single, physically contiguous, zoned magma body.

Table 1.2 Composition and storage conditions of the 1912 rhyolite, dacite, and andesite.

	SiO₂ (wt%)	Temperature* (°C)	Temperature** (°C)	Depth (km)
Rhyolite	76.5–77.8	800–857	780–860	3–5
Dacite	63.0–68.6	848–950	850–880	4–5
Andesite	57.9–63.0	952–990	930–960	4.5–5.7

* From Fe-Ti-oxide geothermometry (Hildreth 1983)

** From phase equilibria experiments (Coombs and Gardner 2001; Hammer et al. 2002)

The leading hypothesis proposes that this magma body was located under Mount Katmai. The evidence supporting this theory includes: 1) synchronous caldera collapse at Katmai, 10 km from Novarupta, 2) extrusion of the now submerged Horseshoe dacite dome within the caldera after the end of the Plinian episodes indicating that magma was present below Katmai, 3) the compositions of the 1912 products have consistent differences with those erupted at other volcanoes within the Katmai Volcanic Cluster (making these volcanoes less likely as candidates for the magma source), 4) Mount Katmai is the only volcano within the cluster to have erupted basalt and rhyodacite, with pyroxene dacite and silicic andesite predominant at the others, prior to 1912, 5) the 1912 suite has a closer affinity to the products erupted by the Southwest Katmai cone, the edifice that has produced the largest pre-historical Plinian eruption and the only pre-1912 rhyodacite among the cluster, and 5) no evidence has been found to suggest recent magma storage beneath the Novarupta depression nor that more than one chamber erupted in 1912 (Hildreth and Fierstein 2000).

The currently favored pre-eruptive magma storage model is depicted in Figure 1.10. The ~3 km depth of the roof is constrained by the 4 wt% water saturated rhyolite estimated by Lowenstern (1993). Formation of a 5.5 km³ caldera, which accounts for no more than 40–45% of the 13.5 km³ of magma erupted, and 1.2 km of vertical displacement at Mount Katmai necessitate that the storage chamber be at least that thick and areally more extensive than the caldera. Shallow overburden and the horizontal bedding planes within the Mesozoic marine sedimentary rocks favor magma transport via a 6-km-long sill. The magma had to crosscut strata as a dike in order to reach the 1912 vent site, but the dike could have been short (<5 km) considering Novarupta broke through a low-lying valley (Hildreth and Fierstein 2000). The amounts of rhyolite, dacite, and andesite within the proposed storage chamber are based upon dense rock equivalents of each erupted component, and thus serve as a minimum for the estimated size of the chamber.

The hypothesized reservoir is zoned from andesite at the base to rhyolite at the top based on 1) likely density contrasts for the different magma compositions and 2) the order in which differing components erupted. Initial eruption of ~3 km³ of rhyolite in the first 3–4 hours of the eruption indicate that the conduit tapped the rhyolitic part of the reservoir first. Conversely, rhyolite is sparse among all the Plinian fall layers of Episodes II and III except the lowermost part of C, suggesting the rhyolite was either exhausted or blocked from the conduit by the influx of dacite (Hildreth and Fierstein 2012). This latter hypothesis is more likely considering the late-stage production of a rhyolite dome during Episode V after the supply of dacitic magma was exhausted. It is suggested that this rhyolite underwent partial open system degassing for an extended period (days-months, possibly since the close of Episode I) within some shallow

storage site and then was extruded passively after the Episode IV dacite was flushed (Hildreth and Fierstein 2012).

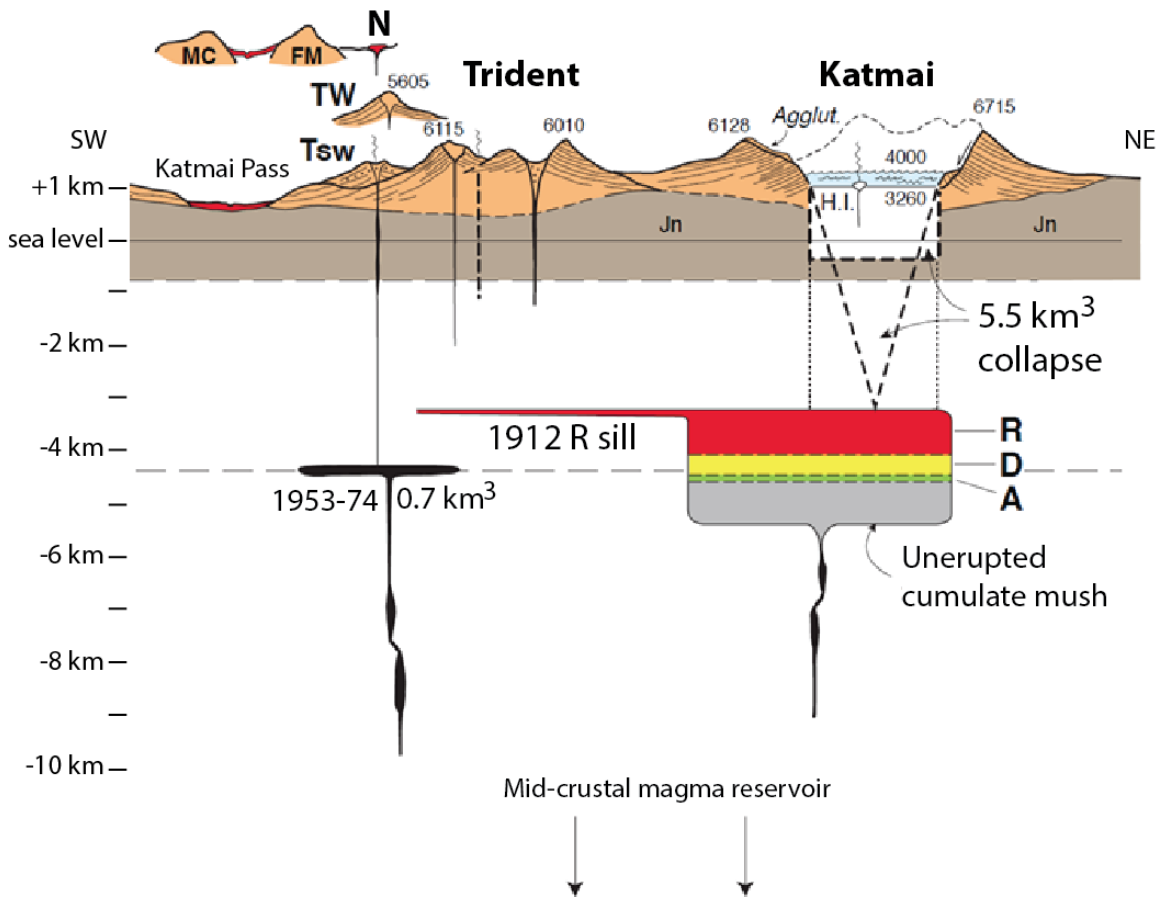


Figure 1.10 Schematic of the plumbing system beneath Katmai and Trident; drawn to scale along N65°E volcanic axis, looking N25°W with no vertical exaggeration, after Hildreth and Fierstein (2012). Elevations on profile are in feet. Wavy vertical lines indicate present-day fumarolic emissions. Novarupta (*N*), Falling Mountain (*FM*), Mount Cerberus (*MC*), and West Trident (*TW*) are not along the section, and so their relative positions are indicated above profile. *Jn*, marine sedimentary rocks of Jurassic Naknek Formation; *H.I.*, Horseshoe Island dacite dome; *Agglut.*, remnant of pre-1912 agglutinated dacite fallout. Magma reservoir for material erupted in 1912 is depicted as a contiguous chamber zoned from andesite (*A*) to dacite (*D*) to rhyolite (*R*) in proportions (1/4.5/7.5) erupted. Chamber would have been larger to the extent that additional magma failed to erupt.

Alternatives to a long-lived zoned reservoir for the model of pre-eruptive magma storage and syneruptive transport include 1) multiple chambers and 2) the arrival of a new magma batch from depth. Given the compositional gap between the phenocryst-poor rhyolite and porphyritic andesite-dacite continuum and the fact that the volume of the collapsed caldera accounts for less than half of the volume erupted, it is plausible that the 1912 magma involved the mixing of magmas from two or more discrete chambers (Curtis 1968; Hildreth 1983). Hildreth (1983) proposed that 8 km³ of magma from Mount Katmai moved toward or into a system below Novarupta in response to eruptive losses suggesting a hydraulic connection between the two sub-systems. However, this would have required the systems to have the same thermal properties (given the thermal continuity of the three compositions) and for there to be a major heat source to maintain the rhyolite in its nearly aphyric condition (Hildreth 1983). A major chamber directly beneath Novarupta now seems unlikely due to the rapid thermal decline of the vent region (Hildreth and Fierstein 2012).

Eruptions may be triggered by the arrival in the magma chamber of a hotter, more mafic magma from depth. Evidence of this generally occurs in the form of mafic enclaves that have chemical and mineral contrasts with the dominant melt composition. No such mafic (or intermediate) material has been found in the deposits, but it has been proposed that the aphyric rhyolite served as such a trigger. Eichelberger and Izbekov (Eichelberger and Izbekov 2000) proposed that a rhyolite dike rose from depth and simultaneously breached the surface at Novarupta and intersected a shallow andesite-dacite reservoir beneath Mount Katmai. Hildreth and co-workers present three main lines of evidence against this hypothesis. First, the east-west strike of the hypothetical dike would have been at a high angle to the closely coinciding vertical

jointing in the basement rock and plate-convergence vectors (Hildreth 1987; Wallmann et al. 1990; Hildreth and Fierstein 2012). Second, such a high volume rhyolite dike would have required partial melting of an equally high volume, deep, felsic pluton plus transport to the surface through mafic and intermediate mush pods without entrainment or mixing (Hildreth and Fierstein 2012). Finally, the close thermal, isotopic, and glass-compositional continuity of the rhyolite with the dacite would have been merely coincidental (Hildreth and Fierstein 2012).

Eruption of compositionally banded pumice (Figure 1.11) during Episodes I–IV and dark colored lenses and layers within the rhyolite dome are the result of mingling of confluent but compositionally distinct magmas. Banded pumice represent 3–5% of all pumice produced in the eruption; however, their fraction varies between 0–37% in the individual subunits (Fierstein and Hildreth 1992). Sharp contacts between compositional bands, e.g. glassy andesite chilled against the rhyolite (Curtis 1968), are indicative of short mingling times (minutes to hours prior to fragmentation) within the system feeding the eruption. Confluence of magmas may have been limited to transport, but it was long enough for the andesite to be partitioned to a peripheral collar around the emerging jet (next section). Rhyolite-andesite and dacite-andesite are much more common than rhyolite-dacite combinations, and pumice containing all 3 are rare. This is more likely due to the difficulty in mingling the high viscosity dacite and rhyolite magmas than to transport processes. The lower viscosity, higher temperature andesite may have been the key to unstable conduit flow promoting entrainment of the two high viscosity magmas (Fierstein and Hildreth 1992; Hildreth and Fierstein 2012).



Figure 1.11 Banded pumice clasts from the VTTS ignimbrite. Knife is 8.5 cm long. Figure from Hildreth and Fierstein (2012).

1.4.3.2 Implications of proximal deposits

Evidence in proximal deposits for near-vent processes is usually lost in large eruptions due to subsequent burial, erosion by PDCs, or caldera collapse. Caldera collapse 10 km from Novarupta and subsequent dome extrusion with only minor fallout from Vulcanian explosions allowed for unprecedented preservation of the ultra-proximal deposits from Episodes II and III. They include the true proximal equivalents to the widespread Plinian fall deposits in addition to intercalated narrow lobes of proximal fallout and sector-confined proximal PDC deposits. The ejecta ring, a 7–225 m thick asymmetric tuff ring surrounding the inner vent plugged by the Novarupta dome, was formed by these deposits during the second half of Episode II and all of III (Fierstein et al. 1997; Houghton et al. 2004).

The stratigraphy of the proximal deposits is far more complex than the medial-distal fall sequence. There are four characteristics unique to the proximal products (Houghton et al. 2004):

- 1) The fall ejecta are fines poor, moderately sorted, and show rapid changes in thickness over tens to hundreds of meters, both radially and concentrically with respect to Novarupta dome.
- 2) The PDC deposits have poor sorting with variable amounts of ash matrix and their distributions vary locally in thickness in response to topographic relief.
- 3) Conspicuous, outsized/meter-scale lithic or pumice blocks were emplaced ballistically.
- 4) Sudden shifts or influxes in composition, particularly andesitic, rhyolitic, and banded pumices, are confined to sectors in both fall and flow deposits and contrast to the dominantly dacite medial and distal deposits.

Fierstein et al. (1997) and Houghton et al. (2004) interpreted these deposits and their distinctive characteristics as the result of sedimentation from the margins of the jet and lower plume (Figure 1.12). These interpretations include (in order of the above list): 1) locally and confined fallout of clasts from the jet because they were not adequately supported by upward gas flow (Regime 3 of Houghton et al. (2004)), possibly in the form of an irregular 'collar' of low-fountaining ejecta partially sheathing the high-velocity dacitic core; 2) PDCs generated by small scale collapses around the plume margins and overspill from the vent because fountaining of all grain sizes prevents entrainment of enough air to attain positive buoyancy (Regime 2); and 3) direct lateral ejection of clasts detached from the rising plume (Regime 4). In regards to the changing composition of the proximally deposited clasts relative to the dacitic Plinian fallout, Fierstein et al. (1997) suggest that the more mafic magma was positioned toward the conduit walls making it more likely to enter the lower velocity sheath of low fountaining ejecta. This may have been due

to viscous segregation while in the conduit or deeper controls relating to the geometry of the conduit and where and how the andesite was released to the vent system. The lateral changes in proportions of andesitic and dacitic pumices at least suggest limited mixing within the jet region (Houghton et al. 2004).

Not only did these deposits reveal processes of early sedimentation from the jet and convective regions of buoyant plumes, but they also challenge certain assumptions made in eruption column models and provide insights to heterogeneities and instabilities within the emerging column (Houghton et al. 2004). The deposits disprove the assumptions that sedimentation from margins of the ascending jet is negligible and that eruption style oscillates between fall and PDC activity (rather than simultaneous buoyant and non-buoyant states). Also, models utilize a 'top-hat' velocity profile (Figure 1.13) for the plume and assume that velocity profiles and particle concentrations are axisymmetric. Rapid lateral changes in 1912 proximal deposit thickness, composition, and transport mechanisms reflect heterogeneities in the emerging jet portion of the column due to complex ascent of the pyroclast/gas mixture. The development of a slower annular zone of higher particle concentration that is more prone to fountaining and collapse relative to the turbulent core implies that a non-uniform (possibly Gaussian) velocity profile should characterize the material as it emerged from the jet (Houghton et al. 2004).

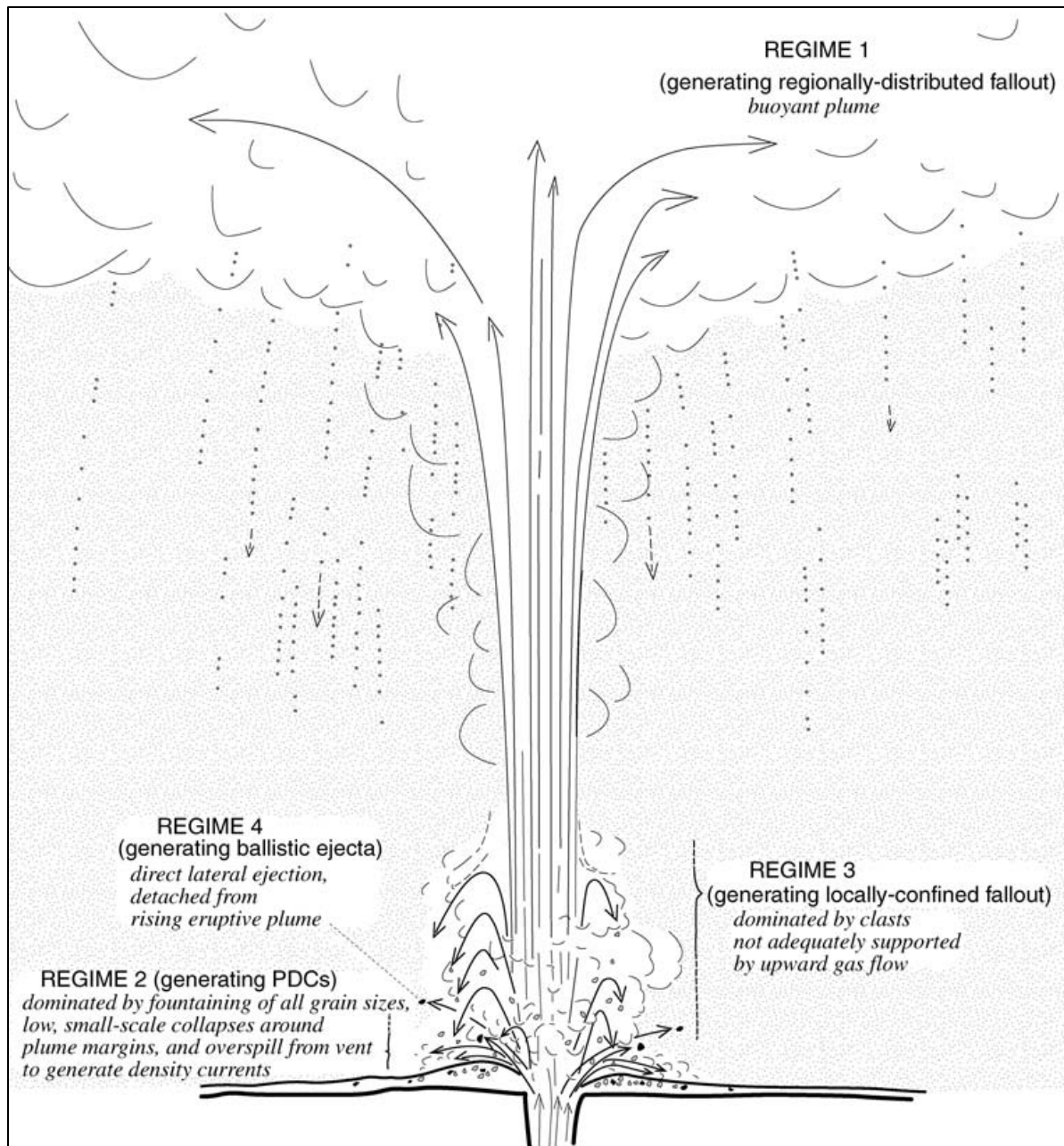


Figure 1.12 Diagram of the regimes of Houghton et al. (2004) that typified the proximal environment throughout Episodes II and III and produced the complex proximal deposits. Figure from Houghton et al. (2004).

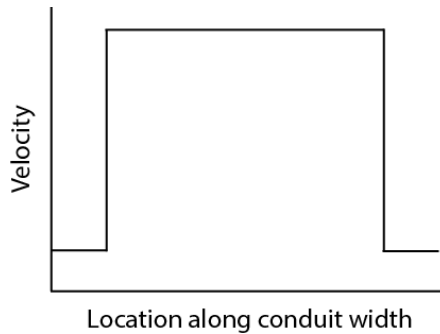


Figure 1.13 Schematic diagram of a “top-hat” velocity profile.

1.4.3.3 Transitions in eruption style

A complete shift from closed to open system degassing generally explains the transition from explosive to effusive silicic volcanism; however, the Vulcanian phase during Episode IV indicates more complex degassing and outgassing processes during this shift. Adams et al. (2006a) developed a conceptual model for development and fragmentation of the dacite dome through a vesicularity and textural analysis of the Episode IV block apron. They suggest that, during Episode III, a partial shift to open system degassing led to the accumulation of slowly ascending dense, degassed/outgassed magma to line the conduit walls while melt along the axis continued to ascend rapidly, nucleating and growing vesicles at shallow depths. The radius of the conduit gradually reduced until the degassed material effectively blocked the conduit, but the upward rise of the volatile-rich melt drove the outgassed material towards the surface resulting in a plug or dome (Figure 1.14). Subsequent intrusion of hotter, vesiculating magma into the cooler, denser material resulted in a heterogeneous dome consisting of complex regions of variably degassed and/or outgassed material (Figure 1.15). Adams et al. (2006a) thus suggest that coeval open and closed system degassing were active at similar levels within the shallow conduit.

Two modes of fragmentation of the dome are proposed by Adams et al. (2006a). In the first scenario, the system became pressurized in response to loss of permeability due to catastrophic bubble collapse. A fracture in the dome or partial gravitational collapse would release the pressurized gas and initiate a Vulcanian explosion. Alternatively, infiltration of external water into the dome could have triggered and provided additional energy to the explosion.

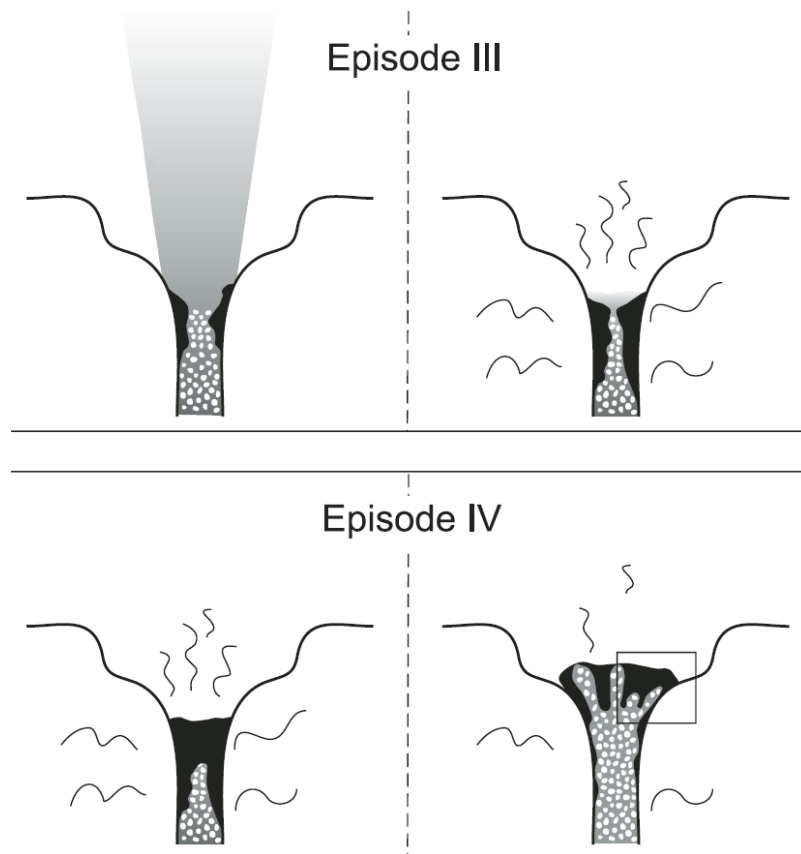


Figure 1.14 Illustrations of the processes that resulted in the shift in eruption style during Episodes III and IV. As open system degassing progressed, dense, degassed magma progressively lined the conduit walls until the vent become blocked. Continued ascent of vesiculating magma pushed this dense cap upwards and intruded into the dome/plug. Rectangular region in last panel is enlarged in Figure 1.15. Figure from Adams et al. (2006a).

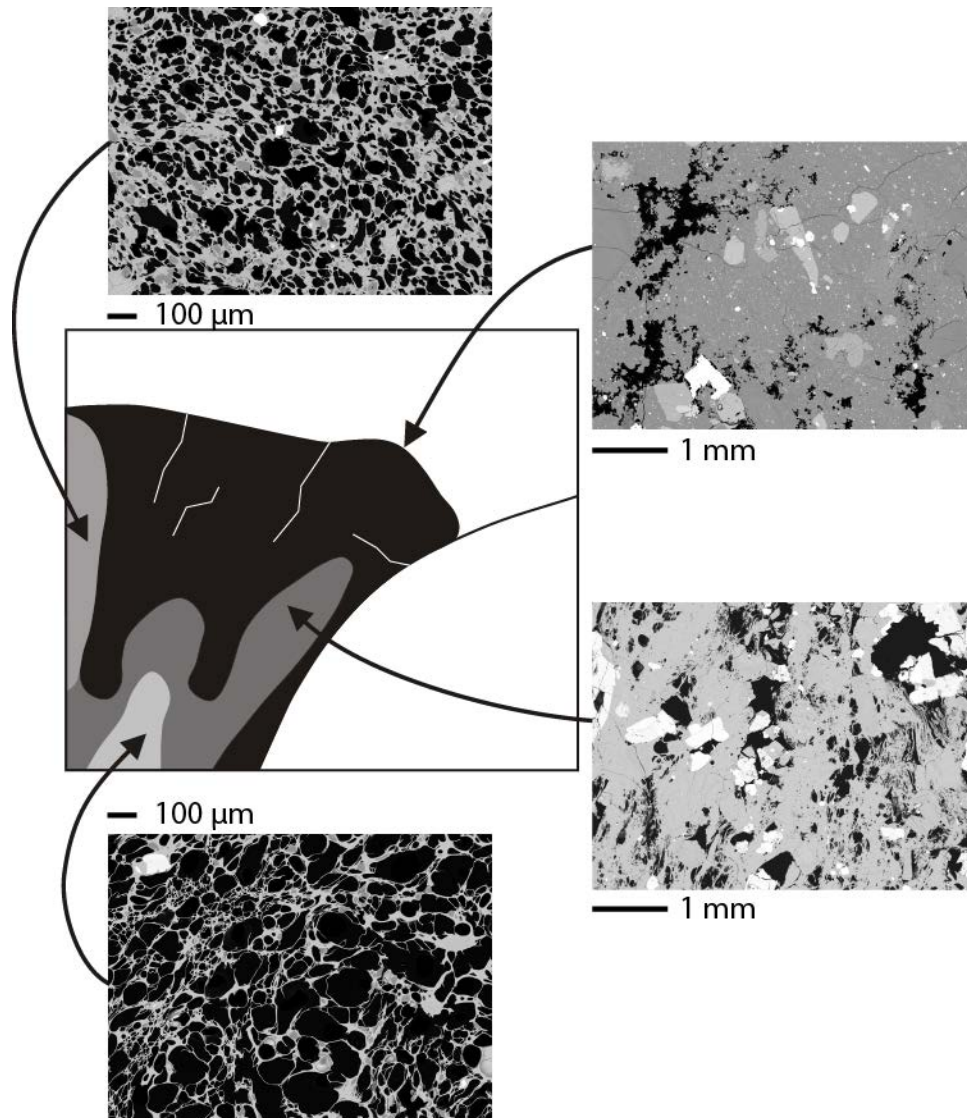


Figure 1.15 Enlarged region of the dome highlighting heterogeneity within the dome lava and the intruding melt. Dome material is highly outgassed, whereas intruding melt is variably partially outgassed and/or actively degassing. Figure modified after Adams et al. (2006a).

1.5 Motivation for research

The work of Adams et al. (2006a) on the Episode IV deposit was among the first studies to propose significant heterogeneity within very shallow depths prior to some Vulcanian

explosions. It was also at the leading edge of research that provided evidence of the shift from closed to open system degassing that plays a significant role in the decline of powerful explosive eruptions. However, development of new and improved laboratory-techniques (e.g. for porosity and permeability, or matrix glass water content) since that study (Rust and Cashman 2004, 2011; Wright et al. 2006; Burgisser et al. 2010; Le Losq et al. 2012; Shea et al. 2014; Drignon et al. 2016) have provided an opportunity to expand on, and provide a greater understanding of, processes occurring within the shallowest conduit during Vulcanian explosions. Additionally, the 2006 work brought about more questions in light of the results, including:

- How did this heterogeneity develop in the shallow conduit/dome?
- Quantitatively, what is the lateral and vertical length scales of this heterogeneity?
- What was the trigger for the explosion(s) that destroyed the dacite dome?
- How do the Vulcanian explosions of Episode IV compare to those observed in recent decades and to the theoretical and numerical models developed from those observations?
- What implications do these results have for the decline of powerful explosive eruptions?

The work for this dissertation addressed aspects of these questions through 1) more extensive field mapping and 2) greater inspection of the block lithologies and (in particular) the differences within individual component groups through the application of existing (bulk vesicularity, qualitative 2D micro-textures) and new/improved (porosity and permeability, matrix glass water measurements) laboratory techniques. For example, breadcrusted and banded blocks are mentioned in the previous work but not studied in detail. Understanding the processes that encouraged/enabled breadcrusting and banding can provide insight to processes occurring within, and the structure of, the conduit. This work also addresses certain aspects of the previous

research that were left unresolved: such as whether or not there were multiple explosions throughout Episode IV.

Although no near-vent observations from the time of the eruption are available for Episode IV, the rationale for focusing on this particular Vulcanian event is two-fold: 1) the preservation of its ultra-proximal deposit is unprecedented due to caldera collapse (a common consequence of large-volume eruptions) occurring 10 km away from the source vent and to it being the last preserved explosive deposit from the 1912 eruption and 2) observations and models of recent Vulcanian explosions were focused on events that dominantly disrupted long-lived dome growth. In contrast, Episode IV involved relatively short-lived passive extrusion that was disrupted by relatively weak explosions that occurred at the *end* of much more powerful explosive activity. The recent rhyolitic Plinian eruptions of Chaitén in 2008 and Cordón Caulle in 2011–2012 also concluded with lava extrusion and intermittent Vulcanian explosions, yet their deposits are not as easily accessible nor as well preserved. Field and laboratory results from this study can, in the future, be combined with such 21st century observations to provide a clearer understanding of what causes these types of Vulcanian explosions.

CHAPTER 2

Eruptive and shallow conduit dynamics during Vulcanian explosions: Insights from the Episode IV block field of the 1912 eruption of Novarupta, Alaska

Published in *Bulletin of Volcanology* as:

Isgett, S.J., Houghton, B.F., Fagents, S.A., Biass, S., Burgisser, A., Arbaret, L. (2017) Eruptive and shallow conduit dynamics during Vulcanian explosions: insights from the Episode IV block field of the 1912 eruption of Novarupta, Alaska. *Bull Volcanol* 79:58. doi: 10.1007/s00445-017-1138-4

Abstract

The study of ~1,300 juvenile and lithic blocks from a Vulcanian phase of the 1912 eruption of Novarupta provides new insight into the state of the magma as an eruption passes from sustained Plinian to dome growth. Blocks that were predominantly ballistically ejected were measured and sampled within an ~2–3-km radius from vent and supply a picture of a dynamic and complex shallow conduit prior to magma fragmentation in repeated small explosions. Extreme conduit heterogeneity is expressed in the diverse range of dacitic block types, including pumiceous, dense, banded, and variably welded breccia clasts, all with varied degrees of surface breadcrusting. We present new maps of block lithology and size, making Episode IV the most thoroughly mapped Vulcanian deposit to date. Sectorial regions rich in specific lithologies together with the block size data suggest multiple, small explosions. Modeling of block trajectories to reproduce the field data indicates that ejection velocities range from 50–124 m/s

with a median of ~70 m/s. We propose that individual explosions originated from a heterogeneous shallow conduit characterized both by the juxtaposition of magma domains of contrasting texture and vesiculation state and by the intimate local mingling of different textures on short vertical and horizontal length scales at the contacts between these domains. In our model, each explosion disrupted the conduit to only shallow depths and tapped diverse, localized pockets within the conduit. This contrasts with existing models for repetitive Vulcanian explosions, and suggests that the dynamics of Episode IV were more complex than a simple progressive top-down evacuation of a horizontally stratified conduit.

2.1 Introduction

Vulcanian eruptions are short-lived, impulsive explosions that are generally episodic and unpredictable. The impacts of individual Vulcanian explosions are typically less devastating than their larger, steady and sustained explosive counterparts, yet they are much more common and can pose protracted risks when they occur in sequences lasting weeks to decades. Vulcanian explosions last seconds to minutes and evacuate only a portion of the magma resident in the upper conduit, producing small volumes of $<0.1 \text{ km}^3$ dense rock equivalent (DRE). The resulting short-lived plumes typically reach heights of $<10 \text{ km}$ and may collapse to form pyroclastic density currents (Clarke et al. 2002b; Clarke 2013). A striking feature of many Vulcanian deposits is an abundance of highly diverse juvenile pyroclasts in varying proportions and textures. In a single eruption pyroclasts may range between dense and highly vesicular and from microlite-free to microlite-rich (Adams et al. 2006a; Clarke et al. 2007; Wright et al. 2007; Cassidy et al. 2015).

The best-studied recent Vulcanian eruptions involved short, more-intense intervals of explosive activity during long-lived dome building eruptions (Melnik and Sparks 1999; Druitt et al. 2002; Kennedy et al. 2005; Scheu et al. 2006, 2008; Clarke et al. 2007; Burgisser et al. 2010; Giachetti et al. 2010). However, Vulcanian behavior can mark the opening stages of larger, sustained sub-Plinian or Plinian eruptions, such as during the 1991 eruption of Mount Pinatubo, Philippines (Hoblitt et al. 1996), or provide a transition from sustained powerful explosions to lava effusion as it did during 1980–1982 at Mount St. Helens, USA (Christiansen and Peterson 1981). At Soufrière Hills volcano, Vulcanian explosions during 1997 comprised short sequences of explosions that were part of longer lived dome growth and collapse (Druitt et al. 2002). Smaller Vulcanian explosions can also occur daily over prolonged periods throughout decades-long dome building eruptions, such as the 1929–present eruption of Volcán Santiaguito, Guatemala (Sahetapy-Engel et al. 2008).

Field observations such as ballistic range and clast size and density have been used to estimate eruptive conditions during transient explosions using models that apply the equations of motion and drag relationships. Early models assumed that pyroclasts were ejected into a stationary atmosphere resulting in an overestimation of the atmospheric drag force early in the explosion and unrealistically high ejection velocities (Minakami 1942; Fudali and Melson 1971; Wilson 1972). More-sophisticated computational schemes have been developed over the last three decades in an attempt to account for changes in the drag force due to moving volcanic and atmospheric gases (Fagents and Wilson 1993; Waitt et al. 1995; Mastin 2001; Alatorre-Ibargüengoitia and Delgado-Granados 2006; de' Michieli Vitturi et al. 2010; Alatorre-

Ibargüengoitia et al. 2010, 2012; Benage et al. 2014; Bertin 2017) and have yielded velocities closer to those estimated from image analysis.

Our current understanding of the initiation of Vulcanian events is firmly tied to models of such systems involving cyclic dome growth, development of a dense outgassed region in the upper conduit, conduit pressurization, dome disruption, fragmentation and conduit evacuation, and finally conduit refill (Druitt et al. 2002; Diller et al. 2006; Burgisser et al. 2010; Clarke 2013; Clarke et al. 2015). In such models, Vulcanian eruptions are the consequence of the sudden downward decompression of a conduit containing pressurized, horizontally stratified, rheologically heterogeneous magma in varying states of degassing and outgassing (Self et al. 1979; Turcotte et al. 1990; Fagents and Wilson 1993; Woods 1995; Clarke et al. 2002a, b).

The variety of pyroclast densities and textures produced in Vulcanian explosions associated with large Plinian eruptions hints at a more complex conduit architecture than a simple horizontal layering (Adams et al. 2006a) and contrasts with the simple pyroclast textures seen in the associated Plinian phases. Opportunities to study the degree of this complexity, and how it influences the style of the overall eruption, are limited. Products of Episode IV of the 1912 eruption of Novarupta provide a unique opportunity to assess conduit complexity as the deposits are exceptionally well preserved. The Novarupta eruption consisted of five episodes ranging from strong Plinian (mass eruption rates of $1.1\text{--}5 \times 10^8$ kg/s) to dome effusion (Fierstein and Hildreth 1992; Hildreth and Fierstein 2000; Houghton et al. 2004; Adams et al. 2006b; Nguyen et al. 2014). Sixty hours of Plinian explosions erupted first predominantly rhyolite (early Episode I) and then dacite with minor amounts of andesite (Episodes II–III). Episode IV produced a dacitic block bed, interpreted as the product of complete destruction of a dacite

plug/dome via Vulcanian explosions, before extrusion of a rhyolite dome in Episode V (Hildreth and Fierstein 2000; Houghton et al. 2004; Adams et al. 2006a). There were no direct observations of any part of the Novarupta eruption, only of events that affected surrounding communities such as earthquakes and ash/lapilli fall (Hildreth and Fierstein 2012). Without direct observations, durations and other source parameters for Episodes IV and V are unknown and we are dependent on the deposits for further understanding.

Compensatory caldera collapse during the Plinian episodes occurred 10 km from vent, preserving the ultra-proximal deposits from Episodes I through IV to within 200 m from source. The Episode IV block and lapilli apron that caps the fine ash from the close of Episode III is the only evidence that a dacite plug/dome formed at this time. The Episode IV deposit permits us to investigate the processes involved in the decline of a voluminous Plinian eruption during the transition from powerful, sustained explosive activity to stable extrusion of a lava dome. We can also contrast Episode IV with well documented Vulcanian explosions during recent dome-building eruptions elsewhere, and address questions such as the following: what were the physical states, and their proportions, of the magma in the conduit; and did a single event destroy the plug/dome or did it involve a series of explosions?

2.2 Methodology

A total of 639 blocks was added to an existing data set (Adams et al. 2006a) yielding a new total of 1,273 mapped blocks (Figure 2.1). The largest blocks within 20–60-m-wide square areas at any distance and azimuth from the vent were located with a handheld GPS. Lithology, textures (including breadcrust rinds), and the three largest orthogonal dimensions were recorded, and an

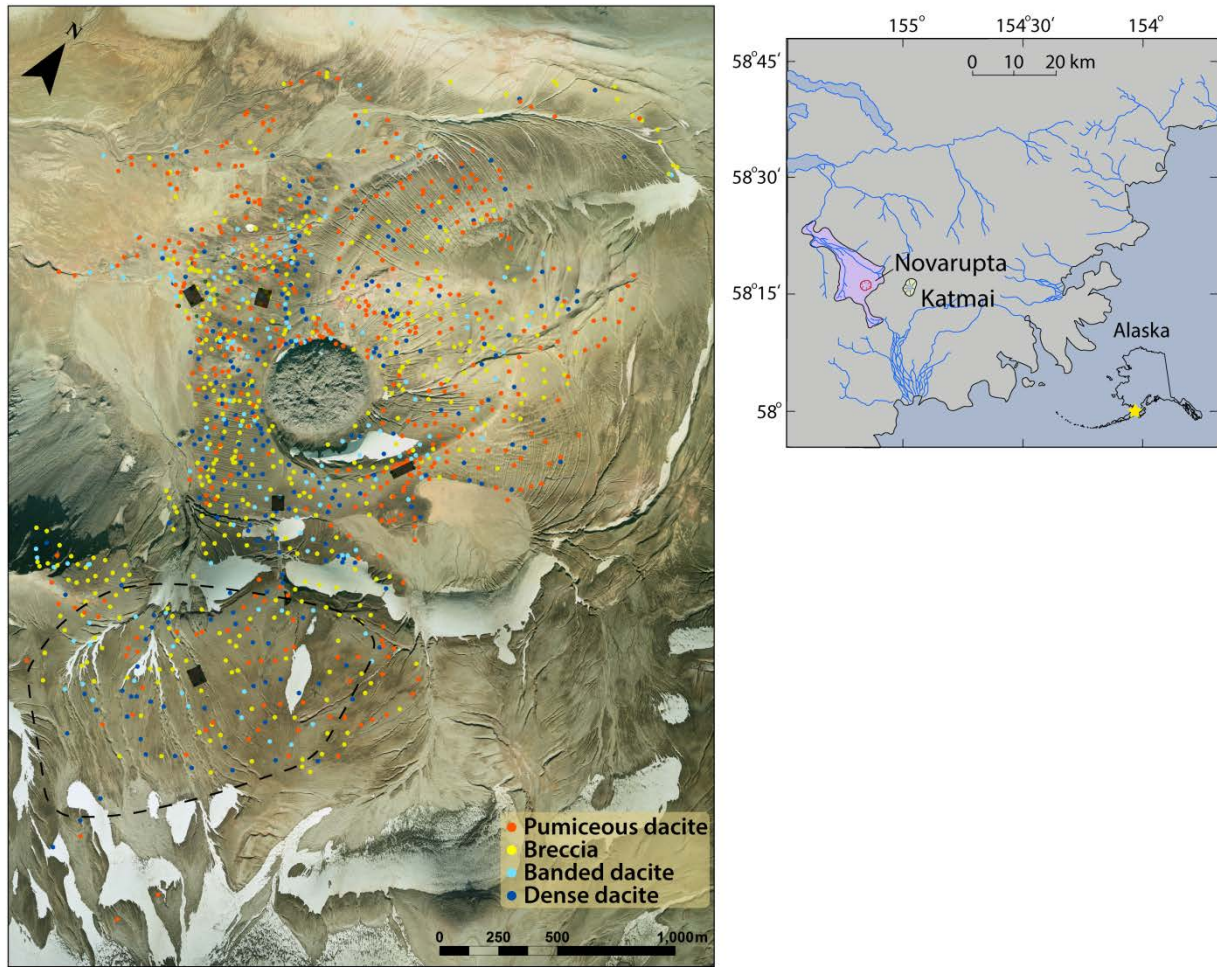


Figure 2.1 (Left) Distribution of the Episode IV blocks according to lithology. Black regions are locations for the componentry quantification. Black dashed line delineates the area overlapping with the Episode IV block apron that contains dense andesites from the 1953–1974 eruptions of Southwest Trident volcano. Round feature in middle is the Episode V rhyolite dome. (Right) Location map for the 1912 deposits, including the Valley of Ten Thousand Smokes (in purple) and the Episode V dome (in red). Yellow star in bottom right denotes the location within Alaska. Figure modified after AVO/ADGGS.

average dimension was calculated from the measurements. Fragments of blocks that broke apart upon landing and could not be reassembled were piled up and average dimension was estimated using the scaling factor of Adams et al. (2006a). A separate componentry quantification was conducted in five areas chosen for their density of blocks, remoteness from post-eruptive channels, and representative radial direction from the dome (black areas in Figure 2.1). Two areas northwest of the Episode V dome were mapped by Adams et al. (2006a) and three areas in the south and southeast were measured in this study; the region northeast of the dome is not represented because of the steep slopes beneath the 1912 ejecta in this area. The 100 largest blocks (regardless of distance from one another) were measured along parallel transects within each area in order to ensure that the proportions of each component were accurately represented. Block densities were measured for a representative number of clasts within each componentry group, and an average density was calculated per group and applied to blocks that were not sampled.

Maps of block distribution according to (i) lithology and (ii) average dimension were constructed in ArcGIS. Note that these maps do not necessarily show the distributions of every large block on the ground surface. For example, if the largest block size is 50 cm (average dimension), then any blocks <50 cm within a 20–60-m square were not mapped. Care was taken to measure only blocks that were preserved in situ. This explains the reduced number of data-points along steep slopes and the major gaps in the regions to the east (a seasonal lake bed) and southwest (a fluvial pumice delta) of the Novarupta dome on our maps.

Individual block trajectories were simulated using the algorithm of Fagents and Wilson (1993) to estimate initial ejection angles and velocities. Due to the difficulty of constraining the

necessary conduit parameters for a detailed description of the drag regime close to the vent (e.g., conduit radius, gas volume fraction), we assume the ejection of blocks into a still atmosphere. We estimated the threshold, in terms of size and density, at which blocks could be treated as ejected into a stationary atmosphere, versus those blocks that were influenced by motions of the ambient (volcanic plus atmospheric) gases. This enabled a narrowing of the results down to the most likely eruptive conditions during Episode IV. A detailed description of the equations of motion is presented in Appendix A.1.

2.3 Block data

2.3.1 Episode IV block componentry

Clasts forming the texturally diverse and chemically homogeneous block apron were categorized into the lithologic groups assigned by Adams et al. (2006a). The majority of blocks are textural variations on phenocryst-rich dacite, and less than 1% include a pumiceous andesite component. Dacites were classified as pumiceous dacite, dense dacite, banded dacite, or breccia. Within each lithologic group, breadcrusting may be present or absent.

The pumiceous dacites are highly vesicular (average of 67%; Figure 2.2) and the dominant lithology in the field (Figure 2.3). Non-breadcrusted pumices are microvesicular with textures very similar to the Episode III Plinian pumices. Dense dacites are crystal-rich and vesicle-poor (Figure 2.2), with 9% average vesicularity, and are the second least abundant lithology by volume. Their vesicle population is not visible to the naked eye. A number of dark, crystal-rich, dense blocks in a restricted area between West Trident and Novarupta basin (within



Figure 2.2 (previous page) Clast lithologies observed within the Episode IV block field. **a** Non breadcrusted pumice, N406. **b** Dense dacite, B126. **c** Breadcrusted dense banded, note that this block has mm banding and consists of dominantly darker gray, denser bands with lighter gray, lower density laminae, N113. **d** Pumiceous banded with overall beige pumiceous texture and light gray slightly denser bands, N322. **e** Mixed banded with bands of varying shades of gray and densities, note how the banding extends into the thin crusts on the outside edges of the flat faces, N197. **f** Breadcrusted mixed banded block with sub-equal amounts of centimeter/decimeter thick dense and eroded pumice bands, B349. **g** and **h** Samples from block B349, note how the centimeter thick dense and pumiceous bands contain laminae of different densities. Banding can be seen extending into the crust (left side of picture in **g** and at top of picture in **h**) in the form of darker/slightly more vesiculated crust that expands into interior pumice (red arrow in **h**). **i** Lightly welded breccia, weathering of the red oxidized and friable ashy matrix has formed a textured surface of outcropping pumice, B297. **j** Moderately welded breccia, B51. **k** Densely welded breccia, N038. **l** Inset of **k** highlighting the flattened pumice. **m** Dense vitrophyre with oxidized red lithics, N305.

the dashed line in Figure 2.1) appear similar to the Novarupta dense dacites; however, they are andesites from the 1953–1974 eruptions of Southwest Trident volcano (Coombs et al. 2000).

Banded blocks exhibit sharp textural banding of juvenile dense and pumiceous dacite and were subdivided into three categories based on the relative proportions of each texture. A spectrum of flow banding types is present ranging from dominantly dense dacite (dense banded) to dominantly pumiceous dacite (pumiceous banded), and end-member vesicularities are 33% and 63%, respectively (Figure 2.2). Other banded clasts contain sub-equal amounts of dense and pumiceous dacite (mixed banded), in often sharply delineated bands. Banding may be on a millimeter or centimeter scale or both, and bands may show plane-parallel contacts to their

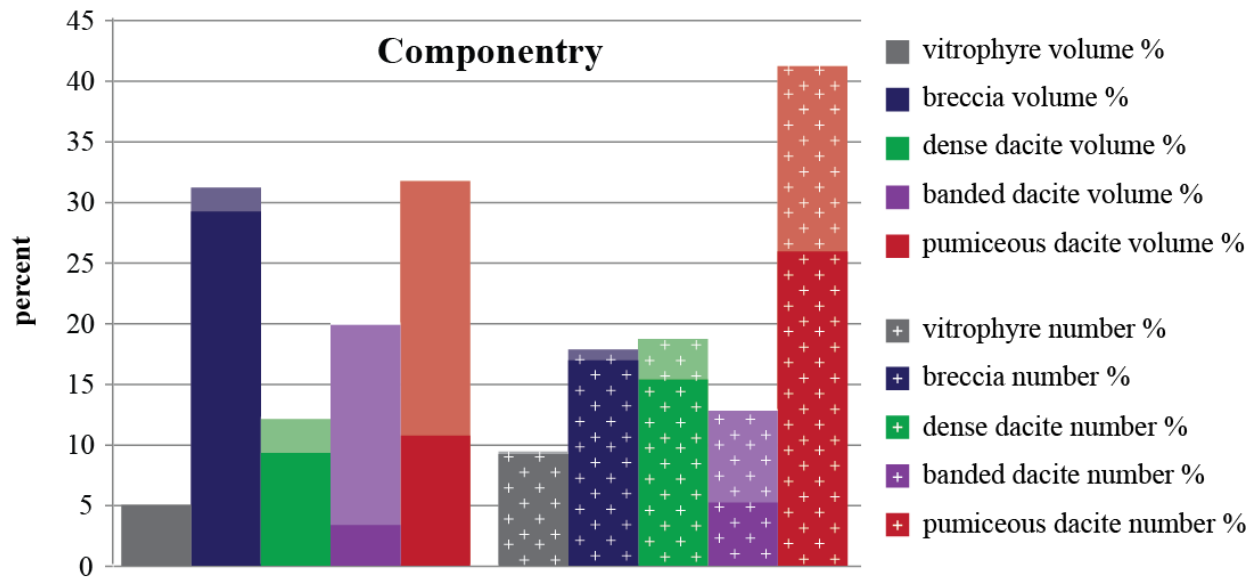


Figure 2.3 Proportions of each component according to volume (left) and number (right). Each column is separated into lighter breadcrusted and darker non breadcrusted proportions. The breccias and pumices are most dominant according to volume, and the pumice blocks are 20% more numerous than any other lithology. The pumice and banded blocks are significantly more breadcrusted than the breccias and dense dacites.

neighbors or pinch and swell. Strikingly, banding extends into rinds of breadcrusted samples (Figure 2.2).

Breadcrusting, a variably cracked, quenched rind that generally is denser than the interior, is present on examples of all the lithologies, but especially on banded and pumiceous blocks (Figures 2.2, 2.4). Breadcrusting is more prevalent amongst the largest pumices but not for the dense dacites or breccias (Figure 2.5). Rind vesicularity ranges from microvesicular but dense pumice to material that resembles dense dacite. The interiors of breadcrusted pumices are microvesicular but have significant numbers of centimeter-sized vesicles. There is always a



Figure 2.4a Breadcrusted moderately welded breccia, B347. **b** Breadcrusted pumiceous dacite, N332. **c** Cross-section of a breadcrusted pumiceous dacite, note the gradational change in color reflecting an increase in bubble size and number towards the interior, N120.

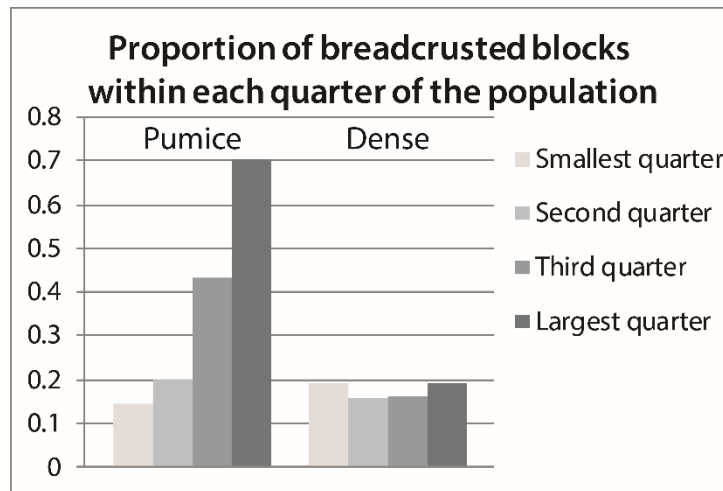


Figure 2.5 Plot of the proportion of breadcrusted pumice (left) and dense dacite (right). Each lithology's block population was ordered by increasing average dimension and divided into quarters. The proportion of breadcrusted blocks was then calculated for each quarter. Note how the proportions of breadcrusted pumices increase with increasing block size whereas the dense dacites show no correlation between block size and the presence of breadcrusting.

gradual increase in number and size of the largest bubbles towards the block interior. Rind thickness is directly correlated with the density contrast between crust and interior.

Breccias are of two types. The dominant breccia type (31% by volume) consists of dacitic pyroclasts and little or no wall rock in an ash matrix and exhibits a range of welding in the form of degree of pumice flattening and welding of the ash (Figure 2.2). Lightly welded breccias have an average density of 1600 kg/m^3 and are characterized by equant dacite pumices in a friable ashy matrix. The moderately welded breccias are defined by a welded matrix showing clear pyroclast outlines with moderate flattening ratios averaging 3:1 and an average density of 1950 kg/m^3 . The lithic-free dense breccias have an average density of 2200 kg/m^3 , a crystal-rich, vitroclastic matrix, and pumice flattening of 5:1 to 7:1. Breadcrusting is present in a small proportion of these blocks. A second, subordinate category of breccias includes densely welded blocks containing pumice and pre-1912 Jurassic siltstone wall-rock lithics, which are commonly oxidized brick-red, set in a dark gray or black obsidian-like matrix (Figure 2.2). They also occur in the Episodes II and III Plinian fall deposits and were inferred by Hildreth (1987) to be vitrophyric breccias formed in the Episode I vent. These breccias will be referred to as ‘dense vitrophyre’ for the rest of this paper.

2.3.2 Block distribution by lithology and size

Adding our observations to those of Adams et al. (2006a) makes Episode IV globally the most comprehensively mapped Vulcanian block field (Nairn and Self 1978; Yamagishi and Feebrey 1994; Waite et al. 1995; Druitt et al. 2002). We mapped the block distribution in terms of lithology and size (i.e., average dimension of the whole or reconstructed block), revealing a roughly N-S elongated elliptical deposit in which block size diminishes radially with distance

from vent. The spatial distribution of blocks suggests preferential clustering along a few radial axes (Figure A.1 in Appendix A). In particular:

- *Dense dacites* are present radially within 600 m of vent (which lies beneath the Episode V dome) and are particularly abundant to the northwest to west and southwest to south. At distances >600 m the dense dacites are weakly and unevenly concentrated to the north and south and are sparse to the east and west.
- *Pumiceous dacites* have a relatively even distribution to the north, east, and west and are moderately sparse south of the dome.
- *Episode I dense vitrophyres* are mostly strongly concentrated in the northeast, with weaker dispersal north, west, and south of the dome.
- *Densely welded breccias* are present in all radial directions within 600 m of vent, but are conspicuously richer in the south and absent from the north at distances >600 m.
- *Moderately welded breccias* are distributed in all sectors within 800 m of vent, and are particularly densely concentrated in the northwest to west and southwest to south quadrants. They are also noticeably absent to the north and present at greater distances to the south.
- *Lightly welded breccias* are concentrated in the west and northeast sectors with a weaker dispersal to the south and are nearly absent north of the dome.
- *Pumiceous banded clasts* have concentrations to the west, east, and southeast and are fairly sparse in the other sectors.

- *Mixed and dense banded clasts* have similar dispersals with stronger concentrations in the northwest to west and southwest to south sectors. They have only a minor presence to the northeast and are conspicuously absent directly north of the dome.

In summary, only the dense dacites and the densely and moderately welded breccias have a consistent presence in all sectors (to within 600 m) around the vent. The pumiceous dacites have a distinct concentration in the northwest to northeast sectors which is not present for the other lithologies. The remaining lithologies have sectoral confined distributions that usually (vitrophyre excluded) include more southerly (rather than northerly) distribution.

Figures 2.6 and 2.7 are isopleth maps for groups of lithologies with closely overlapping density distributions. These maps show proximal polylobate contours for the largest clasts and a smoothing of the smaller blocks' isopleths. The number, geometry, size distribution, and orientation of the lobes are correlated to block density. Higher densities produced lobes extending the farthest and to a smaller size fraction. The denser lithologies have six narrow lobes in the western and southern sectors whereas the lower-density components have fewer (five pumice, four banded, and three breccia) and broader lobes that point towards the NW, SW, SE, NE, and N. The northern sector is characterized by a conspicuous absence of larger blocks and only one well-defined pumice lobe.

The overlap in 125- and 100-cm contours in Figure 2.7 shows how distributions of different block types coincide in the northern sector. This contrasts with individually directed lobes towards the south of the dome. A broadening of fingers with decreasing block size results in a loss of distinct directionality especially in the southern sector, as is evident in the overlapping of fingers in the 75-cm contours.

Pumice (uniform and banded)



Dense dacite



Densely welded breccia and vitrophyre



Lightly and moderately welded breccia



Mixed and dense banded



Figure 2.6 Isopleth maps for the component groups.

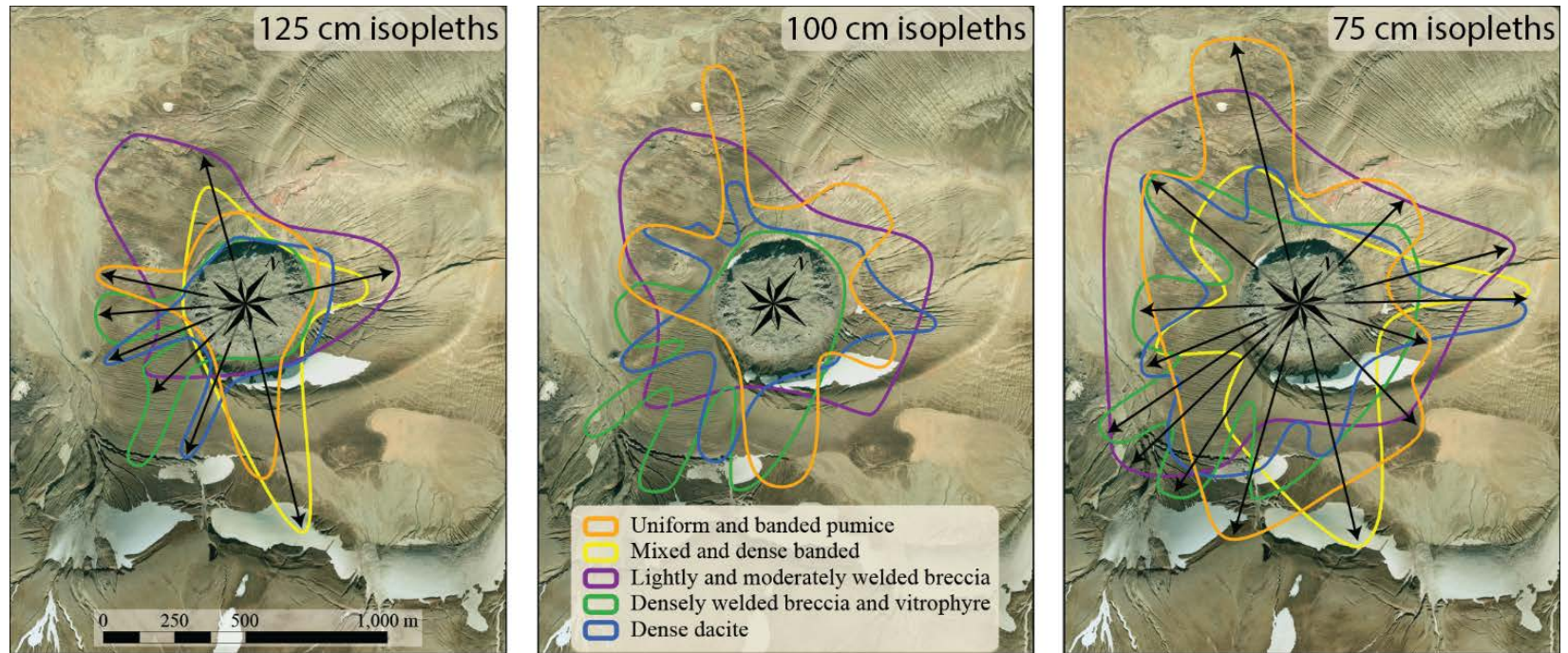


Figure 2.7 Maps of overlapping isopleths of a single size from different lithological groups. Arrows indicate directed lobes within the deposits.

Regardless of lithology or density, there is a general trend for block size to decrease with distance from the vent (Figure 2.8; Table 2.1). However, the spread in block sizes reaching a given distance suggests that this correlation is associated with a large uncertainty. For example, block sizes present at a distance of 500 m in Figure 2.8 range between 25 and 120 cm.

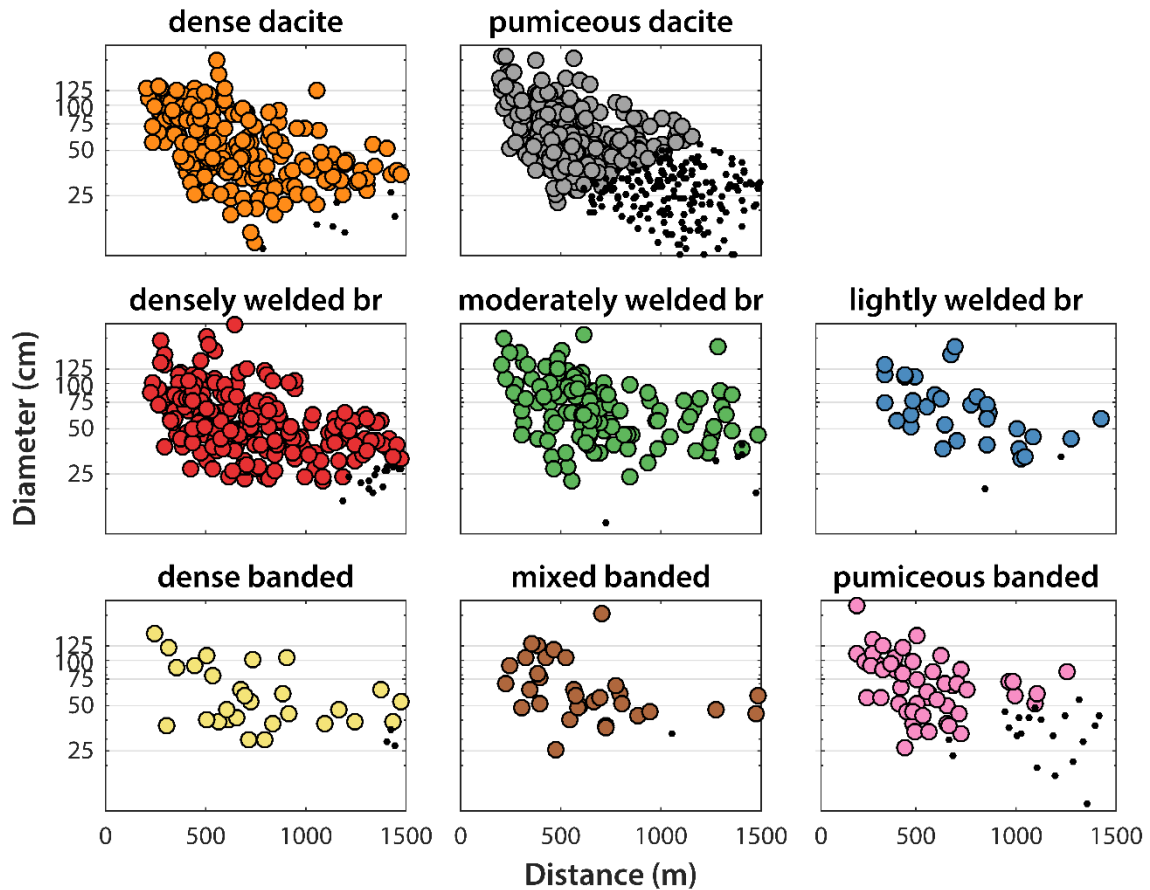


Figure 2.8 Average diameter versus distance for each of the lithologies (br = breccia). Black dots represent blocks for which launch velocity exceeded the 600 m/s upper limit set within the model.

Table 2.1 Minimum, maximum, and the range of distances that the largest and smallest blocks traveled. Note how smaller blocks travelled further and cover a much wider range of distances, regardless of density.

Density group (kg/m ³)	Block size (cm)	Minimum distance (m)	Maximum distance (m)	Range (m)
<1000	≥100	190	818	628
	<50	329	2423	2094
1000–<2000	≥100	206	902 ^a	696
	<50	301	1791	1490
≥2000	≥100	204	942 ^b	738
	<50	295	2264	1969

^aOutlier maximum of 1052 m

^bOutlier maximum of 1286 m

2.3.3 Block trajectory modeling results

2.3.3.1 General features

Initial conditions were estimated with the trajectory-tracking model of Fagents and Wilson (1993) for 1,269 blocks by incrementally cycling through ranges of ejection velocities (between 10 and 600 m/s) and launch angles (between 45 and 89° from horizontal) to find the combinations that reproduced observed block ejection distances within a buffer of ±10 m. Solutions were found for 972 blocks, while the remaining 297 (i.e., 23%) required implausibly high ejection velocities (greater than the 600 m/s limit set within the model). The majority of these 297 blocks were small (<50 cm diameter), pumiceous (i.e., low-density), and landed >500 m from vent (Figure 2.8). Few higher density blocks gave unreasonable results and nearly all that did landed >1 km from vent; the three exceptions were particularly small with average dimensions ≤20 cm.

To analyze the model results, the blocks were split into low-density ($<1000 \text{ kg/m}^3$), intermediate-density ($1000\text{--}<2000 \text{ kg/m}^3$), and high-density ($\geq 2000 \text{ kg/m}^3$) groups and block size classes of small ($<50 \text{ cm}$), medium ($50\text{--}<100 \text{ cm}$), and large ($\geq 100 \text{ cm}$) average dimension. Figure 2.9 displays the complete modeling results for these nine subclasses. Each curve represents model results for one block, i.e., all combinations of ejection velocity and angle that produce the measured travel distance for that block.

Clast diameter has a much more significant influence on the model results than clast density. For all three density classes the largest blocks group tightly in Figure 2.9 and the inferred velocity is relatively insensitive to ejection angle up to $70^\circ\text{--}75^\circ$ from horizontal. Beyond $70\text{--}75^\circ$, model velocities increase steeply with ejection angle. For intermediate sized blocks, velocities are more scattered and higher velocities are required at relatively shallow angles ($55\text{--}65^\circ$). These trends are even more apparent in the wide scatter of results for the smallest blocks.

2.3.3.2 Median velocity

We use the modeled velocities for an ejection angle of 45° to compare both median velocities and velocity ranges among the nine subclasses (Table 2.2). Median velocity increases (from $\sim 70 \text{ m/s}$ to $>150 \text{ m/s}$) as block size decreases. There is no simple relationship between median velocity and clast density.

2.3.3.3 Spread in velocity

The range in modeled velocity, represented by the separation of the 5th and 95th percentiles (range 2 in Table 2.2), narrows with increasing block size, from $>350 \text{ m/s}$ in the $<50\text{-cm}$ -size

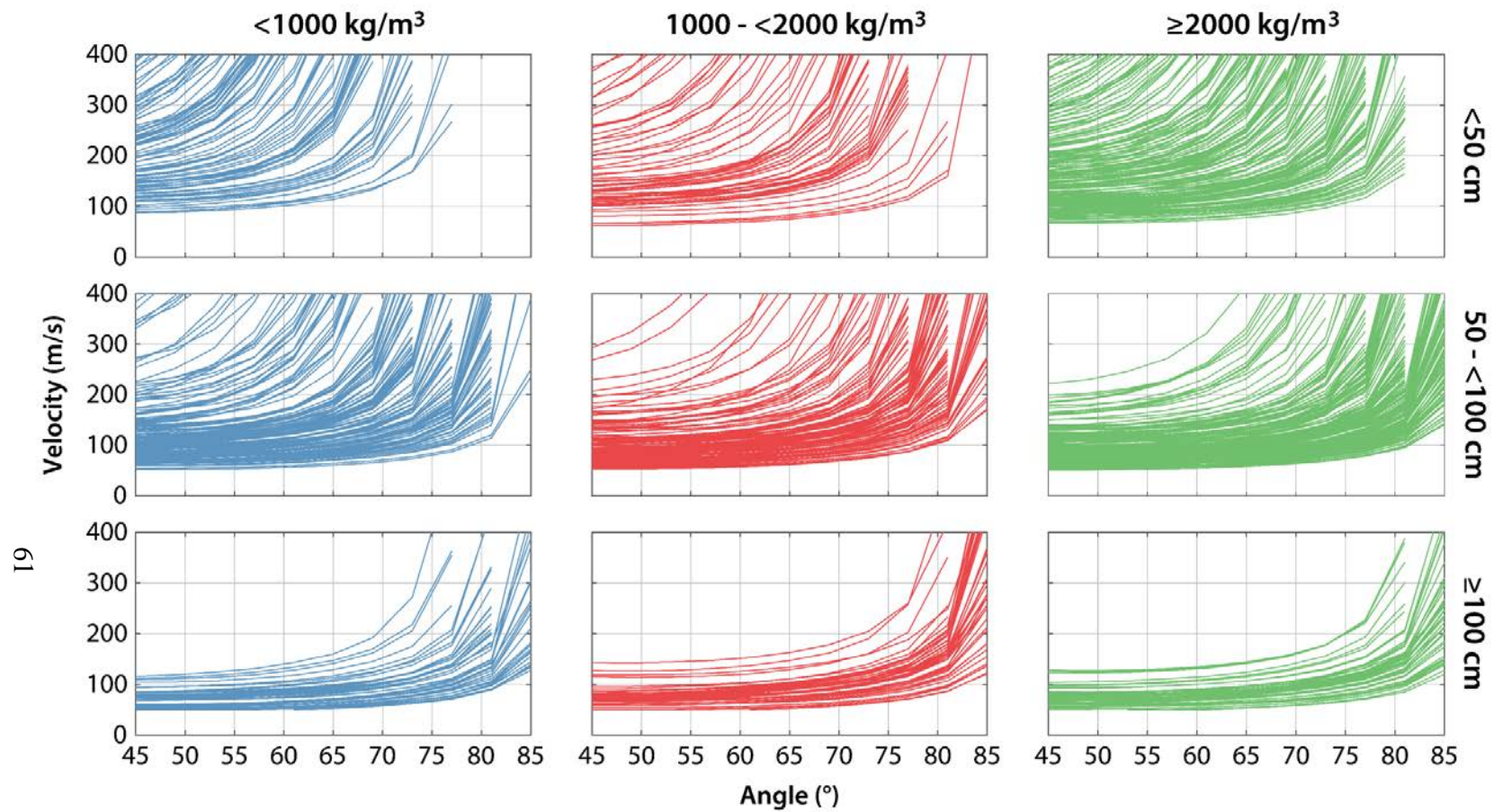


Figure 2.9 Modeled block ejection velocity versus launch angle for all size and density groups. Each curve represents the combinations of initial velocity and launch angle that project a given block to the distances measured in the field.

Table 2.2 Summary of ejection velocities (in m/s and calculated for an angle of 45°) for each of the 9 size and density categories. 5th, 25th, 50th, 75th, and 95th percentiles correspond to p5, p25, p50, p75, and p95, respectively.

Size range (cm)		<1000 kg/m ³	1000–<2000 kg/m ³	≥2000 kg/m ³
<50	p5	100	80	83
	p25	147	114	112
	p50	221	150	159
	p75	306	270	256
	p95	485	500	440
	range 1	159	156	144
	range 2	385	420	357
50–<100	p5	63	59	57
	p25	83	79	70
	p50	108	94	84
	p75	153	129	108
	p95	349	208	164
	range 1	70	50	38
	range 2	286	149	107
≥100	p5	50	53	55
	p25	56	67	63
	p50	70	74	71
	p75	81	82	83
	p95	111	120	124
	range 1	25	15	20
	range 2	61	67	69

range 1 = p75-p25; range 2 = p95-p5

class to 60–70 m/s in the ≥100-cm size. No consistent relationship exists between density and the spread in velocity.

2.3.3.4 Dependence of ejection velocity on launch angle

Across all size classes, velocity is initially consistent across a range of angles and subsequently increases sharply for the steepest angles. This sharp increase occurs at lower angles for smaller blocks (Figure 2.9), reducing the range of angles across which velocity is close to constant. For

the smallest clasts, high ejection angles are not feasible at even extreme ejection velocities. Also note how the velocity range in each class widens as angle increases.

2.3.3.5 Velocity versus distance

Given that the ejection velocity is relatively insensitive to a range of plausible ejection angles, the relationship between ejection velocity and landing distance is assessed in Figure 2.10 for an ejection angle of 45°. The dataset for each size/density class is fit by a linear function and shown with the 95% confidence intervals. For comparison, we have also included a gray shaded region in all plots that represents the 90% confidence interval of a linear fit performed on all blocks with diameters > 1 m (i.e., bottom row of Figure 2.10). First, these plots emphasize that the smallest blocks covered a wider spread of landing distances and required an unreasonably high and broad range in velocities across all densities. Note that a significant proportion of the low-density, <50-cm population is not represented in Figure 2.10 because the model could not replicate their landing distances with any realistic ejection velocities (Figure 2.8). Second, these plots show that velocity is predictably higher for the large blocks that traveled further. Finally, lower density blocks require higher exit velocities to achieve any given distance in the small and intermediate size classes.

2.4 Interpretations

2.4.1 Block componentry interpretations

The distinct textural types amongst the clasts within Episode IV are chemically identical and probably reflect contrasting degrees of vesiculation at the time of fragmentation. Breadcrusting indicates that the exteriors of some blocks had solidified prior to interior vesiculation reaching

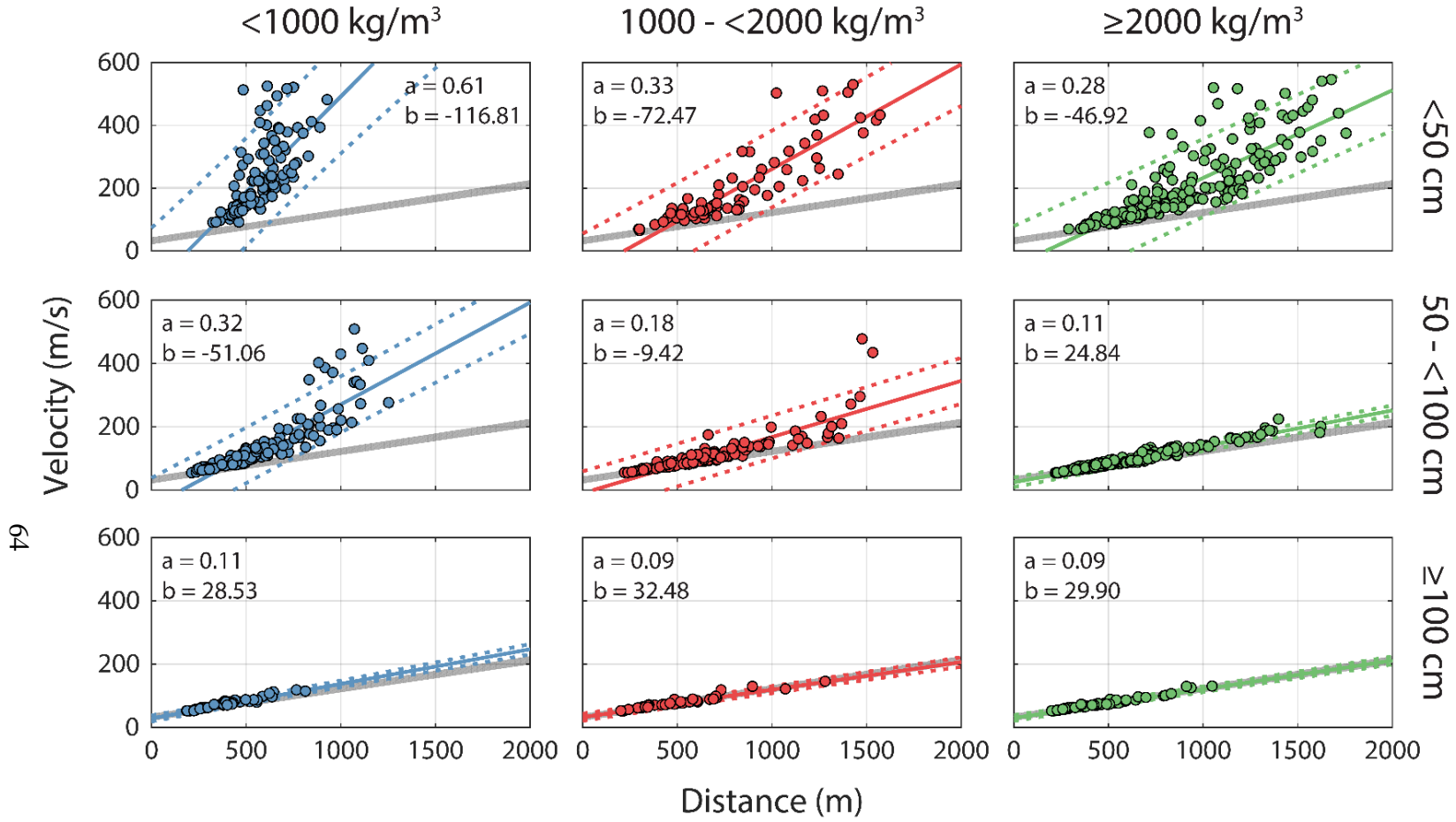


Figure 2.10 Launch velocity versus ejection distance for an ejection angle of 45 degrees, overlain by the best linear fit (solid line, a = slope, b = intercept) and 95% confidence interval (dotted lines). The gray shaded region represents the 90% confidence interval of a linear fit performed on all blocks with diameters $>1 \text{ m}$. Note how more blocks fall within this region with increasing size and density.

equilibrium. Fine-scale flow banding of the range of physically distinct dacite types (e.g., dense/dense, pumiceous/pumiceous, pumiceous/dense; Figure 2.2) suggests complex and intimate mingling, on length scales of millimeters to centimeters, of magma that had undergone different amounts of degassing and probably outgassing within the conduit. It means that mingling occurred at a very late stage and that insufficient time elapsed between mingling and eruption for diffusion of volatiles, thus precluding complete mixing of the disparate melts.

2.4.2 Block distribution interpretations

The pattern of isopleths shown in Figures 2.6 and 2.7 is not easily reconciled with a simple deposit from a single explosion. Instead, the directional polylobate contours, especially for the larger blocks that were less susceptible to the moving volcanic and atmospheric gases (see next section), are most easily interpreted as the deposits of multiple sectorial-confined explosions especially directed towards the south of the vent. A greater number of explosions directed towards the south is supported by the presence of a more continuous pumice lapilli bed in the southern (inferred upwind) region (Figure A.2 in Appendix A).

The pumiceous dacites represent the only component group that is evenly distributed in the northwest to northeast region but this population is composed predominantly of blocks <75 cm in diameter. We propose that these smaller and low-density clasts were preferentially influenced by wind advection during the explosions. It is impossible to know the near-surface wind field during the time of Episode IV (especially since the timing of its commencement and duration are unknown), but currently the wind blows from the south/southwest during 50% of the summer months.

2.4.3 Constraints on modeled ejection velocity and angle

The modeling results and inverse correlation between block size and landing distance suggest that not all of the Episode IV blocks followed ballistic trajectories that were decoupled from the volcanic and atmospheric gases (Self et al. 1980; Sparks et al. 1997). Instead, they were subject to varying aerodynamic drag forces throughout three stages of flight. In the first stage, the blocks experience partial coupling with expanding magmatic volatiles within the shallow conduit. Subsequently, they enter the envelope of air overlying the vent that is displaced by the explosions and thus also moving outwards. Ballistic blocks experience reduced drag during these two stages due to lower relative velocities between the blocks and the ambient gas flow field (Fagents and Wilson 1993; Mastin 2001; de' Michieli Vitturi et al. 2010). In the final stage, the blocks are then transported through the ambient atmosphere which can be stationary or subject to a wind field. Additionally, the blocks may be spinning which can influence their trajectory (see Appendix A.2). The drag forces during this stage would thus depend on that wind field and angular velocity (Waite et al. 1995; Alatorre-Ibargüengoitia and Delgado-Granados 2006, Taddeucci et al. 2017). We reiterate that these variations were not included in our model calculations, but their influences can still be seen in the results.

There is a complex relationship between the aerodynamic properties (i.e., size, shape, and density) of a clast and how much drag forces vary according to the medium that it travels through. We assumed a spherical shape in our model calculations and discuss below the role of block size and density. Crucial shifts in the model results for the intermediate size class indicate a change in the magnitude of the surrounding medium's influence on block trajectory. Relative to the results for the smallest blocks, the median velocity decreases, the spread in velocity

narrows, and a linear relationship between velocity and distance develops as the density increases (Figures 2.9 and 2.10). This suggests that the smaller and low-density clasts with high exit velocities are more readily influenced by the ambient flow field, suggesting that a more complex treatment of their aerodynamics is necessary in order to properly model their trajectories. This also applies to the 297 small and/or low-density blocks with long landing distances that the model could not replicate with a range of plausible ejection velocities. We interpret the gray shaded region in Figure 2.10 to represent the most accurate velocity versus distance relationship for our blocks traveling through a still atmosphere. The model results for blocks that lie outside this region cannot be trusted and do not accurately reflect the true exit conditions throughout Episode IV. Only minor variation in the largest clasts' modeled median and spread in velocities (Figure 2.9) suggests they are minimally influenced by ambient motion. Their ratio of surface area to volume is lower, thus drag per unit mass is much lower, and so the largest blocks are capable of maintaining their inertia.

Reynolds numbers (Re) were calculated for a subset of blocks along a transect from the rhyolite dome to the furthest blocks in the southern sector of the Episode IV deposit. The parameters used in calculating Re include: average block diameter, ejection velocity calculated in the model for a 45° angle, and density and viscosity of the atmosphere (determined from the 1976 standard atmosphere at 850 m elevation or approximately the current elevation of the rhyolite dome). Only the highest and lowest density clasts (dense and pumiceous dacite) were analyzed due to their textural homogeneity and to highlight any differences due to density contrasts. All Re are high ($>2.8 \times 10^8$) indicating that the boundary layer around the blocks is fully turbulent. Figure 2.11 presents a plot of the Re versus normalized landing distance. The

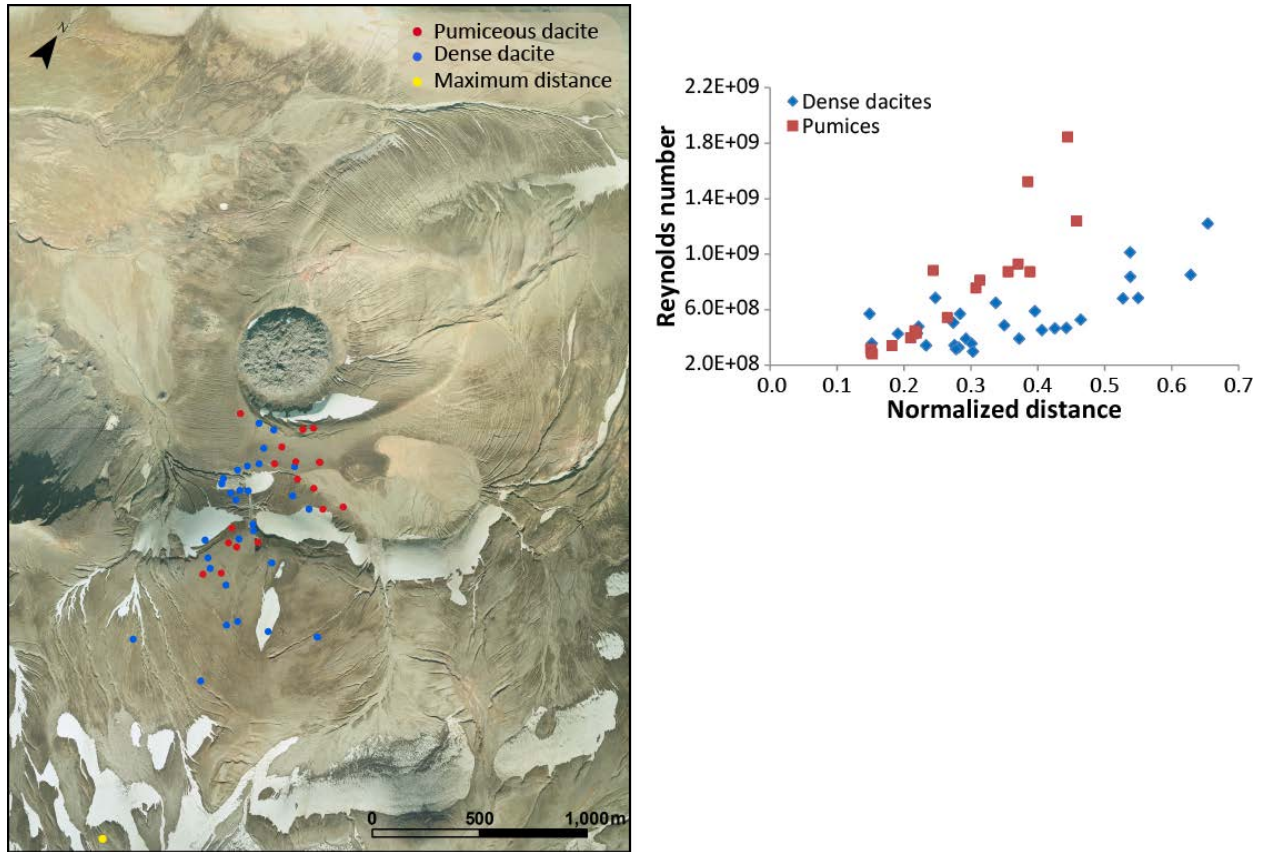


Figure 2.11 (Left) Map of the pumiceous (*red dots*) and dense dacites (*blue dots*) for which Reynolds numbers were calculated. The *yellow dot* in the southern corner of the map represents the block used for the maximum distance value employed in calculating a normalized distance. (Right) Plot of Reynolds number versus normalized distances for the blocks in the map.

Re for the pumiceous and dense dacites overlap one another at normalized distances of <0.4 . At and above this value, the pumices shift to Re higher than the dense dacites. Considering larger blocks landed closer to the vent than smaller blocks, the larger pumices had similar Re to the dense dacites, but the smaller and/or further travelled pumices required greater inertia to reach their landing distances. This shift in the data is another indicator that density has a decreasing influence on ballistic transport as size increases.

We used the *Eject!* model (Mastin 2001) to assess the influence of the presence of a region of reduced drag by comparing the horizontal distance reached by particles i) in a stationary atmosphere and ii) in using a region of reduced drag with a radius above the vent of 200 m. Ejection velocity and angle were set at 100 m/s and 45°, respectively, and various sizes, shapes, and densities were considered. Although the definition of the region of reduced drag as considered by Mastin (2001) is somewhat arbitrary, results suggest that such a region with a 200 m radius has a greater effect on block travel distances for irregular shapes (cubes), smaller sizes (<1 m), and lower densities (<1000 kg/m³; Figure A.3 in Appendix A). While our *Eject!* model runs illustrate how drag forces are dependent on the particle's shape (Alatorre-Ibargüengoitia and Delgado-Granados 2006; Bagheri and Bonadonna 2016; Bertin 2017), cubes are likely to overestimate the drag. Our results emphasize that velocities estimated using a still-air calculation are most accurate for the largest size class within the Episode IV blocks.

Within individual density/diameter subsets (Figure 2.9), the range between the highest and the lowest ejection velocities for a given angle is related to a combination of 1) size and density within each group, 2) distance blocks traveled, and 3) relative landing elevation (the difference between projection and landing elevations). A direct relationship between velocity and distance is confirmed in Figure 2.10. The blocks in the smallest size class spanned a much larger range of distances than the larger classes (Figure 2.6). Additionally, elevation varied irregularly but radially around vent, and so blocks commonly traveled equivalent distances but landed at different elevations. The narrowing of the range of velocities with increasing block size can be related to 1) narrowing of the range of landing distances and 2) block size converging on a critical mass at which drag has a minimal influence.

The broad range of launch angles across which ejection velocity is relatively consistent for the largest and densest blocks suggests that angle was not a significant influence on their trajectories. Combined with the widening of the range of velocities at higher angles, these model results may indicate that the high velocity/high angle combinations are likely unrealistic conditions for most of the largest blocks.

2.5 Discussion

2.5.1 Eruptive conditions at Novarupta and comparisons with historical Vulcanian eruptions

We estimate a total volume of $2 \times 10^5 \text{ m}^3$ DRE for the Episode IV deposit by calculating the volume of blocks within each isopleth and then adding a rough volume estimate for the lapilli component in the far field, which was approximated by isopachs of 10 and 1 cm. This corresponds to 73% ballistics and 27% lapilli fall. An ash-sized component was not included in this calculation because there is no evidence that the plume(s) contained a significant fines population. This volume equates to a hemispherical surficial dome diameter of 90 m or, alternatively, assuming a conduit radius of 10 m, a plug length of 600 m. More plausibly, based on componentry, the explosions tapped a combination of a smaller dome and a smaller part of the underlying conduit, thus these numbers are maxima. We can be sure that explosions reached into the conduit due to the presence of the Episode I dense vitrophyre blocks, but these estimates of dimensions suggest that only the shallowest regions were tapped. In contrast, pressure estimates for Vulcanian activity at Soufrière Hills have been used to suggest explosions

evacuated to conduit depths of ≥ 2 km (Druitt et al. 2002; Melnik and Sparks 2002; Clarke et al. 2007; Burgisser et al. 2011).

Adams et al. (2006a) speculated that Episode IV involved cyclic activity of lava production and disruption, but could not conclude definitively that there was more than one explosion according to their block maps. We suggest that each of the lobes defined from isopleth information represents the products of at least one discrete explosion. It is possible that any lobe equates to more than one explosion; however, we estimate a minimum of 8–14 explosions from the number of lobes within the 125 and 75-cm isopleths, respectively (Figure 2.8). This would equate to an average volume of $1.4\text{--}2.5 \times 10^4 \text{ m}^3$ DRE per explosion, which is roughly an order of magnitude smaller than other well documented Vulcanian events. For example, each of the 88 Vulcanian explosions at Soufrière Hills volcano, Montserrat, in 1997 discharged an average of $3 \times 10^5 \text{ m}^3$ of magma (Druitt et al. 2002). Nine ‘cannon-like explosions’ at Ngauruhoe, New Zealand, on 19 February, 1975 produced a total of $2.0 \times 10^6 \text{ m}^3$ DRE of ejecta (Nairn and Self 1978), which averages to $2.2 \times 10^5 \text{ m}^3$ per explosion. This also suggests that individual explosions during Episode IV disrupted the conduit fill to only shallow depths.

Transport and sedimentation processes during Episode IV contrasted with those from other transient explosions related to dome building eruptions. In particular, the Episode IV deposit is purely a block and lapilli apron, i.e., there is no evidence of pyroclastic density currents, and there is no preserved ash fall. Pyroclastic transport throughout Episode IV was predominantly governed by ballistic trajectory of the block-sized pyroclasts.

Table 2.3 Examples of componentry described in the Vulcanian literature.

Block lithology	Novarupta, 1912	Ngauruhoe, 1975	Tokachi-dake, 1988–1989	Soufrière Hills, 1996–1997						Guagua Pichincha, 1999	
	This study, Adams et al. 2006	Nairn and Self 1978 ^a	Yamagishi and Feebrey 1994 ^a	Robertson et al. 1998 ^b	Druitt et al. 2002 ^c	Kennedy et al. 2005 ^d	Clarke et al. 2007 ^d	Burgisser et al. 2010 ^d	Giachetti et al. 2010 ^d	Wright et al. 2007 ^a	
72 Non breadcrusted	Homogeneous pumice	X	X	X		X	X	X	X	X	
	Banded	X					X		X	X	X
	Dense juvenile	X	X	X		X		X	X	X	X
	Breccia	X		X	X		X				
	Dense lithic	X	X		X	X					
Breadcrusted	X	X	X					X	X	X	

^a Componentry is for ballistic ejecta which has been distinguished from concurrent or subsequent pyroclast fall and flow deposits

^b Dense and brecciated lithic clasts are inferred from vent-clearing Vulcanian explosions; vesicular to dense juvenile material erupted in subsequent sustained explosive eruptions

^c Pyroclastic fall ejecta, including both ballistic and material from plume and umbrella clouds

^d These textures are recognized only in pyroclastic flow deposits

No previous study has documented the detail of textural differences within and between component groups nor calculated their relative proportions for a Vulcanian ballistic deposit. As such, the data pertaining to block lithology and proportions within the Episode IV deposit are unique when compared to other well-documented transient explosions (Table 2.3). For example, a brecciated ballistic component is rarely mentioned in any of the Vulcanian literature (with the exceptions of Yamagishi and Feebrey 1994 and Robertson et al. 1998) and its abundance and role has not been quantified. The proportion of brecciated blocks (by volume) is strikingly high at Novarupta and we attribute it to a combination of Episode I vitrophyric material derived from the conduit margin and syn-eruptive lithic-free, lightly to densely welded breccias (Adams et al. 2006a).

The degree and variety of banding present in the Novarupta blocks is either not present or not documented in other deposits. Banded ejecta is recorded in recent studies (Table 2.3), but described only briefly as “dense parts with tabular shapes that form cm-thick streaks in a more vesicular clast” (Burgisser et al. 2010), “alternating bands of variable vesicularity” (Giachetti et al. 2010), or is not defined at all (Kennedy et al. 2005; Wright et al. 2007). However, flow banding during eruption of silicic magmas is recognized as an important indicator both of viscous and brittle deformation due to shear and of mingling of texturally differing magmas (Seaman et al. 1995; Tuffen et al. 2003; Gonnermann and Manga 2005; Tuffen and Dingwell 2005). We recognize a range of mingled textures within juvenile pyroclasts of varying densities and calculated that they represent roughly 20% by volume of the blocks at Novarupta. The existence of banded blocks of contrasting vesicularity means either (1) that these textures are the result of a single zone of magma that has undergone spatially variable shear-stresses which have

resulted in diverse vesiculation states and textures (Polacci et al. 2001; Gonnermann and Manga 2005) or (2) that portions of the melt with different textures and presumably ascent histories were mingled at a very late stage prior to eruption. Contrasting degrees of post-fragmentation expansion between light (vesicular) and dark (denser) bands suggests that the relevant melts had different levels of residual volatiles, which favors (2) but not (1). Previous studies have set precedents for the mingling and mixing of chemically distinct (e.g., Seaman et al. 1995; Perugini et al. 2004) and texturally diverse magmas (Seaman et al. 2009; Wright et al. 2011). We interpret the banding in Episode IV to indicate the presence of co-existing magma domains that were at varying stages of degassing and outgassing and significant mingling over time periods of hours to days along the margins of these disparate magmas within the shallow conduit. While Vulcanian eruptions commonly show heterogeneities in textures, the Episode IV banded clasts appear to have experienced a very high degree of mingling without complete mixing/hybridization. We suggest this is the result of differing residence times within the upper regions of the conduit and dynamic conditions on short time scales prior to fragmentation that enabled the formation and preservation of local complex millimeter- to centimeter-scale banding between magmas of differing textures.

While breadcrusted clasts are particularly characteristic of Vulcanian eruptions, their abundance has generally not been quantified. They are typically described as a minor component within an otherwise pumice-rich deposit (e.g., Giachetti et al. 2010). In comparison, the proportion of breadcrusted blocks in the Novarupta deposit is high at 25% by number or 37% by volume. Predictably, a large proportion of the uniform and banded pumices are breadcrusted, whereas most of the breccias and dense dacites are not (Figure 2.3). The banded dacite

component has the highest proportion of breadcrusted blocks at 83% by volume. In this case, cracking of the dense exterior rinds on both dense and vesicular bands was likely due to the renewed vesiculation of the light colored vesicular bands, which are conspicuously more expanded than neighboring dark, denser bands (Figure 2.2g, h).

The modeling results suggest that consistent exit conditions, and presumably conduit parameters, prevailed for numerous explosions throughout Episode IV. The trajectories of the largest blocks were most reliably estimated with the model because they were minimally influenced by atmospheric motion that would have been difficult to constrain. Hence, we focus on the results for the >100-cm-size class. Our best estimated velocities range from 50 to 124 m/s with a median of ~70 m/s, which is relatively low when compared to the spectrum of velocities estimated for ballistic deposits (Table 2.4). This, combined with the comparatively small volume produced per explosion, could reflect relatively less energetic conditions at Novarupta — perhaps due to greater complexity within the shallow conduit. Our model velocity range is applicable across all radial sectors (i.e., does not vary with lobe direction). This implies that the multiple explosions within Episode IV consistently ejected these blocks with a narrow range of velocities, and that the conditions that prompted an explosion did not vary substantially across the multiple events within this phase.

2.5.2 Implications and comparisons with respect to other Vulcanian eruptions

Conduit heterogeneity prior to Vulcanian explosions is generally modeled in the form of zoned magma that exhibits progressively decreasing states of degassing and outgassing and thus displays an orderly change in textures and densities with decreasing depth (e.g., Druitt et al. 2002; Melnik and Sparks 2002; Clarke et al. 2007; Wright et al. 2007; Burgisser et al. 2010;

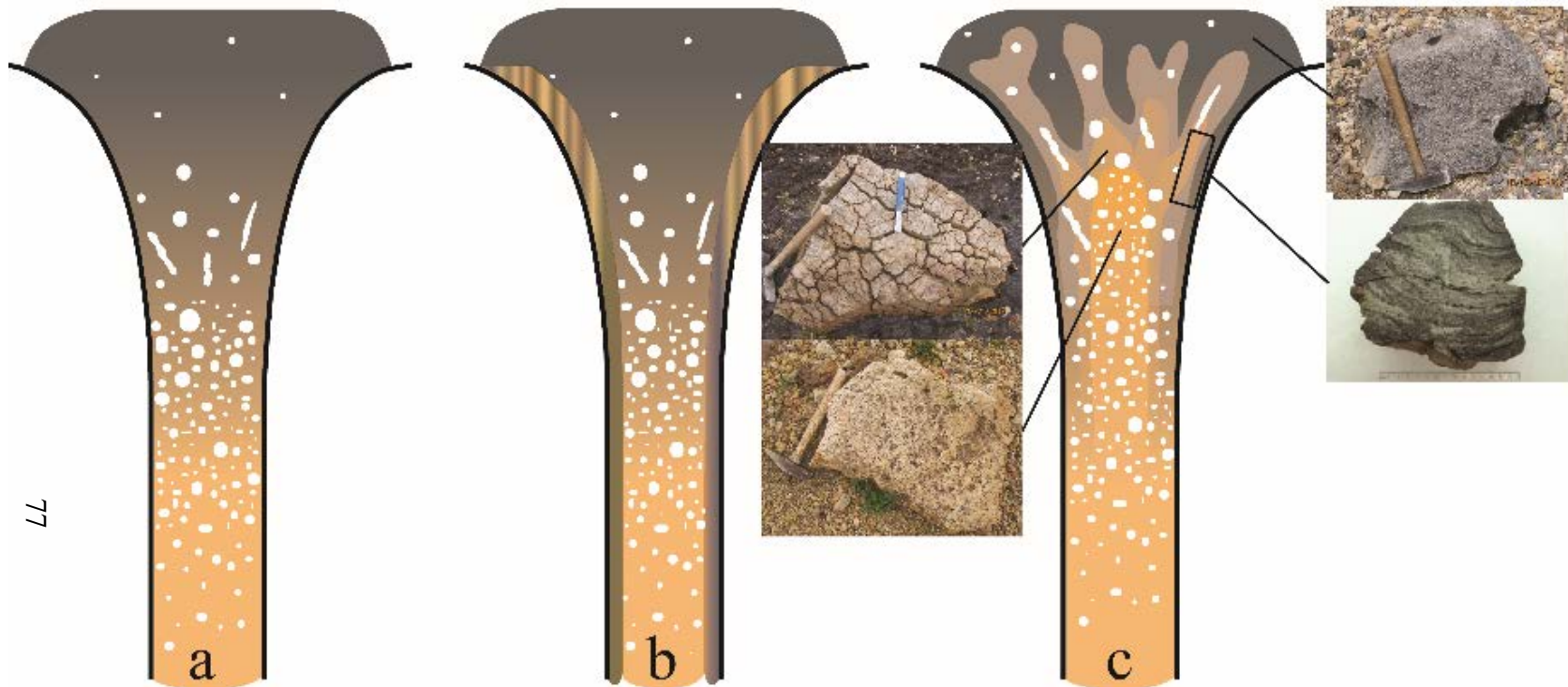
Table 2.4 Comparison of velocities calculated for ballistic particles.

Eruption(s) year(s)	Location	Style	Maximum landing distance ^a (m)	Velocity (m/s)	Reference
1968	Arenal volcano, Costa Rica	Vulcanian	5,000	300–400	Fagents and Wilson 1993
1975	Ngauruhoe, New Zealand	Vulcanian	2,800	220–260	Fagents and Wilson 1993
1977	Ukinrek Maars, Alaska	Phreatomagmatic	700 m	80–85	Fagents and Wilson 1993
1992	Crater peak vent, Mount Spurr, Alaska	Phreatomagmatic	3,500	155–840	Waitt et al. 1995
1997	Soufrière Hills volcano, Montserrat	Vulcanian	1,700	40–140	Clarke et al. 2002
1999	Guagua Pichincha, Ecuador	Vulcanian	800 m	77–100	Wright et al. 2007
1998, 2003, 2008	Popocatepétl, Mexico	Vulcanian	3,700	110–210	Alatorre- Ibarguengoitia et al. 2012
2012	Upper Te Maari, New Zealand	Hydrothermal	1,350	120–215	Breard et al. 2014
1888–1890	La Fossa volcano, Italy	Vulcanian	1,000	100–150	Biass et al. 2016
1912	Novarupta, Alaska	Vulcanian	1,300 ^b	50–124	This study

^aMaximum landing distance used in the modelling.

^b1,300 m refers to the maximum distance of the >1m blocks (from which the velocities were extracted).

Giachetti et al. 2010). Other authors have proposed an approximately vertical layering of the conduit, e.g., Kennedy et al. (2005) suggest that their banded and brecciated clasts originated from the conduit margin and the homogeneous pumice fragments came from the conduit center. Alternatively, Cassidy et al. (2015) proposed that a form of vertical layering develops when gas-rich magma rises rapidly through a slowly ascending gas-poor magma located along the conduit



77

Figure 2.12 Models for the shallow conduit architecture prior to Vulcanian explosions. **a** Zoned magma that is in progressively decreasing states of degassing and outgassing. **b** Vertically layered conduit with older melt along the conduit walls. **c** Complex conduit architecture involving domains of varying textures and vesiculation states. Block pictures represent the products of these melts; note how the banded blocks originated along the margins of contrasting melt domains.

walls. Instead of a simple layering, our data support the model proposed by Adams et al. (2006a) of a complex architecture within the shallow conduit involving both the juxtaposition of domains of contrasting texture and vesiculation state and the mingling of different textures on much shorter vertical and horizontal length scales (Figure 2.12). Three key observations indicate that textural domains occurred on a range of scales: (1) the existence of uniform blocks, each representative of a single component type, which are up to >10 m in length, implies domains of at least these dimensions, (2) entire isopleth lobes dominated by blocks of a single lithology suggest that the largest domains may be even larger than the dimensions of these largest blocks, whereas (3) the banded blocks indicate mingling occurred locally on millimeter to centimeter scales. In regards to (2), lobes consisting of a single component group may have tapped small individual regions in the conduit whereas multiple component lobes either formed by more than one explosion and/or tapped a particularly complex or larger region of the conduit. As highlighted above, the banded blocks are indicative of dynamic conditions within the conduit probably along the margins of individual domains (Figure 2.12).

2.5.3 General implications for modeling ballistic block trajectories

Two types of ballistic blocks have been proposed within the literature: 1) those that are influenced by the motions in the vent, eruption column, and ambient atmosphere and 2) those that are not (Self et al. 1980; Sparks et al. 1997). The first type of blocks require modeling transport through an expanding and decelerating gas stream and estimates of appropriate drag coefficients in order to accurately calculate their trajectories. A simpler model can be used to approximate the trajectories of blocks that are not influenced by ambient motion. However, the distinction between these two types of blocks is not clear; for example where is the threshold, in

terms of size or density, at which complex versus simple models must be applied? The answer to this question depends on the energy of the explosion, amount of volcanic gas and ash (or plume density), and the atmospheric conditions.

Our modeling results suggest that the ballistic trajectories of all blocks with diameters ≥ 1 m projected through a low-density, ash-poor plume produced by relatively low energy explosions can be modeled without significant influence by the medium that they travel through. The eruption conditions throughout Episode IV differ from many of those in Table 2.4 in terms of shorter travel distances, reduced plume density, and weaker explosivity leading to reduced exit velocities. In addition, a greater influence of the expanding gas phase and convective plume on block trajectories might be expected for more energetic eruptions.

The Episode IV data suggest that the thresholds below which ballistic particles are influenced by motions of the surrounding medium are relatively high. Blocks < 1 m and $< 2,000$ kg/m³ fall in a transitional regime where their range is influenced by the expanding magmatic volatiles, the weak convecting plume, the envelope of air overlying the vent that is displaced by the explosion, and the ambient atmosphere. This result may in part reflect the weak energetic conditions inferred at Novarupta but perhaps has a broader application and requires modeling of the background flow field in order to accurately estimate block trajectories.

2.6 Conclusions

The Episode IV block apron and its significant textural diversity, despite chemical homogeneity, suggests that magma domains of varying degrees of degassing and outgassing were juxtaposed within the shallow conduit, with intimate mingling occurring along the margins of these

domains. Some magma was newly arrived within the conduit, and possibly had not equilibrated at the depth of fragmentation as suggested by significant post-fragmentation expansion within breadcrusted pumiceous dacite and banded blocks. Our data suggest that the ejecta of Episode IV are the product of multiple explosions. These explosions tapped small portions of the conduit (horizontally and vertically), with many events directing ejecta towards the south of the vent. Block trajectory modeling revealed that ejection velocities were relatively low at 50–124 m/s, with a median of 70 m/s, and were consistent over a broad range of launch angles. The modeling results were used to establish a size and density threshold between blocks that could be modeled with a simple ballistic trajectory and those that required a more complex treatment of motions within the surrounding gaseous medium. Cumulatively, the field data and modeling results provide insight into conditions within the conduit during the critical transition from effusion to transient explosions at Novarupta that is a part of an overall downscaling from powerful steady Plinian explosions to lava effusion. To better understand the conduit fill, it will be necessary to assess the microvesicular textures of the blocks and to measure residual water contents. In particular, water contents could have implications for depths of fragmentation, degrees of degassing, and whether or not volatiles were able to diffuse between bands (during mingling) prior to fragmentation.

CHAPTER 3

Complex patterns of vesiculation, outgassing, and re-vesiculation during a Vulcanian eruption: Implications for conduit processes

In review for publication in *Bulletin of Volcanology* as:

Isgett, S.J., Houghton, B.F., Gonnermann, H.M. Complex patterns of vesiculation, outgassing, and re-vesiculation during a Vulcanian eruption: Implications for conduit processes.

Abstract

We present evidence for complex conduit textures during the Vulcanian phase of the 1912 eruption of Novarupta, Alaska. Extreme diversity in clasts in the 1912 block apron suggests complex spatial variability of magma types in the shallow conduit. Textural types at Novarupta include homogeneous microvesicular pumice and dense dacite as well as heterogeneous brecciated, breadcrusted, and texturally banded dacite. Variable vesicularities, bubble textures, porosities, and permeabilities as well as fine-scale textural mingling in some blocks indicate disruption of magma that coexisted at various stages of both degassing and outgassing in the shallow conduit. The microvesicular pumiceous dacite blocks contain vesicularities and bubble textures extremely similar to the pumice of the previous Plinian episode, and we suggest that they represent magma that was actively vesiculating at fragmentation. The textures of all remaining juvenile block types reflect magma that underwent both partial degassing and subsequent outgassing well prior to fragmentation. This suggests that different portions of the

magma stagnated at variable shallow depths and for varying durations prior to fragmentation. Even the least vesicular dense dacite blocks are permeable, despite low porosities indicating that the melt compacted yet retained a high degree of pore connectivity during outgassing. The interiors of breadcrusted blocks show highly variable amounts of a second vesiculation after outgassing that post-dates fragmentation. Banded textures formed during mingling between magmas with contrasting vesiculation histories, most noticeably between dense dacite and microvesicular pumice. This mingling requires dynamic conditions within the shallow conduit. Diversity within the Novarupta block apron can thus be explained by a complex shallow conduit fill that consisted of newly juxtaposed texturally disparate magma domains.

3.1 Introduction

3.1.1 Vulcanian eruptions

Vulcanian eruptions involve transient explosions that produce short-lived plumes and ballistic blocks and are sometimes accompanied by pyroclastic density currents and lahars. These hazards are less devastating than those of stronger, sustained sub-Plinian and Plinian eruptions, but Vulcanian explosions still pose protracted risks due to their propensity to occur in sequences over prolonged periods of time and their greater frequency of occurrence (Clarke 2013). Total eruptive volumes are typically $<0.1 \text{ km}^3$ and Vulcanian deposits are characterized by a wide range of textures (Figure 3.1) among juvenile and wall rock components, including dense to highly vesicular juvenile clasts, brecciated and massive wall rock lithics, and a range of breadcrust textures (Adams et al. 2006a; Clarke et al. 2007; Wright et al. 2007; Burgisser et al. 2010; Giachetti et al. 2010).

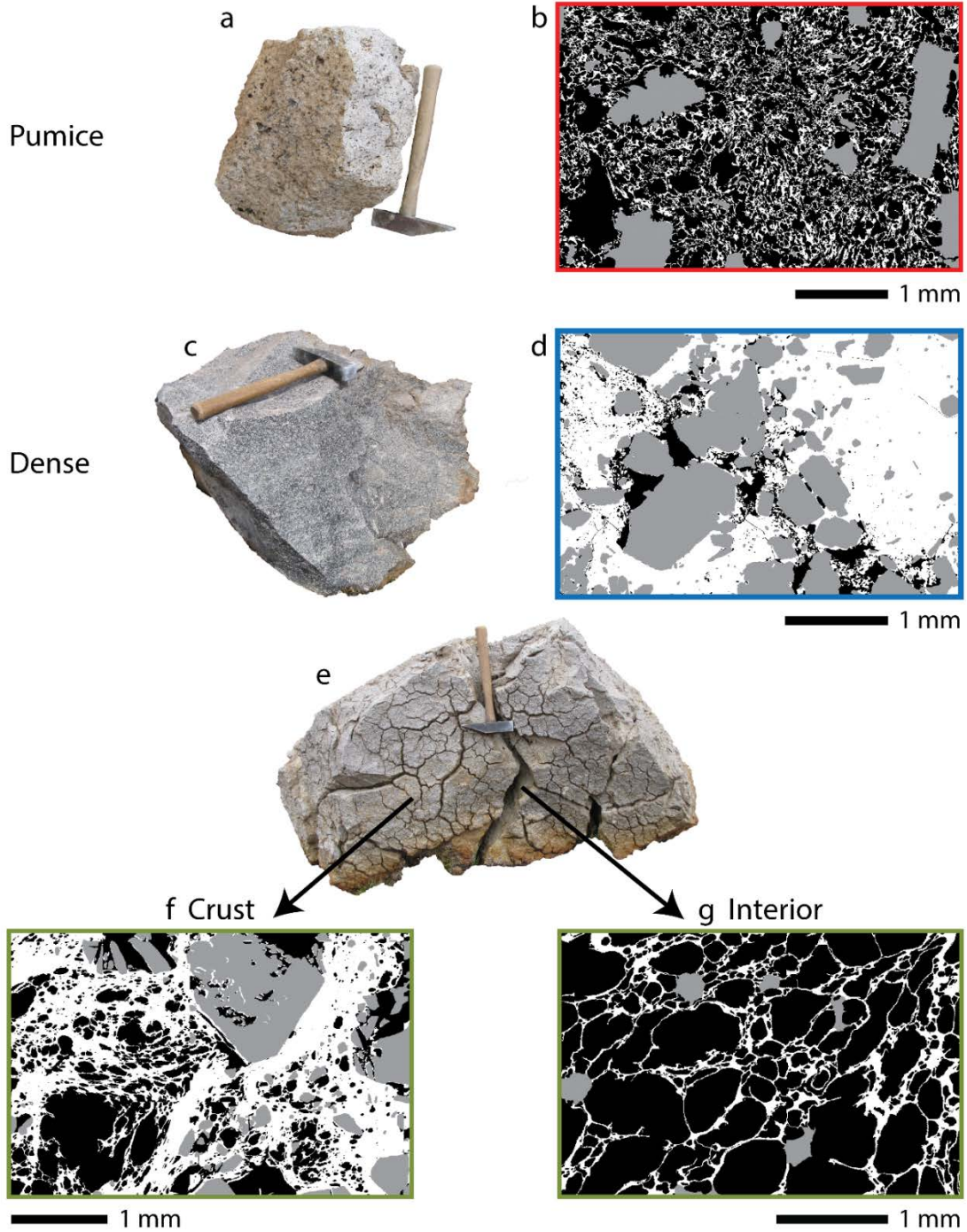


Figure 3.1 Macro- and micro-scale examples of the broad range of juvenile textures in Vulcanian pyroclasts. **a, b** Microvesicular pumice. **c, d** Dense juvenile. **e, f, g** Breadcrust texture with dense crust and vesicular interior.

Early work suggested that magma-water interaction was the trigger for Vulcanian explosions, and this view was supported by a lack of evidence for gas-rich juvenile material (Schmincke 1977; Self et al. 1979; Woods 1995). Most subsequent work has proposed that expansion of already exsolved magmatic volatiles within the conduit and/or lava dome provide the fragmentation mechanism for Vulcanian explosions (Sparks 1997; Stix et al. 1997). In this scenario, a batch of magma ascends within the conduit and develops a horizontal ‘layering’ of progressively less outgassed magma with depth. The densest uppermost material seals the shallow conduit allowing (i) magma pressure to increase due to rheological stiffening (Sparks 1997; Melnik and Sparks 1999; Clarke 2013) and (ii) volatile pressure to increase due to viscosity-limited growth of gas pockets/bubbles (Sparks 1978; Tait et al. 1989; Stix et al. 1997). If the upper portion of the plug then fails or is removed, say by collapse, the model predicts that a decompression-induced fragmentation wave travels down into the conduit (Self et al. 1979; Turcotte et al. 1990; Fagents and Wilson 1993; Woods 1995; Clarke et al. 2002a, b). Once fragmentation ceases, the conduit re-fills, and the cycle starts over (Druitt et al. 2002; Diller et al. 2006; Burgisser et al. 2010; Clarke et al. 2015). In this model, the potential energy for the explosions is stored in pockets of pressurized gas. This concept is widely applied to Vulcanian explosions that are episodic increases in mass flux during long-lived dome extrusion (Clarke et al. 2002a; Druitt et al. 2002; Melnik and Sparks 2002b). This Soufrière Hills-based model permits elegant one-dimensional analysis of the conduit conditions prior to unsteady, non-sustained explosions (Melnik and Sparks 2002b; Diller et al. 2006; Mason et al. 2006; Clarke et al. 2007; Degruyter et al. 2012), but it does not set out to model three-dimensional complexity and heterogeneity. Additionally, these models assume, for large Vulcanian explosions, that a

sudden pressure release at the top of the conduit (generally in response to a partial or complete dome collapse) is the trigger for the transition to Vulcanian explosions (Clarke et al. 2002a, b; Druitt et al. 2002; Melnik and Sparks 2002a, b; Mason et al. 2006). However, several other volcanoes (e.g., Sakurajima, Japan; Santiaguito, Guatemala; Colima, Mexico; Reventador, Ecuador) have exhibited the sudden onset of often weaker Vulcanian explosive activity without any sign of such an external trigger (Global Volcanism Program 2005; Sahetapy-Engel et al. 2008; Yokoo et al. 2009; Cassidy et al. 2015). We document here, in unprecedented detail, the textural diversity for ejecta from an eruption episode at Novarupta which more closely resembles this latter pattern of activity accompanying the close of powerful Plinian eruption.

3.1.2 Degassing, outgassing, and vesiculation

Throughout this paper, we largely follow the terminology of Cashman and Scheu (2015), specifically we define:

- Degassing: as the loss of dissolved volatiles from a melt by exsolution or diffusion
- Outgassing: as the escape of exsolved gas bubbles from magma by permeable flow or buoyant rise
- Vesiculation: as nucleation, growth, and coalescence of gas bubbles within magma

Eruption style and the behavior of volatiles in the ascending magma are closely related. The history of those volatiles, such as the rate and timing of vesiculation relative to fragmentation and the conditions under which they exsolve from the melt, is often preserved in the vesicularity and bubble textures of the juvenile ejecta (e.g., Houghton and Wilson 1989;

Cashman and Mangan 1994; Hammer et al. 1998, 1999, Adams et al. 2006a, b; Houghton et al. 2010). Volatile solubility decreases in response to decreasing pressure as magma ascends from depth driving the nucleation and expansion of gas bubbles. Bubbles evolve due to continued diffusion of volatiles, expansion due to decreasing pressure, and coalescence with other bubbles. Growth may be limited by the volatile content of the melt, rate of volatile diffusion, and/or viscous resistance of the melt (Toramaru 1995; Proussevitch and Sahagian 1998; Gardner et al. 2000; Gonnermann and Manga 2007). The resulting vesicularity and bubble textures depend on the rate of ascent, which also modulates eruption style (Eichelberger 1995). With slow ascent, bubbles eventually form outgassing pathways in silicic magmas (Eichelberger et al. 1986; Klug and Cashman 1996; Burgisser and Gardner 2005; Takeuchi et al. 2009; Nguyen et al. 2014). This generally promotes effusion of lavas with low bubble numbers and complex bubble shapes reflecting outgassing and compaction. With very fast ascent, diffusion into existing bubbles may be rate-limited allowing high rates of late bubble nucleation. If viscosity is high, bubble growth is slow and in disequilibrium, which increases pressure within the bubbles and promotes explosive eruptions. Resulting pyroclasts have high vesicle number densities and small bubbles. More complicated histories are often imprinted in clast vesicularity and texture. For example, different portions of the source magma for Vulcanian pyroclasts experience different ascent rates and residence times in the shallow conduit and thus display a wide range of vesicularities and textures (Kennedy et al. 2005; Adams et al. 2006a; Cassidy et al. 2015). It is through the measurement of clast vesicularity and detailed analyses of bubble sizes, numbers, and shapes that we can retrace parts of the vesiculation history and make inferences about magma ascent.

3.1.3 Porosity and permeability

Porosity and permeability describe the proportion of the volume of an object that is occupied by pores and the ease with which fluid flows through those pores, respectively. Permeability directly influences outgassing of silicic magmas and thus has the potential to modulate eruptive behavior, influence the characteristics of ash plumes and PDCs, and control the expansion and size distributions of pyroclasts (Eichelberger et al. 1986; Jaupart and Allègre 1991; Woods and Koyaguchi 1994; Klug and Cashman 1996; Rust and Cashman 2011; Degruyter et al. 2012). Controls on the permeability of silicic magmas include vesicle size and shape, pore aperture size, and tortuosity of pore pathways (Blower 2001; Rust and Cashman 2004; Mueller et al. 2005; Wright et al. 2006, 2009). Over the last three decades a range of volcanic rocks have been analyzed for porosity, pore connectivity, and permeability, producing a relatively robust data-set for effusive and Plinian products (Eichelberger et al. 1986; Klug and Cashman 1996; Saar and Manga 1999; Jouniaux et al. 2000; Melnik and Sparks 2002a; Rust and Cashman 2004; Bernard et al. 2007; Wright et al. 2007, 2009; Platz et al. 2007; Bouvet de Maisonneuve et al. 2009; Nguyen et al. 2014; Kushnir et al. 2016) and a growing data-set from experimental samples (Westrich and Eichelberger 1994; Burgisser and Gardner 2005; Mueller et al. 2005; Takeuchi et al. 2009; Ashwell et al. 2015; Heap and Wadsworth 2016; Kennedy et al. 2016; Kushnir et al. 2017). However, comparable data-sets for Vulcanian pyroclasts are very restricted to one dense block and thirteen breadcrust bombs from Guagua Pichincha, Ecuador (porosity of crust and interior, permeability only of interior; Wright et al. 2007) and seven pumiceous blocks from the 1912 eruption of Novarupta (Nguyen et al. 2014).

3.1.4 Breadcrusting

Breadcrusting is a characteristic that is commonly found in Vulcanian eruptions (Adams et al. 2006a; Wright et al. 2007; Giachetti et al. 2010; Benage et al. 2014; Isgett et al. 2017). Current understanding of the post-fragmentation formation of breadcrusted clasts includes a) fragmentation and depressurization of magma that is only partially degassed, with immediate quenching of the exterior to produce a rind that preserves the micro-textures present at the time of fragmentation, b) vesiculation and expansion of the still hot interior in response to the drop in pressure, c) brittle cracking of the exterior to accommodate b), d) thermal contraction of the exterior, and possibly e) clast breakage in response to stresses applied upon impact (Walker 1969; Wright et al. 2007). The case for processes (a) through (c) is widely accepted as applying to those clasts that display a contrast in the vesicularities of the crust and interior. The literature discusses the physical processes of cracking the exterior and attempts to estimate the time it takes for the entire rind to quench (Wright et al. 2007; Benage et al. 2014). However, the chemical and physical state of the magma prior to breadcrusting is not well constrained or understood. Hoblitt and Harmon (1993) and Wright et al. (2007) suggested that glassy rinds resulted from pre-eruptive degassing that delayed the nucleation of new bubbles. Giachetti et al. (2010) model breadcrust interiors as forming from bubble nucleation of a largely bubble-free melt. A common conclusion between these different studies is that the breadcrust rinds were largely degassed, however, they do not address any intervening step of shallow outgassing, that is, how the rinds became dense after they underwent a significant primary degassing. Understanding the balance between degassing and outgassing of breadcrust rinds can provide insight to their fragmentation depths and their role in the pre-fragmentation conduit processes.

3.1.5 Novarupta

The largest eruption of the twentieth century, the 1912 eruption of Novarupta, produced an exceptionally well preserved Vulcanian block apron from its fourth episode (Adams et al. 2006a). After three episodes of powerful Plinian-style explosions, spanning a total of 60 hours (Hildreth 1983, 1987; Fierstein and Hildreth 1992), an ephemeral lava dome/plug was formed and completely destroyed by Vulcanian explosions in Episode IV (Figure 3.2). The fifth and final episode consisted of passive dome extrusion, allowing for complete preservation of the earlier Vulcanian deposits. The mappable Episode IV deposit consists of a roughly 4 x 2.5 km N-S elongated elliptical block apron (Figure 3.2) centered on the Episode V lava dome and lacking any deposits of pyroclastic density currents. The Episode IV juvenile blocks are chemically homogeneous but texturally extremely diverse, from pumiceous, dense, and banded dacite to variably-welded breccia clasts, all with differing degrees of surface breadcrusting (Figure 3.3). This diversity offers a window into the state of the magma within the shallow conduit during a critical transition: a decrease in discharge rate and style from steady Plinian eruption (Episodes I–III) to sustained dome effusion (Episode V).

In this paper, we describe and interpret the contrasting block types. In particular, our study of the breadcrusted and mingled clasts yields new insight to the physical state of their magma prior to fragmentation. This allows us to draw conclusions regarding the pre-eruption vesiculation histories of the magma that filled the shallow conduit. In addition, this study more than doubles the global set of porosity and permeability measurements on Vulcanian products and shows a new trend within the porosity and permeability relationships among the different block types.

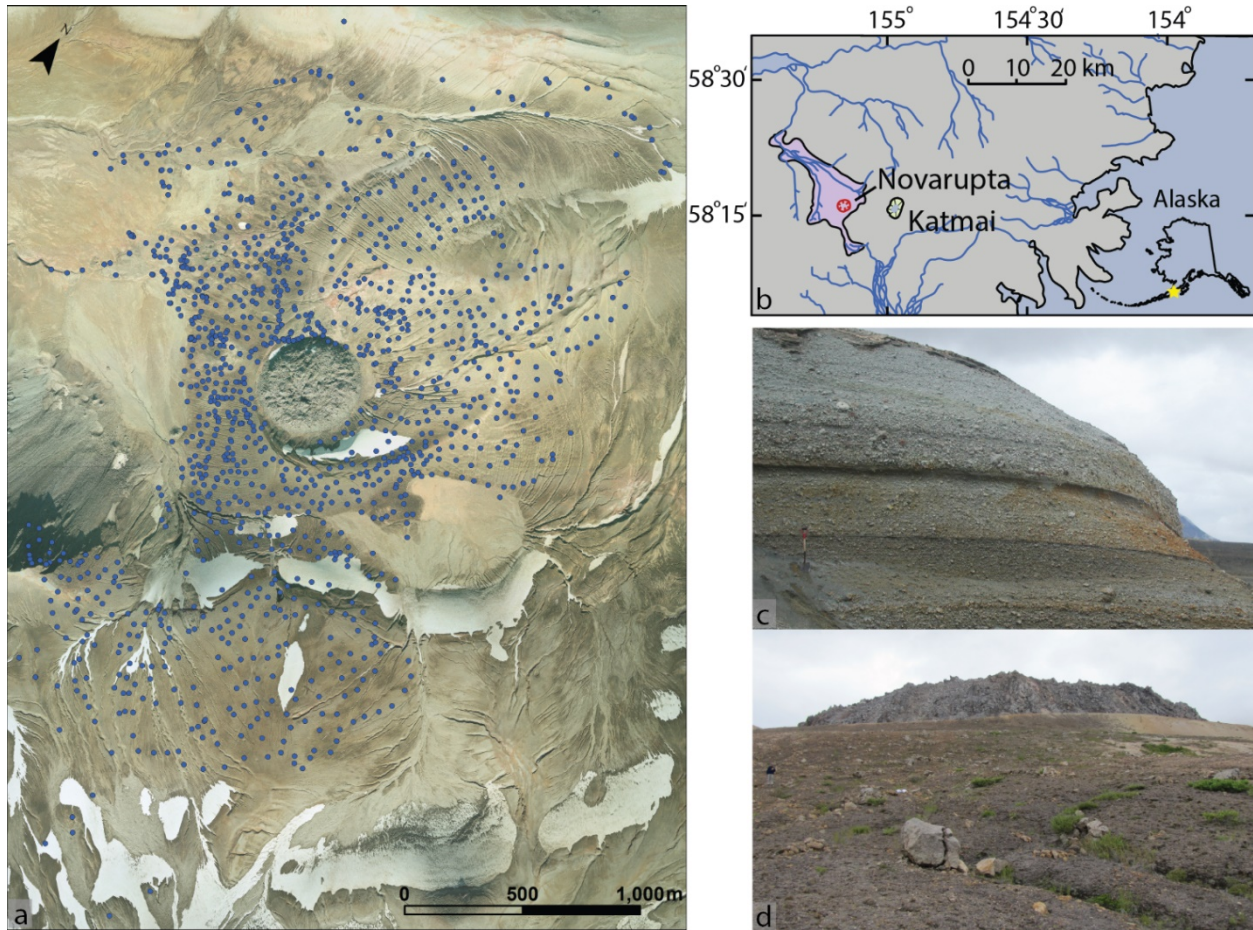


Figure 3.2a Aerial photograph mosaic of the region proximal to the vent: 1,273 mapped Episode IV blocks are overlain in *blue* and the Episode V dome is the *round feature* in the *middle*. Modified after Isgett et al. 2017. **b** Location map for deposits of the 1912 eruption: Novarupta dome (*red*), Valley of Ten Thousand Smokes (*purple*), Katmai Caldera (*yellow*). Inset with the yellow star shows the location of Novarupta within Alaska. Modified after AVO/ADGGS. **c** Image of the Episodes II and III Plinian deposits. **d** Image of the Episode IV blocks (*foreground*) and Episode V dome (*background*). Note, person for scale in *middle, left* of image.

Homogeneous clasts

a Pumice



b Intermediate



c Dense



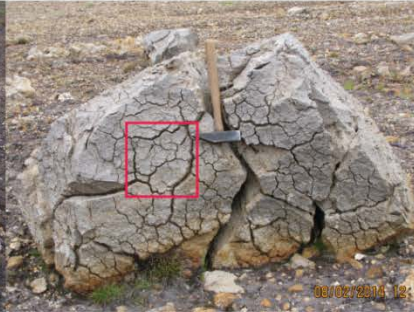
Heterogeneous clasts

Vesicular breadcrusted clasts

d Group 1



e Group 2



f Group 3



Banded clasts

g Pumiceous banded



h Mixed banded



i Dense banded



Other heterogeneous clasts

j Breccia



k Banded breadcrusted



Figure 3.3 (previous page) Categories of different clast types in the Episode IV block apron. Homogeneous blocks include (a) pumice, (b) intermediate, and (c) dense dacite. Heterogeneous blocks include the breadcrusted, banded, and brecciated clasts. The re-vesiculated breadcrusted blocks are divided into three groups as described in the text. **d** Block N004 of group 1; note the cauliflower texture of the crust. **e** Block N011 of group 2; note the clearly defined cracks and multiple generations of cracking *outlined in red*. **f** Block N156 of group 3; note the deep cracks in the middle and multiple generations of cracking in the upper left polygon. The banded clasts exhibit a range in textures that are grouped into (g) pumiceous banded, (h) mixed banded (image taken by Alain Burgisser), and (i) dense banded. The brecciated clasts (j) are not discussed in this paper. All types of clasts can be breadcrusted, as is exhibited in (k) the dense banded breadcrusted clast.

3.2 Methodology

3.2.1 Mapping and sampling

We mapped the largest Episode IV blocks within 20–60 m-wide squares at fixed distances apart, across the entire deposit, and measured and sampled these blocks. Lithology, texture (including breadcrust rinds), and the three largest orthogonal dimensions were recorded. A subset of samples from each lithology were collected from a total of 169 blocks. Care was taken to obtain a sample suite a) on which multiple laboratory analyses could be performed and b) that represented different textural zones of each block. Samples of mingled bands were collected when they were thick enough for analysis. Suites of “crust” (the outer dense, cracked rind), “transition” (the zone between the crust and interior exhibiting changing texture), and “interior” (the middle and/or most expanded zone of a clast) samples were assembled from representative breadcrusted clasts.

3.2.2 Bulk and 2D vesicularity

Sample densities were measured following Houghton and Wilson (1989) and converted to vesicularities using a dense-rock equivalent (DRE) density of $2,600 \text{ kg/m}^3$. Qualitative vesicle size and shape analyses were performed on 9 clasts. Back-scattered electron (BSE) images were collected using a JEOL-5900LV scanning electron microscope (SEM) operating at 15 kV accelerating voltage and 1 nA beam current. Compositional mapping using the NORAN System SIX (NSS) X-ray microanalysis system was utilized in order to discern feldspar phenocrysts from the glass. The NSS system was also used to collect full thin section scans by merging grids of images collected at 50x or 65x magnification. SEM images were processed via converting glass to white, bubbles to black, and crystals to gray in Adobe Photoshop and are referred to as ‘grayscale images’ in this text.

3.2.3 Porosity and permeability

Porosity and permeability were measured using the method following Nguyen et al. (2014) on cores of 1–3-cm diameter and 1–4.5-cm length from the same samples used for textural analyses. Helium pycnometry was performed in order to calculate connected (φ_{con}) and total (φ_{total}) porosities. The cores were then mounted axially on plexiglass plates with their radial surface sealed with impermeable epoxy resin in order to assure axial flow during permeability measurement. The permeability of the sealed cylindrical sample cores was determined using a Capillary Flow Porometer. A more detailed description of the methodology is included in Appendix B.

3.3 Vesicularity data for juvenile clasts

This paper presents data only on the juvenile clasts (i.e., no data for the brecciated clasts are presented). We have divided the juvenile blocks into two categories: 1) homogeneous clasts, i.e., pumiceous, transitional, and dense dacites; and 2) heterogeneous clasts, which include breadcrusted clasts and banded dacites (Figure 3.3).

3.3.1 *Homogeneous clasts*

Microvesicular pumiceous dacites have vesicularities from 59–83% (Figure 3.4a). They predominantly show “primary degassing textures”, i.e., bubble textures that can be shown to have formed prior to fragmentation or outgassing. Vesicle textures are dominated by <100 μm bubbles but also contain a conspicuous volume fraction of >150 μm to larger than or equivalent to mm-size bubbles. The numerically dominant small bubble population has round, elongate, or amoeboid shapes whereas the larger bubbles are very irregular (convoluted/polylobate) and/or elongate in shape (Figure 3.5). Textural heterogeneity is limited to small domains either rich in <25 μm vesicles or elongated vesicles. Note that the “microvesicular pumices” in this paper are referred to as “non-breadcrusted pumices” in previous papers (Adams et al. 2006a; Isgett et al. 2017).

Dense dacite blocks cluster on the low vesicularity end of the spectrum, with values ranging from 4–19% (Figure 3.4a). Dense dacites are dominated by large regions of glass and phenocrysts and contain few intermediate-to-coarse pores (Figure 3.6) that are often aligned along phenocrysts and are very irregular in shape. Note, we use the term ‘pore’ to describe cavities in the dense dacites and breadcrust rinds (described in the following section) as they no longer represent primary degassing processes. In addition, a subordinate population of small

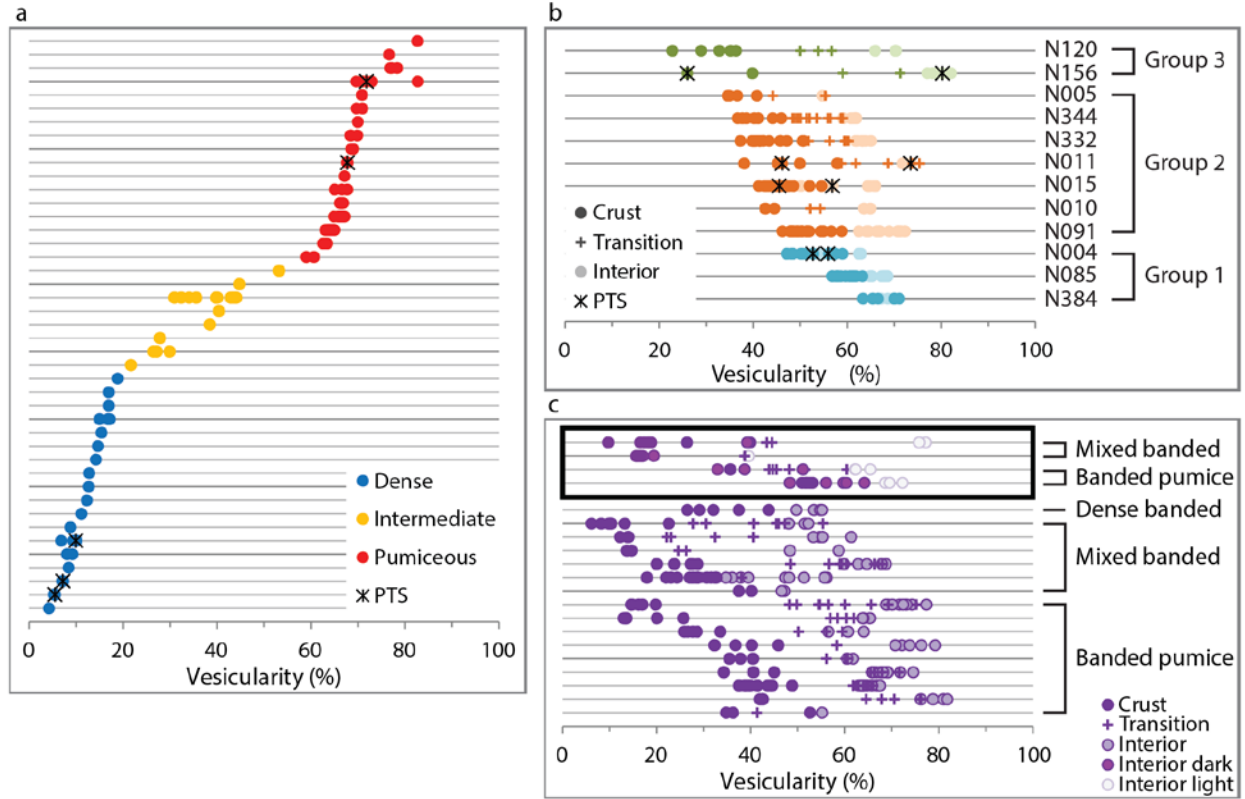


Figure 3.4 Bulk vesicularities for the different clast types. There is no value to the y-axis in these plots. Instead, each line represents the data for all of the samples collected from an individual block. Asterisks indicate blocks for which SEM images were collected from polished thin sections (PTS). **a** Vesicularities of the homogeneous clasts. **b** Vesicularities of the revesiculated breadcrusted clasts. **c** Vesicularities of the breadcrusted banded dacites. Black box highlights blocks for which individual bands were sampled.

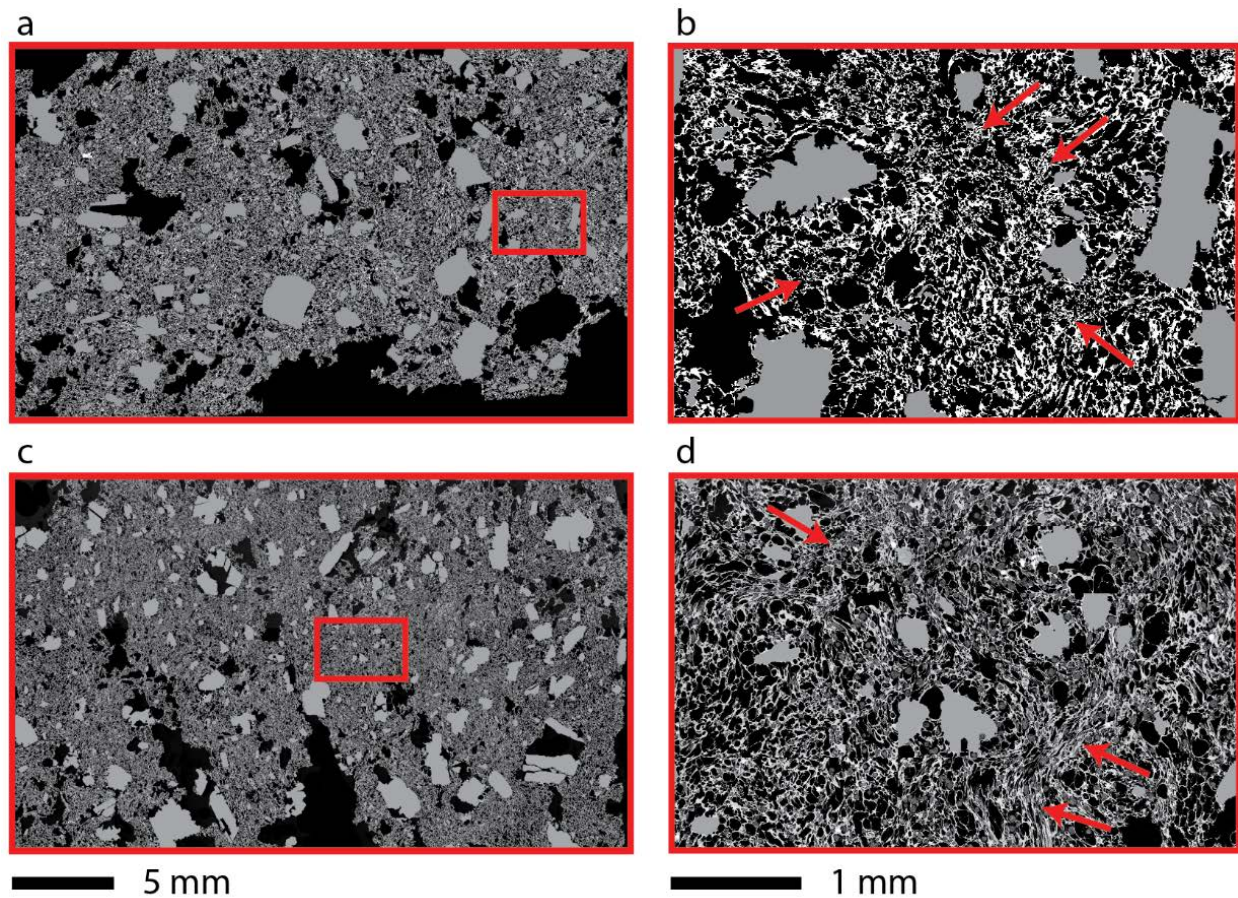


Figure 3.5 Grayscale micro-texture images of the pumice. Crystals are shown in *gray*, glass in *white*, and bubbles in *black*. *Red rectangles* outline the location of the magnified images on the *right* and correlate with the colors used in Fig. 3.3a. **a** Full thin section scan of block N182 with 72% vesicularity. **b** Zoom in of heterogeneous textures in block N182. *Arrows* indicate small domains of small bubbles. **c** Full thin section scan of block N406 with 68% vesicularity. **d** Zoom in of heterogeneous textures in block N406. *Lower right arrows* indicate a domain of elongate bubbles and *top left arrow* identify a domain of small bubbles.

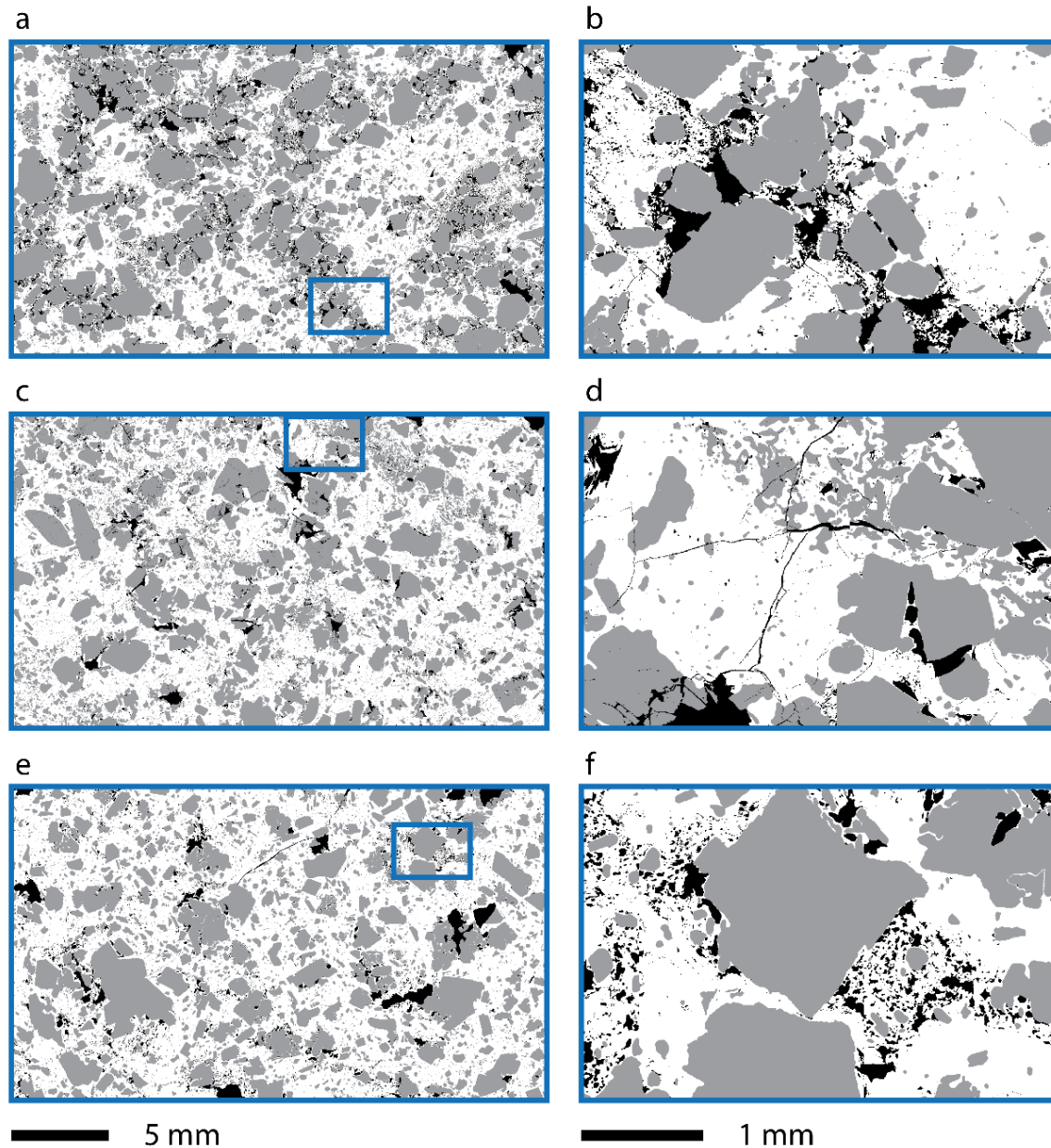


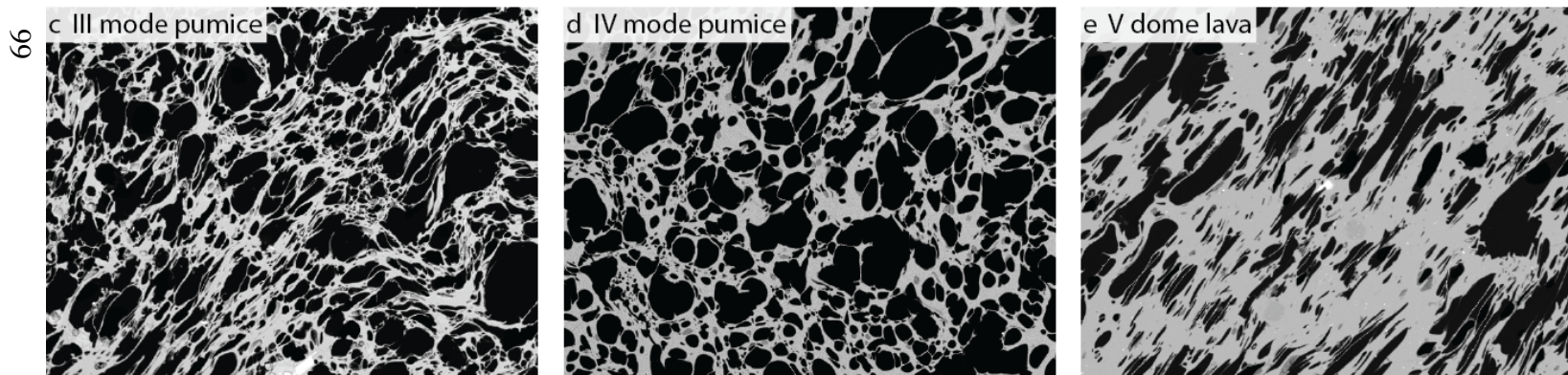
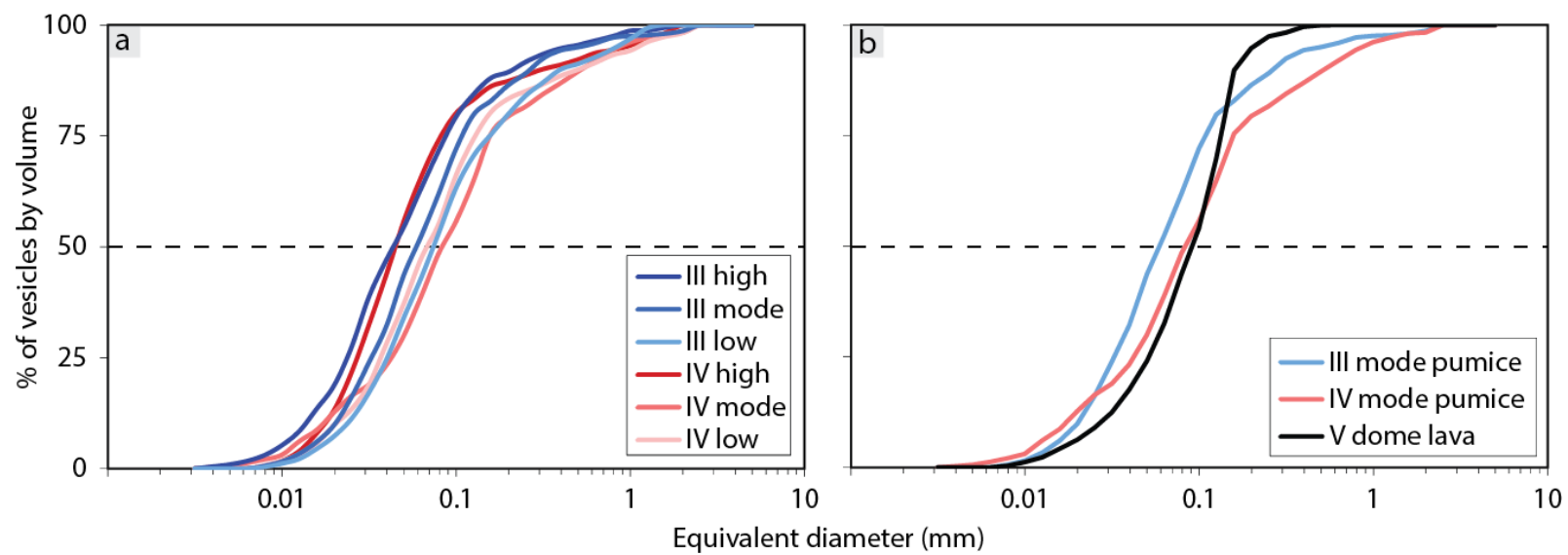
Figure 3.6 Grayscale micro-texture images of dense dacites. *Blue rectangles* outline the location of the magnified images on the *right* and correlate with the colors used in Fig. 3.3a. **a** Full thin section scan of block B126 with 7% vesicularity. **b** Zoom in of collapsed outgassing pathway in B126. **c** Full thin section scan of block B128 with 5% vesicularity. **d** Zoom in of microcracks in B128. **e** Full thin section scan of block N158 with 10% vesicularity. **f** Zoom in of small bubbles focused around a phenocryst.

round bubbles exists in the glassy regions (Figure 3.6f) and there are pervasive micro-fractures throughout the glass and crystals.

A small assemblage of blocks with intermediate vesicularities span the gap between the microvesicular pumiceous and dense dacites (Figure 3.4a). In every other way these blocks appear to be intermediate between the dense and pumiceous dacites.

3.3.1.1 Vesicle size and number density data

Quantitative bubble micro-texture analyses by Adams et al. (2006a, b) showed similarities between Episodes III and IV microvesicular pumices and sharp contrasts with the Episode V rhyolite dome. As the classical interpretation of bubble parameters in the context of simple nucleation and growth cannot be applied to the Episode IV dense clasts (due to the formation and collapse of permeable networks, as interpreted in section 3.5) only one quantitative analysis was conducted by Adams on an Episode V rhyolite dome sample to provide a comparison with the pumice. Cumulative vesicle volume distributions (CVVDs) for the microvesicular pumices (Figure 3.7a) have smooth sigmoidal curves with little variation between the high, modal, and low density clasts from Episodes III and IV. The steeper slope of the rhyolite dome sample's CVVD reflects smaller contributions from both the larger (≥ 0.16 mm) and smaller (≤ 0.025 mm) bubbles when compared to the modal microvesicular pumices (Figure 3.7b). Median vesicle size (determined at the intersection of the curves with the fiftieth percentile) range from 45–92 μm (Table 3.1). For the pumices, median vesicle size roughly increases from high to low density; the dense rhyolite has the largest median. Volumetric bubble number densities (N^{m}_v , referenced to melt only) are commonly used as a proxy for nucleation and ascent rates (Toramaru 1995, 2006; Mangan and Sisson 2000; Mangan et al. 2004; Mourtada-Bonnefoi and Laporte 2004).



66

Figure 3.7 (previous page) a Cumulative vesicle volume distributions (CVVDs) for the microvesicular pumices from Episodes III and IV. Each line represents an individual clast with the color scheme of *dark* to *light* corresponding to high to low density clasts. **b** CVVDs for modal density pumices for Episodes III and IV (*blue* and *red* curves, respectively) and for the Episode V dome sample (*black* curve). **c-e** Backscatter scanning electron microscope (SEM) images for the samples represented by the curves in *b*. Data for the plots and SEM images were collected by Nancy Adams (Adams, 2005).

Table 3.1 Median vesicle size and volumetric vesicle number densities referenced to the melt only ($N^m v$) for the Episodes III and IV microvesicular pumices (high, modal, and low densities) and the Episode V dome.

	III high	III mode	III low	IV high	IV mode	IV low	V
Median (μm)	44	59	74	45	84	68	92
$N^m v$ (cm^{-3})	2.1×10^9	3.8×10^8	2.8×10^8	2.6×10^8	8.0×10^8	4.9×10^8	1.0×10^8

They are approximately one order of magnitude higher for the Episodes III and IV microvesicular pumice with respect to the Episode V rhyolite and the Episode IV modal density clast has a slightly higher $N^m v$ than its Episode III counterpart.

Here, we compare, for the first time, the $N^m v$ data from Adams et al. (2006a, b) to the ratio of the volume of vesicles (gas) to that of glass (liquid; V_G/V_L after Gardner et al. (1996); Figure 3.8). Given the high crystallinities of the Novarupta dacite, the correction for the volume fraction of crystals in Gardner et al. (1996) was employed. The different stages of vesiculation are reflected in characteristic signatures on plots of V_G/V_L versus $N^m v$ (e.g., Stovall et al. 2012).

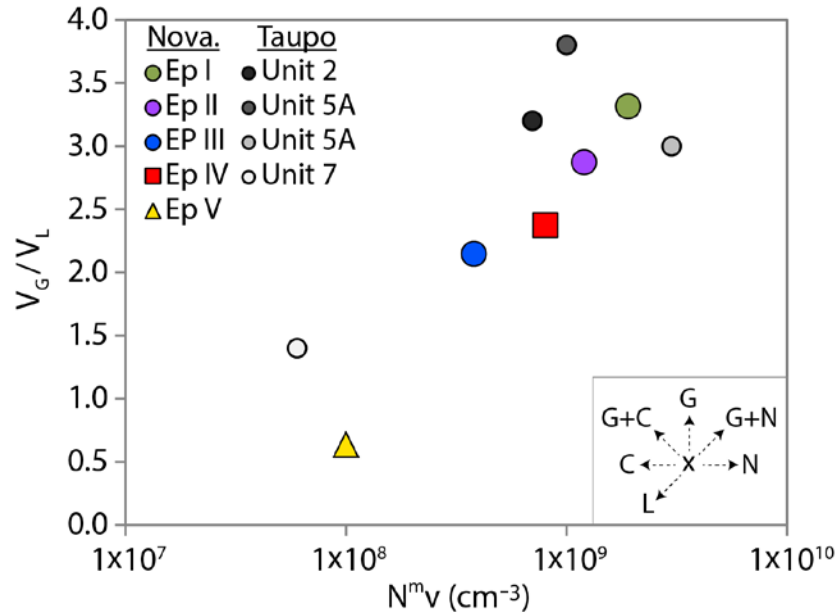


Figure 3.8 Volumetric ratio of vesicles to melt (V_G/V_L) against vesicle number density referenced to melt ($N^m v$) for select modal density clasts from all episodes of the 1912 eruption of Novarupta (Nova.) and from a subset of units from the 1.8 ka Taupo eruption.

Nucleation increases the number density of bubbles while only slightly increasing V_G/V_L whereas growth by diffusion and volume expansion without continued nucleation is reflected by increased V_G/V_L at constant $N^m v$. Coalescence decreases the number of bubbles while keeping the volume of gas constant. Bubble collapse decreases both the volume of gas and the number of bubbles. Simultaneous processes of 1) bubble nucleation and growth and 2) growth and coalescence result in increasing the volume of gas but also increasing and decreasing bubble numbers, respectively. The locations of the data points for all of the Novarupta pumices on Figure 3.8 define a linear trend suggesting the most vigorous nucleation and growth occurred during Episode I which has the highest mass discharge rate. The Episode V data suggest that this material had undergone significant collapse and loss of bubbles with respect to all of the microvesicular pumices. For comparison, samples of three units, three Plinian pumice (Units 2

and 5A) and a pumice from the dome carapace (Unit 7), of the 1.8 ka Taupo eruption (Houghton et al. 2010) show a similar contrast to that between Novarupta microvesicular pumice and dense rhyolite. This highlights the significantly different vesiculation histories for the magma ejected in explosive and effusive phases of such large silicic eruptions.

3.3.2 Heterogeneous clasts

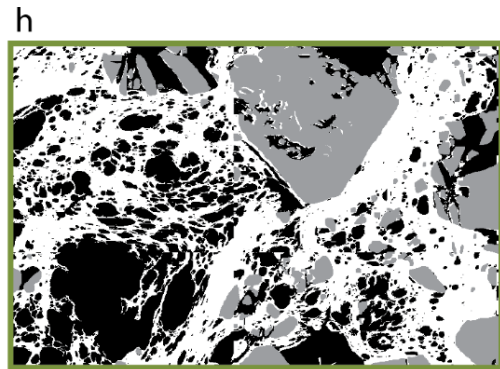
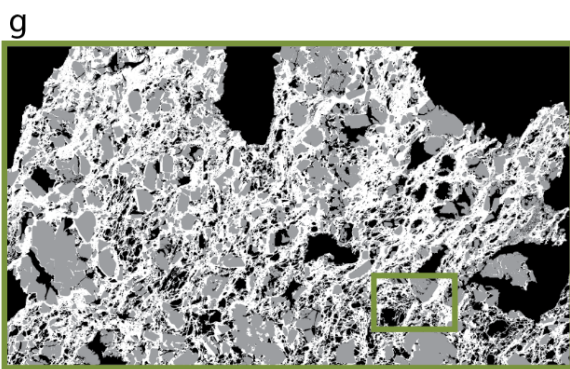
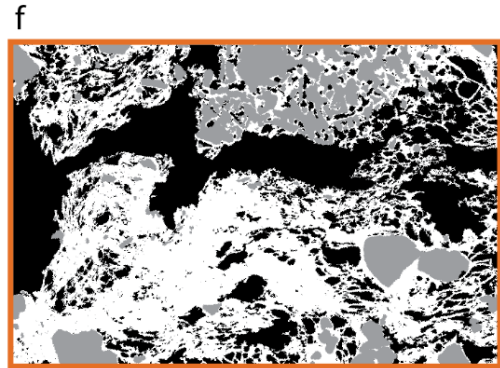
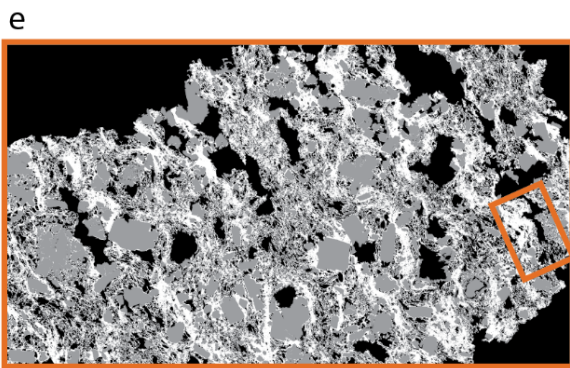
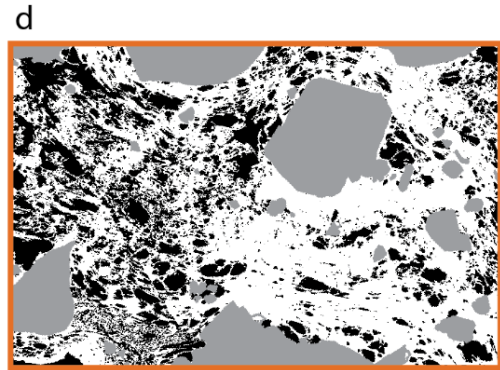
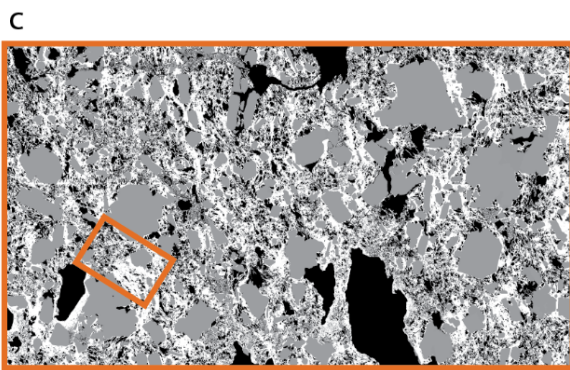
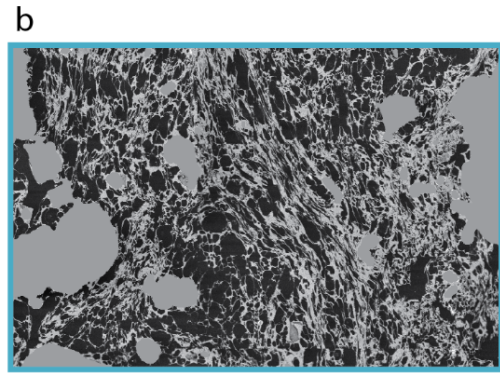
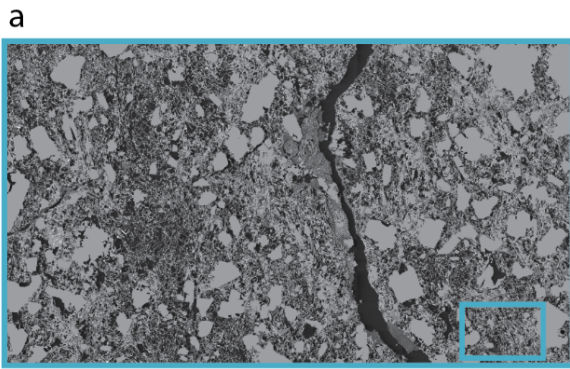
The Episode IV block apron is particularly rich in breadcrusted clasts and breadcrusting is a conspicuous feature among all lithologies (Isgett et al. 2017). We refer to breadcrusted blocks with highly vesicular interiors, and which are not banded, as “re-vesiculated breadcrusted clasts”. This term replaces “pumiceous dacites with bread-crust exteriors” used by Adams et al. (2006a) and “breadcrusted pumice” in Isgett et al. (2017). We have changed the terminology because this paper will show that the high vesicularity of the interiors formed 1) following earlier outgassing of the first bubble population formed in this material and 2) after fragmentation. Re-vesiculated breadcrusted clasts have rinds that vary between 23% and 71% whereas the range of interior vesicularities is higher but narrower (47–82%). For discussion purposes, the re-vesiculated breadcrusted clasts are divided arbitrarily in Figure 3.4b into three groups according to crust and interior vesicularities. In group 1, crust vesicularities are high (>47%) and they significantly overlap with their interiors (Figure 3.4b). The total range of vesicularities within individual blocks is also narrowest in group 1, with samples spanning a minimum of 8% and maximum of 16%. Group 2 has crust vesicularities that are intermediate (35–59%) and there is a clear distinction between crust and interior. Group 3 encompasses the samples with the lowest crust vesicularities and a broad range in vesicularity from rind, to transitional, and to interior samples.

The intensity of breadcrusting increases from group 1 to 3 (Figure 3.3). In group 1, rinds are thin, have a cauliflower texture, and have only one generation of cracking. Crusts in group 3 have deep cracks and multiple generations of cracking (i.e., shallower cracks set within polygons of crust separated by deeper cracks cf., Wright et al. 2007). Micro-textures in the rinds show a similar progression in the size, shape, and number of pores and in the abundance of dense, glassy regions. The volumetrically dominant bubble population in all groups is intermediate-to-coarse in size, but this population becomes less prevalent in groups 2 and 3.

The sample from group 1 in Figure 3.9 is free of large glassy areas and has the greatest density of intermediate sized pores. This crust appears similar to the non-vesicular breadcrusted clasts in terms of the diversity in bubble shapes and the focusing of different textures within regions. One unique aspect of this crust is that it lacks the mm-sized bubbles that are present in all of the other crusts and in the microvesicular pumice blocks.

There is a more significant textural shift between group 1 and 2 crusts than between 2 and 3. Elongate glassy regions containing few small bubbles are present in group 2, and the dominant intermediate-to-coarse population is stretched/elongate and amoeboid in shape and occurs in clusters (Figure 3.9). Similar to the dense dacites, the mm-sized pores in group 2 are complex in shape and are associated with the phenocrysts. The progression continues with group 3; its most representative sample (N156-crust) contains large glassy regions that are bubble free or contain only few small bubbles. The intermediate-to-coarse pore population is greatly diminished (compared to group 1) and pores are rounded to slightly elongate in shape.

Groups 1 and 2 contain porous pathways that permeate in 2D throughout large regions of the thin section and have irregularly shaped, but rounded edges. Some are filled with fine clastic



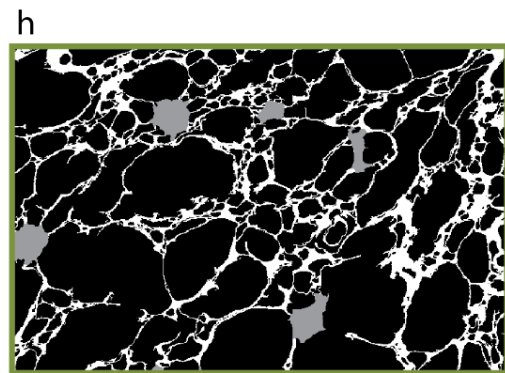
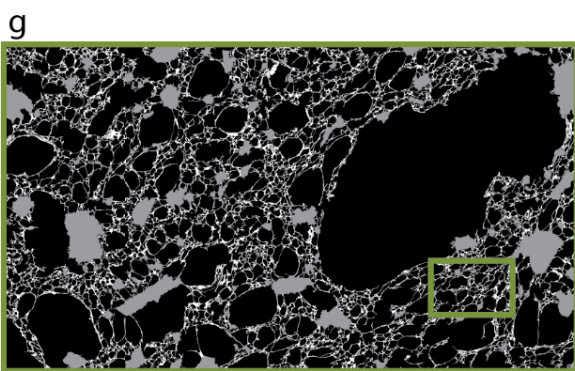
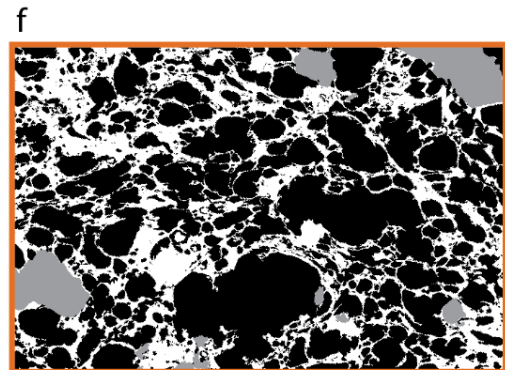
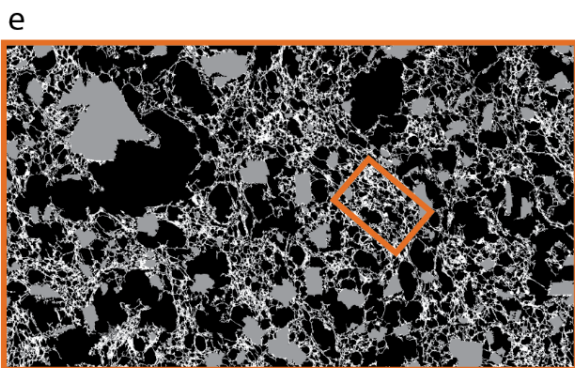
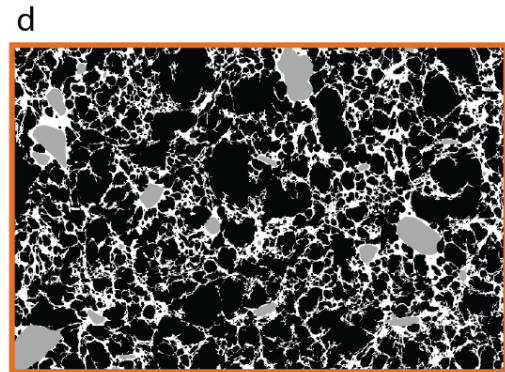
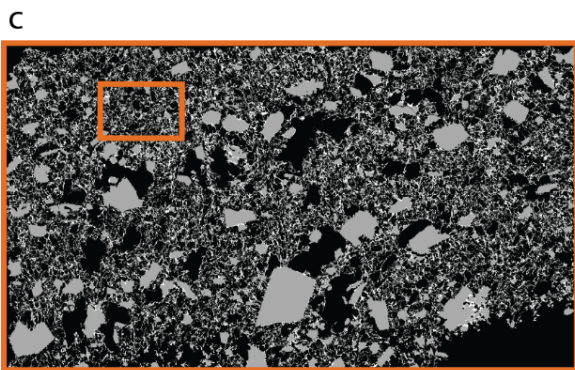
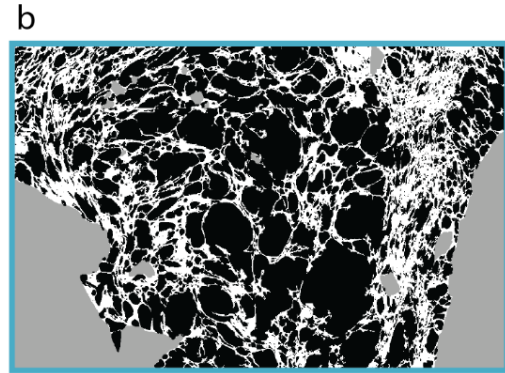
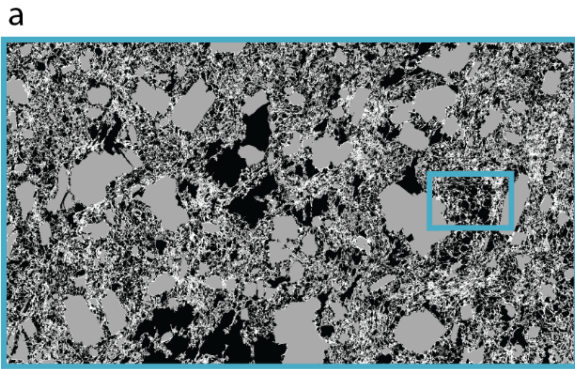
5 mm

1 mm

Figure 3.9 (previous page) Grayscale micro-texture images of the crusts. *Colored rectangles* outline the locations of the magnified images to the right and correlate to the colors used in Fig. 3.3b. **a** Full thin section scan of crust N004 with vesicularity of 53% and in group 1. The large void in the *middle* of the image is a crack that formed via breadcrusting. **b** Inset of *a* highlighting the focusing of different bubble textures in small regions. Note the cluster of small bubbles in the *lower right corner*, the region of elongate bubbles of varying sizes in the *middle*, and the cluster of intermediate sub-rounded bubbles with thin glass walls in the *lower, left of middle* area of the image. **c** Full thin section scan of crust N015 with vesicularity of 46% and in group 2. **d** Zoom in of textures in *c* showing the glassy regions with few small bubbles (*right side*) and the irregularly shaped intermediate-to-coarse bubble population (*left side of image*). **e** Full thin section scan of crust N011 with 46% vesicularity and in group 2. **f** Inset of *e* showing an outgassing pathway and its collapse into a cluster of irregularly shaped pores in a range of sizes. **g** Full thin section scan of crust N156 with 26% vesicularity and in group 3. **h** Magnification of *g* highlighting the thick glassy regions that are bubble free or have few small bubbles and the cluster of irregularly shaped bubbles (*middle, left of center*) located between the phenocryst and the large bubble that may be the remnant of a collapsed pathway.

debris whereas others are open (Figure 3.9f, Figure B.3 in Appendix B). In group 2, some pathways terminate in clusters of complex-shaped intermediate-to-coarse pores (Figure 3.9f). Similar clusters are also located near phenocrysts and the mm-sized pores in group 3 (Figure 3.9h).

There are also contrasts in the textures of the interiors of the vesicular breadcrusted clasts (Figure 3.10). The interior to the group 1 clast resembles the microvesicular pumices but contains regions of round, ~150–300 μm bubbles that contrast in shape with the population of intermediate to coarse (>150 to \geq mm), elongate, amoeboid, and complex shaped bubbles (Figure 3.10b). This interior also contains many more of the small <100 μm bubbles than any of group 2



5 mm

1 mm

Figure 3.10 (previous page) Grayscale micro-texture images of the interiors to the crusts in Figure 3.6. *Colored rectangles* outline the locations of the magnified images on the right. **a** Full thin section scan of N004 interior with 56% vesicularity. **b** Inset of *a* highlighting a region of rounded ~150–300 μm bubbles. **c** Full thin section scan of N015 interior with 57% vesicularity. **d** Inset of *c* highlighting sub-rounded bubbles. **e** Full thin section scan of N011 interior with 73% vesicularity. **f** Inset of *e* highlighting the sub-rounded bubbles and the lack of small <100 μm bubbles. **g** Full thin section scan of N156 with 80% vesicularity. **h** Inset of *g* highlighting the rounded bubbles and the lack of small bubbles.

or 3's interiors. Vesicles in group 2 and 3's interiors contrast more significantly with those in the pumices in terms of size and shape. They are mostly sub-rounded in shape, and the few bubbles that are more irregularly shaped still have rounded edges. Group 2 and 3 interiors have two volumetrically dominant bubbles sizes that are larger than those in the pumices: those that are 500– \geq 1 mm and those that are 125–250 μm (Figure 3.10). Group 2 interiors have fewer of the largest bubbles and slightly more complex shapes than group 3 interiors; however, they are still similar in their striking contrast with the microvesicular pumices.

Dense breadcrusted blocks resemble dense dacites except for minor re-vesiculation of their interiors. We sampled one dense breadcrusted block and it showed a 3% vesicularity difference between the crust (8%) and interior (11%).

Banded blocks contain sub-millimeter to centimeter wide bands of contrasting vesicularity. Banding can appear as (Figure 3.3): i) dominantly highly vesicular (light-colored) blocks containing bands with slightly different vesicularities (pumiceous banded), ii) dominantly dense dacite blocks with a few lighter colored bands (dense banded), and iii) banded clasts that contain sub-equal amounts of dense and microvesicular pumiceous dacite (mixed banded, see

Figure 2 of Isgett et al. 2017 for further details). Unfortunately, it was difficult to collect vesicularity data from individual bands as most were thinner than 2 cm, and so many of the data points in Figure 3.4c represent a mixture of bands. For blocks in which individual bands were sampled, dark (or relatively dense) bands have vesicularities similar to dense or intermediate blocks. Light colored (or more vesicular) bands have vesicularities similar to the pumices or the interiors of the re-vesiculated breadcrusted clasts (Figure 3.4c).

3.4 Porosity and permeability data

Episode IV samples span a uniquely wide range of porosity and permeability for any single eruptive episode of uniform chemical composition. We have included in Figure 3.11 porosity and permeability measurements on Novarupta samples from Plinian Episodes I–III (Nguyen et al. 2014) and from Episode IV (this study). For all samples, there is good agreement between the measured total porosities and the vesicularity measurements described earlier. We use the ratio of connected to total porosity (defined as connectivity, $\varphi_{con}/\varphi_{total}$, Colombier et al. 2017) as a measure of overall pore connectivity in Figure 3.11. Across all block types, the Episode IV samples have high pore connectivities at >0.8 . We highlight that the connectivity of the densest samples (homogeneous dense dacites and the rinds of breadcrusted blocks) is always high despite low total porosities. There is a general trend of increasing connectivity across overlapping total porosities from Episodes I/II to III and from III to IV. For individual blocks, there is a split between the number of blocks that show a marked decrease in connectivity between crust and interior and blocks that have similar or slightly higher connectivity from crust

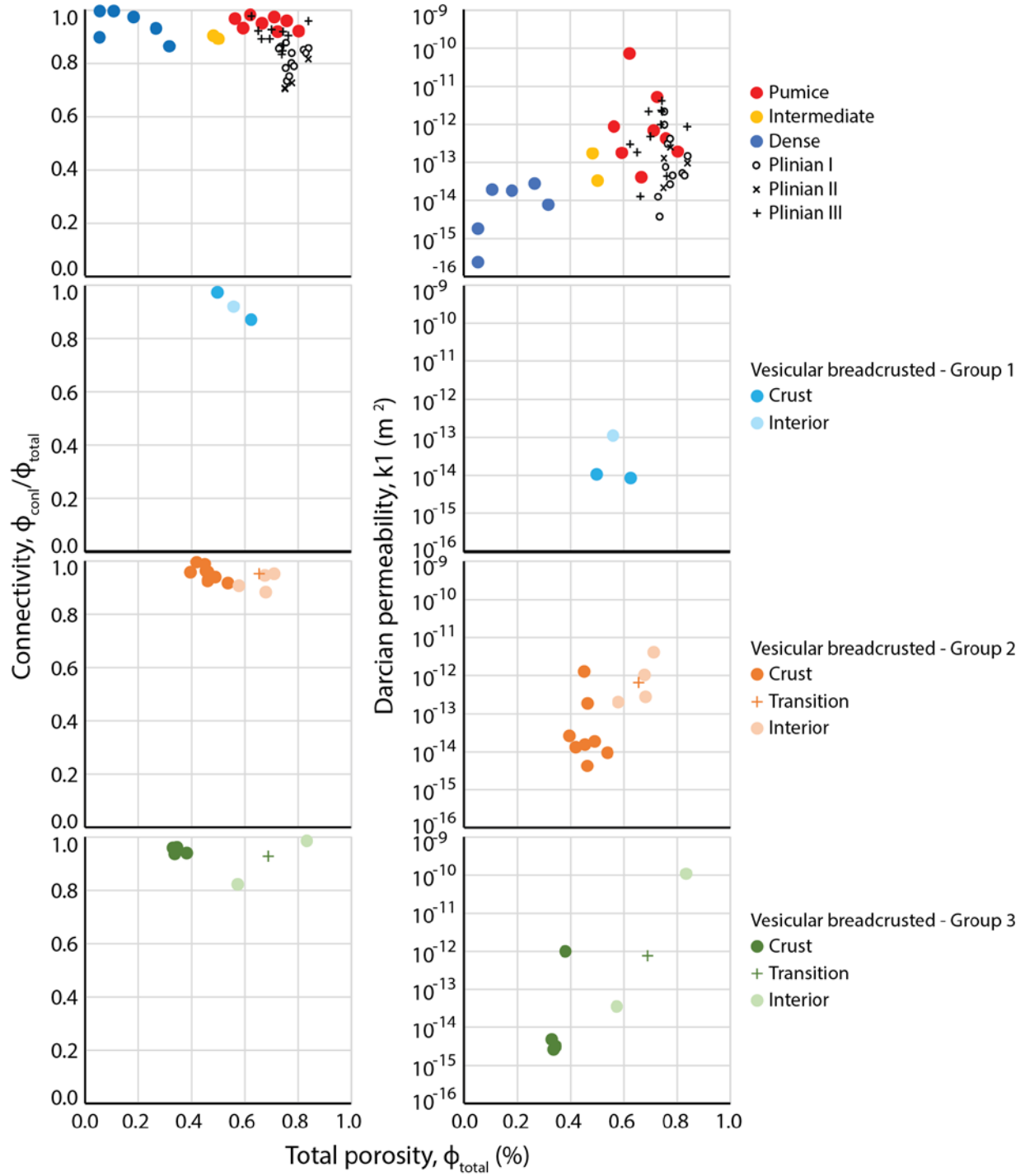


Figure 3.11 Connectivity (*left column*) and Darcian permeability (*right column*) versus total porosity for the homogeneous blocks, Plinian pumices, and the 3 groups of the vesicular breadcrusted blocks.

to interior (Figure B.4 in Appendix B). There is no correlation between clast type and the difference in crust and interior connectivity.

While significantly more scattered, permeability exhibits a direct correlation with porosity (i.e., permeability decreases with decreasing porosity), especially for the non-breadcrusted blocks. Microvesicular pumices from Episodes I, II, III, and IV each span multiple orders of magnitude in permeabilities and overlap significantly with each other in both porosity and permeability. Episode IV microvesicular pumices include the highest permeabilities. The dense dacites maintain measureable permeability down to <10% porosity. The re-vesiculated breadcrusted clasts show an increase in permeability from crust to interior. The crusts span a gap in connectivity, porosity, and permeability between the homogeneous microvesicular pumiceous and dense dacites.

3.5 Vesicularity interpretations

The contrasting block textures can be interpreted in terms of three distinct phases of vesiculation in portions of the melt: **A**) early (primary) degassing in the conduit, **B**) partial outgassing and loss of bubbles from the previous phase while still in the conduit/dome, and **C**) for the breadcrusted blocks only, renewed or ‘secondary’ vesiculation following fragmentation.

Microvesicular pumice preserves vesicles and textures reflecting **A** without significant influence of **B**. Dense dacites and the rinds on breadcrusted clasts preserve syn-fragmentation vesicularities formed during **A** and **B** whereas interiors of breadcrusted clasts have undergone **A**, **B**, and **C**. The complex pore textures of dense dacites and many breadcrust rinds indicate that their vesicles have matured well beyond **A**, i.e., the early stages of bubble nucleation and free-

growth, and undergone extensive outgassing prior to fragmentation. The range in vesicularity and a variety in vesicle textures within each block type imply contrasts in the duration and extent of **A**, **B**, and **C** (Figure 3.12).

Previous work on silicic domes has found similar textural heterogeneity to that described here (Fink and Manley 1987; Vogel et al. 1989; Fink et al. 1992). In particular, Fink et al. (1992) show that the extrusion of a texturally heterogeneous dome involves pre-eruption gas loss (outgassing) and syn-eruption degassing and vesiculation. Multiple micro-analytical studies on natural and experimental silicic samples have shown that both degassing and outgassing play important roles in whether an effusive eruption remains effusive or becomes explosive (Eichelberger et al. 1986; Fink et al. 1992; Rust and Cashman 2004; Gonnermann and Manga 2005; Adams et al. 2006a; Castro et al. 2012; Gaunt et al. 2014; Nguyen et al. 2014; Ashwell et al. 2015; Boudon et al. 2015; Farquharson et al. 2016; Kushnir et al. 2016). Multi-parametric observations of lava domes have also provided evidence of heterogeneity in textures, locations of

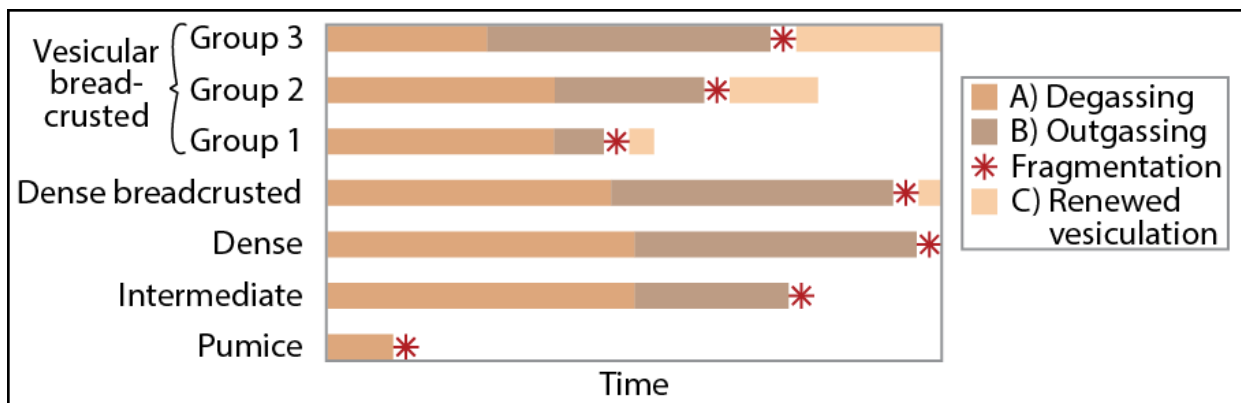


Figure 3.12 Schematic of relative durations of phases **A**) degassing, **B**) outgassing, and **C**) renewed vesiculation for the pumice, intermediate, dense, dense breadcrusted, and vesicular breadcrusted blocks. Banded blocks are not included here due to their added complexity.

fumarolic activity, and deformation (Lavallée et al. 2012; Bernstein et al. 2013; Salzer et al. 2017). Here, and in chapter 4, we invoke similar processes for the formation of the Episode IV blocks, most likely over a similar depth range.

3.5.1 Homogeneous clasts

We emphasize that the microvesicular pumice textures are significantly different from the re-vesiculated breadcrusted clasts' interiors, indicating that the pumices cannot simply be explained as clast interiors that no longer have crusts. Similarities in texture, bubble number density, and size distribution for Episodes III and IV microvesicular pumices suggest comparable vesiculation histories. Adams et al (2006b) showed that the Episode III pumices underwent high nucleation rates and coalescence that overlapped in time with bubble nucleation and growth. Our plot of V_G/V_L versus $N^m v$ (Figure 3.8) suggests that the Episode IV pumice underwent similar short histories of rapid bubble nucleation, free growth, and coalescence. Gonnermann and Houghton (2012) estimated decompression rates of $<10^7$ Pa/s through numerical modeling of magma ascent and vesiculation and replicating the bubble size distributions in the Episode III pumices. Again, the quantitative data imply the Episode IV microvesicular pumices underwent comparable decompression rates and rapid, late stage vesiculation. In sharp contrast, the data for the rhyolite dome would also support our qualitative data that the dense dacites underwent significant loss of bubbles reflecting a strong influence of phase B.

3.5.2 Heterogeneous clasts

The re-vesiculated breadcrusted clasts are much more diverse in vesicularity and complex in texture when compared to the homogeneous lithologies reflecting more complex vesiculation histories. The crusts preserve the pre-fragmentation state of all of the magma that formed the

breadcrusted clasts (i.e., magma that is now crusts, transitions, and interiors). The relatively low vesicularities and mature bubble textures within most crusts suggest extensive outgassing of the population of vesicles formed in phase **A**, in a manner resembling the magma which formed the dense dacites. The interiors reflect the influence of **C**, i.e., post-fragmentation re-vesiculation, presumably as clasts in the conduit as well as during and after transport. Their large, rounded bubbles are interpreted to be the result of a second vesiculation through diffusion, gas expansion, and bubble relaxation. The first process implies the presence of some amount of residual dissolved volatiles in the melt after **B** and indicates that outgassing-induced collapse of permeable pathways followed only partial and arrested degassing, probably due to stagnation of the magma at some depth.

Variability among crust and interior vesicularities and a progression in the diversity and complexity of micro-textures between the three re-vesiculated breadcrusted groups can be interpreted as the result of contrasting degrees of phases **A** and **B** prior to fragmentation (Figure 3.12). Group 3 blocks with the widest contrasts in vesicularity between crust and interior probably degassed to a lesser degree than those of group 1. In this scenario magma forming the group 1 blocks was the most uniformly degassed during primary vesiculation and yet underwent relatively little outgassing. The source magma for group 3 degassed the least and most significantly outgassed prior to fragmentation. Crusts on group 2 clasts lie between those of groups 1 and 3 (Figure 3.4b). The remains of connected pore pathways are present in the grayscale images of group 2 crusts, however, their termination into clusters of irregularly/complex-shaped pores (Figure 3.9f) suggests significant collapse of these pathways.

This suggests that similar clusters located near the extra-large pores in the crust in group 3 are also relict collapsed outgassing pathways.

The rare dense breadcrusted blocks that show a slight vesicularity difference between crust and interior indicate that this source magma extensively but not completely underwent phase **A** and then was extensively modified by **B** in order to retain a small amount of volatiles that allowed limited expansion of the interior.

In the banded blocks, the light-colored, vesicle-rich bands represent magma that had only partially degassed at the depth of fragmentation. Dense bands were sourced from more mature magma that had both completely or near-completely degassed and partially outgassed. The vesicular and dense banded blocks reflect only slight contrasts in degassing/outgassing history between adjacent bands, as is reflected in minor differences in vesicle texture and color. The vesicular banded clasts experienced phase **A** the least and the dense banded blocks most completely underwent **A** and **B**. The mixed banded blocks contain more marked contrasts in degrees of **A** and **B** between adjacent bands, as represented by the sharp contrasts in band color. For the banded breadcrusted blocks, darker more outgassed bands pass outward into a crust of similar appearance and density whereas the light re-vesiculated bands pass outward into dark and dense crust. The light bands were thus only partially degassed prior to undergoing **B**.

3.6 Permeability and connected porosity interpretations

The porosity data indicate that vesicles or pores in most of the Episode IV clasts (excluding breadcrusted blocks' interiors) are more connected than those in the Plinian pumices (Figure 3.11). Increasing connectivity in pumices from Episodes I/II to III and III to IV coincides with

sharp declines in eruption intensity after Episode II and after Episode III (Adams et al. 2006b; Hildreth and Fierstein 2012).

During outgassing of the magma that formed the crusts and dense dacites, most of the originally isolated vesicles became connected and remained connected. We think that the high level of connectivity in the crusts and dense dacites is linked to the fact that the low vesicularity and complex textures reflect the influence of outgassing rather than an early end to bubble nucleation.

The wide range of permeabilities in the Novarupta samples reflects portions of the magma in the shallow conduit reaching different stages within phases **A**, **B** and **C**. The microvesicular pumices have similar permeabilities (at roughly equivalent porosities) to the Episodes II and III Plinian pumices (Figure 3.11). Nguyen et al. (2014) concluded that pre-eruptive permeable outgassing was insignificant during Episodes I–III, and we suggest that this is also true for the Episode IV pumices. Data from the dense dacites show that significant permeability was achieved and maintained during **B** even at porosities $\ll 30\%$. At any rate, the dense dacites represent the latter stages of **B** in which connectivity remained high and permeable pathways still existed, but their source magma had also lost significant porosity and undergone collapse and compaction. The wide range of porosities and permeabilities among the crusts on re-vesiculated blocks confirms that they represent a variation in the extent of **B** ranging from recently developed permeable pathways (groups 1 and 2) to the initiation of pathway collapse and the loss of porosity during permeable outgassing (groups 2 and 3). We discuss later the possibility that the extent is a function of both the depth at which the outgassing occurred and the residence time of the melt at this depth. The transition and interior samples of the re-vesiculated

clasts show an increase in porosity and permeability *after B*. This process involving outgassing prior to renewed degassing (i.e., phase **C**) has not been described in detail for breadcrusted clasts in prior studies.

3.7 Discussion

3.7.1 Controls on degassing and outgassing of Episode IV magma

The variable degrees of degassing and outgassing between and within the block types are related to contrasts in the depth and duration of residence for different magma in the shallow conduit. Solubility limits, and thus depth, determine the extent of degassing/vesiculation phase **A**, i.e., it fixes the residual volatile content of the melt which equates to volatile solubility at the depth where degassing occurs. Duration in the shallow conduit is a strong control on the extent of **B**, i.e., outgassing, loss of porosity, and bubble collapse, as any partially degassed magma that resides at some depth will undergo first equilibrium degassing and then outgassing if it is retained at that depth for sufficient time. However, the final micro-textures at the time of fragmentation are also influenced by the initial porosity reached during **A**, as is elaborated below.

3.7.1.1 Microvesicular pumice

The microvesicular pumice blocks are the only component of the Episode IV ejecta to show a simple history of bubble nucleation and growth that was not overprinted by development and collapse of permeable vesicle pathways. Qualitative and quantitative bubble data suggest that conduit history was very similar in terms of rate and duration of bubble nucleation to microvesicular pumice from the preceding Episode III. Gonnermann and Houghton (2012)

modeled the development of the majority of the Episode III bubbles as occurring over a very short time interval (approximately 0.1 s) just prior to fragmentation. We suggest that the source magma for the Episode IV microvesicular pumices underwent a similar sudden and rapid decompression with vesiculation and fragmentation occurring over a short depth range. These processes were probably what drove fragmentation during the Episode IV explosions? We leave further discussion of this hypothesis until we arrive at some constraints on depths of residence and fragmentation in Chapter 4.

3.7.1.2 Dense dacite

The completely or largely outgassed homogeneous blocks with porosities of <20% stagnated at varying but always very shallow depths. Upon stagnation, their initial porosities would reflect their storage depths prior to outgassing and prior to fragmentation: shallower magma would have higher maximum porosities than deeper magma. We hypothesize that the dense dacites stagnated at the shallowest depths and represent the most degassed and outgassed melt. We also infer the duration of stagnation for the dense dacites must have been long relative to the other homogeneous clasts in order to allow for the loss of most porosity and the collapse of permeable pathways during **B** (Figure 3.12).

3.7.1.3 Breadcrusted blocks

For the breadcrusted blocks, the availability of residual dissolved volatiles for re-vesiculation of their interiors suggests that they stagnated (and fragmented) deeper than the homogeneous blocks. Variations in the extent of re-vesiculation and intensity of breadcrusting indicate that the magma for the breadcrusted blocks probably stagnated at a range of depths and hence volatile solubilities. The more expanded interiors represent where the magma stagnated at the greatest

depths and vice versa. Given that Isgett et al. (2017) implied that explosions tapped depths of <600 m, we are considering much shallower depths overall than those inferred for Vulcanian activity at Soufrière Hills (Druitt et al. 2002; Melnik and Sparks 2002a; Clarke et al. 2007; Burgisser et al. 2011). The highest vesicularity crusts formed with the least storage time in the conduit. Conversely, the lowest vesicularity crusts could have come from magma that started with low vesicularities and/or outgassed for longer durations.

The increase in porosity from crust to interior in the few dense breadcrusted blocks suggests that this magma would have stagnated at depths slightly deeper than the homogeneous dense dacites such that some retained volatiles drove only limited re-vesiculation. They also would have undergone prolonged outgassing in order to reach their very low vesicularity crusts.

3.7.1.4 Banded

The depths and durations of stagnation for the breadcrusted banded blocks are much more complex and this complexity contributes greatly to our understanding of processes in the shallow conduit. See below for further discussion of this topic.

3.7.2 Development of breadcrust textures

Our study casts new insights into the processes effecting breadcrusted clasts. In most publications, it is assumed that the exteriors of breadcrusted clasts preserve a vesiculation state immediately prior to fragmentation. After fragmentation, the thermally insulated clast interiors vesiculate and expand, during and perhaps after transport, and the expansion is accommodated by cracking the exterior rinds. The Episode IV clasts show clear textural evidence of a more complicated vesiculation history, preserving significant evidence for pre-fragmentation outgassing in addition to degassing. Outgassing may have played an important role in the

formation of re-vesiculated breadcrusted clasts in many other Vulcanian eruptions, but it has not been addressed in the literature to-date. The most striking feature of the 1912 breadcrusted clasts is that the rinds preserve collapsed-bubble textures indicating that they were at least partially outgassed before fragmentation. A logical conclusion is that the magma that is now preserved as the block interiors underwent a similar degree of outgassing, but their textures are overprinted by post-fragmentation vesiculation. This is the first documentation that breadcrusted blocks underwent significant outgassing and loss of porosity prior to fragmentation, and, as explained above, its extent has implications for the relative residence time of different portions of the magma within the shallow conduit.

3.7.3 Juxtaposition of contrasting magma in flow-banded blocks

The existence of blocks containing bands of contrasting vesicularity means that either (1) these textures developed *in place* perhaps due to variable shear-stresses on very short length-scales in the melt which resulted in the diverse vesiculation states and textures (Polacci et al. 2001; Gonnermann and Manga 2005) or (2) *dynamically* as rising portions of magma with different textures and presumably ascent histories mingled just prior to eruption (e.g., Lautze and Houghton 2005; Wright et al. 2011). Contrasting degrees of post-fragmentation expansion in adjacent light (vesicular) and dark (denser) bands in single banded breadcrusted blocks suggests that the relevant magmas had equilibrated at different levels prior to mingling and retained different concentrations of residual dissolved volatiles after mingling (i.e., were still in disequilibrium at the time of fragmentation), which favors (2). Mingling thus juxtaposed domains of magma with different vesiculation histories on time scales that precluded their diffusive re-equilibration after the mingling occurred. Koyaguchi (1987) simulated conduit

mingling in an elastic conduit in the laboratory, developing textures similar to the 1912 mingled clasts. This experiment showed that effective mingling can occur between fluids of different viscosities, at low ascent velocities, and where the volume of ascending magma is relatively small.

Most (83%) of the banded clasts are also breadcrusted containing bands exhibiting an inward increase in vesicularity (relative to the crust) ranging from 0–60%. Like the dense dacite blocks, the darker bands that show no internal re-vesiculation are inferred to have equilibrated at shallower depths than the re-vesiculated bands. This means that the source of the lighter-colored, re-vesiculated bands had to rise to come in contact with the source of the dense bands. Mingling of these disparate magmas was followed by fragmentation without diffusive re-equilibration of the volatiles between the magmas (which would have required days to hundreds of days, Table B.1 in Appendix B). The banded blocks that contain the least textural contrasts between bands (i.e., dense/dense, pumiceous/pumiceous) are instances where mingling occurred between domains of magma with only slightly different degassing/outgassing histories. Conversely, blocks with major textural contrasts (pumiceous/dense) suggest significantly different histories for different bands.

The banded blocks thus provide evidence that texturally distinct magmas interacted over only very short time scales prior to disruption. The processes, length scales, and locations of mingling (i.e., how and where disparate magmas became juxtaposed) will be examined in greater detail in Chapter 4.

3.8 Conclusions

Through the measurement of vesicularity, porosity, and permeability and the qualitative and limited quantitative analysis of vesicle textures, we have shown that the Episode IV blocks at Novarupta represent chemically homogeneous magma which was disrupted in various stages of degassing and outgassing. This heterogeneity reflects differing histories of residence and stagnation in the shallow conduit prior to Vulcanian eruptions. The existence of a complex conduit fill would require very dynamic, disequilibrium conditions. Depths for these processes are discussed in Chapter 4 and will be combined with textural data from this chapter to propose an arrangement of texturally disparate magma domains in the shallow conduit during Episode IV.

CHAPTER 4

Constraints from residual water contents on eruptive processes during the 1912 Vulcanian explosions at Novarupta, Alaska

In preparation for submission to *Bulletin of Volcanology* as:

Isgett, S.J., Houghton, B.F., Burgisser, A., Arbaret, L., Gonnermann, H.M. Constraints from residual water contents on eruptive processes during the 1912 Vulcanian explosions at Novarupta, Alaska

Abstract

This chapter of the thesis uses residual water contents of matrix glass in the ejecta from a series of Vulcanian explosions during Episode IV of the 1912 eruption of Novarupta, Alaska, to constrain depth (and timing) of syn-eruptive processes in the shallowest conduit. It suggests a scenario in which texturally heterogeneous magma was fragmented over a relatively narrow range of depths (<400 m) and that volatiles in much of the ejected magma had only partially equilibrated to varying extents with the final depth(s) at which it was fragmented. In the absence of evidence for an external pressure release accompanying collapse of parts of an Episode IV edifice, we suggest that the explosions were triggered by vesiculation of actively degassing magma which formed the dominant pumiceous component of the Episode IV ejecta. Hydrogen isotopic composition of glass from a range of ejecta textures implies limited secondary hydration of the pumice, leaving possibilities for future studies of rapid rehydration of young (~100 years) volcanic glass.

4.1 Introduction

This chapter builds on Chapters 2 (Isgett et al. 2017) and 3 by examining additional aspects of the Vulcanian Episode IV during the 1912 eruption of Novarupta, Alaska. New data sets, namely the residual water content and hydrogen isotopic composition of glass in the juvenile Episode IV ejecta, are investigated in order to constrain depths of the shallowest syn-eruptive processes.

4.1.1 Vulcanian explosions

Transient and episodic in nature, Vulcanian eruptions range from weak explosions that form dilute, short-lived (~minutes) convective ash plumes with accompanying small ballistic blocks to larger explosions that produce denser, higher, and more persistent (~hours) plumes, blocks, pyroclastic density currents, and lahars (e.g., Druitt et al. 2002; Schipper et al. 2013; Cassidy et al. 2015). Their ejecta are typified by a diverse range of juvenile and wall rock pyroclasts including dense to highly vesicular juvenile clasts, brecciated and massive wall rock lithics, and clasts showing a range of breadcrust textures. These styles of eruption are inherently unpredictable, as they are associated with few measurable precursors. Several well-documented examples of relatively large Vulcanian explosions were triggered by the sudden decompression of a plugged conduit, often in response to a partial or complete dome collapse, and involved the downward propagation of a fragmentation wave that evacuates the conduit in a progressive, orderly fashion (Clarke 2013). In contrast, the sudden onset of weaker Vulcanian explosive activity is often observed without such an external trigger, such as at Sakurajima, Japan; Santiaguito, Guatemala; Colima, Mexico; Reventador, Ecuador (Global Volcanism Program 2005; Sahetapy-Engel et al. 2008; Yokoo et al. 2009; Cassidy et al. 2015). These explosions

sometimes do not disrupt material across the entire width of the conduit and instead are restricted to multiple discrete ‘vents’ within a dome or crater (Bluth and Rose 2004; Lavallée et al. 2012; Cassidy et al. 2015).

4.1.2 Theoretical models of the Vulcanian conduit

A well-established model of the pre-fragmentation structure of the magma-filled conduit was developed for the large 1997 Vulcanian explosions at Soufrière Hills volcano, Montserrat (Druitt et al. 2002; Melnik and Sparks 2002a, b). The slow ascent of magma results in a horizontally zoned column with a dense, capping dome/plug (Clarke et al. 2015). Magma filling the lower conduit is less degassed and is inferred to display an orderly change in densities and textures with depth (Druitt et al. 2002; Melnik and Sparks 2002a, b; Clarke et al. 2007; Wright et al. 2007; Burgisser et al. 2010; Giachetti et al. 2010). Either pressure builds within the shallow regions until it overcomes the overlying pressure of the dome or some portion of the dome fails initiating decompression-induced fragmentation (Sparks 1997; Melnik and Sparks 1999; Clarke 2013).

Textural heterogeneity of silicic magma in shallow conduits had been proposed for lava domes prior to detailed studies of Vulcanian products (e.g., Fink and Manley 1987; Vogel et al. 1989; Fink et al. 1992), and observations of texturally diverse pyroclasts of Vulcanian eruptions (Yamagishi and Feebrey 1994; Adams et al. 2006; Clarke et al. 2007; Wright et al. 2007; Burgisser et al. 2010; Giachetti et al. 2010; Isgett et al. 2017) show a predictably similar textural range to dome samples. This textural heterogeneity has been used to propose models of the structure of the magma column prior to Vulcanian explosions that are more complex than that used in models for Soufrière Hills by e.g., Druitt et al. (2002). These include pulses of gas-rich

magma rising rapidly through other slowly ascending, gas-poor magma (Cassidy et al. 2015) and production of banded and brecciated pyroclasts along conduit margins (Kennedy et al. 2005). Burgisser et al. (2010, 2011) suggest that the magma structure is likely both vertically and horizontally more complex than a simple horizontal layering. However, for modeling purposes, they also assigned depths to horizontal zones of magma including a heterogeneous zone at a specific depth. Our previous work on the Vulcanian deposit at Novarupta, Alaska, has started to provide a qualitative picture of the structure of the magma column by providing evidence for the lateral juxtaposition of texturally contrasting domains of magma within the very shallow parts of the 1912 conduit (Adams et al. 2006; Isgett et al. 2017). This scenario, however, currently lacks quantitative estimates of pre-eruptive pressures and fragmentation depths, which are the topic of this chapter.

4.1.3 Glass H₂O measurement and pressure/depth estimates

The measurement of residual water trapped within glass (matrix glass or melt inclusions) can be used to determine quench pressures according to solubility laws (Tamic et al. 2001; Newman and Lowenstern 2002; Liu et al. 2005). These pressures can then be converted to fragmentation (using matrix glass data) or storage (melt inclusion) depths. For Vulcanian eruptions, estimates of fragmentation depths and the locations of the magma that formed the diverse pyroclast textures are crucial for understanding the rheology of the pre-explosion magma. Understanding the state of the magma in the shallow conduit and/or dome may provide insight to why eruptions pass from effusive to explosive styles and vice versa.

Two processes secondary to the degassing of volatiles influence the measured amount of water dissolved in the glass: secondary hydration by meteoric water at low or ambient

temperatures (DeGroat-Nelson et al. 2001; Giachetti and Gonnermann 2013; Nolan and Bindeman 2013; Giachetti et al. 2015; Dingwell et al. 2016), and/or syn-eruptive resorption of magmatic water vapor due to the increase in the equilibrium solubility of water as a consequence of temperature and pressure changes during quench (Yoshimura and Nakamura 2008; Watkins et al. 2012; McIntosh et al. 2014). Studies have shown that isotopic variations of magmatic versus meteoric water impart distinctive signatures on the measured values for (e.g.,) hydrogen and oxygen isotopes which can thus be used to determine if pyroclasts have undergone rehydration by meteoric water (DeGroat-Nelson et al. 2001; Nolan and Bindeman 2013; Drignon et al. 2016; Seligman et al. 2016). McIntosh et al. (2014) showed that systematic changes in molecular water ($\text{H}_2\text{O}_{\text{mol}}$) and hydroxyl (OH) distributions relative to bubble rims can record processes of resorption and diffusive bubble growth, respectively. However, if a glass has undergone rehydration by meteoric water then determining if resorption has also occurred becomes much more difficult due to the fact that both forms of rehydration involve $\text{H}_2\text{O}_{\text{mol}}$. Given the potential for changes due to these processes, volcanic glasses must be tested for rehydration and/or resorption in order to insure against inaccurate depth estimates due to erroneously high water contents.

The conversion from H_2O content to pressure is based on the assumption of equilibrium degassing such that the volatile solubility pressure within the melt is in equilibrium with the ambient (magmatic) pressure. In disequilibrium degassing, the rate of volatile diffusion is slower than the decompression rate and the volatiles become supersaturated within the melt (Hurwitz and Navon 1994; Proussevitch and Sahagian 1996; Gardner et al. 1999; Mangan and Sisson 2000; Mangan et al. 2004; Mourtada-Bonnefoi and Laporte 2004; Burgisser and Gardner

2005; Gonnermann and Manga 2005a). If the system is in disequilibrium, then pressure and depth estimates based on water content would be over-estimates.

Disequilibrium degassing is inferred to play a role in models of Vulcanian explosions that either replicate sudden decompression of the top of a magma column (Melnik and Sparks 2002b; Mason et al. 2006; La Spina et al. 2017) — such as a dome collapse, sector collapse, or the development of an excess pressure at the top of the conduit that exceeds the fragmentation threshold. In these models, disequilibrium degassing occurs because a downward propagating rarefaction wave causes a decrease of pressure that is too fast to be matched by diffusion. The fragmentation threshold may be met if gas/bubble expansion cannot be accommodated due to viscous resistance. Many Vulcanian eruptions are understood in the context of a sudden external trigger for decompression (i.e., a dome collapse); however, the potential for disequilibrium degassing in the *initiation* of Vulcanian explosions without an external trigger is not clear.

4.1.4 Novarupta Episode IV

Episode IV of the 1912 eruption of Novarupta, Alaska involved a series of Vulcanian explosions that completely destroyed a newly formed dacite plug/dome. The deposit consists of a roughly 4 x 2.5 km elliptical block apron that is uniquely and exceptionally well preserved, and this has allowed for detailed studies into the eruption and shallow conduit dynamics throughout Episode IV (Adams et al. 2006; Isgett et al. 2017). The blocks are dacite and exhibit a wide range of pumiceous, dense, banded, breadcrusted, and brecciated textures (Figure 4.1). The banded blocks exhibit alternating bands of the juvenile pumiceous and dense dacite. Breadcrusting is found on all block types, but it is most prevalent on the banded and vesicular breadcrusted clasts. In Chapter 3, we showed, through textural differences, that the coarsely vesicular breadcrusted

clasts are genetically different from the microvesicular pumices in terms of their resident histories in the shallow conduit. Each of the block types came from a different source within the shallow conduit, as is evident from their bubble textures (Chapter 3). It has thus been proposed that the shallow conduit consisted of complex juxtaposition of magma domains with contrasting textures, but confirmation of their relative depths can only be established through the measurement of the volatiles trapped within the quenched glass.

Episode IV occurred after 60 hours of powerful Plinian eruption, divided into three episodes, that produced voluminous rhyolitic and dacitic ignimbrites and widespread, predominantly dacite Plinian fall beds (Hildreth 1983, 1987; Fierstein and Hildreth 1992). The eruption concluded with passive extrusion of a rhyolite dome in Episode V. Episode IV thus provides insight to the ending of Plinian eruptions such as those observed at Mount St. Helens, USA, during 1980–1982 (Christiansen and Peterson 1981), Chaitén, Chile, 2008 (Castro et al. 2012), and Cordón Caulle, Chile, 2011–2012 (Schipper et al. 2013).

This manuscript combines evidence from block textures, vesicularities, 2D bubble micro-textures (presented in Chapters 2 and 3) with measured glass water content to infer the magma column ‘stratigraphy’ and eruptive conditions throughout Episode IV at Novarupta. The source mechanism for the initiation of explosions throughout Episode IV is also uncertain as there were no witnesses during the time of the eruption. However, there are two lines of field evidence against an external trigger such as the sudden failure of a dome: a) there are no deposits from a dome collapse, and b) the sectorial confinement of block lobes and small volumes attributed to individual explosions (Isgett et al. 2017) precludes the presence of a single conduit-wide,

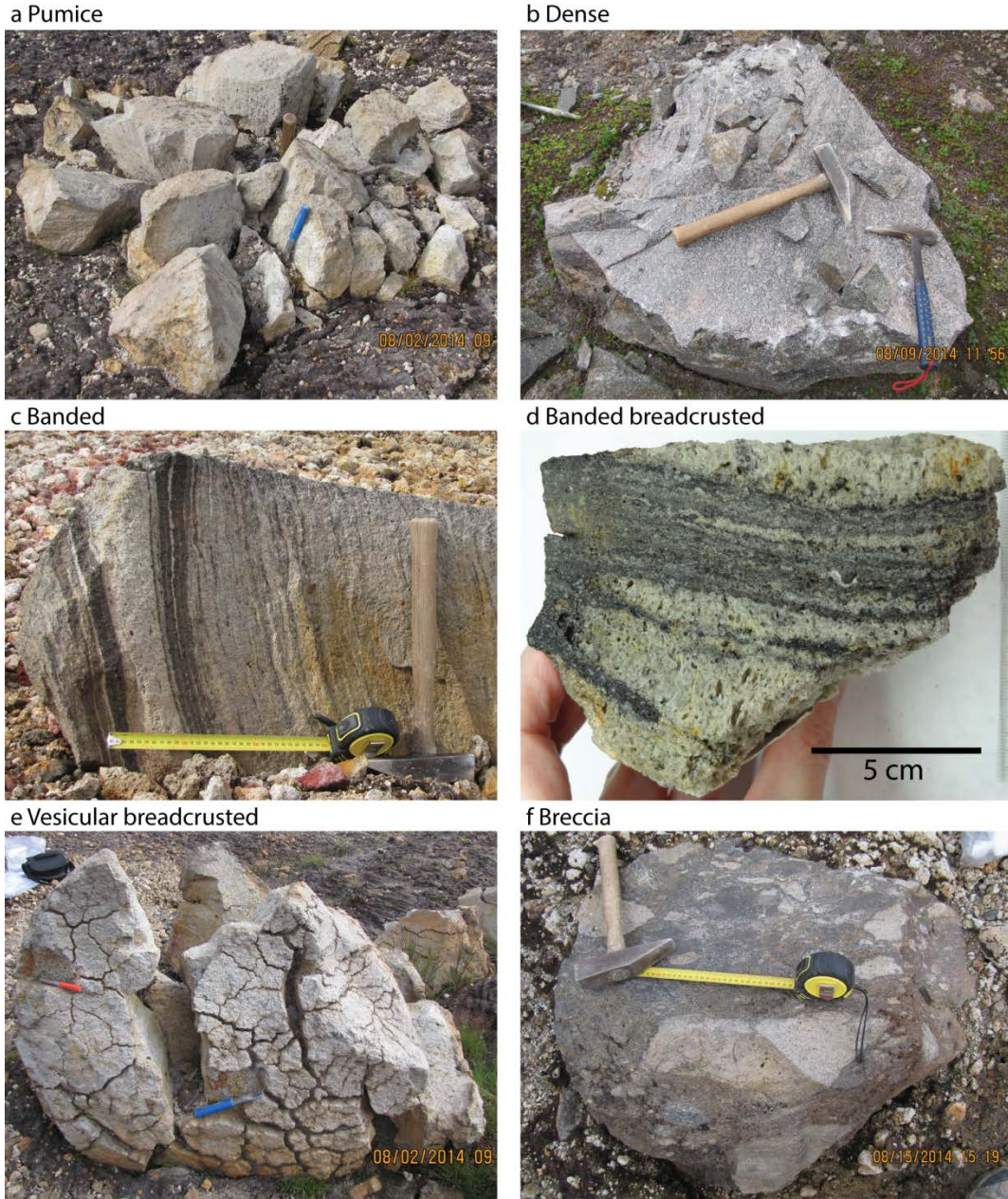


Figure 4.1 Examples of the block textures within the Episode IV deposit. **a** Microvesicular pumiceous dacite, broken on impact with the ground, block N006. **b** Dense dacite, block N158. **c** Banded block exhibiting bands of dense (dark) and pumiceous (light) dacite, block N222. **d** Close up of the banded textures adjacent to a crust (left side of sample), from block B349. Note how the overall dense crust extends into bands of differing vesicularities. **e** Vesicular breadcrusted clast, block N005. **f** Moderately welded breccia, block N299.

downward propagating fragmentation event. This chapter will thus also attempt to establish a mechanism for the repeated initiation of fragmentation throughout Episode IV.

4.2 Methodology

4.2.1 Glass H₂O measurement

Measuring volatiles in silicate glasses can be achieved using a range of analytical and experimental methods (Ihinger et al. 1994). The three main classes of volatile analysis are bulk extraction, energetic particle bombardment, and vibrational spectroscopy. Each class has a range of techniques with varying accuracies, advantages, and disadvantages (see Ihinger et al. 1994; Shea et al. 2014). Due to anticipated low water contents, we employed two bulk extraction and one vibrational spectroscopy methods for measuring residual glass H₂O in our blocks.

As the name implies, bulk extraction involves the measurement of the total volatile content within a sample. Known as ‘loss on ignition’, this method involves subjecting the sample to high temperatures in order to remove physically all volatile elements and analyze them and/or the refractory residue (Ihinger et al. 1994).

METHOD 1: We employed a bulk measurement apparatus that utilizes a gas chromatograph called the FLASH 2000 CHNS/O Analyzer (ISTO, Université d’Orléans). Cores 1 cm in diameter were drilled from samples, and a portion was crushed with an agate mortar to obtain powder <30 μm. The remaining core was used to make thick sections. The powder was enclosed in a tin capsule and analyzed by the Flash 2000: samples were heated to ~1800°C in the presence of O₂, and the released H was transported in H₂O form to a gas chromatograph by helium flux and analyzed by thermal conductivity. The certified standard SOIL was used for

calibration, and we ensured that each Novarupta sample measurement lay between the highest and lowest standard values (yields from variable weights of standard introduced to the FLASH; recorded at regular intervals throughout a measurement day). Each sample was analyzed three times to yield a 1σ error relative to their average. The thick sections were imaged with a petrographic microscope at 5x or 10x magnification (depending on the visibility of crystals). The crystals in the image were drawn in gray and the remainder of the sample was turned white within Adobe Photoshop. ImageJ was then used to calculate the proportion of oxides (x_{ox}) and the proportion of all other crystals (x_{cr}) in the 2D images. Measurements of bulk vesicularity, conducted via density analysis using the method of Houghton and Wilson (1989), were used to estimate the proportion of bubbles (x_{bu}). Finally, the proportion of glass (x_{gl}) was estimated as

$$x_{gl} = 1 - x_{bu} - x_{cr} - x_{ox}. \quad (4.1)$$

Total H content was converted to H₂O using H and O molar masses. Bulk H₂O ($X_{H_2O}^{bu}$) was converted to glass wt% H₂O ($X_{H_2O}^{gl}$) by correcting for phenocrysts and oxides using the equation (modified after Drignon et al. 2016):

$$X_{H_2O}^{gl} = \frac{X_{H_2O}^{bu} (x_{gl}\rho_{gl} + x_{cr}\rho_{cr} + x_{ox}\rho_{ox})}{x_{gl}\rho_{gl}} \quad (4.2)$$

where ρ is density ($\rho_{gl} = 2350$, $\rho_{cr} = 2650$, and $\rho_{ox} = 4720$ kg/m³). Water in amphibole was neglected due to the very low abundance of hornblende (Hildreth 1983; Hildreth and Fierstein 2012). The proportion of microlites was not used in equation 2 due to the minimal volume fraction they represent within the total crystal content in the Episode IV samples (Figure 4.2).

METHOD 2: The Thermal Conversion Elemental Analyzer (TCEA) continuous flow and sampling system at the University of Oregon stable isotope laboratory was also used for bulk extraction of both glass H₂O content and δD (where D represents the ratio of the hydrogen isotopes deuterium and protium: D/H) following the methodology of Martin et al. (2017). Six representative samples from each textural group (one dense, two pumice, two crusts, and one interior) were chosen for this method as a test for secondary hydration by meteoric water. Prior to analysis, samples were lightly crushed, rinsed a minimum of three times with 18 M Ω H₂O, and then dried in an oven at 110°C. Individual glass shards were picked under microscope and then crushed to 50–250 μm (the range of particle sizes determined by Martin et al. 2017 to yield the best reproducibility of water content by the TCEA). The densest samples had oxides that were too small to be separated from the matrix, and equation (2) was modified for only glass and



Figure 4.2 A falsely colored scanning electron microscope image at 1000x magnification of a crust sample from block N004. Bubbles are black, glass is white, and microlites are red. Note the small proportion of microlites within the image and the heterogeneous distribution of mostly elongate vesicles. The vesicle texture is indicative of outgassing and bubble collapse.

oxides in order to correct the bulk water measurement for an average oxide proportion of 0.01 (determined from thick sections as described above). Powdered samples were dried in vacuum at 130°C for two hours, and then 1–10 mg (depending on water content from Flash and Raman measurements) of sample was loaded into silver capsules and dried in the vacuum oven for an additional four days. The samples were then loaded into the TCEA which introduces the samples to a high temperature furnace and analyses the released gases by a gas chromatograph and a Thermo Scientific MAT253 mass spectrometer (see Martin et al. 2017 for further details). For maximum reproducibility and precision, the peak intensity measured on the mass 2 of the MAT253 mass spectrometer was >1000 mV (Martin et al. 2017). Standardization was conducted with USGS57 and USGS58 mica for solid standards, and a calibration using the offsets between measured and nominal δD values (with an R^2 value of 0.9978) was employed to correct the raw δD measured for each sample.

METHOD 3: The absorption and scattering of light due to the vibrational properties of volatiles' species in glass can be used to quantify their content. MicroRaman spectroscopy was attempted to conduct direct analyses of glass H₂O due to its very high spatial resolution (~1–2 μm^2) and good precision (Le Losq et al. 2012; Shea et al. 2014). Glass spectra were collected with a Witec® Alpha 300R confocal Raman microscope (University of Hawai'i at Mānoa) equipped with a green laser (532 nm wavelength) with a power of 5 mW. Four spot measurements, with total acquisition times of 60 s, were collected within each region of a thin section, and three to four regions were analyzed per thin section.

The regions of interest on the glass spectra are 1) the peaks between ~200–1,200-cm⁻¹ resulting from the vibrations produced by the aluminosilicate framework, the “ASF” band, and

2) a broad peak around 3,100–3,800-cm⁻¹ attributed to the bending and stretching of H₂O and OH molecules, the “H₂O” band (Thomas 2000; Behrens et al. 2006; Di Muro et al. 2006).

Calculating water content from the spectra was conducted following the methods of Le Losq et al. (2012) and Shea et al. (2012). The areas (A) beneath the ASF and H₂O bands were calculated after establishing a baseline and removing the influence of the epoxy mounting medium from the raw spectrum. A raw water content is estimated by calculating their ratio (A_{H₂O}/A_{ASF}). This ratio is then corrected by the slope of the best fit line to known H₂O (determined by FTIR) versus A_{H₂O}/A_{ASF} collected for a series of standards that span the range of compositions (basalt to rhyolite, Figure C.1 in Appendix C).

Water measurements were converted to quench pressures using the empirical solubility model of Liu et al. (2005) developed for rhyolitic melts at low pressures. Although dacite in bulk composition, the matrix glass in the Episode IV blocks is rhyolitic, allowing for the use of such a model. Depth was estimated from the quench pressures assuming magmastatic pressure and a density of 1,800 kg/m³.

4.3 Results

The total range of measured water values from all three methods is 0.11 to 2.89 wt% (Table 4.1). There are nonsystematic differences in the water values between the different methods for any single sample ranging from no overlap in water values (even between the error bars; numbers 2, 4, 5, 6, 7, 8, and 10 in Figure 4.3) to the estimates being statistically indistinguishable for each method (numbers 1, 3, and 9 in Figure 4.3). The six samples analyzed by the TCEA form a group with a narrow range of δD with the exception of one pumice with a lower δD and higher

Table 4.1 Summary of textural features (used in equation 2); Flash bulk and corrected, Raman, and TCEA H₂O contents in interstitial glass; TCEA hydrogen isotope estimate; pressure; and depth for each of the analyzed samples. Vesicularity, oxides, phenocrysts, and melt are proportions that sum to 1. Pressure and depth were not calculated for 1) the transition and interior samples as their original H₂O contents and vesicularities have been over-printed by post-fragmentation vesiculation and 2) the two pumice with H₂O > 1 wt% due to the influence of rehydration. Final H₂O (used for the pressure estimate) was calculated using the average of the multiple estimates if within error, otherwise the bulk H₂O estimate was used. Pressure was calculated using the solubility model of Liu et al. (2005) at 850 °C and P_{CO2} = 0.

Sample	x_{bu}	x_{ox}	x_{cr}	x_{gl}	Flash bulk H ₂ O error	Flash glass H ₂ O error	Raman H ₂ O error	TCEA H ₂ O error	TCEA δD error	Final H ₂ O error	Pressure standard deviation	Depth standard deviation								
					(wt%)	(wt%)	(wt%)	(wt%)	(‰)	(wt%)	(Mpa)	(m)								
<u>Dense</u>																				
B126	0.07	0.017	0.46	0.45	0.26	0.03	0.47	0.01		0.53	0.07	2.51	0.61	168	41					
N158	0.10	0.015	0.31	0.57	0.09	0.01	0.39	0.03	0.11	0.01	-107.8	-5	0.13	0.01	0.17	0.03	11	2		
B125	0.17	0.012	0.27	0.55	0.23	0.01	0.37	0.08		0.37	0.08	1.30	0.52	87	35					
N159	0.04						0.16	0.03		0.16	0.03	0.26	0.09	17	6					
<u>Pumice</u>																				
N366	0.70	0.008	0.13	0.16	0.34	0.03	0.68	0.2		0.68	0.2	4.04	1.61	272	107					
N006	0.61	0.003	0.09	0.29	0.26	0.01	0.35	0.07	0.35	0.02	0.31	0.03	-109.5	-5	0.34	0.03	1.06	0.15	70	10
N427	0.66	0.005	0.09	0.25	0.77	0.02	1.11	0.2		1.11	0.2									
N430	0.66	0.048	0.14	0.15	1.09	0.07	2.89	0.6		1.30	0.1	-131.5	-7	1.30	0.1					
N341	0.66						0.36	0.05		0.36	0.05	1.21	0.32	81	21					
<u>Intermediate</u>																				
N368	0.27	0.013	0.41	0.31	0.19	0.01	0.48	0.1		0.48	0.10	1.45	0.57	83	18					
N019	0.28						0.25	0.06		0.25	0.06	0.60	0.29	40	20					
<u>Crust</u>																				
N004	0.47	0.004	0.20	0.33	0.37	0.01	0.63	0.1	0.33	0.08		0.63	0.1	3.48	1.28	233	85			
N005	0.35	0.007	0.24	0.41	0.44	0.07	0.75	0.2	0.27	0.04		0.75	0.2	4.76	2.14	319	143			
N011	0.38	0.017	0.38	0.23	0.30	0.02	0.91	0.2	0.39	0.09	0.26	0.03	-109.5	-5	0.33	0.05	1.01	0.26	67	18
N014	0.28	0.013	0.30	0.41	0.41	0.01	0.77	0.2	0.38	0.02		0.77	0.2	5.01	1.75	337	117			
N015	0.46	0.006	0.21	0.33	0.29	0.02	0.52	0.1		0.52	0.1	2.45	0.94	165	63					
N156	0.27	0.000	0.29	0.44	0.27	0.02	0.47	0.1	0.48	0.03	0.44	0.04	-102.2	-5	0.46	0.04	1.94	0.28	130	18
N455	0.14	0.009	0.38	0.48	0.16	0.02	0.30	0.08		0.30	0.08	0.89	0.41	61	28					
B129	0.25						0.33	0.08		0.33	0.08	1.05	0.47	71	32					
N010	0.48						0.34	0.05		0.34	0.05	1.09	0.31	73	20					
<u>Transition</u>																				
N004	0.57	0.006	0.14	0.28	0.31	0.03	0.49	0.1		0.49	0.1									
N156	0.59						0.40	0.09		0.40	0.09									
N011	0.59						0.52	0.05		0.52	0.05									
<u>Interior</u>																				
N004	0.56	0.003	0.15	0.29	0.42	0.02	0.67	0.1		0.67	0.1									
N156	0.80						0.36	0.06	0.67	0.07	-114.6	-5	0.67	0.07						
N011	0.69						0.28	0.05		0.28	0.05									

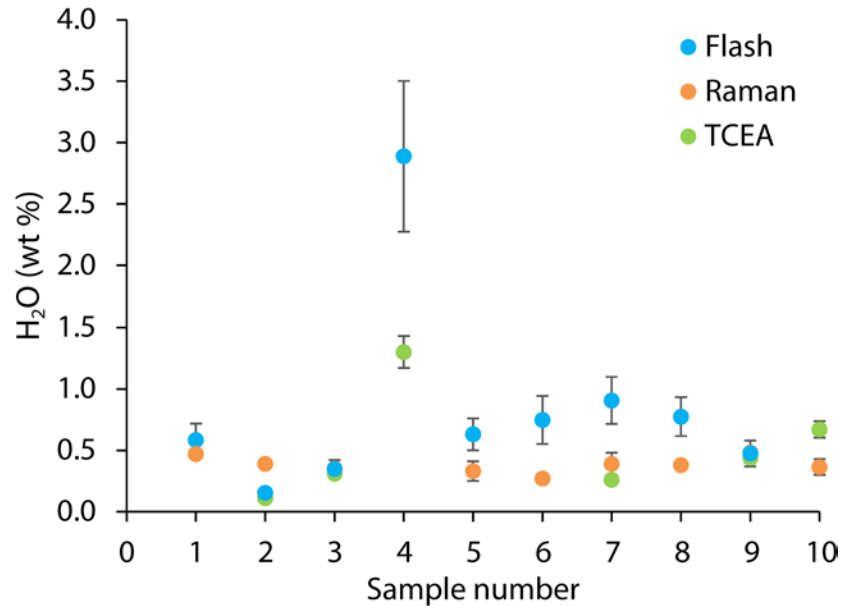


Figure 4.3 Estimates of glass water content for samples on which multiple methods of measurement were employed. Sample numbers are arbitrary. Error bars are smaller than symbol size when not shown and represent the combination of natural variability and analytical uncertainty for each sample and method. There is no consistent relationship between the estimates using the different techniques. See text for full explanation.

water content (Table 4.1). Based on the hydrogen isotope data, discussed in Section 4.4, we have excluded this and all other water values >1 wt% H₂O from further consideration in determining depth ranges for fragmentation. The remaining data correspond to a pressure range of 0.2 to 6.7 MPa (Table 4.1).

The water data from different clast types form partially overlapping groups on the plot of dissolved H₂O versus vesicularity (Figure 4.4). The lowest dissolved water contents (≤ 0.2 wt% H₂O) are from two dense dacites. The crusts of breadcrusted clasts include some samples with higher water values than the three pumices. The crust, transition, and interior samples from an individual block (for blocks N004, N011, and N156) show no correlation with vesicularity and

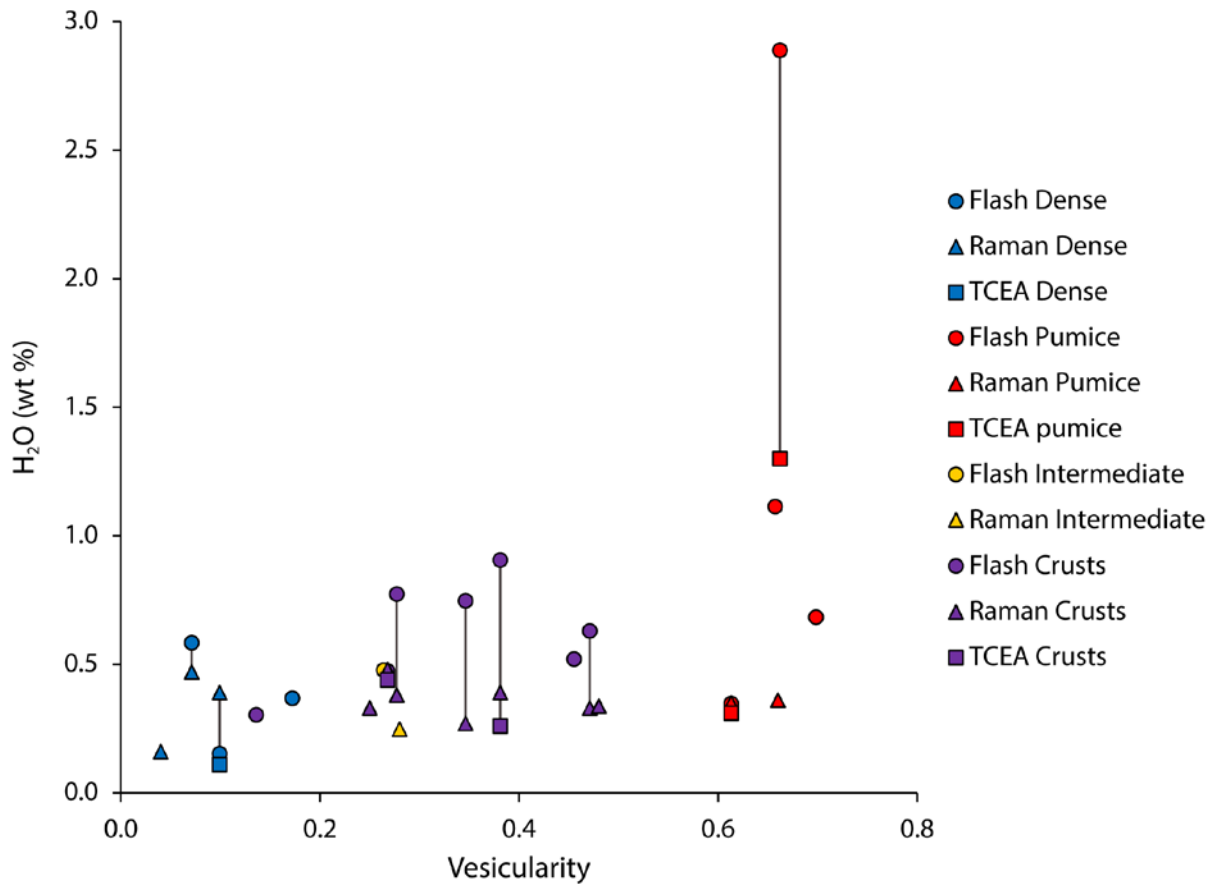


Figure 4.4 Dissolved H₂O versus vesicularity for the dense, pumiceous, and intermediate blocks and the crusts of the breadcrusted blocks (represented by different *colors*). Water estimates for the different methods are represented by different *symbols* and connected by tie-lines. Nine out of the 20 blocks represented in this plot were analyzed by multiple methods; two of those nine blocks have overlapping water contents and thus did not need tie lines (see Table 1).

most have similar H₂O values with overlapping error bars (Figure 4.5). Pressure and depth were not calculated for the transition and interiors as their water values do not represent fragmentation conditions due to post-fragmentation continued vesiculation.

Total crystallinities (phenocrysts + oxides) collected from thick sections show no relationship between water content (measured via the Flash 2000 — the method for which crystal

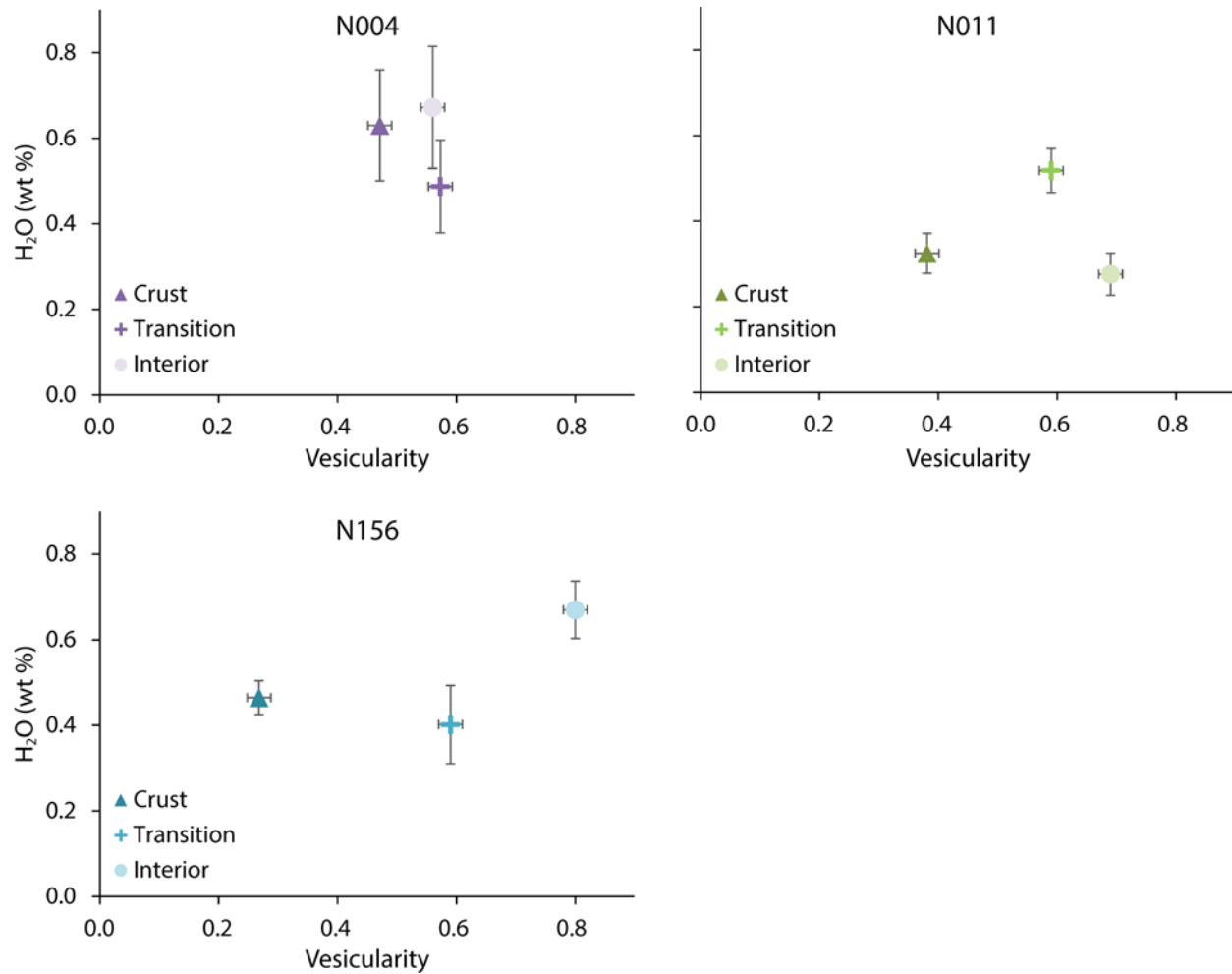


Figure 4.5 Dissolved H₂O versus vesicularity for the crust, transition, and interior samples of blocks N004, N011, and N156. Vesicularity of the crust decreases from block N004 to N156 whereas transition and interior vesicularities increase, yet there is no correlation between vesicularity and water content.

content was necessary) and crystallinity (Figure C.2 in Appendix C). There is an inverse correlation with vesicularity; however, crystallinities referenced to solid (glass + crystals) only show no correlation with vesicularity and, in fact, span a wide range of values within a single textural group.

4.4 Interpretations

4.4.1 Discriminating primary magmatic water from secondary hydration by meteoric water

The wt% H₂O and δD measured by the TCEA are plotted with modeled regions for closed system degassing, open system degassing/outgassing, and rehydration by meteoric water in Figure 4.6. During degassing of water from the melt, deuterium is preferentially partitioned into the vapor phase. This will cause subtle to extreme D/H fractionation depending on whether the system is closed or open, respectively, during degassing (Taylor et al. 1983). If the system remains closed, the melt and the vapor remain in contact and thus are able to equilibrate and the D/H fractionation can be modeled using a linear mass balance equation (Taylor et al. 1983). The removal of exsolved volatiles during open system degassing prevents isotopic equilibrium and drives strong D/H fractionation as described by the Rayleigh distillation equation (Taylor 1991). The closed-system degassing and outgassing regions in Figure 4.6 were modeled using (Taylor et al. 1983; Taylor 1991; Castro et al. 2014):

$$\delta D_{degas} = \delta D_i - (1 - F)(1000)(\ln \alpha_{v-m}) \quad (4.3)$$

$$\delta D_{outgas} = (\delta D_i + 1000)(F^{\alpha_{v-m}-1}) - 1000 \quad (4.4)$$

for a melt initially containing 3 wt% H₂O (estimated for the Novarupta dacite, Hildreth and Fierstein 2012), where δD_i is the initial δD of the melt, F is the ratio of the H₂O remaining in the melt, and $\alpha_{v-m} = 1.0343$ is the fractionation factor (from Martin et al. 2017). Since the true value is currently unknown, degassing and outgassing curves were calculated for δD_i values ranging from -55‰ (dacite value from Mount St. Helens, Underwood et al. 2013) to -75‰ (the maximum value modeled by Castro et al. 2014 for the 2008 rhyolitic eruption at Chaitén) and

plotted as shaded regions. At low temperatures, rehydration of meteoric water largely occurs in the form of $\text{H}_2\text{O}_{\text{mol}}$ whereas (at low total H_2O concentrations) magmatic water is in the form of OH^- (Newman et al. 1986; Silver et al. 1990; Giachetti et al. 2015). The influence secondary hydration on the δD of the measured water in glass depends on the initial δD of the magma, the δD value of local meteoric water, and the degree of volcanic degassing that has occurred (Seligman et al. 2016 and references therein). During rehydration, the δD of secondary water is depleted by 30–35‰ relative to that of local meteoric water at typical surface temperature and hydration conditions (Friedman et al. 1993a; Bindeman and Lowenstern 2016; Seligman et al. 2016; Martin et al. 2017). The rehydrated region in Figure 4.6 was modeled for erupted glass starting with 0.2 wt% H_2O using the equation of Martin et al. (2017):

$$\delta D_{\text{rehyd}} = X(\delta D_{\text{met}} - 34) + (1 - X)(\delta D_{\text{degas}}) \quad (4.5)$$

where X is the fraction of rehydration (meteoric water/total water), $\delta D_{\text{met}} = -110\text{‰}$ is the value for meteoric water at Katmai (unpublished data from Mike Hudak, University of Oregon), -34 corresponds to $1000(\ln \alpha_{v-m})$, and δD_{degas} is the starting δD estimated from the degassing model for 0.2 wt% H_2O . There is therefore a range of δD_{degas} as it was calculated for the range of δD_i in Equation 4.3 producing the shaded region of rehydration in Figure 4.6. The four samples that cluster between -110‰ and -100‰ plot on the lower end of the closed system degassing region or between the closed and open degassing regions. These samples are interpreted to represent complex degassing histories involving multiple events of closed system degassing and disruption that leads to outgassing (similar to the batched degassing proposed by Taylor 1991 and Castro et al. 2014). While two of these data points lie at the beginning of the

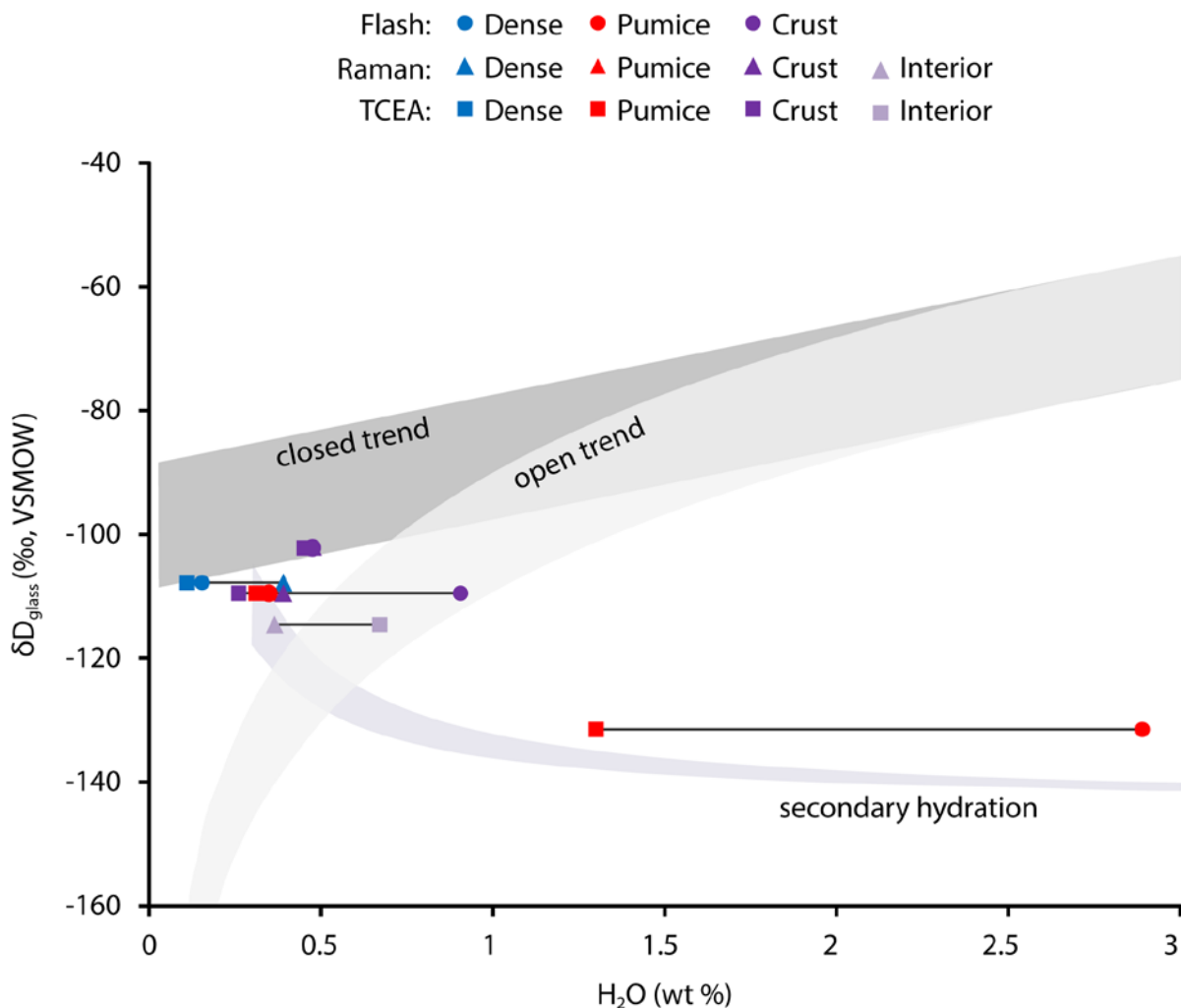


Figure 4.6 Episode IV δD and water content plotted against modeled trends for closed system degassing (*dark gray region*), open system degassing/outgassing (*light gray region*), and secondary hydration by meteoric water (*blue-gray region*). The initial δD of the magma at Katmai is currently unknown and so we included gray regions for the degassing and outgassing models for a range of δD_i (Equations 4.3 and 4.4) from -55‰ to -75‰. The blue-gray shaded region represents the evolution of volcanic glass composition during rehydration assuming an initial H_2O content of 0.2 and for the range of δD s calculated using the degassing model for 0.2 wt% H_2O water (starting δD of -85‰, -95‰, and -105‰ corresponding to δD_i of -55‰, -65‰, and -75‰, respectively). See text for further details.

rehydration region, this specific region is for closed system degassing — if those pyroclasts did undergo batched degassing this would draw their δD values closer to the rehydration curve (i.e., closer to the outgassing region) without secondary hydration. The interior sample with a δD of approximately -155‰ plots in the middle of the outgassing region but also extends into the region between the two degassing trends due to its wide range of water estimates. This probably reflects the influence of a range of degassing/outgassing/rehydration events due to 1) the fact that the interior re-vesiculated from an outgassed crust (reflecting batched degassing), and 2) some rehydration might be possible due to the high water content and vesicularity, but its range of water values actually overlaps with that of its crust (the 0.45 wt% H₂O crust) so this is left uncertain. The pumice with a δD of -131‰ plots much closer to the rehydration trend; this combined with its high water content is taken to indicate secondary hydration by meteoric water. Given where these six samples plot relative to the modeled degassing, outgassing, and rehydration regions, we assume that it is prudent to assume any values >1 wt% measured by the Flash 2000 and the Raman reflect some amount of low-temperature rehydration.

Due to continued problems with the apparatus, we were unable to use the Raman spectrometer to test samples with <1 wt% H₂O for resorption that would manifest as increasing water content towards bubble walls. However, McIntosh et al. (2014) observed such increases in H₂O content of roughly 1 wt% (or more) within 10 μm of bubble walls. If similar amounts of resorption occurred within the Episode IV clasts, then higher water contents than those that we have recorded should be expected. In fact, in general, the low water contents measured here would suggest that resorption was not a major contributor to the majority of the Episode IV glass water contents. This chapter will continue with the assumption that samples with <1 wt% H₂O

can be confidently taken to represent the residual magmatic water in the glass at the time and depth of fragmentation.

4.4.2 Implications of measured water contents

The data show a range of residual water contents but one that is restricted with respect to many other Vulcanian eruptions. The range of acceptable water data, of 0.11 to 0.91 wt%, presented here contrasts with: 0.2–2.79 wt% H₂O at Soufrière Hills in 1997 (Burgisser et al. 2010); 0.4 to 3.1 wt% H₂O (with a majority ≤ 1.5 wt%) at Guagua Pinchincha in 1999 (Wright et al. 2007); 1–1.7 wt% H₂O at Volcán de Colima in 2013 (Cassidy et al. 2015) and is more consistent with the 0.1–0.5 wt% estimated for 1991 Unzen Vulcanian pyroclasts (Kusakabe et al. 1999) and the 0.73–0.95 wt% found in a tuffisite vein within a 2008–2009 Volcan Chaitén pyroclast (Saubin et al. 2016). At face value then, it would appear that a narrow and shallow range of depths of fragmentation is likely for the Novarupta samples.

Combined with vesicularity and micro-texture analyses, the water data can provide insight to the pre- and syn-fragmentation residence depths and times in the conduit for the magma producing the diverse suite of block textures. With the exception of the interiors of breadcrusted clasts, the vesicularity and micro-textures of a clast reflect bubble nucleation, growth, and outgassing prior to fragmentation. The residual water contents indicate the maximum depths at which these processes occurred. We now apply these lines of reasoning to the Episode IV ejecta.

4.4.3 Dense dacites

The dense dacites contain comparatively few bubbles and, instead, show large regions of vesicle-free glass. The vesicle/pore population is volumetrically dominated by large, elongate and complex-shaped pores that are generally aligned along the margins of phenocrysts. We know

that exsolution of only a small proportion of the volatiles (10–20%) is necessary for Novarupta magma to have reached vesicularities of 52 to 75 volume % (Gonnermann and Houghton 2012). Given that the pre-eruptive H₂O contents in the storage region are estimated at 2–3 wt% (Westrich et al. 1991; Lowenstern 1993; Hildreth and Fierstein 2012), all of the water contents in Figure 4.4 indicate that all portions of the Episode IV magma underwent significant degassing prior to final fragmentation. It was necessary, then, for the densest magmas to have also undergone outgassing to preserve measured porosities of <20%. This is an indicator that the residual volatile content in the dense dacite magma was in equilibrium with solubility versus depth relationships at fragmentation, and the depth estimates are realistic values. As such, the combination of low H₂O contents and dense, outgassed textures in the dense dacites indicate their magma source underwent significant vesiculation followed by, and concurrent with, prolonged outgassing at depths of 170 m or less.

4.4.4 Microvesicular pumices

With micro-textures, bubble number densities, and size distributions similar to the Episode III Plinian pumice (Chapter 3), the Episode IV pumices contain a significant, population of very small bubbles that 1) was newly formed at the time of fragmentation and quenching, and 2) perhaps indicates bubble nucleation extended right to fragmentation (Adams et al. 2006; Gonnermann and Houghton 2012). The residual water contents (0.31 to 0.68 wt% H₂O) may indicate some combination of a narrow range of shallow fragmentation depths and also variable re-equilibration of the volatiles with the final depth of fragmentation (see Section 4.5.1).

4.4.5 Breadcrusted clasts

With a wide range of vesicularities and corresponding bubble micro-textures that span from microvesicular to dense/outgassed, the crusts represent magmas that were resident in the shallow conduit for contrasting durations and achieved variable degrees of equilibration with their residence/fragmentation depths (Chapter 3). All of the crusts except sample N004 have bubble textures showing elongate, permeable porous pathways which have undergone partial collapse or narrowing.

Sample N004, with the highest vesicularity (47%) of the crusts, exhibited evidence of a much lesser extent of outgassing than the other crusts. It seems likely that it had a much shorter residence time at its final depth prior to fragmentation, to permit this to occur, and so its H₂O content (0.63 wt%) could be in slight disequilibrium (similar to the pumices).

The *banded* breadcrusted blocks supply strong evidence for some magma in the conduit being in disequilibrium with its residence and fragmentation depth. In these blocks, dense crusts extend into interiors with bands of different vesicularities (i.e., banding is more conspicuous in the interiors than in the crusts, Figure 4.1d). One way of interpreting this is that bands underwent different amounts of post-fragmentation vesiculation which would be the result of adjacent magmas with slightly different chemical and/or physical properties (Chapter 3). Likely, the band that expanded was in chemical and/or physical disequilibrium with its fragmentation depth and its adjacent/non expanded band was in equilibrium.

4.5 Discussion

4.5.1 Variation in measured water contents

In considering variations in water estimates from the different methods, it is worth mentioning the difference in spot versus bulk measurement. Due to its high spatial resolution, the Raman technique can detect heterogeneities within the sample (e.g., increasing water contents towards bubble walls). During a measurement, care was taken to collect spectra on glass away from bubbles walls and to conduct multiple measurements on different regions in the thin section. Measurement of bulk samples averages all heterogeneities that we attempted to avoid in the Raman analysis. Indeed thick sections of samples analyzed by the Flash show heterogeneities (in vesicularity/texture) that would yield an averaged result in the bulk analysis (Figure C.3 in Appendix C). Shea et al. (2014) showed that water content varied with small-scale textural heterogeneities in 40% of pumices containing such contrasts in texture. It is worth noting that a reliable water content could not be estimated for a few of the samples analyzed by the Raman due to large variability in the water content of different regions in the samples. This existence of heterogeneities in a single sample could explain why there is nonsystematic differences between the Raman and bulk analyses.

4.5.2 The rehydration problem

The implications of secondary hydration by meteoric water for paleoclimate studies and for relating total H₂O content to degassing histories has been studied for over half a century. It is understood that volcanic glasses must be exposed to atmospheric conditions for prolonged periods of time (thousands to hundreds of thousands of years) for meteoric water to be incorporated into the aluminosilicate structure under ambient conditions (Friedman et al. 1966,

1993a, b; Dobson et al. 1989; Giachetti and Gonnermann 2013; Seligman et al. 2016). Evidence for rehydration in 100 year old Novarupta pyroclasts thus poses a problem if it occurs under such conditions. For example, 1 μm of hydration in 100 years requires diffusion rates of $10^{-22} \text{ m}^2/\text{s}$ and 15 μm requires rates of $10^{-20} \text{ m}^2/\text{s}$. These rates are considered fast compared to the average of $10^{-23} \text{ m}^2/\text{s}$ calculated for a range of timescales at ambient temperature by Giachetti and Gonnermann (2013). Additionally, one pumice analyzed by the TCEA shows rehydration while the other does not, despite similar bulk vesicularities (Table 4.1). The rehydration of a pumice relative to a young dense sample may be understandable due to the larger surface area of glass per unit mass exposed to the atmosphere (e.g., Giachetti and Gonnermann 2013). However, the selective rehydration of one pumice over another may reflect bubble wall thickness (e.g., Seligman et al. 2016). For example, 1 μm of rehydration will more greatly modify the bulk measurement of H_2O and δD for a pumice with comparatively thin walls (such as 5 μm thick versus 15 μm) due to the smaller volume of glass. There is potential for further research into diffusion rates at low temperature and the rehydration of young pyroclasts. Water diffusion rates are much faster at higher temperatures (Newman and Lowenstern 2002 and references therein); however, this would require some pumices to remain at high temperatures after fragmentation or infiltration of meteoric water through the dome to reach the pocket of pumice-forming magma that resulted in the one measured rehydrated pumice.

4.5.3 Architecture of the dome and shallow conduit

The essential characteristics of our eruption scenario are:

- i) The magma was fragmented over a narrow range of depths of less than 400 m, one that is limited compared to larger Vulcanian explosions at long-lived lava domes,

- ii) Some of the magma was not in volatile or physical equilibrium at the depth of fragmentation, i.e., volatile contents cannot be directly correlated with depths of stagnation or fragmentation,
- iii) Blocks with different textures still came from overlapping depths suggesting significant lateral textural heterogeneity of the magma at shallow depths,
- iv) Rapid vesiculation of the microvesicular pumice-forming magma is inferred to provide the energy required for the explosions.

The water data support the structure of the shallow magma column proposed by Adams et al. (2006) and Isgett et al. (2017). In it, magmas in different stages of degassing, outgassing, and volatile disequilibrium were juxtaposed and mingled with one another. These data (Table 1) show for the first time that this heterogeneity occurred at depths of <400 m, possibly reflecting disruption of a texturally complex dome and its shallow roots. This heterogeneity and estimated fragmentation depths are much shallower than those estimated for Vulcanian explosions at Soufrière Hills (Druitt et al. 2002; Melnik and Sparks 2002b; Clarke et al. 2007; Burgisser et al. 2011).

We cannot detect temporal shifts by applying a chronology to the mapped block deposit as there is no clear ‘stratigraphy’ due to lack of spatial overlap between products of discrete explosions and the eruption was not observed. However, we can be certain of lateral textural heterogeneity in the magma (as opposed to the classical model of changing texture with depth) due to two lines of evidence. First there are two scales of texturally variability — meter-scale homogeneous clasts (indicating homogeneous regions at least that large) and centimeter- to millimeter-scale banding in banded blocks (Isgett et al. 2017) which show that melts of

contrasting degrees of degassing and outgassing co-existed and mingled at single depths. Second, both volume estimates for individual explosions (Isgett et al. 2017) and the new water data suggest explosions tapping only shallow regions of the conduit implying the diversity of the ejecta must reflect spatial variability across the conduit and/or dome. Additionally, the preferable ejection of the dense blocks towards the south of the vent (Isgett et al. 2017) may provide evidence of regions of heterogeneity in the dome. Inclined explosions observed at Soufrière Hills volcano were attributed to an asymmetric vent/shallow conduit region that evolved in response to prior explosions (Cole et al. 2014). At Volcán de Colima, explosion loci were discrete, and spatially variable within the crater and dome, which was related to heterogeneity in the conduit fill (Lavallée et al. 2012; Cassidy et al. 2015).

We expand on this model by placing each block type in a more specific framework (Figure 4.7). In this, the densest material has been intruded by multiple domains of newer magma of contrasting residence times and thus in differing stages of degassing and outgassing. Magma with lesser amounts of primary degassing formed the re-vesiculated breadcrusted clasts with the highest H₂O contents. Tongues of actively vesiculating magma that resulted in the pumices were restricted to meter-wide domains within the shallow conduit. They intruded through, and locally mingled along their margins with, domains of the denser, cooler, more viscous magma in all stages of degassing and outgassing. This mingling resulted in the banded blocks with sharply contrasting bands of dense and highly vesiculated material. Vesiculated bands in banded breadcrusted blocks represent material that had recently intruded and was thus at disequilibrium (their source magma, represented by the crust, was dense and outgassed and the interior band re-vesiculated after fragmentation). The conduit fill was thus constantly evolving

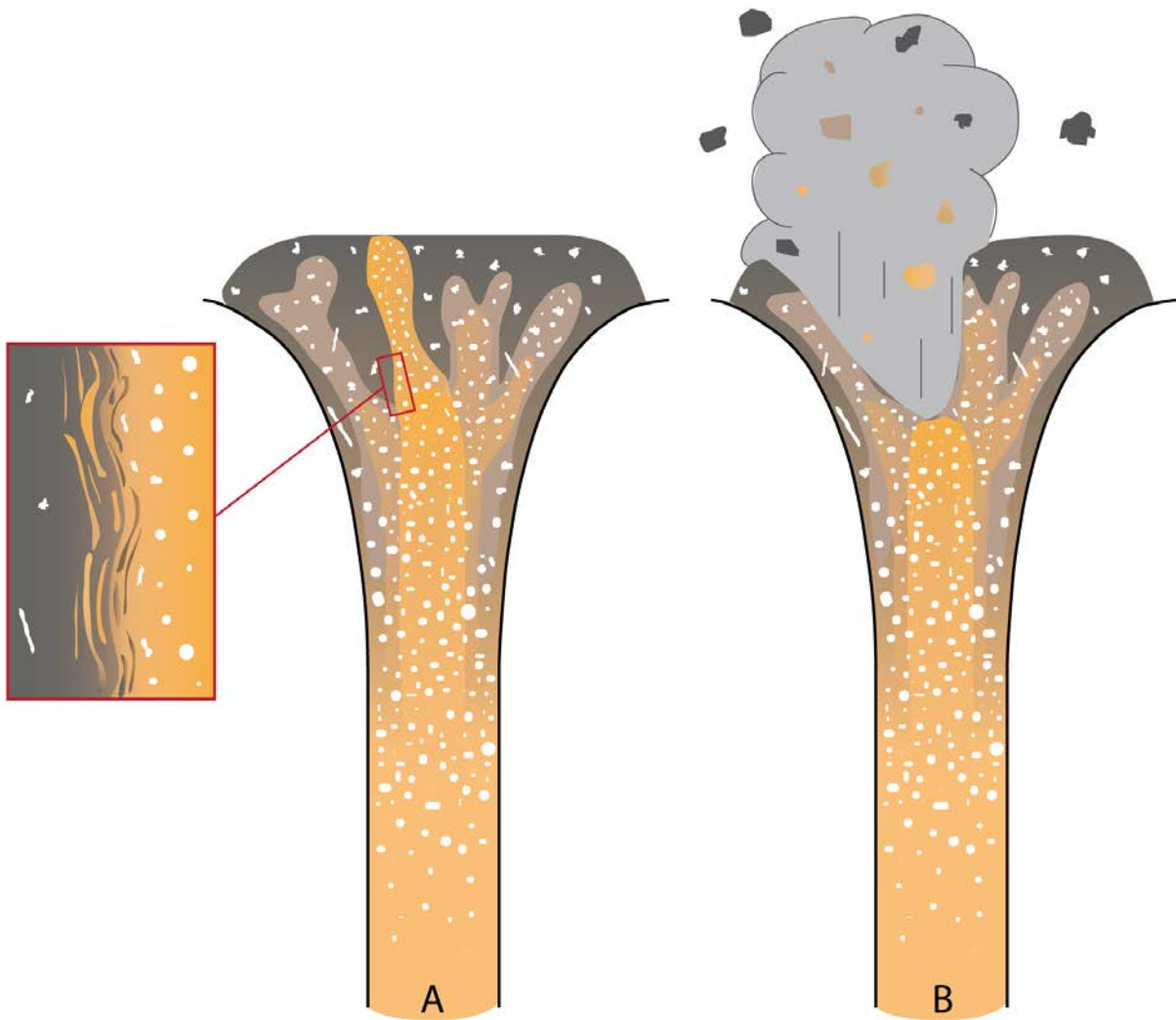


Figure 4.7 Theoretical model of the pre- and syn-fragmentation shallow conduit throughout Episode IV. The densest material, that generates dense dacite blocks, is represented by *dark gray*, the magma source for pumices is represented by the *bright orange* intrusion, and the *lighter purple-gray* and *orange* intrusions represent the source magma for the breadcrusted blocks. **A:** As the rising, actively vesiculating magma rose into the shallow conduit, shearing along its margins with the material that it was intruding formed the banded blocks (*left inset*). **B:** Sudden decompression of the actively vesiculating magma triggered fragmentation resulting in a small explosion that disrupted only a localized portion of the conduit-fill. Due to the textural heterogeneity of the dome and shallow conduit, a wide range of pyroclast textures was produced despite the limited depth range for fragmentation.

throughout Episode IV at Novarupta due to the intermittent arrival of new magma. This contrasts with the conventional view of a stagnant, horizontally layered conduit (Clarke 2013, p. 132 and references therein) prior to Vulcanian explosions at long-established dome complexes. Studies of hybrid effusive-explosive activity following the cessation of powerful Plinian phases at Chaiten (2008) and Cerdón Caulle (2012) have also inferred shallow fragmentation depths and shallow dome/conduit heterogeneity. However, a crucial difference there is the presence of tuffisite veins that connect deeper gas-rich and degassing magma to outgassing pathways and become the source of ash-venting when they become blocked (Schipper et al. 2013; Castro et al. 2014; Saubin et al. 2016). No obvious tuffisite veins were observed in the Episode IV blocks at Novarupta.

4.5.4 Magma ascent and storage histories

4.5.4.1 Microvesicular pumice

We suggest that the magma that formed the Episode IV microvesicular pumices underwent a sudden and rapid decompression with vesiculation and fragmentation occurring at similar depths (Chapter 3). As hinted above, the ascent history for the Episode IV pumices is still unclear, but we can address the merits of certain options. The pressure change could have occurred in three ways: 1) during ascent of the pumice-forming magma to the depth of fragmentation immediately prior to the eruption, 2) while the magma resided and equilibrated at some depth (i.e., at some pressure) and was disrupted in situ by a downward propagating rarefaction wave, or 3) when the magma was resident at shallower depths but held at some overpressure which was eventually, but very suddenly, released. Residual water contents for the pumices (Table 1) suggest fragmentation depths of 70 to 270 m which rules out option 2). Option 3) would involve some

unknown residence times at those depths (which would be supported by the small population of large, >1 mm, and complex-shaped bubbles observed in the microvesicular pumices). In this scenario, the magma would have intruded into an already pressurized system without triggering significant vesiculation until just prior to fragmentation; however, there is no evidence of an external trigger such as dome collapse.

We imagine that both options 1) and 3) are viable, and, considering the textural heterogeneity of the shallow dome and its roots, it could be a combination of these. Both scenarios require the intermittent pulsed arrival of small batches of volatile-rich magma into the shallow conduit in order to produce the multiple explosions proposed by Isgett et al. (2017) that were localized to small portions of the conduit. Geophysical and geochemical observations of inflation and fluid movement (i.e., intrusion) prior to Vulcanian explosions at Mount St. Helens in the summer of 1980, Soufrière Hills in 1997, and Sakurajima in 2009 are attributed to the arrival of new magma on varying but short time-scales (e.g., Calder et al. 2002; Cashman and McConnell 2005 and references therein; Williamson et al. 2010; Yokoo et al. 2013). Periods of increased effusion rates at long-lived domes have also coincided with more frequent Vulcanian explosions (Calder et al. 2002; Melnik et al. 2009; Lavallée et al. 2012). Rapid vesiculation in response to this ascent may trigger fragmentation directly, through bubble expansion and exceedance of the tensile strength of the bubble walls (option 1). Alternatively, the arrival of this magma may still increase pressure of an already pressurized system until it overcomes the tensile strength of the dome rock (option 3). Some batches of magma may remain at some level of volatile disequilibrium with ambient pressure after intrusion but prior to fragmentation. This

allowed time to partially outgas and collapse any vesicles that formed during ascent ultimately resulting in some of the breadcrusted blocks.

4.5.4.2 Complex combinations of degassing histories

The evidence presented in Section 4.1.1 for batched degassing to have had a role in all block textures provides critical support for our argument that the magma in the very shallow conduit was in varying states of degassing and outgassing. Closed system degassing occurs within isolated parcels of magma producing exsolved gas bubbles that remain coupled with the magma. Due to this mechanical coupling the exsolved fluid and melt remain isotopically equilibrated following the closed system degassing model in Figure 4.6 (Taylor et al. 1983). If vesiculation occurs in an open system (resulting in outgassing) chemical equilibrium is not maintained, driving strong D/H fractionation according to the outgassing model in Figure 4.6 (Taylor 1991). In batched degassing, a parcel of magma may degas in a closed system producing exsolved gas, followed by extraction of the gas after an open system develops. This can occur cyclically and gradually drive δD towards the outgassing trend, and so data reflecting batched degassing plot intermediate between closed and open system models (Taylor 1991; Castro et al. 2014).

Batched degassing could have occurred in response to the multiple conduit-changing events throughout Episode IV: explosions and the pulsed arrival of new magma. Clearly, intermittent explosions that disrupt small regions of the dome facilitate the removal of exsolved gas. Shearing, along the margins of an intruding magma domain, can both open and close permeable pathways, resulting in the outgassing of local domains. Shearing of magma can increase its permeability by deforming bubbles and increasing connectivity and also via brittle fracturing (Gonnermann and Manga 2003; Tuffen et al. 2003; Rust et al. 2004; Okumura et al.

2008, 2009, 2013; Namiki 2012; Shea et al. 2014; Shields et al. 2014; Kushnir et al. 2017).

Shear-induced outgassing may have been locally variable across the shallow conduit due to the arrival of, and shearing along, narrow (meter-wide) domains of magma; however, depending on the extent of these shear zones, they may not have permitted complete outgassing. A system may become closed again due to the collapse of the sheared bubbles into a dense material (e.g., Okumura et al. 2013; Shea et al. 2014) and the healing/annealing of the fractured network (e.g., Tuffen et al. 2003). One can start to imagine how complex the degassing and outgassing histories may have been on very short length scales for magma in the conduit throughout Episode IV, especially considering how localized both explosions and the arrival of new magma were, resulting in magma domains in differing states of degassing, outgassing, and disequilibrium.

4.5.4.3 Dense dacite

Could the magma represented by the dense dacite blocks have been left in the conduit at the close of Episode III? If so, what time was available for magma remaining in the conduit from the end of Episode III to evolve prior to fragmentation during Episode IV? The duration of the pause between Episodes III and IV puts an upper limit on this. As there were no direct observations of the eruption source, we must use the deposits to estimate the duration in question. The Episode IV blocks lie directly on layer H which is a “muddy” ash layer that formed after the cessation of Episode III (Hildreth and Fierstein 2000; Houghton et al. 2004). Proximally, layer H consists of >50 wt% ash that is finer than 63 μm in diameter and 85–100% of the glass shards are dacite (Fierstein and Hildreth 1992). We estimate a total of 22 hours for a 63 μm diameter, irregularly shaped (elongation of 0.7) ash particle with a density of 2500 kg/m^3

to fall from a plume height of 25 km (Fierstein and Hildreth 1992). If, instead the ash fell as loose aggregates then this time estimate is reduced; for example, an aggregate that is 600 μm in diameter, has a density of 750 kg/m^3 , and an elongation factor of 0.7 would have a fall time of 2 hours (fall times calculated using the formulations of Bagheri and Bonadonna 2016 and Bagheri et al. 2016). These fall times are minimum estimates for the duration of the pause, considering $\geq 50\%$ of the ash in layer H is smaller than 63 μm in diameter.

In addition to fall times, small erosional gullies within the Episode III tephra and underlying a few Episode IV blocks are indicative of a longer time period between the accumulation of layer H and the onset of Episode IV. Thunderstorms, which occur in King Salmon (64 miles from Novarupta) on average of <1 per month during the summer months (Western Regional Climate Center, <https://wrcc.dri.edu/cgi-bin/clilcd.pl?ak25503>) would have caused significantly more erosion. Instead, the gullies are likely the product of minor sheet wash accompanying more frequent but minor rain storms and indicate a pause of deposition on the order of weeks between Episodes III and IV. This is ample time for the melt forming the densest blocks to reach diffusive equilibrium and to undergo significant loss of porosity due to outgassing.

4.5.5 Formation of textural differences in banded clasts

Banding within pyroclasts can form through the mixing/mingling of two different magmas (e.g., Perugini and Poli 2012 and references therein) or variability in degassing within a magma in space and time (e.g., Gonnermann and Manga 2005b; Shea et al. 2012). As highlighted by Perugini and Poli (2012) mingling, defined as the physical dispersion of one magma within a host magma, rarely occurs without chemical exchanges due to the increase in contact area

between the two fluids. Mixing, or the simultaneous mingling and diffusion between two magmas, is thus much more common. The literature largely addresses mixing between magmas of different compositions between which large chemical and temperature gradients occur (Eichelberger 1980; Seaman et al. 1995; Flinders and Clemens 1996; Perugini et al. 2003, 2004, 2007; Perugini and Poli 2012). However, the kinematics of mixing/mingling can be applied to magmas of different textures (as throughout Episode IV) assuming the magmas were in their contrasting textural state prior to mingling.

We address two kinematical processes of mingling: chaotic mixing and instabilities formed along margins of one magma traveling through another. Mixed/mingled rocks that exhibit lamellae across a range of length scales are in fact fractals formed by repeated events of stretching and folding (Flinders and Clemens 1996; Perugini et al. 2003). The basic dynamics leading to chaotic behavior in fluids is stretching and folding, and modeling of chaotic mixing has produced structures and morphological features similar to those found in natural samples (Perugini et al. 2003; de Campos et al. 2011). Stretching and folding within the conduit would indicate quite dynamic conditions that could form in response to disruptions to the system (e.g., very localized explosions and subsequent reorganization of the conduit or injection of magma from below).

Fluid dynamical experiments and inferences from natural samples have demonstrated that the mingling of texturally and/or compositionally contrasting magma through flow within a conduit can play the key role in the formation of banded clasts (Blake and Campbell 1986; Freundt and Tait 1986; Koyaguchi 1987; Wada 1995; Perugini et al. 2004; Rosi et al. 2004; Lautze and Houghton 2005). Early research showed that as a lower viscosity fluid flows through

a higher viscosity fluid, the diameter of the former increased and the margins became unstable. This instability promotes entrainment of one fluid into another (Figure C.4 in Appendix C; Blake and Campbell 1986; Freundt and Tait 1986) and repeated shearing and folding results in banding (Wada 1995; Perugini et al. 2004; Rosi et al. 2004). In particular, Wada (1995) showed through fractal analysis that their compositionally heterogeneous clasts characterized by bands, vortices, and blebs with fingering patterns have similar fractal dimensions to those of fluid turbulent structures such as clouds or jets. For their system, they interpreted this to mean that the lower viscosity magma was ‘drawn’ into the higher viscosity magma as the eruption began, and that the two magmas ascended through the conduit in a turbulent state (Wada 1995).

Further fractal analyses of compositional banded clasts and fluid-dynamical experiments showed an inverse relationship between estimated Reynolds numbers (Re) and mixing intensity (Koyaguchi and Blake 1989; Perugini et al. 2004), i.e., the higher the turbulence the lower the mixing between two magmas. More efficient mixing results in a more homogeneous fluid so poor mixing efficiency would mean a starker contrast between two fluids (i.e., mingled but not mixed). This is confirmed by the dimensionless parameter I_{mix} defined (for the sub-turbulent – turbulent regime) as:

$$I_{mix} = \frac{4(\rho_r - \rho_m)\rho_1}{k \Delta\rho \rho_m} Re_1^{-1} \quad (4.6)$$

where ρ_r is the density of the country rock, ρ_m is the density of the bulk magma, ρ_1 is the density of the upper magma, $\Delta\rho$ is the density difference between magmas, k is a friction factor (Koyaguchi and Blake 1989). Equation 4.6 was analyzed for fluids with viscosity ratios between 1 and 10^3 and $10^2 < Re < 10^6$ in a conduit in which a more viscous magma overlays a less viscous magma. Length scales investigated by Koyaguchi and Blake (1989) for I_{mix} are on the

order of 10^{-2} m. This inverse relationship contrasts with that found for mixing in magma chambers (Huppert et al. 1986; Campbell and Turner 1989)(Campbell and Turner 1989; Huppert et al. 1986) and is similar to experimental models for shear layers and pipes (Dimotakis 2000). This suggests similar conditions between magmas of different viscosities ascending within a conduit (Koyaguchi 1987; Koyaguchi and Blake 1989; Perugini et al. 2004).

Viscosities calculated by Gonnermann and Houghton (2012) using a temperature of 850°C and the formulation of Hui and Zhang (2007) estimate values of $\geq 10^8$ Pa s for Novarupta dacite magmas <0.25 wt% H_2O and $<10^7$ and $>10^6$ Pa s for H_2O contents of >0.7 wt% and <1 wt%, respectively. We apply these values to the shallowest and most outgassed magmas and the pumice-generating, actively degassing magmas, respectively. Realistic (lower) temperature estimates for the shallowest magmas would increase this contrast by up to another order of magnitude which yields a total viscosity difference of two to three orders of magnitude. Under these circumstances, the rising, actively vesiculating magma would be significantly less viscous than the surrounding magma such that it intruded via propagation of elastic fractures. We propose that mingling occurred along the margins of these two texturally contrasting fluids due to shearing induced by the high velocity gradients (Figure 4.7 inset).

Banding may also form without the mingling of two disparate magmas. As described above, shearing can locally alter the texture of a magma by 1) increasing porosity and permeability and 2) inducing bubble collapse and thus decreasing porosity (Shea et al. 2012, 2014). Studies have shown that repeated fracture and healing along shear zones can lead to banded material containing sharp boundaries between highly texturally diverse (dense versus vesicular, microlite poor versus microlite rich) layers (Figure C.5 in Appendix C; Gonnermann

and Manga 2003, 2005b, Tuffen et al. 2003, 2008). While these shear zones are generally attributed to conduit margins (Polacci et al. 2001; Rosi et al. 2004; Wright et al. 2011), these zones could have also occurred along the margins of narrow domains of intruding magma.

One common aspect of the varied processes described in this section is that banding requires dynamic conditions and often occurs within shear zones. Due to the complexity of the Episode IV dome and shallow conduit and the varied disruptions to the metastasis, shearing would have occurred in various locales across the width of the conduit resulting in both the mingling of two texturally diverse magmas and the in-situ development of heterogeneous textures (Figure 4.7 inset). Further analyses into the diversity of banding (i.e., blocks that are banded across the entire clast and exhibit bands across a range of length scales — potential fractals — versus blocks that contain only one or a few bands that contrast in texture with the dominant texture of the block) are needed to confirm this hypothesis.

4.6 Conclusions

Our scenario contrasts in four ways with the theoretical model and analytical and numerical simulations of pre- and syn-Vulcanian-explosion conduits in the case of long-lived dome-forming eruptions. First, the use of 1D or 2D simulations (e.g., Clarke et al. 2002a, b, Melnik and Sparks 2002a, b; La Spina et al. 2017) typically precludes analysis of lateral heterogeneity in the conduit. Two-dimensional modeling of heterogeneities within domes during effusion is within its nascent stages (e.g., Hale et al. 2009; Chevalier et al. 2017) and we hope that the evidence for great complexity in the very shallow conduit presented here will foster further development of numerical simulations that can replicate conditions such as those of Episode IV.

Second, slow ascent rates selected for modeled magma ascent and dome extrusion prior to fragmentation means internal bubble pressure remains in equilibrium with ambient magmatic pressure (e.g., Melnik and Sparks 2002a). This is almost certainly not the case for the breadcrusted blocks with re-vesiculated bands in contact with dense outgassed bands and possibly not so for portions of the microvesicular pumice component of the Episode IV ejecta. Third, the *external* initiation of fragmentation through a rapid pressure drop near the top of the conduit (Clarke et al. 2002a, b; Druitt et al. 2002; Melnik and Sparks 2002a, b; Mason et al. 2006) is not a potential trigger for fragmentation throughout Episode IV. Another option is through the *internal* development of overpressures in isolated bubbles within localized pockets of actively vesiculating magma. Finally, current models simulate large explosions that evacuate across the entire width of the conduit to depths of kilometers whereas we propose that only a small volume of magma within the conduit was disrupted in each Episode IV explosion.

A small number of papers propose similar variations on the standard model. For example, Kennedy et al. (2005) and Burgisser et al. (2010, 2011) proposed more complex and variable melt textures in the conduit at Soufrière Hills volcano in 1997. Cassidy et al. (2015) suggested that batches of fast-ascending, gas-rich magma rose through a slowly-ascending, homogeneous gas-poor magma at intermediate depths in the conduit (i.e., >250 m to the shallow storage region at ~1 km) at Volcán de Colima. Finally, Williamson et al. (2010) proposed that the injection of new vesicular magma into the dome at Soufrière Hills on 21 September, 1997 triggered both a dome collapse and explosive activity. While this scenario still involves the external trigger of fragmentation through decompression via the dome collapse, it aligns more closely with our hypothesis that actively vesiculating magma intruded into the shallowest regions

of the 1912 conduit. Validating the hypothesis for Episode IV requires more complex and time-consuming numerical simulations that are not tractable in the context of this study; however, we stress the importance of showing that Vulcanian explosions can result from a variety of different magma ascent histories, conduit lengths and architectures, and initiation mechanisms for fragmentation.

Numerical modeling of rates of bubble nucleation and growth, and the volatile overpressures needed to initiate fragmentation of the microvesicular pumice, are the next segment of the Novarupta study.

CHAPTER 5

Conclusions

Due to unique preservation, the Episode IV block apron at Novarupta allowed for unprecedented mapping and sampling of the ballistic pyroclasts from a Vulcanian eruption. It is an excellent case study for highlighting the diversity in Vulcanian explosions in terms of eruption and conduit processes. Key differences of interpretation from models of Vulcanian eruptions associated with long-lived dome-forming eruptions include:

- 1) The pre- and syn-eruptive conduit is filled with a complex three dimensional assemblage of magma with varying physical and chemical (in terms of residual volatiles) properties,
- 2) These magma ‘domains’ reflect variable residence times at their final depths of fragmentation,
- 3) Triggering of a Vulcanian explosion does not have to be external (i.e., via the failure of the conduit-capping plug or dome), but instead can initiate internally through vesiculation of newly arrived magma.

These contrasts are elucidated in greater detail within each of the chapters.

Chapter one sets the scene for the study in the context of both the powerfully explosive 1912 eruption and of Vulcanian explosivity globally.

Chapter two (*Eruptive and shallow conduit dynamics during Vulcanian explosions: Insights from the Episode IV block field of the 1912 eruption of Novarupta, Alaska*) presents the most complete delineation of a Vulcanian ballistic deposit to-date, detailed documentation of the diverse clast types and their proportions within the block apron, and uses size-density-range data

to model ejection velocities and trajectories. The componentry study revealed the diversity of brecciated, banded, and breadcrusted clasts that has not been previously documented for other Vulcanian eruptions and which can be used to infer complexity of conduit dynamics. The mapping and modeling showed that Vulcanian explosions at Novarupta were relatively weak and small when compared to other well-studied and observed Vulcanian eruptions. It also showed that the conditions that promoted explosions did not vary substantially across the multiple events within this phase. Estimated velocities, Reynolds numbers, and measured travel distances indicate that density has a decreasing influence on ballistic transport as size increases. This highlights how more sophisticated models of ballistic trajectory are required for pyroclasts <1 m in diameter. My study has shown that more real time observations of rotating pyroclasts and better constraints on rotation rates and their influence on trajectory are needed to enhance numerical modelling.

Using vesicularity data, porosity and permeability measurements, and qualitative and limited quantitative analysis of vesicle textures for each of the juvenile block types, Chapter three (*Complex patterns of vesiculation, outgassing, and re-vesiculation during a Vulcanian eruption: Implications for conduit processes*) showed that magma in the shallow conduit was in a variety of stages of both degassing (exsolution of volatiles from the melt) and outgassing (escape of the degassed volatiles). Dense dacite clasts represent magma that was largely both outgassed and degassed whereas the source magma for the pumice clasts was at the peak of its degassing, without significant outgassing at the time of fragmentation. Breadcrusted blocks came from magma that has experienced both partial degassing and outgassing. This implies that magma domains in the shallow conduit with these contrasting textures had different residence times at

their depth of fragmentation, with the pumice-forming magma most newly arrived and the dense dacite magma stored for the longest durations at the depth of fragmentation. Blocks with bands which are either pumiceous or dense indicate that there was local mingling along the margins of magma domains close to the time of fragmentation, and this was interpreted as a consequence of very late juxtaposition of magma domains with contrasting ascent and residence times.

Chapter four (*Constraints from residual water contents on eruptive processes during the 1912 Vulcanian explosions at Novarupta, Alaska*) provides depth estimates for all the processes outlined above, based on residual water content for glasses in each block type. The blocks came from a relatively narrow and shallow range of depths (<400 m deep) compared to Vulcanian explosions that disrupt long-lived dome growth complexes to depths of several kilometers. There is also significant overlap in the source depths for each block type, proving that their magma domains were closely adjacent to one another at the time of fragmentation. Hydrogen isotopic composition of dissolved water in glass from a range of ejecta implies limited secondary hydration of the pumice and possibly the interiors of breadcrusted blocks (which opens the possibilities for future studies of rapid rehydration of young, ~100 years, volcanic glass). This indicates that the pumices with >1 wt% H₂O actually have lower magmatic water contents that may be closer to the range of the other block types, and emphasizes their similar source depths (even accounting for disequilibrium). Vesicle textures, and lack of evidence for an external trigger (such as dome collapse), suggest that the rapid vesiculation of the pumice-forming magma after emplacement at shallow depths was likely the source of fragmentation.

5.1 Future directions

5.1.1 Further micro-analytical approaches to Episode IV

An important aspect currently missing from this study is the measurement of volatiles trapped within the glass of crusts in contact with internal bands of contrasting vesicular and dense textures. If they show significantly different water contents (i.e., higher water contents above the vesiculated bands than those above the dense bands), then this would prove local disequilibrium. An extension of this would involve collecting profiles of the water across the transition (within the crust) from one band to another, which could be used to establish diffusion profiles. Volatile diffusion has been established as a chronometer that acts on very short timescale such as minutes to weeks (Humphreys et al. 2008). Such a tool could be applied in determining timescales of mingling prior to fragmentation. One limitation to this is the possibility of rehydration of meteoric water, which occurs largely via the diffusion of molecular water (over hydroxyl) into the quenched glass (McIntosh et al. 2014; Giachetti et al. 2015). New micro-analytical techniques that determine the speciation of dissolved water do not have this limitation and could be used to further this study.

5.1.2 Breadcrusted blocks

One question left un-answered in this dissertation is why do some blocks breadcrust and others do not? The water data presented in Chapter 4 contrasted with my expectations for the breadcrusted blocks. I expected the blocks that show the greatest amount of post-fragmentation expansion to have the highest water contents, as this would provide more volatiles for re-vesiculation and make expansion easier due to lower melt viscosity. However, the two crusts associated with the most expanded interiors contained the lowest water content of all crusts.

Further study is need to understand how and why post-fragmentation vesiculation occurs, possibly with a focus on other physical or chemical differences with the non-breadcrusted blocks. This could have implications for the differences within their magma sources and thus provide further insight to conduit dynamics.

5.1.3 Numerical modeling

Some questions arising from the theoretical model of the magma within the conduit in Chapter 4 are: What overpressures were necessary to initiate fragmentation of the microvesicular pumice? What decompression/ascent rates were achieved by the pumice-forming magma? If bubble nucleation and growth occurred in the last few hundred milliseconds of ascent, what depths does this equate to? How did the pumice-forming magma travel through a conduit filled with colder, higher viscosity magma? What conditions promoted the transient and unsteady nature of the explosions throughout Episode IV? Why were explosions constrained to narrow and shallow regions of the conduit? Such questions could be addressed using numerical models that replicate magma ascent, volatile diffusion, bubble nucleation and growth, and overpressures (e.g., Gonnermann and Houghton, 2012). This would require a simplification from the three-dimensional complex organization of the magma column, but could provide first order constraints on certain fragmentation and ascent conditions.

5.1.4 Integration with further micro-textural data from Episode III

Other questions arising out of this dissertation are: How is the arrival of new magma in the shallow conduit throughout Episode IV related to the end of Plinian activity? Does it represent an attempt to continue with sustained explosions but something inhibited this process? The answers to these questions could have implications for how and why a voluminous Plinian

eruption ends. Was the magma or gas source exhausted? Did a blockage form deeper in the plumbing system? All of these are viable questions considering 1) the 1912 eruption ended after a switch from dacite extrusion and evacuation via Vulcanian explosions to rhyolite extrusion, and 2) the inferred storage region was located laterally 10 km from vent. A current study into the details of the end of Episode III via micro-textural analyses could be integrated with the results of this study to further understand the decline of the Novarupta eruption.

5.1.5 Extension of these approaches to other Vulcanian eruptions

A useful application of the findings of this study is to other historical Vulcanian eruptions that show no evidence of an external trigger. In well documented examples, other observations such as geophysical data and measurement of gas flux could be combined with the scenario of the conduit presented here to assist with forecasting the shift from effusive to explosive activity. This could be applicable first to scenarios like Novarupta 1912 where a plug/dome forms at the end of a sustained explosive eruption under conditions of highly variable magma ascent rates.

APPENDIX A

Chapter 2 Supplementary Material

A.1 Modeling methodology

We used the model of Fagents and Wilson (1993) in order to simulate the trajectory of the blocks assuming they are not influenced by an expanding gas phase, i.e. the blocks were projected through a still atmosphere. The trajectory calculation algorithm employs the computational scheme of Wilson (1972). The horizontal and vertical components of velocity v are given by

$$v_x = v \cos\theta \quad (\text{A.1})$$

$$v_y = v \sin\theta \quad (\text{A.2})$$

where θ is the trajectory angle measured from horizontal. The motion of the projectile of mass m and cross-sectional area A are defined by solutions of the rate of change of v_x and v_z :

$$\frac{dv_x}{dt} = \frac{-v_x \rho_a(z) v A C_d}{2m} \quad (\text{A.3})$$

$$\frac{dv_z}{dt} = \frac{-v_z \rho_a(z) v A C_d}{2m} - g \quad (\text{A.4})$$

where t is time, $\rho_a(z)$ is air density as a function of altitude, C_d is the drag coefficient on the block and g is gravitational acceleration. The cross-sectional area is calculated by

$$A = \pi \left(\frac{D_{avg}}{2} \right)^2 \quad (\text{A.5})$$

where D_{avg} is the mean of the three orthogonal dimensions measured in the field. The mass for each block was calculated by multiplying the volume of the block (each of the blocks dimensions

multiplied together) by the density; block densities were measured for a representative number of clasts within each componentry group and an average density was calculated per group and applied to blocks that were not sampled. The drag coefficient is dependent on the Reynolds number Re which is defined as

$$Re = \frac{D_{avg} v \rho_a(z)}{\eta_a(z)} \quad (\text{A.6})$$

where $\eta_a(z)$ (air viscosity) and $\rho_a(z)$ are calculated from a standard atmosphere. Per the method of Wilson (1972), equations 3 and 4 were integrated throughout the trajectory using a fourth-order Runge-Kutta method. The block trajectory was calculated until the vertical position was equal to that of the block's landing elevation. The velocity and angle combinations that projected the block to within ± 10 m of its measured horizontal distance were retained. The model was limited to $\theta = 45 - 89^\circ$ (as it is assumed that the majority of blocks had to escape from the ejecta ring and possibly from some depth in the conduit) and velocities < 600 m/s. The source location was set at an elevation of 771 m which is at the base of the current Novarupta dome. The horizontal source location was determined by calculating where the slopes of the ejecta ring theoretically meet below the dome as the Episode IV plug/dome pushed up through the Episode III backfill and it can be assumed that the latter would have filled the conduit according to the slopes present on the inside of the ejecta ring.

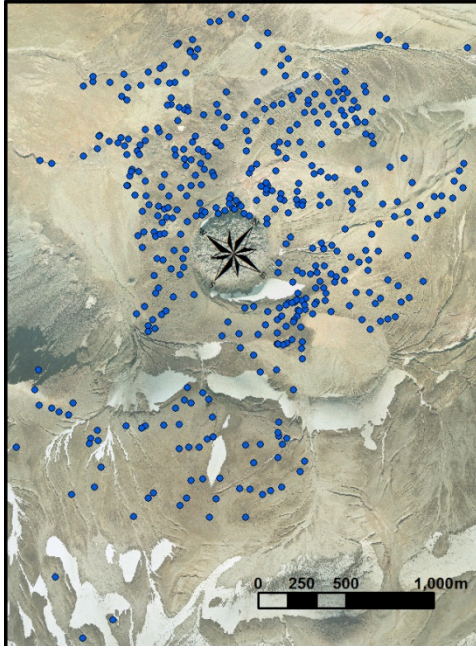
A.2 Spinning ballistics

Observations of spinning pyroclasts have shown that an angular velocity can influence the travel path of a ballistic (Chouet et al. 1974; Waitt et al. 1995; Vanderkluyesen et al. 2012; Taddeucci et al. 2017). Namely, spinning can curve the trajectory of a ballistic according to the Magnus force (Chouet et al. 1974; Waitt et al. 1995; Taddeucci et al. 2017), enhance conductive heat loss/cooling (Vanderkluyesen et al. 2012), influence the velocity of and drag force exerted on the pyroclast, and cause changes in shape or stretching/tearing of more fluidal projectiles (Taddeucci et al. 2017). These interpretations are based largely on observations of explosions at Stromboli volcano which produces more mafic compositions of lower viscosity than the common products of Vulcanian explosions. The influence of spinning on Vulcanian pyroclasts is more likely to be in the form of the Magnus effect on the particles' trajectories. For example, Waitt et al. (1995) interpreted deviations of impact craters away from the straight line trajectory from the vent at Mount Spurr volcano (Alaska) as due to an angular velocity in the direction of the deviation. This has serious implications for the method of inferring vent locations from ballistic distributions. Cumulatively, the influence of spinning on a pyroclast's trajectory can add errors to numerical models that do not account for rotation. However, Bertin (2017) suggests that the Magnus force may be neglected at very small ratios of air density/particle density and/or at low angular velocities. More observations of rotating pyroclasts and better constraints on rotation rates and their influence on the trajectory, especially in Vulcanian explosions, are needed to better understand how it can be accounted for in numerical models.

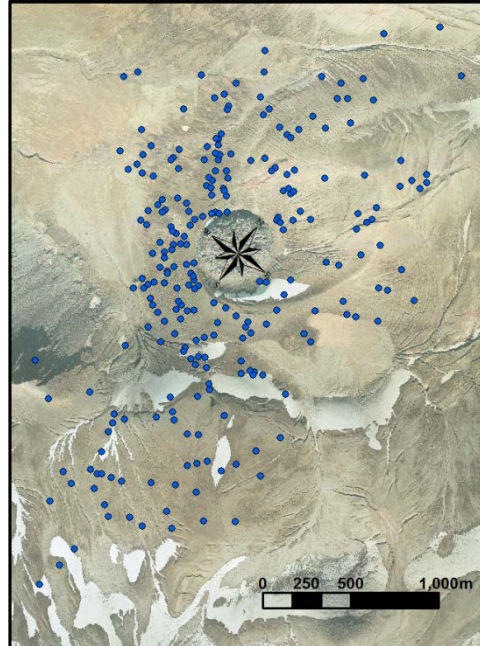
A.3 Additional figures

Figure A.1 Block maps for each of the components.

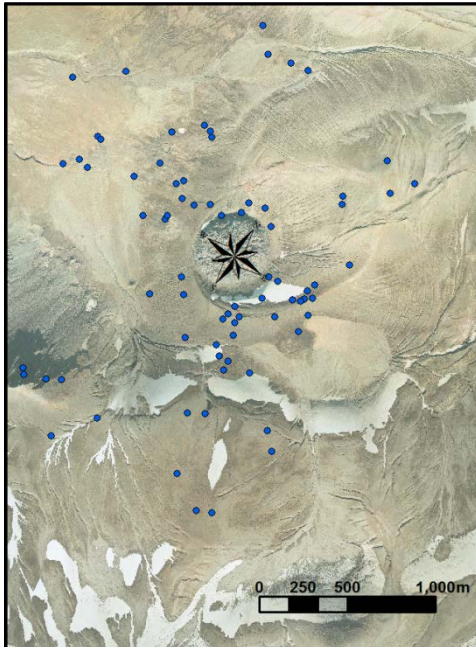
Pumiceous dacite



Dense dacite



Pumiceous banded



Mixed banded

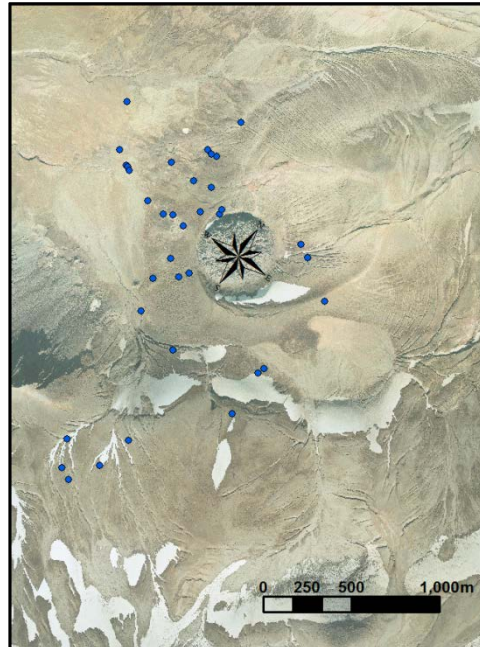
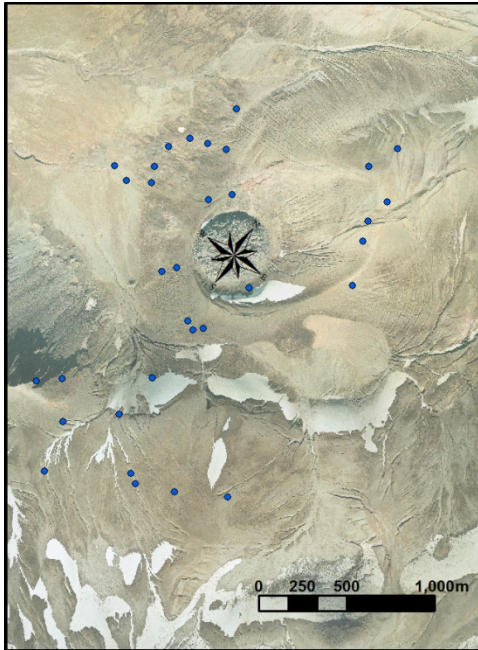
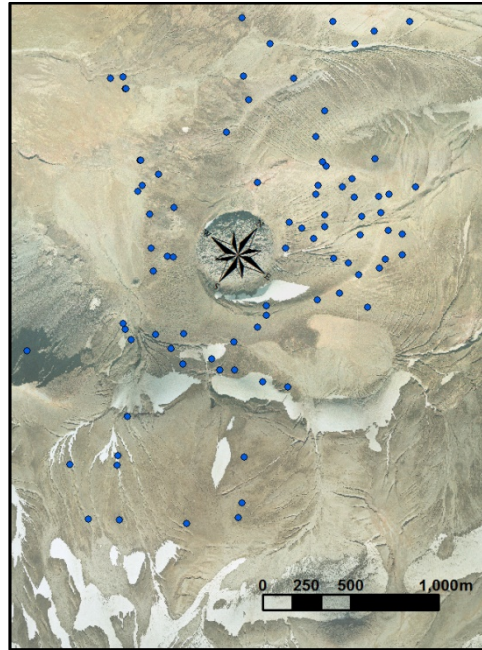


Figure A.1 continued.

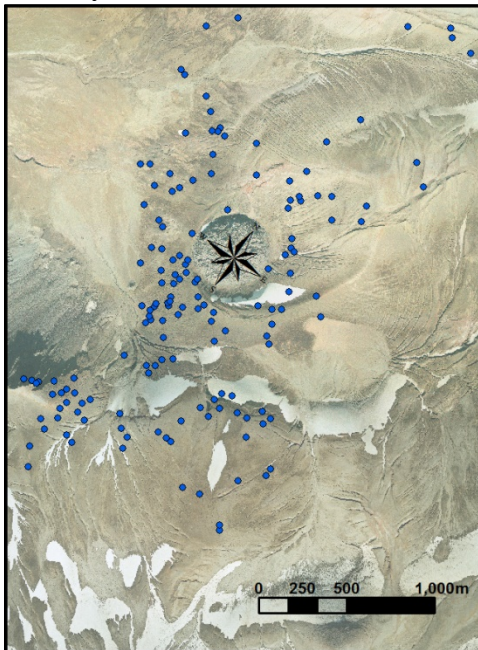
Dense banded



Dense vitrophyre



Densely welded breccia



Moderately welded breccia

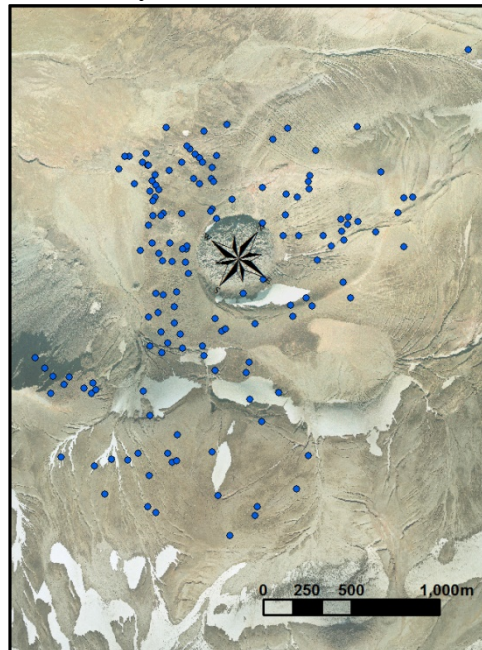


Figure A.1 continued.

Lightly welded breccia

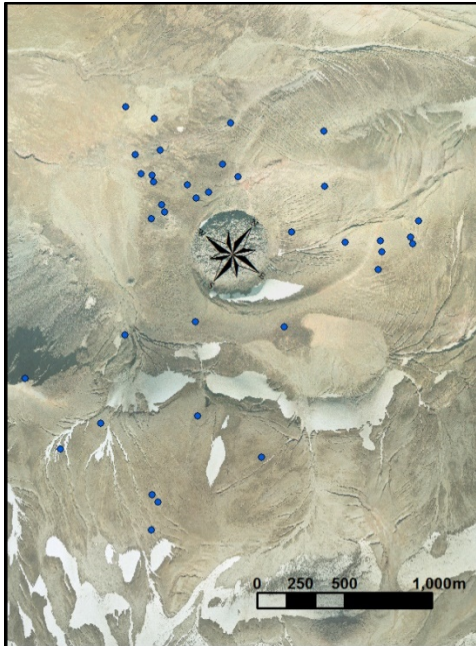


Figure A.2 Images of density of the pumice lapilli bed.

B051: ~475 m SSW of dome center; thick pumice lapilli/small-block bed.



Top of Ziess: ~925 m SSE of center of dome: person is sitting on top of the Episode IV pumice lapilli bed, also in foreground. Thick, dense pumice lapilli/small-block bed.



Figure A.2 continued.

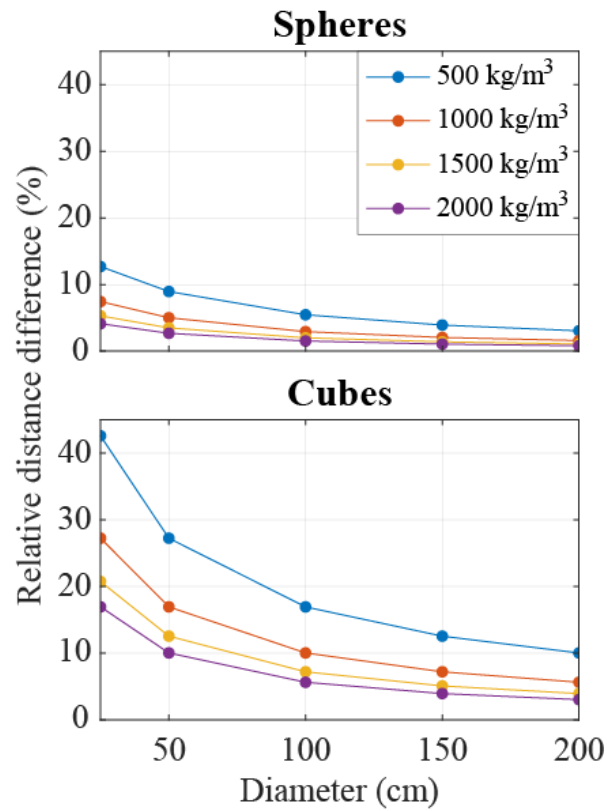
K14-02: ~490 m SE of center of dome, picture taken looking towards vent; thinner pumice lapilli/small-block bed.



N010: ~450 m west of center of dome; pumice lapilli/small-block apron is no longer continuous.



Figure A.3 Difference in horizontal distances between *Eject!* runs using 1) a stationary atmosphere and 2) a radius of reduced drag of 200 m above the vent for various block diameters and densities and for spheres and cubes. Velocity and angle were set at 100 m/s and 45°, respectively.



APPENDIX B

Chapter 3 Supplementary Material

B.1 Porosity and permeability methodology

B.1.1 Porosity measurement

Helium pycnometry was performed using a Micromeritics AccuPycII 1340 © at Rice University, which measures the sample's skeletal volume using the gas displacement method. The skeletal volume is the sum of the volumes of the three-dimensional solid skeleton and the isolated pores, which are the volumes of the sample that are inaccessible to the gas during the measurement. Helium is used because of its small atomic size and because it is inert and the most ideal gas.

A measurement is conducted by sealing the sample in a calibrated chamber of known volume (V) and releasing the helium into the compartment. Pressure (P) is measured as the gas fills any space not occupied by the sample and then is released into a second empty chamber also of a known volume. The $P \propto \frac{1}{V}$ relationship of Boyle's law is employed to calculate the volume of the gas. The difference between the volume of the sample chamber and the volume of gas that filled any voids in the sample is the skeletal volume (V_{ske}). The AccuPyc repeats this cycle in order to purge water and other volatiles from the sample until consecutive measurements converge on a consistent result. This method is also used on powderized samples of known mass in order to calculate the density of the skeleton. This dense rock equivalent (DRE) is then divided by the mass of the cylindrical sample core in order to determine the volume of its solid

skeleton (V_{solid}). The volume of connected pores (V_{con}) is calculated by subtracting V_{ske} from the volume of the cylindrical sample core (V_{sample}). The volume of isolated pores (V_{iso}) is then calculated by subtracting V_{solid} and V_{con} from V_{sample} . Finally connected (ϕ_{con}) and total (ϕ_{total}) porosities are calculated as:

$$\phi_{con} = \frac{V_{con}}{V_{sample}} \quad (B1)$$

$$\phi_{total} = \frac{(V_{con} + V_{iso})}{V_{sample}} \quad (B2)$$

B.1.2 Equations governing permeability

The permeability of a rock sample is determined using Darcy's law (Rust and Cashman 2004, and references therein), i.e. a constitutive equation that describes the flow of fluid through a porous medium:

$$\frac{\Delta P}{L} = \frac{\mu}{k_a} v \quad (B3)$$

where ΔP is the change in pressure over the sample length (L ; Figure B.1), μ is the fluid viscosity, k_a is apparent permeability, and v is the filter velocity. The variable v is measured as

$$v = \frac{Q}{A} \quad (B4)$$

where Q is the volumetric flow rate and A is the cross-sectional area of the sample orthogonal to fluid flow (Figure B.1). This equation only calculates an apparent permeability because it is only valid for laminar or low-Reynolds number flow in which there is a linear relationship between the pressure gradient and the fluid velocity. In laminar flow, energy loss is entirely due to viscous effects, which result from internal friction due to shear along the no-slip boundary between the fluid and the sample. This criterion becomes insufficient for determining

permeability when energy is also lost due to inertia at higher flow rates, causing a decrease in the apparent permeability calculated using Darcy's law.

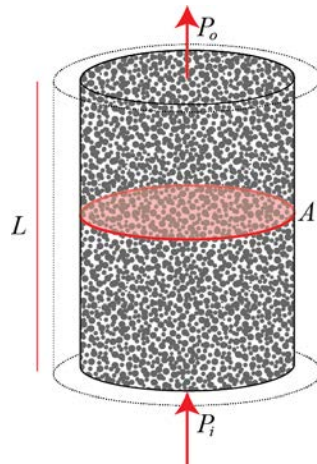


Figure B.1 Schematic of fluid flow through a sample during a permeability measurement. The sample core is of length L , cross sectional area A , and the outside is sealed by impermeable epoxy resin (dotted cylinder). Air is injected at increasing flow rates by increasing the inlet pressure (P_i); the outlet pressure (P_o) is atmospheric.

Rust and Cashman (2004) first recognized that the parabolic relationship between flow rate and the pressure gradient proposed by Reynolds (1900) and Forcheimer (1901) is necessary to determine the permeability of volcanic rocks as high flow rates are used in the measurement.

The Ergun equation calculates a viscous (k_1) and inertial (k_2) permeability in the form of:

$$\frac{\Delta P}{L} = \frac{\mu}{k_1} v + \frac{\rho}{k_2} v^2 \quad (\text{B5})$$

where ρ is the fluid density. Lower resistance due to viscous effects increases k_1 (which has dimensions of length-squared) whereas decreasing resistance to flow from inertial effects (including turbulence) increases the k_2 value (dimensions of length). The equation reduces to Darcy's law as $k_2 \rightarrow \infty$ indicating that inertial effects are negligible.

Due to the compressibility of the fluids used to measure permeability, the fluid expands as it travels from the high to low pressure ends of the sample increasing the gas velocity at the exit. The Forcheimer equation is thus a modification of equation B5 in order to account for compressible fluids:

$$\frac{P_i^2 - P_o^2}{2PL} = \frac{\mu}{k_1} v + \frac{\rho}{k_2} v^2 \quad (\text{B6})$$

In this equation P_i and P_o are the pressure at the sample entrance and exit, respectively, and P is the pressure at which velocity and viscosity are measured or calculated. Often, $P = P_o = 1$ atmosphere so that μ and ρ equate to values at atmospheric pressure. Viscous and inertial permeabilities are derived from the coefficients of a second degree polynomial curve that is fit to a plot of the volumetric flow rate versus the pressure gradient.

B.1.3 Permeability measurement

The permeability of the cylindrical sample cores was measured using a Capillary Flow Porometer (Model CFP-1100AXL-AC, Porous Media, Inc. ©) at Rice University. The samples were mounted on plexiglass plates and their outside edges were sealed with impermeable epoxy resin. They were placed in a cylindrical chamber and sealed except at the base (the inlet) and the top (the outlet). Air was injected at increasing pressure (P_{in}) and flow rate at the inlet, whereas the outlet remained at atmospheric pressure (P_{out}). In order to measure flow rates over several orders of magnitude, to achieve optimal accuracy, each sample was analyzed with 2–3

interchangeable flow meters. The measured volumetric flow rate of air (Q) ranged between 3×10^{-3} and 5×10^{-7} m³/s with an accuracy of $\sim 5 \times 10^{-8}$ m³/s ($\sim 1\%$ of the minimum measured flow rate).

The viscous and inertial permeability were estimated by fitting the Forcheimer equation for a compressible gas to a plot of Q versus ΔP (Figure B.2). In this equation, $P = P_{out} = 1$ atmosphere and so the corresponding air viscosity and density are $\mu = 1.86 \times 10^{-5}$ Pa s and $\rho = 1.28$ kg/m³. A grid search was used to find the k_1 and k_2 combination that minimized the root-mean-square error between the measured and predicted values of $Q(\Delta P)$, defined as

$$\chi = \left[\frac{1}{N} \sum_1^N \left(1 - \frac{Q_{predicted}}{Q_{measured}} \right)^2 \right]^{1/2} \quad (\text{B7})$$

where N is the number of data points for a given sample.

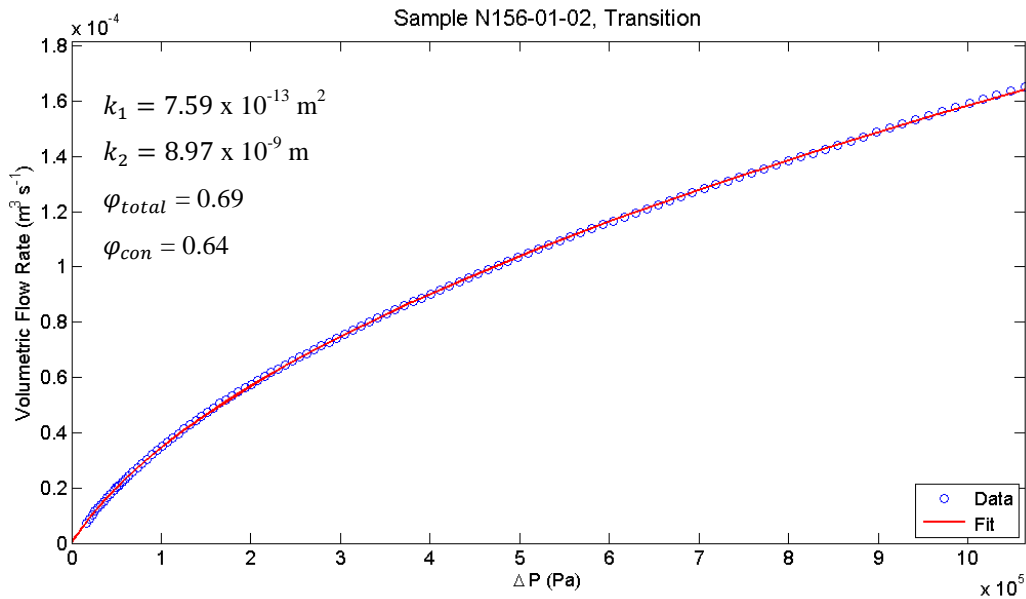
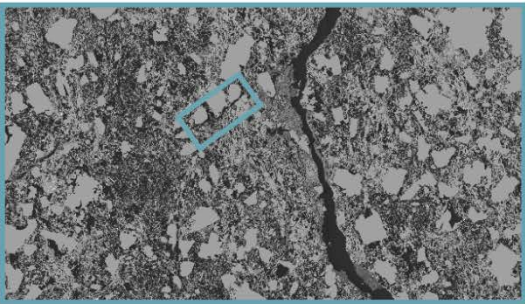


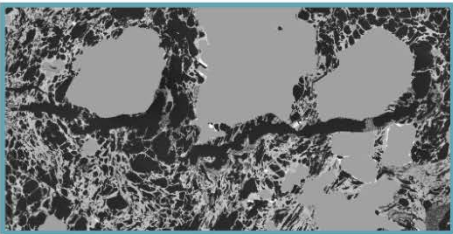
Figure B.2 Estimation of permeability by fitting the Forcheimer equation (*red line*) to the measured volumetric flow rate as a function of pressure difference across the sample.

B.2 Images of porous pathways in thin section

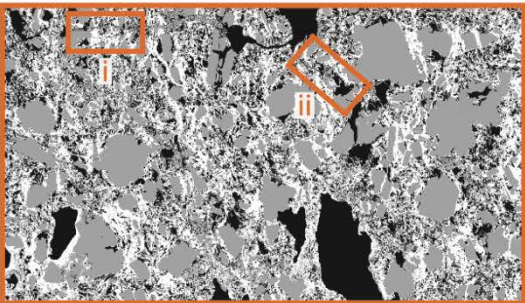
a



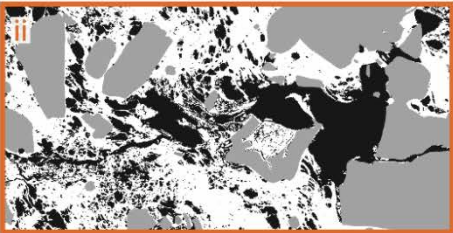
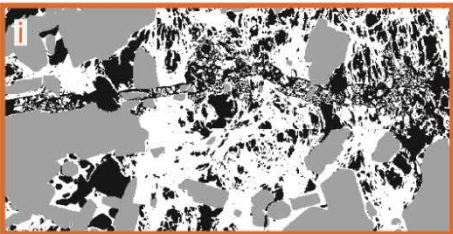
b



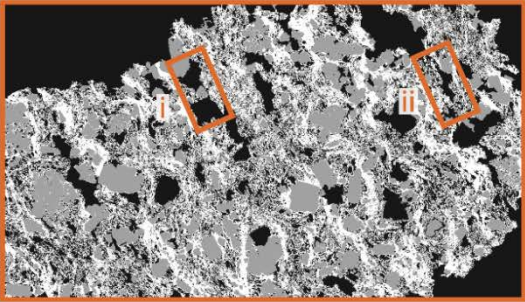
c



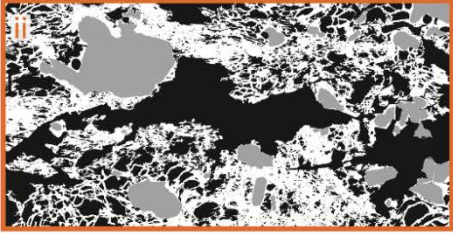
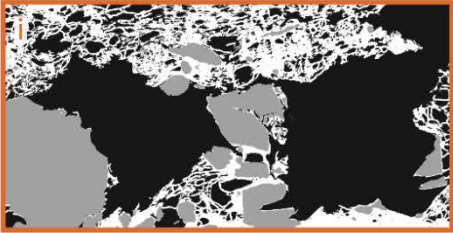
d



e



f



5 mm

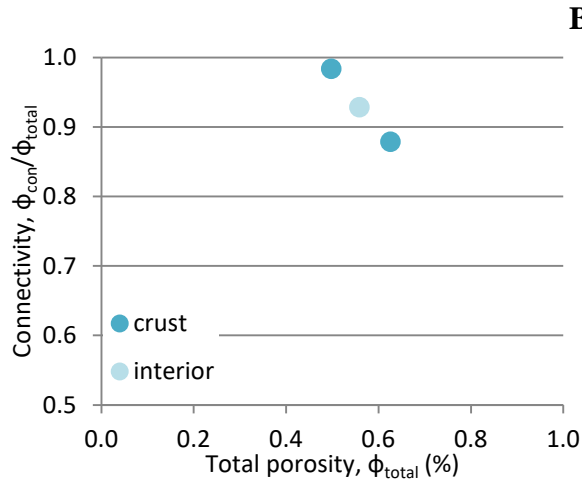
1 mm

Figure B.3 (previous page) Examples of porous pathways within grayscale images of the crusts. Colored rectangles outline the locations of the magnified images on the right. Images **a**, **c**, and **e** match those in Figure 3.6 of the main paper. **b** Example of a porous pathway with rounded edges. **d(i)** Example of a porous pathway that is filled with fine clastic debris (i.e. crystals and glass). **d(ii)** A porous pathway of varying throat size as it is connected with (or ‘travels through’) bubbles of different sizes. **f(i and ii)** Examples of clear porous pathways of varying throat size.

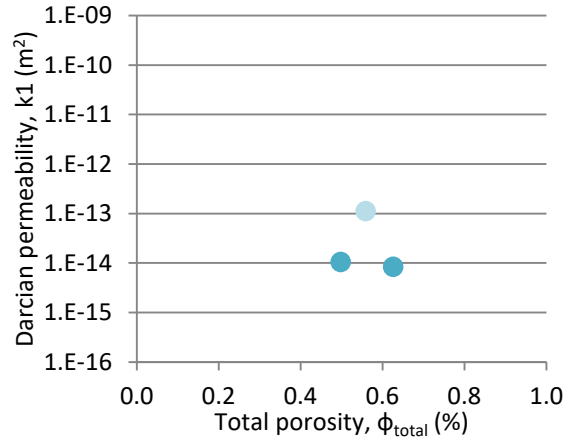
B.3 Additional data

Figure B.4 Connectivity and permeability for individual breadcrusted blocks

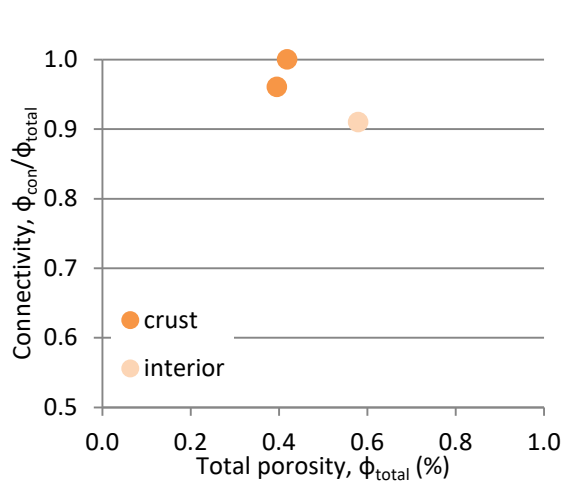
Vesicular breadcrusted group 1



Block N004



Vesicular breadcrusted group 2



Block N005

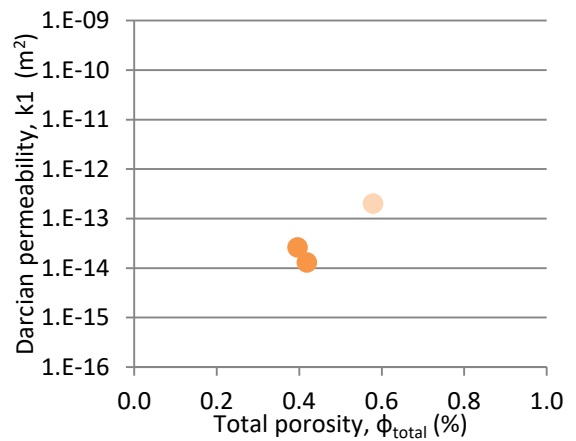


Figure B.4 Continued. *Vesicular breadcrusted group 2*

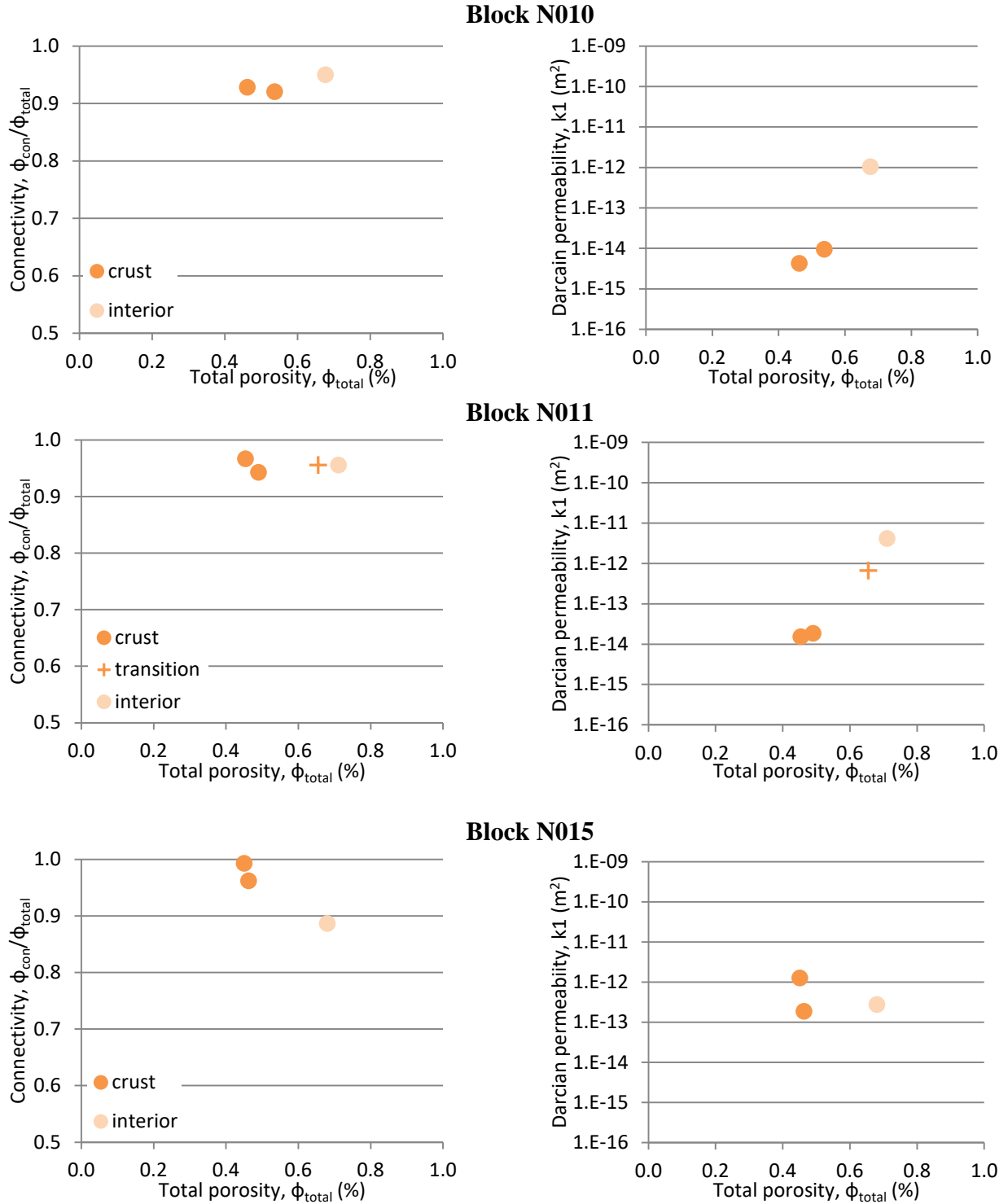
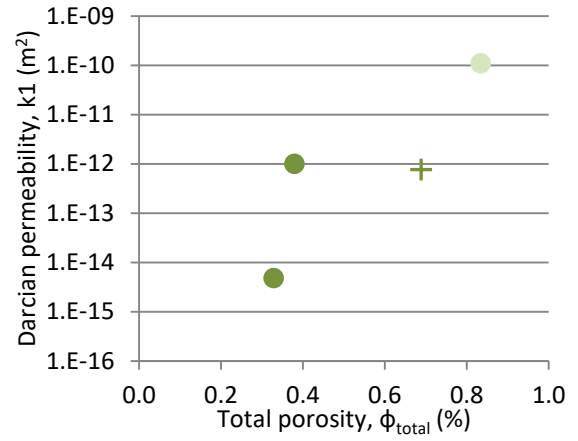
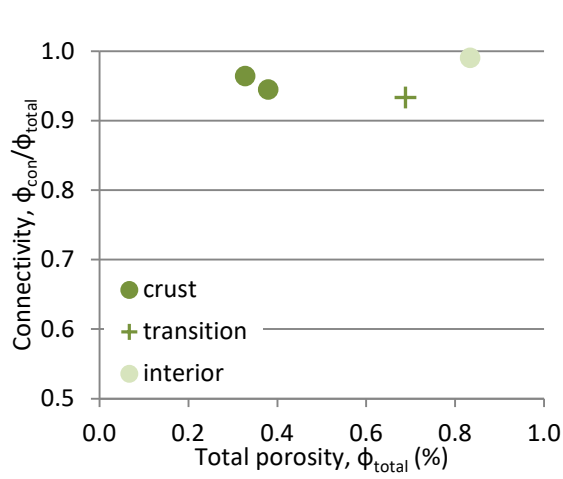
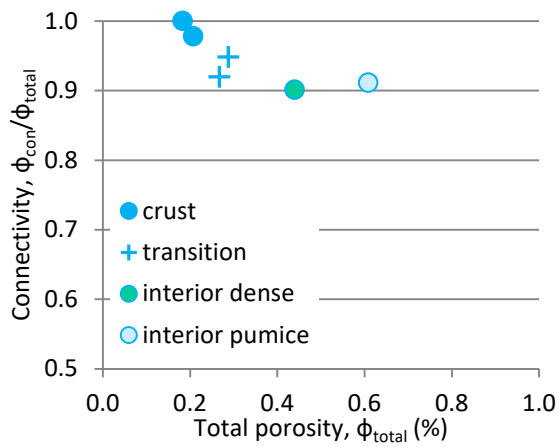


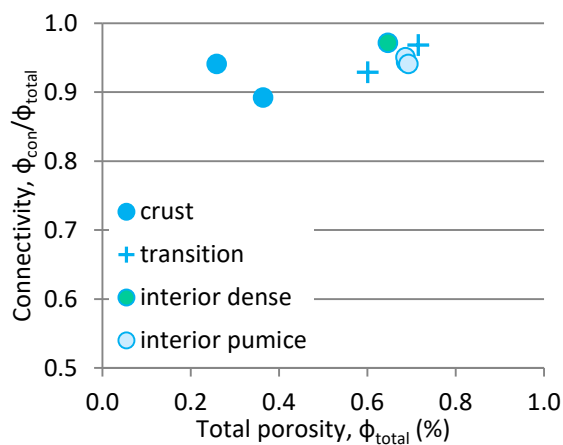
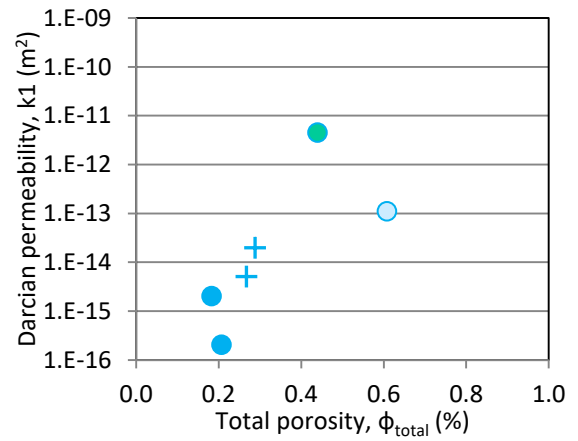
Figure B.4 Continued. Vesicular breadcrusted group 3



Breadcrusted mixed banded



Block B281



Block B129

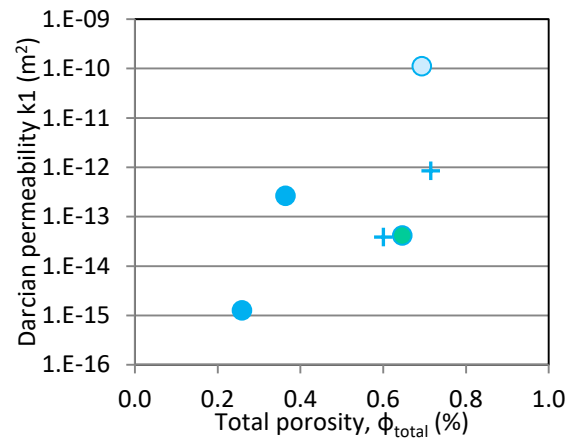
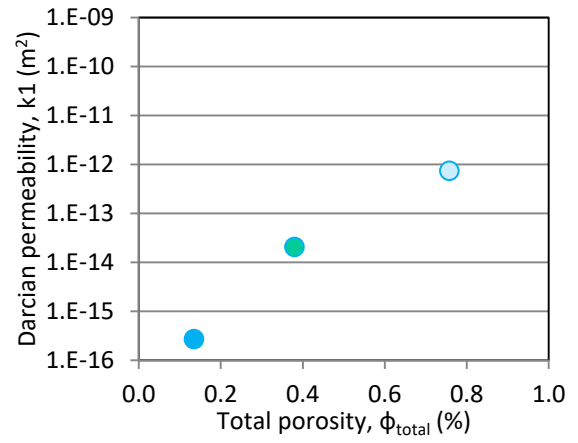
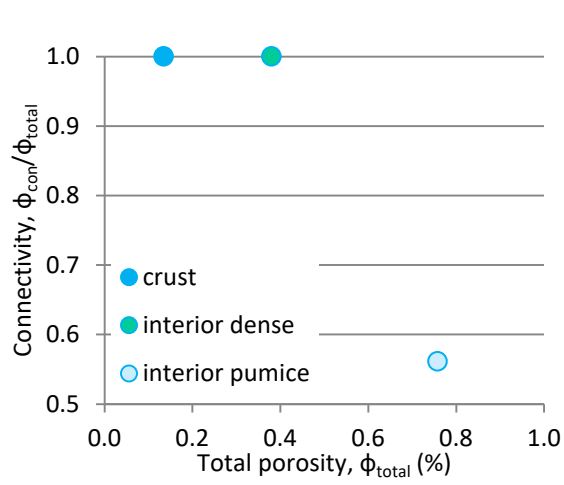


Figure B.4 Continued. *Breadcrusted mixed banded*



Breadcrusted banded pumice

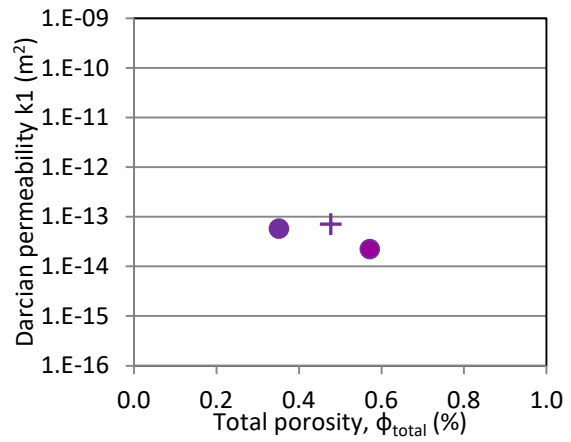
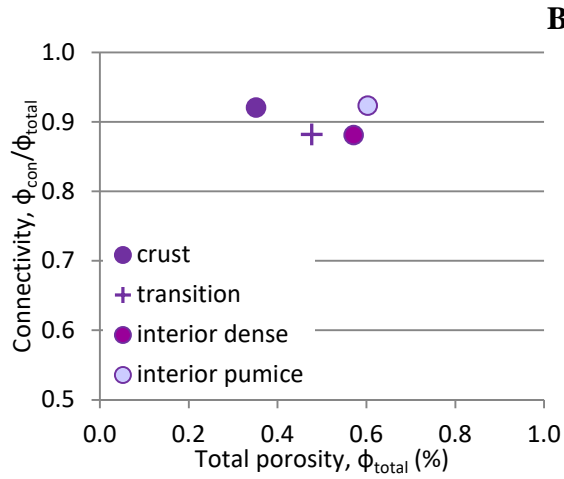


Table B.1 Timescales for diffusion of water in a low water content (<2 wt%) rhyolite melt

H ₂ O (wt%)	D* (m ² /s)	Time (days) for given distance		
		1 mm	1 cm	1 m
0.1	2.70E-13	21.4	2139.4	2.14E+07
0.5	1.35E-12	4.3	427.9	4.28E+06
1	2.70E-12	2.1	213.9	2.14E+06
1.5	4.06E-12	1.4	142.6	1.43E+06
2	5.41E-12	1.1	107.0	1.07E+06

*Diffusivity calculated using the equation for water diffusivity from Baker et al. (2005), modified after Zhang and Behrens (2000), and using a temperature of 1123 K and for low pressure (<5 MPa).

APPENDIX C

Chapter 4 Supplementary Material

C.1 Additional figures

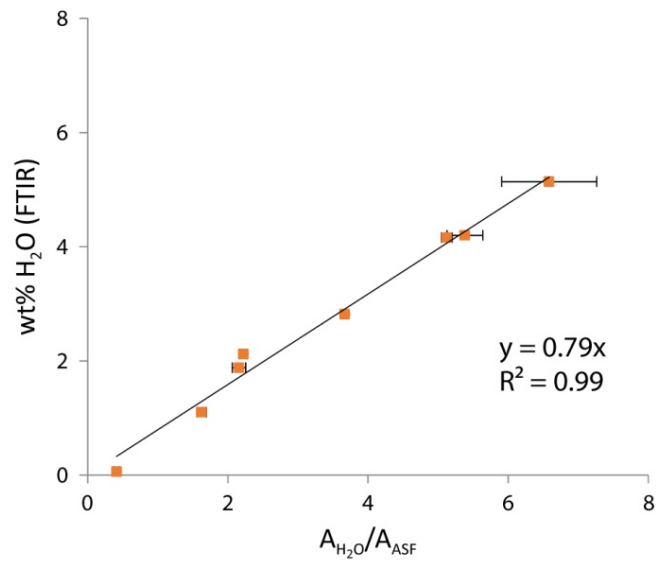


Figure C.1 The H₂O versus band ratio calibration curve used for the estimate of glass water content via microRaman spectroscopy. The band ratio is the area underneath the H₂O band divided by the area under the ASF band. Error bars not shown are smaller than symbol size.

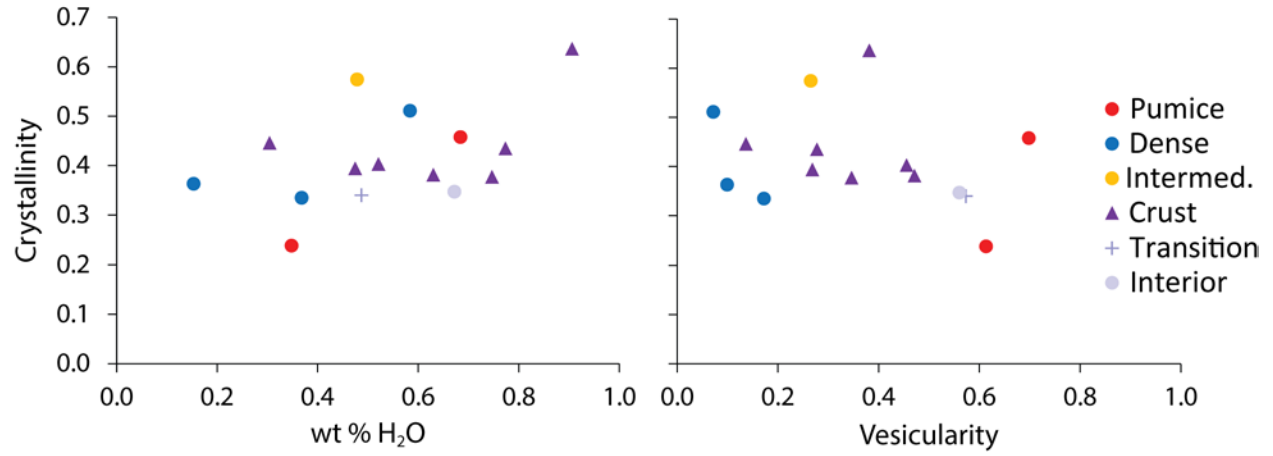


Figure C.2 Phenocryst crystallinities (vesicle-free, i.e., referenced to glass + crystals) versus water content (*left*) and vesicularity (*right*) for clasts measured by the Flash 2000 (water contents are measured by Flash 2000 only).



Figure C.3 Reflected light image of textural heterogeneity in thick section C43 from the crust of breadcrusted block N455 (see Table 4.1 for bulk properties). Vesicles/pores are shown in *black*; oxides are *white*, all other phenocrysts are generally a *lighter olive-yellow* color than the glass; however, some phenocrysts are the same color as the glass and are discernable only by texture. *Diameter* of the thick section is 1 cm. Note how the lower half of the section appears more porous than the upper portion.

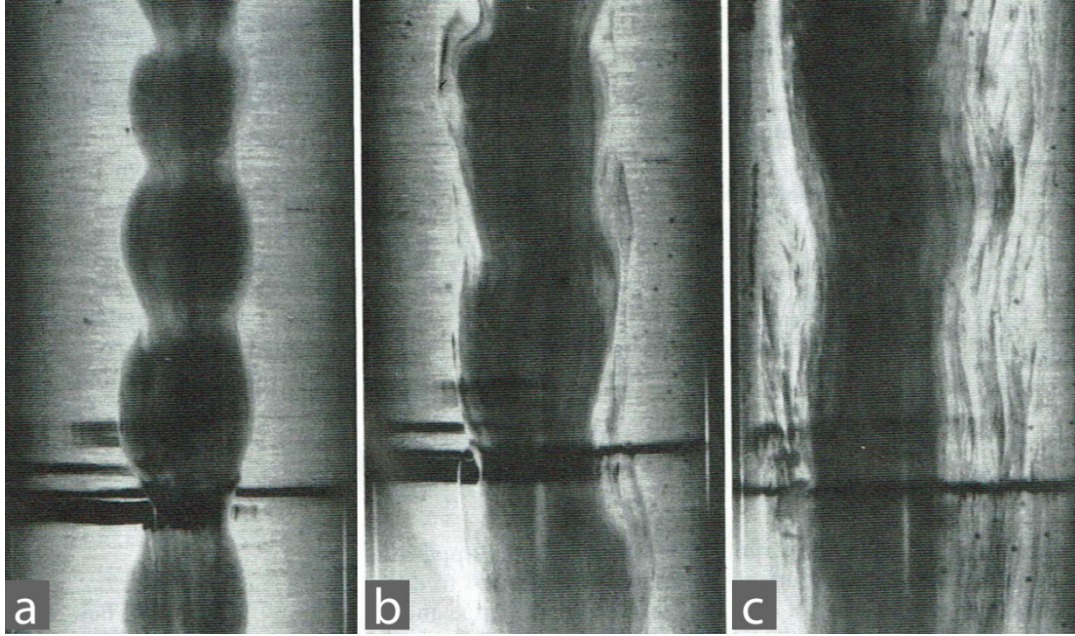


Figure C.4 Photographs of the development of instabilities between lower viscosity (*dark interior*) and higher viscosity (*lighter exterior*) fluids traveling through a pipe under changing flow conditions ($Q' = Q_o/(Q_o + Q_i)$) where Q_o is the flow rate of the outer fluid and Q_i is the flow rate of the inner fluid. The outer more viscous fluid was either glycerol or an aqueous carboxymethylcellulose (CMC) solution. The less viscous inner fluid was made from 28% aqueous potassium carbonate solution \pm glycerol or from dilute aqueous NaCl solutions if the outer fluid was CMC solution. The authors did not specify which fluids were utilized in these photographed experiments. The densities were equal and the ratio of kinematic viscosities for the outer (ν_o) and inner (ν_i) fluids is $\nu_o/\nu_i \cong 40$. *Outer diameter* of the pipe is 19 mm and flow direction is from top to bottom. **a** $Q' = 0.84$; note the development of periodic pinch and swell structures. **b** $Q' = 0.68$; with increasing flow rate of the lower viscosity fluid the edges of the swell structures become sheared off into eddies on their upstream side. **c** $Q' = 0.45$; at even higher Q_i the instabilities become amplified such that wavy streaks of the inner fluid become entrained into the more viscous outer fluid. Over a range of viscosity and flow rate ratios across numerous experiments, instability and mixing/mingling proceeded when Re (calculated using the properties of the inner fluid: $Re_i = Q_i/\pi\nu_i R_i$ where R_i is the radius of the inner fluid) was greater than ~ 3 if 10–90% of the total fluid was composed of the more viscous fluid. Figure and observations/data from Blake and Campbell (1986).

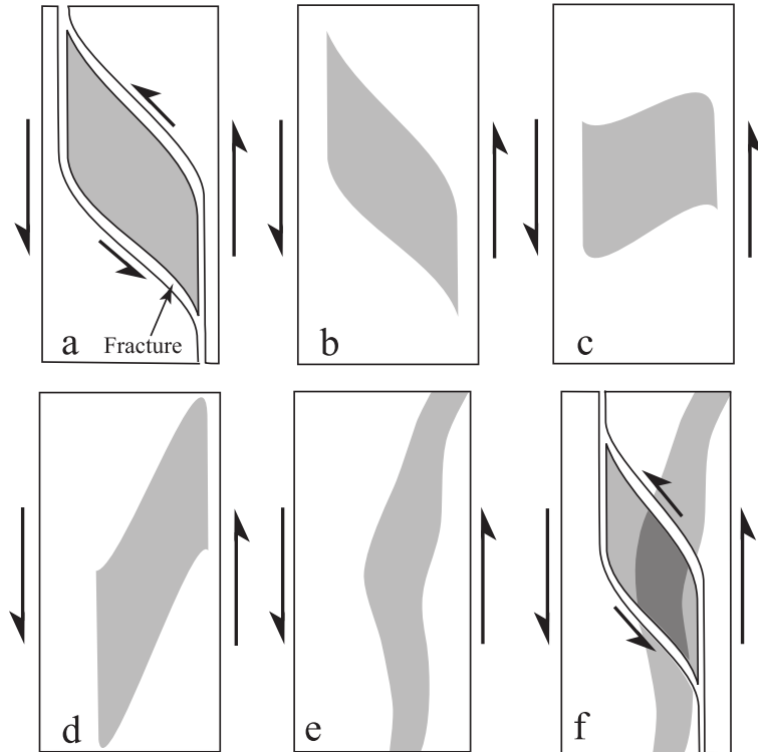


Figure C.5 Conceptual model of Gonnermann and Manga (2005) for the in-situ formation of texturally contrasting bands. **a** Brittle deformation during simple shear results in a single fragment that has undergone a change in texture (represented by the *dark color*). **b** The fragments then weld back together. **c-e** Viscous deformation in response to simple shear stretches the welded fragment into light and dark colored bands. **f** Brittle deformation alters the textures of adjacent bands resulting in a second generation texture. Continued cycles of brittle and viscous deformation results in multifractal bands. Figure from Gonnermann and Manga (2005).

References

- Abe K (1992) Seismicity of the caldera-making eruption of Mount Katmai, Alaska in 1912. *Bull Seismol Soc Am* 82:175–191.
- Adams NK (2005) Magma degassing during the 1912 eruption of Novarupta, Alaska: Textural analyses of pyroclasts representing changes in eruptive intensity and style. Dissertation, University of Hawai‘i at Mānoa
- Adams NK, Houghton BF, Fagents SA, Hildreth W (2006a) The transition from explosive to effusive eruptive regime: The example of the 1912 Novarupta eruption, Alaska. *Bull Geol Soc Am* 118:620–634. doi: 10.1130/B25768.1
- Adams NK, Houghton BF, Hildreth W (2006b) Abrupt transitions during sustained explosive eruptions: Examples from the 1912 eruption of Novarupta, Alaska. *Bull Volcanol* 69:189–206. doi: 10.1007/s00445-006-0067-4
- Alatorre-Ibargüengoitia MA, Delgado-Granados H (2006) Experimental determination of drag coefficient for volcanic materials: Calibration and application of a model to Popocatepetl volcano (Mexico) ballistic projectiles. *Geophys Res Lett* 33:1–5. doi: 10.1029/2006GL026195
- Alatorre-Ibargüengoitia MA, Delgado-Granados H, Dingwell DB (2012) Hazard map for volcanic ballistic impacts at Popocatepetl volcano (Mexico). *Bull Volcanol* 74:2155–2169. doi: 10.1007/s00445-012-0657-2
- Alatorre-Ibargüengoitia MA, Scheu B, Dingwell DB, et al (2010) Energy consumption by magmatic fragmentation and pyroclast ejection during Vulcanian eruptions. *Earth Planet Sci Lett* 291:60–69. doi: 10.1016/j.epsl.2009.12.051
- Alidibirov MA (1994) A model for viscous magma fragmentation during volcanic blasts. *Bull Volcanol* 56:459–465. doi: 10.1007/BF00302827
- Allen ET, Zies EG (1923) A chemical study of the fumaroles of the Katmai region. National Geographic Society, Contributed Technical Papers, Katmai Series 2, 75-155
- Ashwell PA, Kendrick JE, Lavallée Y, et al (2015) Permeability of compacting porous lavas. *J Geophys Res Solid Earth* 120:1605–1622. doi: 10.1002/2014JB011519
- Bagheri G, Bonadonna C (2016) Aerodynamics of Volcanic Particles. In: Mackie S, Cashman K, Ricketts H, et al. (eds) *Volcanic Ash*. Elsevier, Amsterdam, pp 39–52
- Bagheri G, Rossi E, Biass S, Bonadonna C (2016) Timing and nature of volcanic particle clusters based on field and numerical investigations. *J Volcanol Geotherm Res* 327:520–530. doi: 10.1016/j.jvolgeores.2016.09.009

- Baker DR, Freda C, Brooker RA, Scarlato P (2005) Volatile diffusion in silicate melts and its effects on melt inclusions. *Ann Geophys* 48:699–717. doi: 10.4401/ag-3227
- Behrens H, Roux J, Neuville DR, Siemann M (2006) Quantification of dissolved H₂O in silicate glasses using confocal microRaman spectroscopy. *Chem Geol* 229:96–112. doi: 10.1016/j.chemgeo.2006.01.014
- Benage MC, Dufek J, Degruyter W, et al (2014) Tying textures of breadcrust bombs to their transport regime and cooling history. *J Volcanol Geotherm Res* 274:92–107. doi: 10.1016/j.jvolgeores.2014.02.005
- Bernard ML, Zamora M, Géraud Y, Boudon G (2007) Transport properties of pyroclastic rocks from Montagne Pelée volcano (Martinique, Lesser Antilles). *J Geophys Res Solid Earth* 112:1–16. doi: 10.1029/2006JB004385
- Bernstein M, Pavez A, Varley N, et al (2013) Estilos de crecimiento del domo de lava riolítico del Chaitén (2008-2009): Interpretación de imágenes térmicas. *Andean Geol* 40:295–309. doi: 10.5027/andgeoV40n2-a07
- Bertin D (2017) 3-D ballistic transport of ellipsoidal volcanic projectiles considering horizontal wind field and variable shape-dependent drag coefficients. *J Geophys Res Solid Earth* 122:1126–1151. doi: 10.1002/2016JB013320
- Bindeman IN, Lowenstern JB (2016) Low- δ D hydration rinds in Yellowstone perlites record rapid syneruptive hydration during glacial and interglacial conditions. *Contrib to Mineral Petrol* 171:1–24. doi: 10.1007/s00410-016-1293-1
- Blake S, Campbell IH (1986) The dynamics of magma-mixing during flow in volcanic conduits. *Contrib to Mineral Petrol* 94:72–81. doi: 10.1007/BF00371228
- Blower J (2001) Factors controlling permeability-porosity relationships in magma. *Bull Volcanol* 63:497–504. doi: 10.1007/s004450100172
- Blundy J, Cashman K (2001) Ascent-driven crystallisation of dacite magmas at Mount St Helens, 1980-1986. *Contrib to Mineral Petrol* 140:631–650. doi: 10.1007/s004100000219
- Blundy J, Cashman K (2005) Rapid decompression-driven crystallization recorded by melt inclusions from Mount St. Helens volcano. *Geology* 33:793–796. doi: 10.1130/G21668.1
- Bluth GJS, Rose WI (2004) Observations of eruptive activity at Santiaguito volcano, Guatemala. *J Volcanol Geotherm Res* 136:297–302. doi: 10.1016/j.jvolgeores.2004.06.001
- Boudon G, Balcone-Boissard H, Villemant B, Morgan DJ (2015) What factors control superficial lava dome explosivity? *Sci Rep* 5:14551. doi: 10.1038/srep14551
- Bouvet de Maisonneuve C, Bachmann O, Burgisser A (2009) Characterization of juvenile pyroclasts from the Kos Plateau Tuff (Aegean Arc): insights into the eruptive dynamics

- of a large rhyolitic eruption. *Bull Volcanol* 71:643–658. doi: 10.1007/s00445-008-0250-x
- Burgisser A, Arbaret L, Druitt TH, Giachetti T (2011) Pre-explosive conduit conditions of the 1997 Vulcanian explosions at Soufrière Hills Volcano, Montserrat: II. Overpressure and depth distributions. *J Volcanol Geotherm Res* 199:193–205. doi: 10.1016/j.jvolgeores.2010.11.014
- Burgisser A, Gardner JE (2005) Experimental constraints on degassing and permeability in volcanic conduit flow. *Bull Volcanol* 67:42–56. doi: 10.1007/s00445-004-0359-5
- Burgisser A, Poussineau S, Arbaret L, et al (2010) Pre-explosive conduit conditions of the 1997 Vulcanian explosions at Soufrière Hills Volcano, Montserrat: I. Pressure and vesicularity distributions. *J Volcanol Geotherm Res* 194:27–41. doi: 10.1016/j.jvolgeores.2010.04.008
- Calder ES, Lockett R, Sparks RSJ, Voight B (2002) Mechanisms of lava dome instability and generation of rockfalls and pyroclastic flows at Soufrière Hills Volcano, Montserrat. *Geol Soc London, Mem* 21:173–190. doi: 10.1144/GSL.MEM.2002.021.01.08
- Campbell IH, Turner JS (1989) Fountains in Magma Chambers. *J Petrol* 30:885–923. doi: 10.1093/petrology/30.4.885
- Cas RAF, Wright JV (1987) Volcanic successions, modern and ancient: a geological approach to processes, products and successions. Allen & Unwin, London, 528 pp.
- Cashman K V, Mangan MT (1994) Physical aspects of magmatic degassing; II, Constraints on vesiculation processes from textural studies of eruptive products. *Rev Mineral Geochemistry* 30:447–478.
- Cashman K V, McConnell SM (2005) Multiple levels of magma storage during the 1980 summer eruptions of Mount St. Helens, WA. *Bull Volcanol* 68:57–75. doi: 10.1007/s00445-005-0422-x
- Cashman K V, Scheu B (2015) Magmatic Fragmentation. In: Sigurdsson H, Houghton BF, McNutt SR, et al. (eds) *The Encyclopedia of Volcanoes, Second*. Academic Press, pp 459–472
- Cassidy M, Cole PD, Hicks KE, et al (2015) Rapid and slow: Varying magma ascent rates as a mechanism for Vulcanian explosions. *Earth Planet Sci Lett* 420:73–84. doi: 10.1016/j.epsl.2015.03.025
- Castro JM, Bindeman IN, Tuffen H, Ian Schipper C (2014) Explosive origin of silicic lava: Textural and $\delta D-H_2O$ evidence for pyroclastic degassing during rhyolite effusion. *Earth Planet Sci Lett* 405:52–61. doi: 10.1016/j.epsl.2014.08.012
- Castro JM, Cordonnier B, Tuffen H, et al (2012) The role of melt-fracture degassing in defusing

- explosive rhyolite eruptions at volcán Chaitén. *Earth Planet Sci Lett* 333–334:63–69. doi: 10.1016/j.epsl.2012.04.024
- Chevalier L, Collombet M, Pinel V (2017) Temporal evolution of magma flow and degassing conditions during dome growth, insights from 2D numerical modeling. *J Volcanol Geotherm Res* 341:371–373. doi: 10.1016/j.jvolgeores.2017.06.008
- Chojnicki K, Clarke AB, Phillips JC (2006) A shock-tube investigation of the dynamics of gas-particle mixtures: Implications for explosive volcanic eruptions. *Geophys Res Lett* 33:L15309. doi: 10.1029/2006GL026414
- Chouet B, Hamisevicz N, McGetchin TR (1974) Photoballistics of volcanic jet activity at Stromboli, Italy. *J Geophys Res B Solid Earth* 79:4961–4976. doi: 10.1029/JB079i032p04961
- Christiansen RL, Peterson DW (1981) Chronology of the 1980 eruptive activity. In: Lipman PW, Mullineaux DR (eds) *The 1980 Eruptions of Mount St. Helens, Washington*. U.S. Geological Survey Professional Paper 1250, pp 17–31
- Cioni R, Pistolesi M, Rosi M (2015) Plinian and subplinian eruptions. In: Sigurdsson H, Houghton BF, McNutt SR, et al. (eds) *Encyclopedia of Volcanoes*, 2nd edn. Academic Press, pp 519–536
- Clarke AB (2013) Unsteady explosive activity: vulcanian eruptions. In: Fagents SA, Gregg TKP, Lopes RMC (eds) *Modeling Volcanic Processes*. Cambridge University Press, pp 129–152
- Clarke AB, Esposti Ongaro T, Belousov A (2015) Vulcanian Eruptions. In: Sigurdsson H, Houghton BF, McNutt SR, et al. (eds) *The Encyclopedia of Volcanoes*, Second. Academic Press, pp 505–518
- Clarke AB, Neri A, Voight B, et al (2002a) Computational modelling of the transient dynamics of the August 1997 Vulcanian explosions at Soufrière Hills Volcano, Montserrat: influence of initial conduit conditions on near-vent pyroclastic dispersal. In: Druitt TH, Kokelaar BP (eds) *The eruption of Soufrière Hills volcano, Montserrat, from 1995 to 1999*. The Geological Society, London, pp 319–348
- Clarke AB, Stephens S, Teasdale R, et al (2007) Petrologic constraints on the decompression history of magma prior to Vulcanian explosions at the Soufrière Hills volcano, Montserrat. *J Volcanol Geotherm Res* 161:261–274. doi: 10.1016/j.jvolgeores.2006.11.007
- Clarke AB, Voight B, Neri A, Macedonio G (2002b) Transient dynamics of vulcanian explosions and column collapse. *Nature* 415:897–901. doi: 10.1038/415897a
- Cole PD, Stinton AJ, Odbert HM, et al (2014) An inclined Vulcanian explosion and associated

- products. *J Geol Soc London* 172:287–293. doi: 10.1144/jgs2014-099
- Colombier M, Wadsworth FB, Gurioli L, et al (2017) The evolution of pore connectivity in volcanic rocks. *Earth Planet Sci Lett* 462:99–109. doi: 10.1016/j.epsl.2017.01.011
- Coombs ML, Bull KF, Vallance JW, Schneider DJ, Thoms EE, Wessels RL, McGimsey RG (2010) Timing, Distribution, and Volume of Proximal Products of the 2006 Eruption of Augustine Volcano. In: Power JA, Coombs ML, Freymueller JT (Eds.) *The 2006 Eruption of Augustine Volcano, Alaska, U.S. Geological Survey Professional Paper* 1769, pp. 145-185.
- Coombs ML, Eichelberger JC, Rutherford MJ (2000) Magma storage and mixing conditions for the 1953-1974 eruptions of Southwest Trident volcano, Katmai National Park, Alaska. *Contrib to Mineral Petrol* 140:99–118. doi: 10.1007/s004100000166
- Coombs ML, Gardner JE (2001) Shallow-storage conditions for the rhyolite of the 1912 eruption at Novarupta, Alaska. *Geology* 29:775–778. doi:10.1130/0091-7613(2001)029<0775:SSCFTR>2.0.CO;2
- Couch S (2003) The Kinetics of Degassing-Induced Crystallization at Soufriere Hills Volcano, Montserrat. *J Petrol* 44:1477–1502. doi: 10.1093/petrology/44.8.1477
- Curtis GH (1968) The stratigraphy of the ejecta from the 1912 eruption of Mount Katmai and Novarupta, Alaska. In Coats RR, Hay RL, Anderson, CA (Eds.) *Studies in Volcanology*, Geological Society of America Memoir 11, pp.153-210.
- de Campos CP, Perugini D, Ertel-Ingrisch W, et al (2011) Enhancement of magma mixing efficiency by chaotic dynamics: An experimental study. *Contrib to Mineral Petrol* 161:863–881. doi: 10.1007/s00410-010-0569-0
- de' Michieli Vitturi M, Neri A, Esposti Ongaro T, et al (2010) Lagrangian modeling of large volcanic particles: Application to Vulcanian explosions. *J Geophys Res Solid Earth* 115:1–18. doi: 10.1029/2009JB007111
- DeGroat-Nelson PJ, Cameron BI, Fink JH, Holloway JR (2001) Hydrogen isotope analysis of rehydrated silicic lavas: Implications for eruption mechanisms. *Earth Planet Sci Lett* 185:331–341. doi: 10.1016/S0012-821X(00)00379-4
- Degruyter W, Bachmann O, Burgisser A, Manga M (2012) The effects of outgassing on the transition between effusive and explosive silicic eruptions. *Earth Planet Sci Lett* 349–350:161–170. doi: 10.1016/j.epsl.2012.06.056
- Detterman RL, Case JE, Miller JW, Wilson FH, Yount ME (1996) Stratigraphic Framework of the Alaska Peninsula. *U.S. Geological Survey Bulletin* 1969-A, 80 p.
- Di Muro A, Giordano D, Villemant B, et al (2006) Influence of composition and thermal history

- of volcanic glasses on water content as determined by micro-Raman spectrometry. doi: 10.1016/j.apgeochem.2006.02.009
- Diller K, Clarke AB, Voight B, Neri A (2006) Mechanisms of conduit plug formation: Implications for vulcanian explosions. *Geophys Res Lett* 33:1–6. doi: 10.1029/2006GL027391
- Dimotakis PE (2000) The mixing transition in turbulent flows. *J Fluid Mech* 409:S0022112099007946. doi: 10.1017/S0022112099007946
- Dingwell DB, Lavallée Y, Hess KU, et al (2016) Eruptive shearing of tube pumice: Pure and simple. *Solid Earth* 7:1383–1393. doi: 10.5194/se-7-1383-2016
- Dobson PF, Epstein S, Stolper EM (1989) Hydrogen isotope fractionation between coexisting vapor and silicate glasses and melts at low pressure. *Geochim Cosmochim Acta* 53:2723–2730. doi: [https://doi.org/10.1016/0016-7037\(89\)90143-9](https://doi.org/10.1016/0016-7037(89)90143-9)
- Drignon MJ, Bechon T, Arbaret L, et al (2016) Preexplosive conduit conditions during the 2010 eruption of Merapi volcano (Java, Indonesia). *Geophys Res Lett* 43:11,595–11,602. doi: 10.1002/2016GL071153
- Druitt TH, Young SR, Baptie B, et al (2002) Episodes of cyclic Vulcanian explosive activity with fountain collapse at Soufrière Hills Volcano, Montserrat. In: Druitt TH, Kokelaar BP (eds) *The eruption of Soufrière Hills volcano, Montserrat, from 1995 to 1999*. The Geological Society, London, pp 281–306
- Eichelberger JC (1980) Vesiculation of mafic magma during replenishment of silicic magma reservoirs. *Nature* 288:446.
- Eichelberger JC (1995) Silicic Volcanism: Ascent of Viscous Magmas from Crustal Reservoirs. *Annu Rev Earth Planet Sci* 23:41–63. doi: doi:10.1146/annurev.ea.23.050195.000353
- Eichelberger JC, Carrigan CR, Westrich HR, Price RH (1986) Non-explosive silicic volcanism. *Nature* 323:448–450. doi: 10.1038/323598a0
- Eichelberger JC., Izbekov PE. (2000) Eruption of Andesite Triggered by Dyke Injection: Contrasting Cases at Karymsky Volcano, Kamchatka and Mt Katmai, Alaska. *Philos Trans Math , Phys Eng Sci* 358:1465–1485.
- Fagents SA, Wilson L (1993) Explosive volcanic eruptions-VII. The ranges of pyroclasts ejected in transient volcanic explosions. *Geophys J Int* 113:359–370.
- Farquharson JJ, Heap MJ, Lavallée Y, et al (2016) Evidence for the development of permeability anisotropy in lava domes and volcanic conduits. *J Volcanol Geotherm Res* 323:163–185. doi: 10.1016/j.jvolgeores.2016.05.007

- Fenner, CN (1920) The Katmai region, Alaska, and the great eruption of 1912. *Journal of Geology* 28, 569-606.
- Fierstein J, Hildreth W (1992) The plinian eruptions of 1912 at Novarupta, Katmai National Park, Alaska. 54:646–684. doi: 10.1007/BF00430778
- Fierstein J, Houghton BF, Wilson CJN, Hildreth W (1997) Complexities of plinian fall deposition at vent: an example from the 1912 Novarupta eruption (Alaska). *J Volcanol Geotherm Res* 76:215–227. doi: 10.1016/S0377-0273(96)00081-9
- Fierstein J, Wilson CJN (2005) Assembling an ignimbrite: Compositionally defined eruptive packages in the 1912 Valley of Ten Thousand Smokes ignimbrite, Alaska. *Bull Geol Soc Am* 117:1094–1107. doi: 10.1130/B25621.1
- Fink JH, Anderson SW, Manley CR (1992) Textural constraints on effusive silicic volcanism: Beyond the permeable foam model. *J Geophys Res* 97:9073–9083. doi: 10.1029/92JB00416
- Fink JH, Manley CR (1987) Origin of pumiceous and glassy textures in rhyolite flows and domes. In: *The emplacement of silicic domes and lava flows*, 212th edn. Geological Society of America, pp 77–88
- Flinders J, Clemens JD (1996) Non-linear dynamics, chaos, complexity and enclaves in granitoid magmas. In: *Special Paper 315: The Third Hutton Symposium on the Origin of Granites and Related Rocks*. Geological Society of America, pp 217–223
- Forcheimer, P (1901) Wasserbewegung durch Boden. *Z Ver Dtsch Ing* 45:1781-1788.
- Freundt A, Tait SR (1986) The entrainment of high-viscosity magma into low-viscosity magma in eruption conduits. *Bull Volcanol* 48:325–339. doi: 10.1007/BF01074464
- Friedman I, Gleason J, Sheppard RA, Gude AJ (1993a) Deuterium Fractionation as Water Diffuses into Silicic Volcanic Ash. In: *Climate Change in Continental Isotopic Records*. American Geophysical Union, pp 321–323
- Friedman I, Gleason J, Warden A (1993b) Ancient Climate from Deuterium Content of Water in Volcanic Glass. In: *Climate Change in Continental Isotopic Records*. American Geophysical Union, pp 309–319
- Friedman I, Smith RL, Long WD (1966) Hydration of natural glass and formation of Perlite. *Geol Soc* 77:323–328.
- Fudali RF, Melson WG (1971) Ejecta velocities, magma chamber pressure and kinetic energy associated with the 1968 eruption of Arenal volcano. *Bull Volcanol* 35:383–401. doi: 10.1007/BF02596963
- Gardner JE, Hilton M, Carroll MR (1999) Experimental constraints on degassing of magma:

- Isothermal bubble growth during continuous decompression from high pressure. *Earth Planet Sci Lett* 168:201–218. doi: 10.1016/S0012-821X(99)00051-5
- Gardner JE, Hilton M, Carroll MR (2000) Bubble growth in highly viscous silicate melts during continuous decompression from high pressure. *Geochim Cosmochim Acta* 64:1473–1483. doi: 10.1016/S0016-7037(99)00436-6
- Gardner JE, Thomas R, Jaupart C, Tait S (1996) Fragmentation of magma during Plinian volcanic eruptions. *Bull Volcanol* 58:144–162. doi: 10.1007/s004450050132
- Gaunt HE, Sammonds PR, Meredith PG, et al (2014) Pathways for degassing during the lava dome eruption of Mount St. Helens 2004–2008. *Geology* 42:947–950. doi: 10.1130/G35940.1
- Geschwind C-H, Rutherford MJ (1995) Crystallization of microlites during magma ascent: the fluid mechanics of 1980–1986 eruptions at Mount St Helens. *Bull Volcanol* 57:356–370. doi: 10.1007/BF00301293
- Giachetti T, Druitt TH, Burgisser A, et al (2010) Bubble nucleation, growth and coalescence during the 1997 Vulcanian explosions of Soufrière Hills Volcano, Montserrat. *J Volcanol Geotherm Res* 193:215–231. doi: 10.1016/j.jvolgeores.2010.04.001
- Giachetti T, Gonnermann HM (2013) Water in volcanic pyroclast: Rehydration or incomplete degassing? *Earth Planet Sci Lett* 369–370:317–332. doi: 10.1016/j.epsl.2013.03.041
- Giachetti T, Gonnermann HM, Gardner JE, et al (2015) Discriminating secondary from magmatic water in rhyolitic matrix-glass of volcanic pyroclasts using thermogravimetric analysis. *Geochim Cosmochim Acta* 148:457–476. doi: 10.1016/j.gca.2014.10.017
- Global Volcanism Program (2005) Report on Reventador (Ecuador). In: Winderman R (Ed.) *Bulletin of the Global Volcanism Network*. 30: 8. Smithsonian Institution. Downloaded November 15, 2017. <http://dx.doi.org/10.5479/si.GVP.BGVN200508-352010>
- Gonnermann HM, Houghton BF (2012) Magma degassing during the Plinian eruption of Novarupta, Alaska, 1912. *Geochemistry, Geophys Geosystems* 13:n/a-n/a. doi: 10.1029/2012GC004273
- Gonnermann HM, Manga M (2005a) Nonequilibrium magma degassing: Results from modeling of the ca. 1340 A.D. eruption of Mono Craters, California. doi: 10.1016/j.epsl.2005.07.021
- Gonnermann HM, Manga M (2003) Explosive volcanism may not be an inevitable consequence of magma fragmentation. *Nature* 426:432–435. doi: 10.1038/nature02138
- Gonnermann HM, Manga M (2005b) Flow banding in obsidian: A record of evolving textural heterogeneity during magma deformation. *Earth Planet Sci Lett* 236:135–147. doi:

10.1016/j.epsl.2005.04.031

Gonnermann HM, Manga M (2007) The Fluid Mechanics Inside a Volcano. *Annu Rev Fluid Mech* 39:321–356. doi: 10.1146/annurev.fluid.39.050905.110207

Gonnermann HM, Manga M (2013) Dynamics of magma ascent in the volcanic conduit. In: Fagents SA, Gregg TKP, Lopes RMC (Eds.) *Modeling Volcanic Processes: The Physics and Mathematics of Volcanism*. Cambridge University Press, pp. 55–84.

Griggs RF (1922) *The Valley of Ten Thousand Smokes*. The National Geographic Society, Washington D.C., 340 p.

Hale AJ, Calder ES, Loughlin SC, et al (2009) Modelling the lava dome extruded at Soufriere Hills Volcano, Montserrat, August 2005-May 2006. Part II: Rockfall activity and talus deformation. *J Volcanol Geotherm Res* 187:69–84. doi: 10.1016/j.jvolgeores.2009.08.014

Hammer JE, Cashman K V., Hoblitt RP, Newman S (1999) Degassing and microlite crystallization during pre-climactic events of the 1991 eruption of Mt. Pinatubo, Philippines. *Bull Volcanol* 60:355–380. doi: 10.1007/s004450050238

Hammer JE, Manga M, Cashman K V (1998) Non-equilibrium and unsteady fluid degassing during slow decompression. *Geophys Res Lett* 25:4565–4568. doi: 10.1029/1998GL900194

Hammer JE, Rutherford MJ (2002) An experimental study of the kinetics of decompression-induced crystallization in silicic melt. *J Geophys Res Solid Earth* 107:ECV 8-1-ECV 8-24. doi: 10.1029/2001JB000281

Hammer JE, Rutherford MJ, Hildreth W (2002) Magma storage prior to the 1912 eruption at Novarupta, Alaska. *Contrib to Mineral Petrol* 144:144–162. doi: 10.1007/s00410-002-0393-2

Heap MJ, Wadsworth FB (2016) Closing an open system: Pore pressure changes in permeable edifice rock at high strain rates. *J Volcanol Geotherm Res* 315:40–50. doi: 10.1016/j.jvolgeores.2016.02.011

Hildreth W (1983) The compositionally zoned eruption of 1912 in the Valley of Ten Thousand Smokes, Katmai National Park, Alaska. *J Volcanol Geotherm Res* 18:1–56. doi: 10.1016/0377-0273(83)90003-3

Hildreth W (1987) New perspectives on the eruption of 1912 in the Valley of Ten Thousand Smokes, Katmai National Park, Alaska. *J Volcanol Geotherm Res* 49:680–693. doi: 10.1007/BF01080359

Hildreth W (1991) The timing of caldera collapse at Mount Katmai in response to magma withdrawal toward Novarupta. *Geophys Res Lett* 18:1541–1544.

Hildreth W, Fierstein J (2000) Katmai volcanic cluster and the great eruption of 1912. *Geol Soc*

- Am Bull 112:1594–1620. doi: 10.1130/0016-7606(2000)112<1594
- Hildreth W, Fierstein J (2012) The Novarupta-Katmai Eruption of 1912--Largest Eruption of the Twentieth Century; Centennial Perspectives. U.S. Geological Survey Professional Paper 1791
- Hoblitt RP (1986) Observations of the Eruptions of July 22 and August 7, 1980, at Mount St. Helens, Washington. U.S. Geological Survey Professional Paper 1335, 44p.
- Hoblitt RP, Harmon RS (1993) Bimodal Density Distribution of Cryptodome Dacite from the 1980 Eruption of Mount St. Helens, Washington. Bull Volcanol 55:421–437. doi: 10.1007/BF00302002
- Hoblitt RP, Wolfe EW, Scott WE, et al (1996) The preclimatic eruptions of Mount Pinatubo, June 1991. In: Newhall CG, Punongbayan RS (eds) Fire and Mud: Eruptions and Lahars of Mount Pinatubo, Philippines. University of Washington Press, Seattle, WA, pp 457–511
- Houghton BF, Carey RJ, Cashman K V., et al (2010) Diverse patterns of ascent, degassing, and eruption of rhyolite magma during the 1.8ka Taupo eruption, New Zealand: Evidence from clast vesicularity. J Volcanol Geotherm Res 195:31–47. doi: 10.1016/j.jvolgeores.2010.06.002
- Houghton BF, Wilson CJN (1989) A vesicularity index for pyroclastic deposits. Bull Volcanol 51:451–462. doi: 10.1007/BF01078811
- Houghton BF, Wilson CJN, Fierstein J, Hildreth W (2004) Complex proximal deposition during the Plinian eruptions of 1912 at Novarupta, Alaska. Bull Volcanol 66:95–133. doi: 10.1007/s00445-003-0297-7
- Hui H, Zhang Y (2007) Toward a general viscosity equation for natural anhydrous and hydrous silicate melts. Geochim Cosmochim Acta 71:403–416. doi: 10.1016/j.gca.2006.09.003
- Humphreys MCS, Menand T, Blundy JD, Klimm K (2008) Magma ascent rates in explosive eruptions: Constraints from H₂O diffusion in melt inclusions. Earth 270:25–40. doi: 10.1016/j.epsl.2008.02.041
- Huppert HE, Sparks SJ, Whitehead JA, Hallworth MA (1986) Replenishment of Magma Chambers by Light Inputs. J Geophys Res 91:6113–6122. doi: 10.1029/JB091iB06p06113
- Hurwitz S, Navon O (1994) Bubble nucleation in rhyolitic melts: Experiments at high pressure, temperature, and water content. Earth Planet Sci Lett 122:267–280. doi: 10.1016/0012-821X(94)90001-9
- Ihinger PD, Hervig RL, McMillan PF (1994) Analytical methods for volatiles in glasses. In: Carroll MR, Holloway JR (eds) Volatiles in Magmas, 30th edn. Mineralogical Society of

America, *Reviews in Mineralogy*, pp 67–121

- Isgett SJ, Houghton BF, Fagents SA, et al (2017) Eruptive and shallow conduit dynamics during Vulcanian explosions: insights from the Episode IV block field of the 1912 eruption of Novarupta, Alaska. *Bull Volcanol* 79:58. doi: 10.1007/s00445-017-1138-4
- Jaupart C, Allègre CJ (1991) Gas content, eruption rate and instabilities of eruption regime in silicic volcanoes. *Earth Planet Sci Lett* 102:413–429. doi: 10.1016/0012-821X(91)90032-D
- Jouniaux L, Bernard M-L, Zamora M, Pozzi J-P (2000) Streaming potential in volcanic rocks from Mount Peleé. *J Geophys Res* 105:8391–8401. doi: 10.1029/1999jb900435
- Kennedy BM, Spieler O, Scheu B, et al (2005) Conduit implosion during Vulcanian eruptions. *Geology* 33:581–584. doi: 10.1130/G21488.1
- Kennedy BM, Wadsworth FB, Vasseur J, et al (2016) Surface tension driven processes densify and retain permeability in magma and lava. *Earth Planet Sci Lett* 433:116–124. doi: 10.1016/j.epsl.2015.10.031
- Klug C, Cashman K V. (1996) Permeability development in vesiculating magmas: implications for fragmentation. *Bull Volcanol* 58:87–100. doi: 10.1007/s004450050128
- Koyaguchi T (1987) Magma mixing in a squeezed conduit. *Earth Planet Sci Lett* 84:339–344. doi: 10.1016/0012-821X(87)90097-5
- Koyaguchi T, Blake S (1989) The dynamics of magma mixing in a rising magma batch. *Bull Volcanol* 52:127–137. doi: 10.1007/BF00301552
- Kusakabe M, Sato H, Nakada S, Kitamura T (1999) Water contents and hydrogen isotopic ratios of rocks and minerals from the 1991 eruption of Unzen volcano, Japan. *J Volcanol Geotherm Res* 89:231–242. doi: 10.1016/S0377-0273(98)00134-6
- Kushnir ARL, Martel C, Bourdier JL, et al (2016) Probing permeability and microstructure: Unravelling the role of a low-permeability dome on the explosivity of Merapi (Indonesia). *J Volcanol Geotherm Res* 316:56–71. doi: 10.1016/j.jvolgeores.2016.02.012
- Kushnir ARL, Martel C, Champallier R, Arbaret L (2017) In situ confirmation of permeability development in shearing bubble-bearing melts and implications for volcanic outgassing. *Earth Planet Sci Lett* 458:315–326. doi: 10.1016/j.epsl.2016.10.053
- La Spina G, de Michieli Vitturi M, Clarke AB (2017) Transient numerical model of magma ascent dynamics: application to the explosive eruptions at the Soufrière Hills Volcano. *J Volcanol Geotherm Res* 336:118–139. doi: 10.1016/j.jvolgeores.2017.02.013

- Lautze NC, Houghton BF (2005) Physical mingling of magma and complex eruption dynamics in the shallow conduit at Stromboli volcano, Italy. *Geology* 33:425. doi: 10.1130/G21325.1
- Lavallée Y, Varley NR, Alatorre-Ibargüengoitia MA, et al (2012) Magmatic architecture of dome-building eruptions at Volcán de Colima, Mexico. *Bull Volcanol* 74:249–260. doi: 10.1007/s00445-011-0518-4
- Le Losq C, Neuville DR, Moretti R, Roux J (2012) Determination of water content in silicate glasses using Raman spectrometry: Implications for the study of explosive volcanism. *Am Mineral* 97:779–790. doi: 10.2138/am.2012.3831
- Liu Y, Zhang Y, Behrens H (2005) Solubility of H₂O in rhyolitic melts at low pressures and a new empirical model for mixed H₂O-CO₂ solubility in rhyolitic melts. *J Volcanol Geotherm Res* 143:219–235. doi: 10.1016/j.jvolgeores.2004.09.019
- Lowenstern JB (1993) Evidence for a copper-bearing fluid in magma erupted at the Valley of ten thousand smokes, Alaska. *Contrib to Mineral Petrol* 114:409–421. doi: 10.1007/BF01046542
- Mangan M, Mastin L, Sisson T (2004) Gas evolution in eruptive conduits: combining insights from high temperature and pressure decompression experiments with steady-state flow modeling. *J Volcanol Geotherm Res* 129:23–36.
- Mangan M, Sisson T (2000) Delayed, disequilibrium degassing in rhyolite magma: decompression experiments and implications for explosive volcanism. *Earth Planet Sci Lett* 183:441–455.
- Mangan MT, Sisson TW, Hankins WB (2004) Decompression experiments identify kinetic controls on explosive silicic eruptions. *Geophys Res Lett* 31:1–5. doi: 10.1029/2004GL019509
- Manville V, Major JJ, Fagents SA (2013) Modeling lahar behavior and hazards. In: Fagents SA, Gregg TKP, Lopes RMC (Eds.) *Modeling Volcanic Processes: The Physics and Mathematics of Volcanism*. Cambridge University Press, pp. 300-330.
- Martel C, Iacono-Marziano G (2015) Timescales of bubble coalescence, outgassing, and foam collapse in decompressed rhyolitic melts. *Earth Planet Sci Lett* 412:173–185. doi: 10.1016/j.epsl.2014.12.010
- Martin GC (1913). The recent eruption of Katmai Volcano in Alaska: an account of one of the most tremendous volcanic explosions known in history. *National Geographic Magazine* 24, 131-181.
- Martin E, Bindeman IN, Balan E, et al (2017) Hydrogen isotope determination by TC/EA technique in application to volcanic glass as a window into secondary hydration. *J*

- Volcanol Geotherm Res. doi: 10.1016/j.jvolgeores.2017.10.013
- Mason RM, Starostin AB, Melnik OE, Sparks RSJ (2006) From Vulcanian explosions to sustained explosive eruptions: The role of diffusive mass transfer in conduit flow dynamics. doi: 10.1016/j.jvolgeores.2005.08.011
- Mastin LG (2001) A simple calculator of ballistic trajectories for blocks ejected during volcanic eruptions. US Geol Surv Open-File Rep 2001-45 13 p.
- Matthews SJ, Gardeweg MC, Sparks RSJ (1997) The 1984 to 1996 cyclic activity of Lascar Volcano, northern Chile: cycles of dome growth, dome subsidence, degassing and explosive eruptions. Bull Volcanol 59:72–82. doi: 10.1007/s004450050176
- McIntosh IM, Llewellyn EW, Humphreys MCS, et al (2014) Distribution of dissolved water in magmatic glass records growth and resorption of bubbles. Earth Planet Sci Lett 401:1–11. doi: 10.1016/j.epsl.2014.05.037
- Melnik O, Sparks RSJ (1999) Nonlinear dynamics of lava dome extrusion. Nature 402:37–41. doi: 10.1038/46950
- Melnik O, Sparks RSJ (2002a) Dynamics of magma ascent and lava extrusion at Soufriere Hills Volcano, Montserrat. In: Druitt TH, Kokelaar BP (eds) The eruption of Soufrière Hills volcano, Montserrat, from 1995 to 1999. Geol Soc Lond Mem 21:153–171. doi: 10.1144/GSL.MEM.2002.021.01.07
- Melnik O, Sparks RSJ (2002b) Modelling of conduit flow dynamics during explosive activity at Soufrière Hills Volcano, Montserrat. In: Druitt TH, Kokelaar BP (eds) The eruption of Soufrière Hills volcano, Montserrat, from 1995 to 1999. Geol Soc Lond Mem 21:307–318. doi: 10.1144/GSL.MEM.2002.21.01.14
- Melnik OE, Sparks RSJ, Costa A, Barmin AA (2009) Volcanic Eruptions : Cyclicity during Lava Dome Growth. In: Meyers RA (ed) Encyclopedia of Complexity and Systems Science. Springer Verlag, New York, pp 1–22
- Minakami T (1942) On the distribution of volcanic ejecta (Part I.): The distributions of volcanic bombs ejected by the recent explosions of Asama. Bull. Earthq. Res. Inst. 20:65–92.
- Mourtada-Bonnefoi CC, Laporte D (2004) Kinetics of bubble nucleation in a rhyolitic melt: an experimental study of the effect of ascent rate. Earth Planet Sci Lett 218:521–537. doi: 10.1016/S0012-821X(03)00684-8
- Mueller S, Melnik O, Spieler O, et al (2005) Permeability and degassing of dome lavas undergoing rapid decompression: An experimental determination. Bull Volcanol 67:526–538. doi: 10.1007/s00445-004-0392-4
- Nairn IA, Self S (1978) Explosive eruptions and pyroclastic avalanches from Ngauruhoe in

- February 1975. *J Volcanol Geotherm Res* 3:39–60.
- Namiki A (2012) An empirical scaling of shear-induced outgassing during magma ascent: Intermittent magma ascent causes effective outgassing. *Earth Planet Sci Lett* 353–354:72–81. doi: 10.1016/j.epsl.2012.08.007
- Namiki A, Manga M (2005) Response of a bubble bearing viscoelastic fluid to rapid decompression: Implications for explosive volcanic eruptions. *Earth Planet Sci Lett* 236:269–284. doi: 10.1016/j.epsl.2005.02.045
- Namiki A, Manga M (2007) Transition between fragmentation and permeable outgassing of low viscosity magmas. doi: 10.1016/j.jvolgeores.2007.07.020
- Newman S, Lowenstern JB (2002) VolatileCalc: a silicate melt–H₂O–CO₂ solution model written in Visual Basic for excel. *Comput Geosci* 28:597–604.
- Nguyen CT, Gonnermann HM, Houghton BF (2014) Explosive to effusive transition during the largest volcanic eruption of the 20th century (Novarupta 1912, Alaska). *Geology* 42:703–706. doi: 10.1130/G35593.1
- Nolan GS, Bindeman IN (2013) Experimental investigation of rates and mechanisms of isotope exchange (O, H) between volcanic ash and isotopically-labeled water. *Geochim Cosmochim Acta* 111:5–27. doi: 10.1016/j.gca.2013.01.020
- Okumura S, Nakamura M, Takeuchi S, et al (2009) Magma deformation may induce non-explosive volcanism via degassing through bubble networks. *Earth Planet Sci Lett* 281:267–274. doi: 10.1016/j.epsl.2009.02.036
- Okumura S, Nakamura M, Tsuchiyama A, et al (2008) Evolution of bubble microstructure in sheared rhyolite: Formation of a channel-like bubble network. *J Geophys Res Solid Earth* 113:1–18. doi: 10.1029/2007JB005362
- Okumura S, Nakamura M, Uesugi K, et al (2013) Coupled effect of magma degassing and rheology on silicic volcanism. *Earth Planet Sci Lett* 362:163–170. doi: 10.1016/j.epsl.2012.11.056
- Papale P (1999) Strain-induced magma fragmentation in explosive eruptions. *Nature* 397:425–428. doi: 10.1038/17109
- Perugini D, Poli G (2012) The mixing of magmas in plutonic and volcanic environments: Analogies and differences. *Lithos* 153:261–277. doi: 10.1016/j.lithos.2012.02.002
- Perugini D, Poli G, Mazzuoli R (2003) Chaotic advection, fractals and diffusion during mixing of magmas: evidence from lava flows. *J Volcanol Geotherm Res* 124:255–279. doi: 10.1016/S0377-0273(03)00098-2
- Perugini D, Valentini L, Poli G (2007) Insights into magma chamber processes from the analysis

- of size distribution of enclaves in lava flows: A case study from Vulcano Island (Southern Italy). *J Volcanol Geotherm Res* 166:193–203. doi: 10.1016/j.jvolgeores.2007.07.017
- Perugini D, Ventura G, Petrelli M, Poli G (2004) Kinematic significance of morphological structures generated by mixing of magmas: a case study from Salina Island (southern Italy). *Earth Planet Sci Lett* 222:1051–1066. doi: 10.1016/j.epsl.2004.03.038
- Platz T, Cronin SJ, Cashman K V., et al (2007) Transition from effusive to explosive phases in andesite eruptions - A case-study from the AD1655 eruption of Mt. Taranaki, New Zealand. *J Volcanol Geotherm Res* 161:15–34. doi: 10.1016/j.jvolgeores.2006.11.005
- Polacci M, Papale P, Rosi M (2001) Textural heterogeneities in pumices from the climactic eruption of Mount Pinatubo, 15 June 1991, and implications for magma ascent dynamics. *Bull Volcanol* 63:83–97. doi: 10.1007/s004450000123
- Proussevitch AA, Sahagian DL (1996) Dynamics of coupled diffusive and decompressive bubble growth in magmatic systems. *J Geophys Res* 101:455:447–17. doi: 10.1029/96JB01342
- Proussevitch AA, Sahagian DL (1998) Dynamics and energetics of bubble growth in magmas: Analytical formulation and numerical modeling. *J Geophys Res Solid Earth* 103:18223–18251. doi: 10.1029/98JB00906
- Proussevitch AA, Sahagian DL, Anderson AT (1993) Dynamics of diffusive bubble growth in magmas: Isothermal case. *J Geophys Res Solid Earth* 98:22283–22307. doi: 10.1029/93JB02027
- Reynolds, O (1900) *Papers on Mechanical and Physical Subjects*. Cambridge University Press.
- Robertson R, Cole PD, Sparks RSJ, et al (1998) The explosive eruption of Soufriere Hills Volcano, Montserrat, West Indies, 17 September, 1996. *Geophys Res Lett* 25:3429–3432.
- Rosi M, Landi P, Polacci M, et al (2004) Role of conduit shear on ascent of the crystal-rich magma feeding the 800-year-b.p. Plinian eruption of Quilotoa Volcano (Ecuador). *Bull Volcanol* 66:307–321. doi: 10.1007/s00445-003-0312-z
- Rust AC, Cashman K V. (2011) Permeability controls on expansion and size distributions of pyroclasts. *J Geophys Res Solid Earth* 116:1–17. doi: 10.1029/2011JB008494
- Rust AC, Cashman K V. (2004) Permeability of vesicular silicic magma: Inertial and hysteresis effects. *Earth Planet Sci Lett* 228:93–107. doi: 10.1016/j.epsl.2004.09.025
- Rust AC, Cashman K V., Wallace PJ (2004) Magma degassing buffered by vapor flow through brecciated conduit margins. *Geology* 32:349–352. doi: 10.1130/G20388.2
- Saar MO, Manga M (1999) Permeability-porosity relationship in vesicular basalts. *Geophys Res Lett* 26:111–114. doi: 10.1029/1998GL900256

- Sahetapy-Engel ST, Harris AJL (2009) Thermal structure and heat loss at the summit crater of an active lava dome. *Bull Volcanol* 71:15–28. doi: 10.1007/s00445-008-0204-3
- Sahetapy-Engel ST, Harris AJL, Marchetti E (2008) Thermal, seismic and infrasound observations of persistent explosive activity and conduit dynamics at Santiaguito lava dome, Guatemala. *J Volcanol Geotherm Res* 173:1–14. doi: 10.1016/j.jvolgeores.2007.11.026
- Salzer JT, Milillo P, Varley N, et al (2017) Evaluating links between deformation, topography and surface temperature at volcanic domes: Results from a multi-sensor study at Volcán de Colima, Mexico. *Earth Planet Sci Lett* 479:354–365. doi: <https://doi.org/10.1016/j.epsl.2017.09.027>
- Saubin E, Tuffen H, Gurioli L, et al (2016) Conduit Dynamics in Transitional Rhyolitic Activity Recorded by Tuffisite Vein Textures from the 2008–2009 Chaitén Eruption. *Front Earth Sci*. doi: 10.3389/feart.2016.00059
- Scheu B, Kueppers U, Mueller S, et al (2008) Experimental volcanology on eruptive products of Unzen volcano. *J Volcanol Geotherm Res* 175:110–119. doi: 10.1016/j.jvolgeores.2008.03.023
- Scheu B, Spieler O, Dingwell DB (2006) Dynamics of explosive volcanism at Unzen volcano: An experimental contribution. *Bull Volcanol* 69:175–187. doi: 10.1007/s00445-006-0066-5
- Schipper CI, Castro JM, Tuffen H, et al (2013) Shallow vent architecture during hybrid explosive-effusive activity at Cordón Caulle (Chile, 2011–12): Evidence from direct observations and pyroclast textures. *J Volcanol Geotherm Res* 262:25–37. doi: 10.1016/j.jvolgeores.2013.06.005
- Schmincke H-U (1977) Eifel-Vulkanismus ostlich des Gebiets Rieden-Mayen. *Fortschritte der Mineral* 55:1–31.
- Seaman SJ, Dyar MD, Marinkovic N (2009) The effects of heterogeneity in magma water concentration on the development of flow banding and spherulites in rhyolitic lava. *J Volcanol Geotherm Res* 183:157–169. doi: 10.1016/j.jvolgeores.2009.03.001
- Seaman SJ, Scherer EE, Standish JJ (1995) Multistage magma mingling and the origin of flow banding in the Aliso lava dome, Tumacacori Mountains, southern Arizona. *J Geophys Res Solid Earth* 100:8381–8398. doi: 10.1029/94JB03260
- Self S, Keinle J, Huot J-P (1980) Ukinrek Maars, Alaska, II. Deposit and formation of the 1977 craters. *J Volcanol Geotherm Res* 7:39–65.
- Self S, Wilson L, Nairn IA (1979) Vulcanian eruption mechanisms. *Nature* 277:440–443.

- Seligman AN, Bindeman IN, Watkins JM, Ross AM (2016) Water in volcanic glass: From volcanic degassing to secondary hydration. *Geochim Cosmochim Acta* 191:216–238. doi: 10.1016/j.gca.2016.07.010
- Shea T, Gurioli L, Houghton BF (2012) Transitions between fall phases and pyroclastic density currents during the AD 79 eruption at Vesuvius: Building a transient conduit model from the textural and volatile record. *Bull Volcanol* 74:2363–2381. doi: 10.1007/s00445-012-0668-z
- Shea T, Hellebrand E, Gurioli L, Tuffen H (2014) Conduit- to localized-scale degassing during plinian eruptions: Insights from major element and volatile (Cl and H₂O) analyses within Vesuvius AD 79 pumice. *J Petrol* 55:315–344. doi: 10.1093/petrology/egt069
- Shields JK, Mader HM, Pistone M, et al (2014) Strain-induced outgassing of three-phase magmas during simple shear. *J Geophys Res B Solid Earth* 119:6936–6957. doi: 10.1002/2014JB011111
- Silver LA, Ihinger PD, Stolper E (1990) The influence of bulk composition on the speciation of water in silicate glasses. *Contrib to Mineral Petrol* 104:142–162. doi: 10.1007/BF00306439
- Sparks RSJ (1997) Causes and consequences of pressurisation in lava dome eruptions. *Earth Planet Sci Lett* 150:177–189. doi: 10.1016/S0012-821X(97)00109-X
- Sparks RSJ (1978) The dynamics of bubble formation and growth in magmas: A review and analysis. *J Volcanol Geotherm Res* 3:1–37. doi: 10.1016/0377-0273(78)90002-1
- Sparks RSJ, Barclay J, Jaupart C, Mader HM, Phillips JC (1994) Physical aspects of magmatic degassing I. Experimental and theoretical constraints on vesiculation. In: Carroll MR, Holloway JR (Eds.) *Volatiles in Magmas, Reviews in Mineralogy* 30, 415–445.
- Sparks RSJ, Bursik MI, Carey SN, et al (1997) *Volcanic Plumes*. John Wiley, New York
- Spieler O, Kennedy B, Kueppers U, et al (2004) The fragmentation threshold of pyroclastic rocks. *Earth Planet Sci Lett* 226:139–148. doi: 10.1016/j.epsl.2004.07.016
- Stix J, Torres RC, Narváez LM, et al (1997) A model of vulcanian eruptions at Galeras volcano, Colombia. *J Volcanol Geotherm Res* 77:285–303. doi: 10.1016/S0377-0273(96)00100-X
- Stovall WK, Houghton BF, Hammer JE, et al (2012) Vesiculation of high fountaining Hawaiian eruptions: Episodes 15 and 16 of 1959 Kīlauea Iki. *Bull Volcanol* 74:441–455. doi: 10.1007/s00445-011-0531-7
- Tait S, Jaupart C, Vergnolle S (1989) Pressure, gas content and eruption periodicity of a shallow, crystallising magma chamber. *Earth Planet Sci Lett* 92:107–123. doi: 10.1016/0012-821X(89)90025-3

- Taddeucci J, Alatorre-Ibargüengoitia MA, Cruz-Vázquez O, et al (2017) In-flight dynamics of volcanic ballistic projectiles. *Rev Geophys* 1–44. doi: 10.1002/2017RG000564
- Taddeucci J, Edmonds M, Houghton B, James MR, Vergnolle S (2015) Hawaiian and Strombolian Eruptions. In: Sigurdsson H, Houghton BF, McNutt SR, Rymer H, Stix J (Eds.) *Encyclopedia of Volcanoes* (2nd edition). Academic Press, pp. 485–504.
- Takeuchi S, Tomiya A, Shinohara H (2009) Degassing conditions for permeable silicic magmas: Implications from decompression experiments with constant rates. *Earth Planet Sci Lett* 283:101–110. doi: 10.1016/j.epsl.2009.04.001
- Tamic N, Behrens H, Holtz F (2001) The solubility of H₂O and CO₂ in rhyolitic melts in equilibrium with a mixed CO₂–H₂O fluid phase. *Chem Geol* 174:333–347.
- Taylor BE (1991) Degassing of Obsidian Dome rhyolite, Inyo volcanic chain, California. In: Taylor Jr. HP, O’Neil JR, Kaplan IR (eds) *Stable Isotope Geochemistry: A Tribute to Samuel Epstein*. The Geochemical Society, Special Publication, pp 339–353
- Taylor BE, Eichelberger JC, Westrich HR (1983) Hydrogen isotopic evidence of rhyolitic magma degassing during shallow intrusion and eruption. *Nature* 306:541.
- Thomas R (2000) Determination of water contents of granite melt inclusions by confocal laser Raman microprobe spectroscopy. *Am Mineral* 85:868–872.
- Toramaru A (2006) BND (bubble number density) decompression rate meter for explosive volcanic eruptions. *J Volcanol Geotherm Res* 154:303–316. doi: 10.1016/j.jvolgeores.2006.03.027
- Toramaru A (1995) Numerical study of nucleation and growth of bubbles in viscous magmas. *J Geophys Res Solid Earth* 100:1913–1931. doi: 10.1029/94JB02775
- Tuffen H, Dingwell D (2005) Fault textures in volcanic conduits: Evidence for seismic trigger mechanisms during silicic eruptions. *Bull Volcanol* 67:370–387. doi: 10.1007/s00445-004-0383-5
- Tuffen H, Dingwell DB, Pinkerton H (2003) Repeated fracture and healing of silicic magma generate flow banding and earthquakes? *Geology* 31:1089–1092. doi: 10.1130/G19777.1
- Tuffen H, Smith R, Sammonds PR (2008) Evidence for seismogenic fracture of silicic magma. *Nature* 453:511–514. doi: 10.1038/nature06989
- Turcotte DL, Ockendon H, Ockendon JR, Cowley SJ (1990) A mathematical model of vulcanian eruptions. *Geophys J Int* 103:211–217. doi: 10.1111/j.1365-246X.1990.tb01763.x
- Underwood SJ, Feeley TC, Clyne MA (2013) Hydrogen isotope investigation of amphibole and glass in dacite magmas erupted in 1980–1986 and 2005 at Mount St. Helens, Washington. *J Petrol* 54:1047–1070. doi: 10.1093/petrology/egt005

- Vanderkluyzen L, Harris AJL, Kelfoun K, et al (2012) Bombs behaving badly: unexpected trajectories and cooling of volcanic projectiles. *Bull Volcanol* 74:1849–1858. doi: 10.1007/s00445-012-0635-8
- Vallance JW, Bull KF, Coombs ML (2010) Pyroclastic Flows, Lahars, and Mixed Avalanches Generated During the 2006 Eruption of Augustine Volcano. In: Power JA, Coombs ML, Freymueller JT (Eds.) *The 2006 Eruption of Augustine Volcano, Alaska, U.S. Geological Survey Professional Paper 1769*, pp. 219-267.
- Vogel TA, Eichelberger JC, Younker LW, et al (1989) Petrology and emplacement dynamics of intrusive and extrusive rhyolites of Obsidian Dome, Inyo Craters Volcanic Chain, eastern California. *J Geophys Res* 94:17937–17956. doi: 10.1029/JB094iB12p17937
- Voight B, Sparks RSJ, Miller AD, et al (1999) Magma Flow Instability and Cyclic Activity at Soufriere Hills Volcano, Montserrat, British West Indies. *Science* 283 (5405): 1138-1142. doi:10.1126/science.283.5405.1138
- Wada K (1995) Fractal structure of heterogeneous ejecta from the Me-akan volcano, eastern Hokkaido, Japan: implications for mixing mechanism in a volcanic conduit. *J Volcanol Geotherm Res* 66:69–79. doi: 10.1016/0377-0273(94)00052-I
- Waitt RB, Mastin LG, Miller TP (1995) Ballistic showers during Crater Peak eruptions of Mount Spurr Volcano, summer 1992. In: Keith TEC (ed) *The 1992 Eruptions of Crater Peak Vent, Mount Spurr Volcano, Alaska*. U.S. Geological Survey Bulletin B-2139, pp 89–106
- Walker GPL (1969) The breaking of magma. *Geol Mag* 106:166–173. doi: 10.1017/S0016756800051979
- Walker GPL (1973) Explosive volcanic eruptions – a new classification scheme. *Geologische Rundschau* 62:431–446. doi:10.1007/BF01840108
- Wallmann PC, Pollard DD, Hildreth W, Eichelberger JC (1990) New structural limits on magma chamber locations at the Valley of Ten Thousand Smokes, Katmai National Park, Alaska. *Geology* 18:1240–1243. doi: 10.1130/0091-7613(1990)018<1240:NSLOMC>2.3.CO;2
- Watkins JM, Manga M, DePaolo DJ (2012) Bubble geobarometry: A record of pressure changes, degassing, and regassing at Mono Craters, California. *Geology* 40:699–702. doi: 10.1130/G33027.1
- Westrich HR, Eichelberger JC (1994) Gas transport and bubble collapse in rhyolitic magma: an experimental approach. *Bull Volcanol* 56:447–458. doi: 10.1007/BF00302826
- Westrich HR, Eichelberger JC, Hervig RL (1991) Degassing of the 1912 Katmai magmas. *Geophys Res Lett* 18:1561–1564. doi: 10.1029/91GL01667
- Williamson BJ, Di Muro A, Horwell CJ, et al (2010) Injection of vesicular magma into an

- andesitic dome at the effusive-explosive transition. *Earth Planet Sci Lett* 295:83–90. doi: 10.1016/j.epsl.2010.03.027
- Wilson CJN, Houghton BF (2000) Pyroclast transport and deposition. In: Sigurdsson H, Houghton BF, McNutt SR, Rymer H, Stix J (Eds.) *Encyclopedia of Volcanoes* (1st edition). Academic Press, pp. 546–554.
- Wilson L (1972) Explosive Volcanic Eruptions-II The Atmospheric Trajectories of Pyroclasts. *Geophys J Int* 30:381–392. doi:10.1111/j.1365-246X.1972.tb05822.x
- Woods AW (1995) A model of vulcanian explosions. *Nucl Eng Des* 155:345–357. doi: 10.1016/0029-5493(94)00881-X
- Woods AW, Koyaguchi T (1994) Transitions between explosive and effusive eruptions of silicic magmas. *Nature* 370:641–644. doi: 10.1038/370641a0
- Wright HMN, Cashman K V., Rosi M, Cioni R (2007) Breadcrust bombs as indicators of Vulcanian eruption dynamics at Guagua Pichincha volcano, Ecuador. *Bull Volcanol* 69:281–300. doi: 10.1007/s00445-006-0073-6
- Wright HMN, Cashman K V, Gottesfeld EH, Roberts JJ (2009) Pore structure of volcanic clasts: Measurements of permeability and electrical conductivity. *Earth Planet Sci Lett* 280:93–104. doi: 10.1016/j.epsl.2009.01.023
- Wright HMN, Folkes CB, Cas RAF, Cashman K V. (2011) Heterogeneous pumice populations in the 2.08-Ma Cerro Gal??n Ignimbrite: Implications for magma recharge and ascent preceding a large-volume silicic eruption. *Bull Volcanol* 73:1513–1533. doi: 10.1007/s00445-011-0525-5
- Wright HMN, Roberts JJ, Cashman K V. (2006) Permeability of anisotropic tube pumice: Model calculations and measurements. *Geophys Res Lett* 33:L17316. doi: 10.1029/2006GL027224
- Yamagishi H, Feebrey C (1994) Ballistic ejecta from the 1988–1989 andesitic Vulcanian eruptions of Tokachidake volcano, Japan: morphological features and genesis. *J Volcanol Geotherm Res* 59:269–278. doi: 10.1016/0377-0273(94)90082-5
- Yokoo A, Iguchi M, Tameguri T, Yamamoto K (2013) Processes Prior to Outbursts of Vulcanian Eruption at Showa Crater of Sakurajima Volcano. *Bull Volcanol Soc Japan* 58:163–181. doi: 10.18940/kazan.58.1_163
- Yokoo A, Tameguri T, Iguchi M (2009) Swelling of a lava plug associated with a Vulcanian eruption at Sakurajima Volcano, Japan, as revealed by infrasound record: Case study of the eruption on January 2, 2007. *Bull Volcanol* 71:619–630. doi: 10.1007/s00445-008-0247-5

Yoshimura S, Nakamura M (2008) Diffusive dehydration and bubble resorption during open-system degassing of rhyolitic melts. *J Volcanol Geotherm Res* 178:72–80. doi: 10.1016/j.jvolgeores.2008.01.017

Zhang Y (1999) A criterion for the fragmentation of bubbly magma based on brittle failure theory. *Nature* 402:648–650. doi: 10.1038/45210

Zhang Y, Behrens H, Zhang Y (2000) H₂O diffusion in rhyolitic melts and glasses. *Chem Geol* 169:243–262. doi: 10.1016/S0009-2541(99)00231-4